Low-temperature gettering in multicrystalline silicon materials for photovoltaics

By

Mohammad Al-Amin

A thesis submitted in partial fulfilment of the requirements for the degree of

Doctor of Philosophy

Supervisor: Dr John D. Murphy

School of Engineering, University of Warwick

August 2017

Table of contents

List of figures

List of tables

Acknowledgements

Firstly, I thank God the most almighty for giving me the ability to complete my PhD thesis. I would like to express my indebted gratitude to my thesis supervisor, Dr John D. Murphy. He has always been extremely generous and enthusiastic throughout this thesis work. He has helped me develop critical thinking and designing experiments. He has provided scientific resources and helped me in connecting with the other research groups in silicon material field. He has provided me an exceptional support in analysing experimental results, preparing manuscripts for journal publications. Without his contribution, it could not have been possible to publish our results in leading journals.

I would like to acknowledge the team in the Engineering School at Warwick University for providing a Departmental Scholarship which allowed to this research work. I thank Professor Tim Ashley for his support. I would like to thank Dr Peter Gammon and Dr Nicholas Grant for valuable discussion. I am also grateful to Dr Mark Crouch and Corinne Maltby for their support and training in the Science City Cleanroom Facility. I thank the all the staff members in the Materials Lab in the Engineering School for providing support in using the SEM and Profilometer. I thank my friend Chun Wa Chan at Warwick and all other friends for their support. I would like to give special thanks to my colleagues at the Coventry University College for their support.

I like to acknowledge PV Crystalox Solar for providing experimental wafers for this thesis work. I also thank the Technical team in the BT Imaging in Australia and Adrienne Blum from Sinton Instruments in the USA for their support in developing and calibrating lifetime characterisation tools in the Semiconductor Materials lab at Warwick.

I would like to thank Dr Karsten Bothe at ISFH, Germany for providing support in passivating samples by PECVD silicon nitride. I also thank Professor Giso Hahn at Universität Konstanz, Germany for proving support in phosphorus diffusion gettering process for a large number of samples. I thank EPSRC and the Engineering School at Warwick for providing financial support for my attendance at the IEEE PVSC conference.

I am grateful to my parents and family members for their prayers and support in completing this thesis. I would like to give a special thank to my wife Shaila Yeastarin for her amazing sacrifice and support during my study period. Finally, I thank my little son Tahmeed Anaam for making my life enjoyable in last two years.

Declaration

This thesis is submitted in partial fulfilment for the degree of Doctor of Philosophy under the regulations set out by the Graduate School at the University of Warwick. I certify that this thesis does not incorporate any material without acknowledgement previously submitted to any institution for a higher degree or previously published. The work is this thesis is my own except where stated, under the supervision of Dr John D. Murphy.

Mohammad Al-Amin

August 2017

List of publications

Work presented in this thesis has been published and submitted in the following scientific journals or conference proceedings:

Journal articles

1. M. Al-Amin and J. D. Murphy, "Passivation effects on low temperature gettering in multicrystalline silicon," *IEEE Journal of Photovoltaics*, vol. 7, 68-77, 2017.
2. M. Al-Amin and J. D. Murphy, "Increasing minority carrier lifetime in as-grown multicrystalline silicon by low temperature internal gettering," *Journal of Applied Physics*, vol. 119, 235704, 2016.
3. M. Al-Amin and J. D. Murphy, "Low temperature internal gettering of bulk defects in silicon photovoltaic materials," *Solid State Phenomena*, vol. 242, 109 - 119, 2016.
4. M. Al-Amin, J. D. Murphy, Combining low-temperature gettering with phosphorus diffusion gettering for improved multicrystalline silicon, *IEEE Journal of Photovoltaics*, (accepted), 2017.

Conference papers

1. M. Al-Amin, J. D. Murphy, Hydrogenation effect on low temperature internal gettering in multicrystalline silicon, *Proceedings of the 43rd IEEE Photovoltaic Specialists Conference*, 0585 – 0590, Oregon, USA, 2016.
2. M. Al-Amin, J. D. Murphy, Low temperature gettering for improved multicrystalline silicon, *7th International Conference on Crystalline Silicon Photovoltaics*, Freiburg, Germany, 2017.
3. M. Al-Amin, J. D. Murphy, Using low temperature gettering to improve multicrystalline silicon for photovoltaics, *17th Gettering and Defect Engineering in Semiconductor Technology*, (accepted for an oral presentation), Georgia, 2017.

Abstract

This thesis presents results on the effects of low-temperature gettering processes on minority carrier lifetime in multicrystalline silicon. Wafers are sourced from different height positions of a commercially-grown ingot. The distribution of different key material properties including bulk lifetime, interstitial iron concentration, and dislocation density are characterised and are found to vary widely with ingot height position. Lifetimes are measured by using temporary liquid iodine-ethanol passivation at room temperature or silicon nitride films deposited by plasma-enhanced chemical vapour deposition. Lifetimes are lower in samples from the extrema of ingot than the centre parts. Interstitial iron concentrations are found to be highest in the bottom samples and lowest at the centre of the ingot. Dislocation density is lowest at the bottom of the ingot and increases with ingot height position.

In as-grown wafers, low-temperature gettering can improve lifetime substantially in relatively poor samples from the extrema of the ingot. Iodine-ethanol passivation is used to separate thermal effects of annealing from any bulk passivation which may occur during surface passivation from lifetime measurement. The largest relative lifetime improvement (from 5.5 μs to 38.7 μs) is achieved in material from the bottom of the ingot with annealing at 400 °C for 35 h. The benefit of low-temperature annealing is marginal for middle samples. Bulk interstitial iron concentrations decrease by up to 2.1 order of magnitude in the bottom samples. The reduction in interstitial iron concentration is not found to be systematically dependent on annealing temperature. For bottom samples a good correlation between the changes in lifetime and interstitial iron concentration is found.

The effects of different passivation schemes on low-temperature gettering is also investigated. The results show that starting lifetime and interstitial iron concentration strongly depends on the choice of passivation scheme. The effect of different surface passivation schemes is more pronounced in relatively high lifetime samples. In samples from the bottom of the middle of the wafer, lifetime improves from 113 μs to 171 μs with silicon nitride passivation upon annealing at 400 °C for 25 h. Supporting results from secondary ion mass spectrometry show that substantial concentrations of iron exist in the silicon nitride film after low-temperature annealing. This suggests silicon nitride layer might be an additional gettering centre for interstitial iron.

This thesis also studies the effects of low-temperature annealing combined with a standard phosphorus diffusion process to form an emitter. Lifetime in samples from the top and bottom of the ingot can be improved by annealing at 300 °C and 400 °C even after the phosphorus diffusion process. The largest improvement is from 54 μs to 78 μs upon post-diffusion annealing of bottom samples at 300 °C, and the results suggest gettering of impurities other than interstitial iron is likely. The phosphorus diffused emitter layers do not act as effective additional gettering sites for interstitial iron upon low-temperature annealing. The lifetime improvement upon pre-diffusion annealing is retained after the diffusion process. In summary, low-temperature annealing has the potential to improve the lifetime in as-grown multicrystalline silicon and after a phosphorus diffusion gettering under some conditions. Low-temperature annealing thus provides a potential low cost route to improve multicrystalline solar cell efficiencies.

List of symbols and abbreviations

B	Bottom
CO_2	Carbon dioxide
c-Si	Crystalline silicon
Cz	Czochralski
Fe	Iron
Fe_i	Interstitial iron
FeB or Fe_iB_s	Iron-boron pair
$[Fe_i]$	Interstitial iron concentration
FZ	Float zone
GBs	Grain boundaries
I-E	Iodine-ethanol
LTG	Low-temperature gettering
mc-Si	Multicrystalline silicon
MB	Bottom middle
MT	Top middle
N_A	Acceptor concentration
PECVD	Plasma-enhanced chemical vapour deposition
PDG	Phosphorus diffusion gettering
PV	Photovoltaics
PL	Photoluminescence
QSS-PC	Quasi-steady-state photoconductance
Si	Silicon
SIMS	Secondary ion mass spectrometry

SiN_x	Silicon nitride
sc-Si	Single crystal silicon
SRH	Shockley-Read-Hall
T	Top
τ	Carrier lifetime
Δn	Excess electron concentration

Chapter 1 Introduction

1.1. Thesis motivation

The emission of carbon dioxide (CO_2) and other greenhouse gasses has increased rapidly because of the extensive use of fossil fuels to meet global energy demand as shown in Figure 1.1 [1]. Additionally, rapid depletion and shortage of fossil fuel resources mean urgent attention to alternative renewable energy (known as 'clean energy') is required. This is currently 1.4% of world's total primary energy supply as shown in Figure 1.2 [1]. Among the various renewable energy resources, photovoltaics (PV), which enables the direct conversion of sunlight into electricity without CO_2 emission during operation, can play a significant role in securing increasing global energy supply in the 21st century whilst potentially reducing CO_2 emissions.

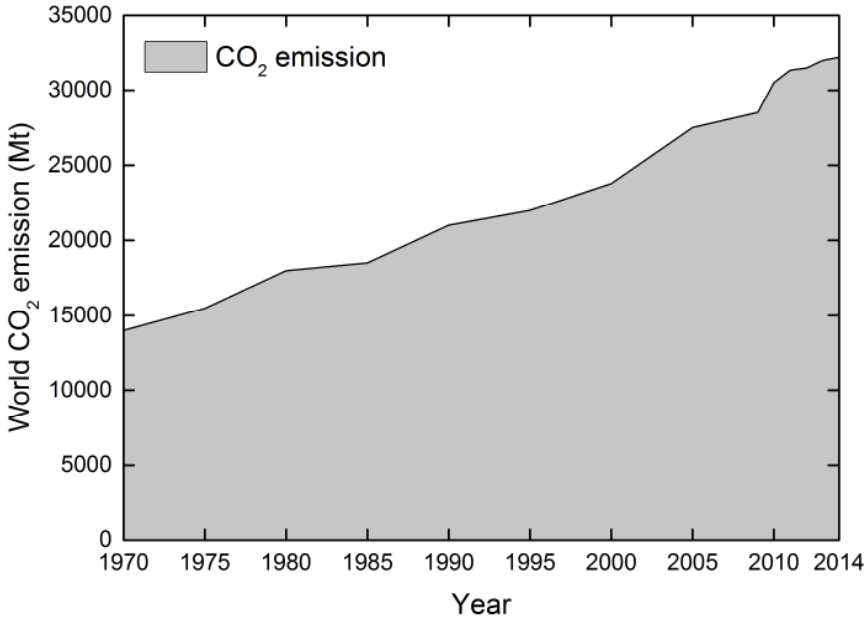

Figure 1.1. World total CO_2 emission from 1971 to 2014 from the combustion of fossil fuels, industrial waste and non-renewable municipal waste [1].

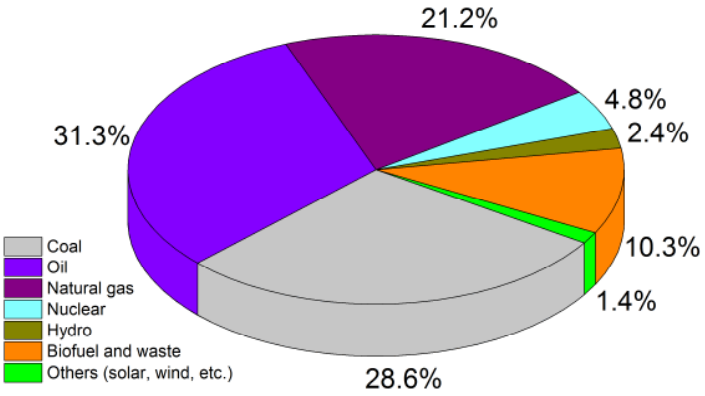

Figure 1.2. Distribution of world total primary energy supply in 2014 from different fuel resources [1].

Recently, the world's cumulative photovoltaic (PV) capacity has surpassed 200 GW installed peak capacity, as shown in Figure 1.3, which is capable of saving more than 100 million tonnes of CO_2 emission on an annual basis [2]. Over the past decade, the average annual growth rate of the global PV market is 40%, and wafer-based crystalline silicon (c-Si) represent more than 90% of the PV industry [3]. Crystalline silicon is expected to remain a dominant PV technology due to it being a proven and reliable technology, having long operational lifetimes and there being abundant primary resources. Although the PV market is expanding rapidly, the main challenge for c-Si cell technology is to improve efficiency without increasing (and ideally reducing) fabrication processing cost. In the last two decades, the cost of silicon solar cell was reduced by more than a factor of ten [4] but it requires further reduction to compete with the energy supply from conventional fossil fuel resources under all conditions.

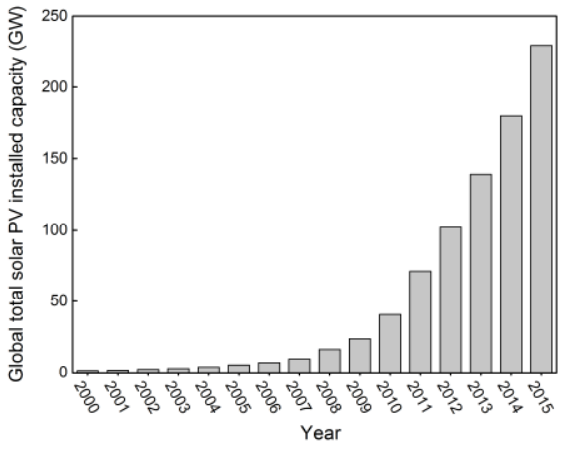

Figure 1.3. Evolution of global total PV cumulative installed capacity. The European market accounts for the largest global share (42.3%) [2].

In the standard silicon solar cell technologies, the bulk silicon material accounts for more than 50% of the total cell manufacturing cost [3]. Therefore, it is important to lower the material cost which can be achieved either by (a) reducing wafer thickness or (b) lowering the manufacturing cost. Recently, the PV industry uses silicon wafers with a thickness of ~150 μm to 180 μm [3, 5]. However, further reduction in thickness would require more sophisticated cell processing tools which would increase cell processing cost. It is, therefore, important to use cheap silicon material and lower wafer processing cost. Multicrystalline silicon (mc-Si) material has ~20% lower production cost compared to single crystal silicon (sc-Si) material [6]. Currently, mc-Si wafers dominate the PV market and, due to their lower manufacturing cost, it is expected this will continue. Figure 1.4 shows that 69% of total PV production was from mc-Si material in 2015 [7]. However, a number of challenges need to be overcome to make this material more viable in the PV industry.

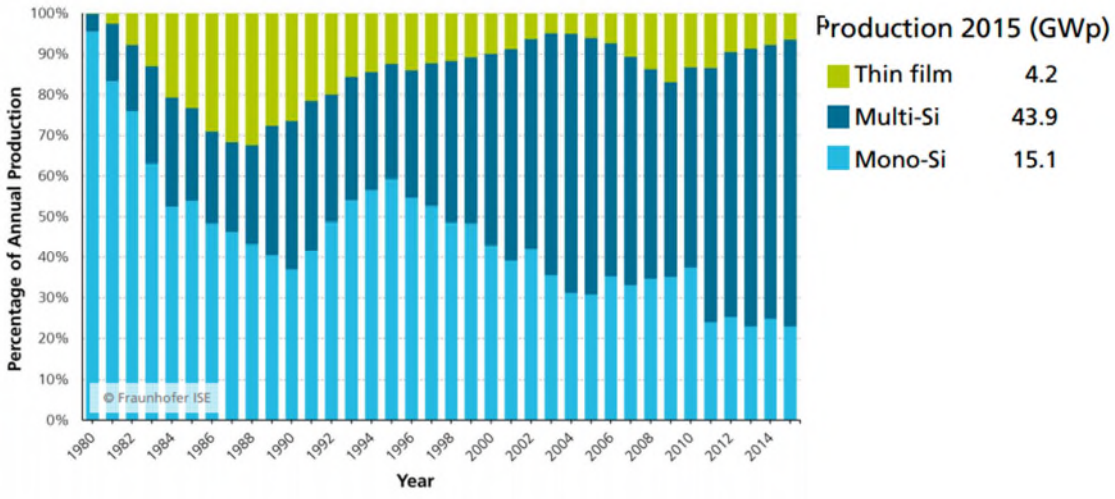

Figure 1.4. Worldwide usage of the different type of silicon materials in cell processing (under standard operating conditions (Wp)) at photovoltaic industries [7].

1.2. Multicrystalline silicon material for photovoltaics

Standard multicrystalline silicon solar cells use *p* or *n*-type 150-200 μm thick wafers. A schematic of a conventional *p*-type (usually boron doped) solar cell structure is shown in Figure 1.5 in which a *p*-*n* junction is formed on the front surface by diffusion of *n*-type dopant (usually phosphorus). The incident light is absorbed by the emitter and bulk material and generates electron-hole pairs. Electrons are separated and extracted at the

front electrodes and deliver electrical power to the external load. An anti-reflection coating is used to increase light absorption and to passivate the surface.

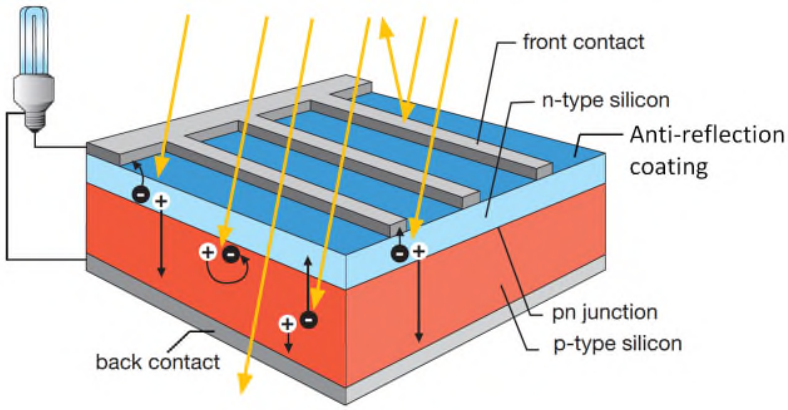

Figure 1.5. Schematic of a standard front-contact multicrystalline silicon solar cell under illumination. The absorbed light creates electron-hole pairs. The carriers need to diffuse to the *p*-*n* junction and are separated before being extracted at the metal contacts [8].

Multicrystalline silicon wafers for PV are generally produced by directional solidification (details in Section 2.1). Other methods include ribbon and sheet growth and these are explained in Ref. [9]. Producing mc-Si wafers by casting is one of the least complex technologies and has a relatively low production cost. Although multicrystalline silicon materials have a lower production cost compared to single crystal silicon, mc-Si technologies give with 2-3% lower cell efficiencies [10]. Mc-Si wafers contain various extended defects, *e.g.* grain boundaries and in particular grown-in dislocations, which are formed due to high thermal stress in rapidly growth ingot [11, 12]. Furthermore, mc-Si wafers contain a high concentration of metallic impurities in the form of both point-like defects and precipitates originating from the feedstock, crystal growth environment and also wafer processing under non-clean processes [9, 13, 14]. These impurities are recombination active for photogenerated carriers which reduce minority carrier lifetime and therefore degrade cell performance [9].

Iron (Fe) is considered one of the most harmful and ubiquitous impurities, forming point defects on interstitial sites or as iron boron pairs (in boron-doped *p*-type silicon), also accumulating at structural defects due to segregation or precipitation, which act as active recombination centres and degrades carrier lifetime substantially and therefore solar cell efficiency [15-18]. Recent investigation has shown surprisingly high iron concentration *e.g.* 10^{14}-10^{16} cm^{-3} in different mc-Si materials [19].

Mc-Si can be made viable through extensive use of effective gettering processes, which remove unwanted impurities from the active regions and trap them in defect-containing regions or in zones where their solubility is enhanced [19-51]. The gettering efficiency is likely to be limited by the interaction of metallic impurities with extended defects, particularly grown-in dislocations [52]. This thesis focuses on the effect of low-temperature annealing (≤ 500 °C) to improve carrier lifetime and to reduce interstitial iron concentration in mc-Si material sourced from a commercially-grown ingot.

1.3. Thesis objective and outlines

The overall goal of this thesis is to improve bulk lifetime in multicrystalline silicon material by applying low-temperature annealing and to develop a scientific understanding of the interaction between metallic impurities and other defects in mc-Si. A series of comprehensive studies have been designed and performed on multicrystalline silicon materials sourced from different height positions of a commercially-grown ingot. Annealing can potentially be performed under non-cleanroom conditions as the solubility of main impurities is very low at the processing temperatures used [31]. The work performed in this thesis is presented in the following way:

Chapter 2 reviews different crystallographic defects including grain boundaries, dislocations, metallic impurities particularly iron and their effects on lifetime studied in the literature. Different gettering processes (*external* and *internal*) and their limitations are also reviewed. Based on this critical review, a series of low-temperature gettering experiments are proposed to obtain more accurate results on the effect of annealing temperature, time, and passivation schemes. Furthermore, experiments are also proposed to demonstrate the effect of low-temperature gettering on carrier lifetime after an industrial standard phosphorus diffusion process.

In Chapter 3, all the key process including sample selection, chemical polishing, cleaning, passivation scheme, lifetime characterisation techniques, interstitial iron concentration modelling, and dislocation density mapping are described. The working principle of different characterisation tools including a newly-installed BT Imaging LIS-L1 (PL imaging tool), Sinton QSS-PC tool, and four-point-probe resistivity meter used in this thesis are also discussed. Additionally, the calibration of different key factors in the

PL imaging tool such as power of the LEDs, exposure time, density of injection level and their effects on calibrated lifetime measurement the PL imaging tool is discussed.

Chapter 4 focuses on the distribution of different key properties such as minority carrier lifetime, bulk interstitial iron concentration, photoluminescence, and dislocation density distribution at different height positions of an as-received mc-Si ingot. A temporary liquid iodine-ethanol (I-E) chemical solution and silicon nitride (SiN_x) passivation schemes are used for this study. This provides a starting characterisation of the materials used in later chapters.

Chapter 5 presents on a comprehensive study into the effect of low-temperature gettering ($\leq$ 500 °C) on lifetime and interstitial iron concentration in as-grown mc-Si wafers sourced from four different height positions. For more detail investigations, spatially resolved carrier lifetime images and iron concentration maps were produced to establish the changes induced by the gettering processes at every annealing step. A temporary liquid iodine-ethanol (I-E) passivation at room temperature is used to separate the thermal effects of annealing from any bulk passivation which may occur during surface passivation in lifetime measurement. Lifetime improvements are discussed in terms of reduction in interstitial iron concentration and possible interaction of crystallographic defects such as grain boundaries and dislocations. The gettering kinetics are investigated based on experimental results, and the interaction between crystal defects in gettering processes are quantitatively characterised. The results presented in this Chapter is published in Ref. [53].

Chapter 6 focuses on effects of different type of surface passivation schemes in low-temperature gettering in mc-Si materials from different height positions. Two different passivation schemes (iodine-ethanol and PECVD silicon nitride) are used. Samples with silicon nitride passivation are annealed with the dielectric layers to passivate bulk (perhaps by hydrogen). Lifetime and interstitial iron concentration are measured at every annealing step and quantitatively compared with the results in Chapter 5. The impact of silicon nitride passivation layer as an *external* gettering site of interstitial iron is also discussed, and supporting secondary ion mass spectrometry (SIMS) data are presented. The results presented in this Chapter in published in Ref. [54].

Chapter 7 focuses on three set of experiments on low-temperature gettering in samples after an industrial standard phosphorus diffusion gettering (PDG) process. As before, sister samples from different height positions are used. The first experiment is used to evaluate whether low-temperature gettering has the potential to improve lifetime further after the standard phosphorus diffusion gettering process. The iodine-ethanol passivation scheme is used for lifetime characterisation to avoid ambiguities associated with bulk passivation or *external* gettering identified in Chapter 6. In the second set experiments, the *external* gettering of interstitial iron to phosphorus diffused layer in low-temperature gettering is investigated. The final set of experiment focuses on the potential of low-temperature gettering in pre-PDG and post-PDG in poor lifetime mc-Si wafers.

Chapter 8 summarises the key findings of this thesis and outlines possible future work.

Chapter 2 Literature review

2.1. Introduction

Multicrystalline silicon (mc-Si) is generally produced by using an ingot growth technique in which silicon is melted in a quartz crucible with an inner coating of silicon nitride and solidified in a unidirectional vertical Bridgman or gradient-freeze growth technique. A schematic diagram of a directional solidification furnace is shown in Figure 2.1. This is a relatively simple process in which silicon material is melted and heat is extracted from the melted silicon in a controlled manner to ensure high-quality crystallization. In this technique, a large column of silicon up to 26 cm in height with a cross section more than of 84 cm × 84 cm can be grown [11, 55]. It is well known that mc-Si material contains a large number of structural crystallographic defects such as grain boundaries, dislocations compared to single crystal silicon which is dislocation-free. It also contains a large number of metallic impurities because of using less pure feedstocks and because of contamination from the crucible [9]. These metallic impurities are present in various forms including as point-like defects, in precipitates or decorated crystallographic defects which become recombination active and thus degrade device performance substantially.

The aim of this chapter is to give an overview of defects in multicrystalline silicon material, their impact on minority carrier lifetime and possible techniques already used to mitigate the detrimental behaviour of these defects. Firstly, properties of crystallographic defects such as grain boundaries and dislocations and metallic impurities are discussed. Details of the fundamental recombination mechanisms in semiconductor materials are then briefly discussed. Finally, a brief overview of different gettering processes reported in earlier experiments is presented and the objectives of this thesis are given.

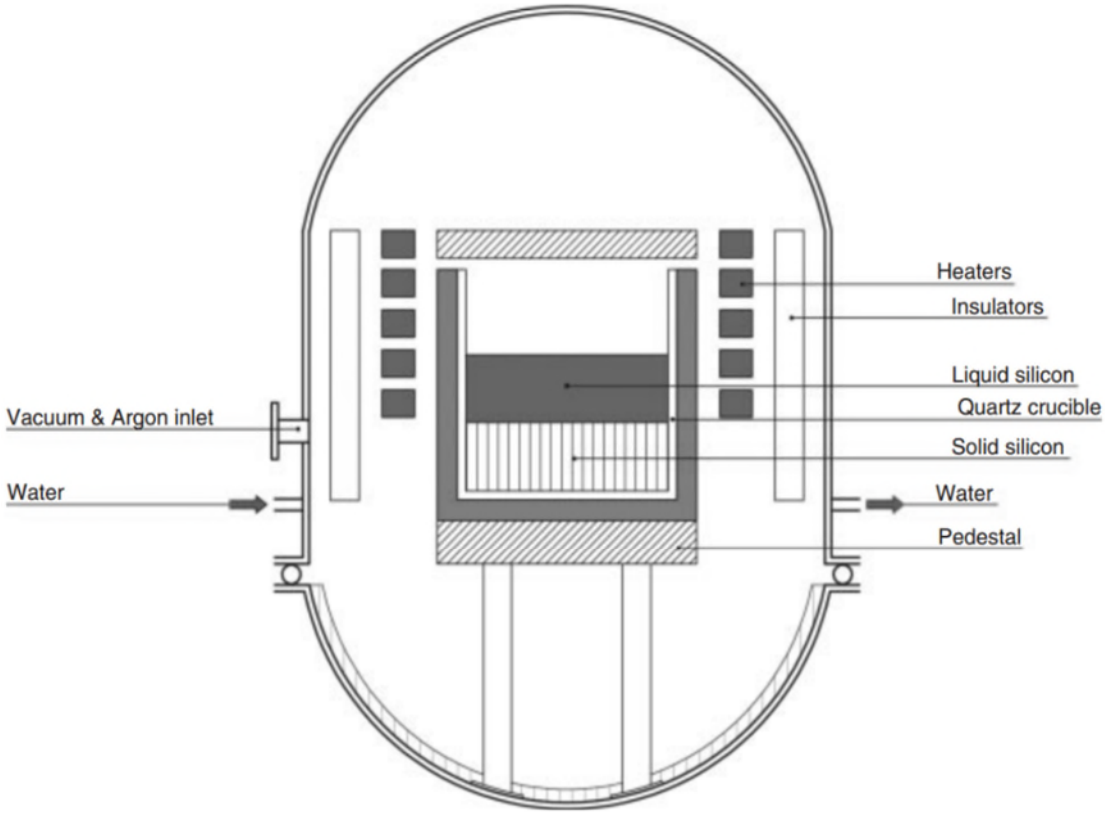

Figure 2.1. A growth of multicrystalline silicon ingot (up to 800 kg) in a directional solidification furnace [56].

2.2. Defects in multicrystalline silicon

The defect distribution in multicrystalline silicon material depends on the details of the growth used and controlling process parameters for ingot processing. Defects such as grain boundaries, dislocations and metallic impurities are widely known for their detrimental impacts on minority carrier lifetime and hence solar cell efficiency. The distribution of such defects varies widely with ingot position, but they are mainly dominating in the top, bottom and edge areas (also known as ‘red zone’). In the following sections the main defects, their properties, and the impact on material quality are discussed.

2.2.1. Grain boundaries

Grain boundaries (GBs) are the interface of two different grains and are generally formed during the crystallization process of the ingot. They can be associated with a

shallow or deep level of an energy state in the band-gap and affect the electronic properties. An equilibrium atomic structure of ∑5 grain boundary with different atomic configuration is presented in Figure 2.2 [57]. The electrical properties of grain boundaries depend on their crystal configurations and symmetries [57]. GBs are classified according to the value of ∑ which is the reciprocal of the misorientation between two grains is known as coincidence site lattice (CSL). A high number of ∑ represents a low symmetry between two grains. A grain boundary with higher symmetry exhibits lower energy [58, 59]. Often twin boundaries (without any distortion in bonding) are formed during the cooling process with high crystal growth rate [60].

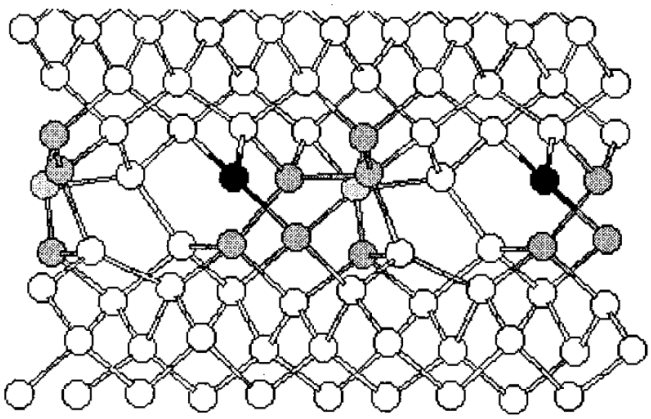

Figure 2.2. An equilibrium configuration of the ∑5 grain boundary, with the atoms displaying localised gap or edge states where all the black, dark grey and light grey circles represent threefold, fourfold and fivefold coordinated atoms, respectively [57].

Grain boundaries in multicrystalline silicon act as recombination centres which are due to intrinsic structural defects or presence of extrinsic impurities [61]. The recombination activity of grain boundaries strongly depends on decoration by metallic impurities [62]. Contamination free (clean) grain boundaries show very weak, or perhaps no recombination activity [62]. However, a large number of metallic impurities segregate at grain boundaries due to the non-symmetric interface during ingot solidification [63]. Buonassisi *et al.* studied metallic impurities at different types of grain boundary of the thermal annealing and suggested the degree of segregation depends on the ∑-value [64]. In the same study [64], it is reported that metallic impurities are likely to segregate at grain boundaries with a high ∑ value, as shown in Figure 2.3. The recombination activity of GBs strongly depends on ∑ values and presence of metallic impurities at grain boundaries even with very low concentrations. *Clean* grain boundaries (without being decorated by metallic impurities) are less recombination active, which increases with the

presence of metallic impurities [62]. It is important to note that ∑3 GBs (twin boundaries) contain a lower concentration of metallic impurities because of having significantly lower energy and thus show no detectable recombination activity [13, 58, 64, 65].

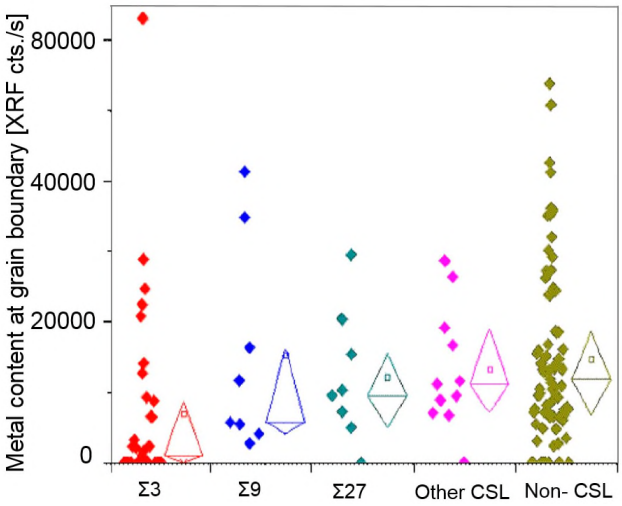

Figure 2.3. The dependence of metal precipitate concentration (measured by X-ray fluorescence microscopy) on grain boundary characteristic. Metal precipitate decoration tends to increase with decreasing degree to atomic coincidence in the grain boundary plane (increasing ∑ value). To the right side of each data cluster, the open diamonds represent the 25th and 75th percentiles and the median. The open box is the mean [64].

2.2.2. Dislocations

Dislocations are generally formed by plastic deformation of materials to reduce thermal stress during crystal growth and spread both vertically and laterally with ingot position [66]. The various mechanisms of nucleation of dislocations and their structure are discussed in the textbooks [67, 68]. There are two basic types of dislocation such as screw dislocations and edge dislocations. In the basis geometry of screw dislocations, the defect line movement is perpendicular to the direction of stress rather than parallel. In Edge dislocation, an extra plane of atoms is in a lattice. For an applied stress, the defect line shear along the top of the extra plane and inter-atomic bonds are distorted and re-established. Dislocations are formed at a very early stage of solidification process near grain boundaries due to induced stress during solidification [69, 70]. As the dislocation density is governed by the stress produced by cooling rate used, fast cooling rate generates higher dislocation density [71]. It is also suggested in Ref. [70] that initially occurred dislocations propagate with solidification and act as a source of other dislocations. In the same study, it is also reported that generation of dislocations depends on crystallographic

orientation [70]. The distribution of dislocations varies widely with ingot height position as it increases due to plastic deformation of the material under thermoelastic stress during crystal growth. Ryningen *et al.* [66] and Stokkan [72] studied dislocation cluster size and density with ingot height position. It is reported that dislocation clusters originate at grain boundaries and increase in size and number with ingot height. The average density varies from 10^4 to 10^6 cm^{-2} and local density may occur higher than 10^8 cm^{-2} [11]. A distribution of dislocation density in a typical etch multicrystalline sample under an optical microscope is shown in Figure 2.4 in which dislocation clusters are visible in relatively high defective regions and the intragrain regions show comparatively lower dislocation density.

The structure and electronic behaviour of dislocations in silicon have been studied by Seibt *et al*. [73, 74]. An example of dislocation structure core of 30° and 90° partials can be reconstructed as shown in Figure 2.5 which can produce a deep donor and an acceptor level in the band gap. Dislocations interact with metallic impurities during thermal annealing process and act as a precipitation sink for transition metals. The interaction of metallic impurities with dislocations has been studied by several authors [13, 74-83]. It is suggested that metal impurities can bind (chemically) with dislocation cores in various configurations and migrate along the dislocation core [74]. Kivambe *et al.* suggested that the metallic precipitation at dislocations depends on core structure [76].

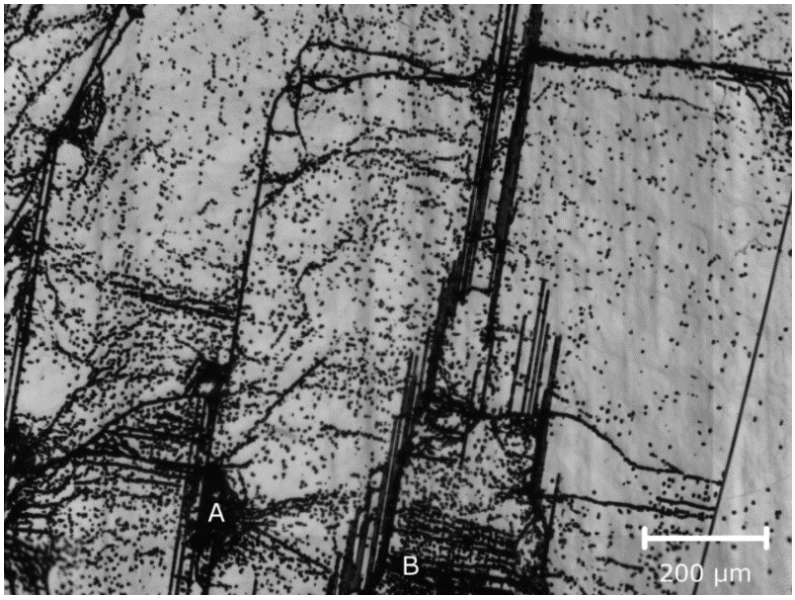

Figure 2.4. Distribution of dislocation under an optical microscope in a typical multicrystalline silicon material after revealing with a chemical solution. A and B indicate dislocation cluster regions and the solid dark lines represent grain boundaries.

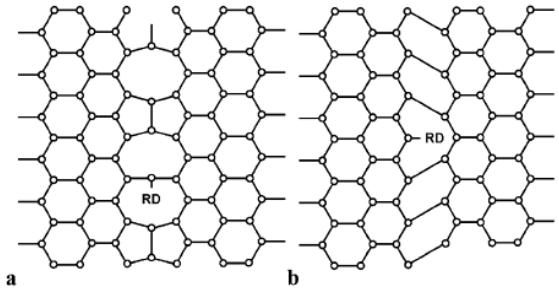

Figure 2.5. Core view in the (111) glide plane of (a) 30° and (b) and 90° Shockley partial dislocations in their reconstructed states; RD denote reconstruction defects that are mobile at high temperature and possibly give rise to deep states [73].

Recombination of charge carriers at dislocations depends on processing and the presence of metallic impurities [84]. Like grain boundaries, dislocations are strongly recombination active while they are decorated with metallic impurities [80]. These dislocations introduce deep energy level in the band-gap. The recombination of charge carrier is explained by an energy band diagram of dislocation decorated with metallic impurities as shown in Figure 2.6 [85]. Dislocations provide the shallow energy level E_{De} and E_{Dh} whereas metallic impurities give a deep energy level E_M. At 'clean' dislocations (in absence of metallic impurities), the recombination takes place (R_{De-Dh}) by the direct transition between E_{De} and E_{Dh}. In presence of metallic impurities, the recombination rate becomes 20-30 times larger compared to 'clean' dislocations as charge carriers can be recombined through additional recombination channels R_{C-M}, R_{V-M}, R_{De-M} and R_{Dh-M}.

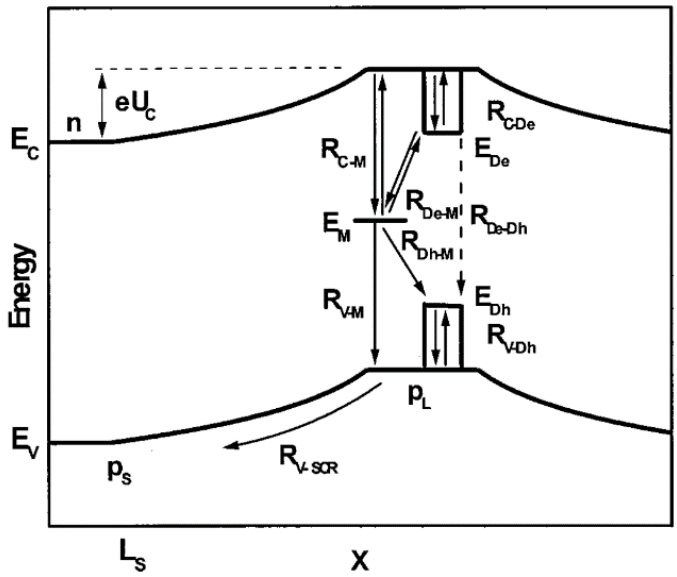

Figure 2.6. A schematic illustration of an energy band in a dislocation and possible recombination pathways through dislocation with and without being decorated by metallic impurities [85].

A relationship between dislocation density and their effect on carrier lifetime is presented in Figure 2.7 in which it can be seen that material with higher dislocation density ~10^6 cm^{-2} has lower carrier lifetime. Another study by Donolato [86] suggested that the effective diffusion length of minority carriers in mc-Si is reduced by more than 30% when a dislocation density higher than 10^5 cm^{-2}. It is desirable to suppress the density of dislocations which can be done substantially by maintaining a flat solid/liquid interface and controlling cooling rate [87]. Gregori *et al*. [88] studied dissolving of dislocation cores but no improvement in electrical properties was demonstrated. Another study by Hartman *et al*. [89] suggested using high-temperature annealing to reduce dislocation density and reported a reduction of 95% upon annealing at 1366 °C for 6 h. Although dislocation density is reduced remarkably, high-temperature annealing affects the impurity distribution considerably and no effects on electrical properties have been reported.

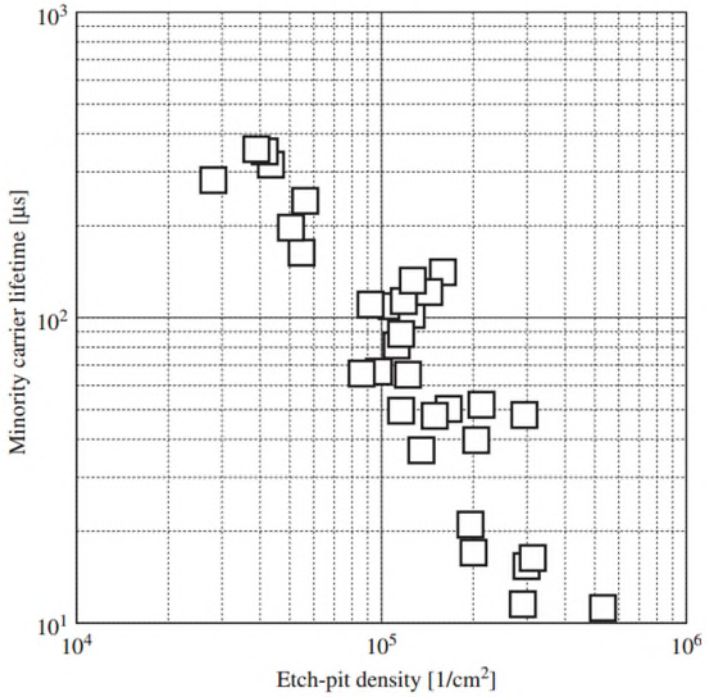

Figure 2.7. Relationship between minority carrier lifetime (measured using the laser/microwave photoconductance decay (μ-PCD) method) and dislocation density in multicrystalline silicon [90].

2.3. Metallic impurities

Metallic impurities are introduced into multicrystalline silicon material from relatively low-grade feedstock material and the crucible walls. The distribution of metallic

impurities depends on a number of factors including cooling rate during crystal growth, the total metal content and variation of growth condition during crystallisation process [9]. A comparison of average metallic impurities concentration present in multicrystalline silicon material produced by different technologies is presented in Figure 2.8 [9, 91]. It can be seen that iron has a relatively high concentration in mc-Si, which is independent of the manufacturing technology used. The distribution widely varies due to having different segregation and relaxation behaviour. A profile of metallic impurities was determined by Macdonald *et al.* [92] which suggested that the higher concentration of metallic impurities at the bottom of the ingot is due to the solid state in diffusion from the crucible and higher concentration at the top part of the ingot due to segregation of molten phase. Nevertheless, it is reported that the metallic impurities present in mc-Si are much higher in concentration than the concentration required to degrade minority carrier lifetime even in relatively good regions of wafers [91].

In general, these metallic impurities, whether in precipitates or point defect like form, are recombination active and are a key contributor to the degradation of minority carrier lifetime. The degradation depends on the chemical/structural state of metallic impurities [9]. The impact of different transition metallic impurities and respective concentration on solar cell efficiency was studied by Coletti *et al*. [93], who reported a substantially lower cell efficiency for wafers from the extrema compared to the centre part of the ingot.

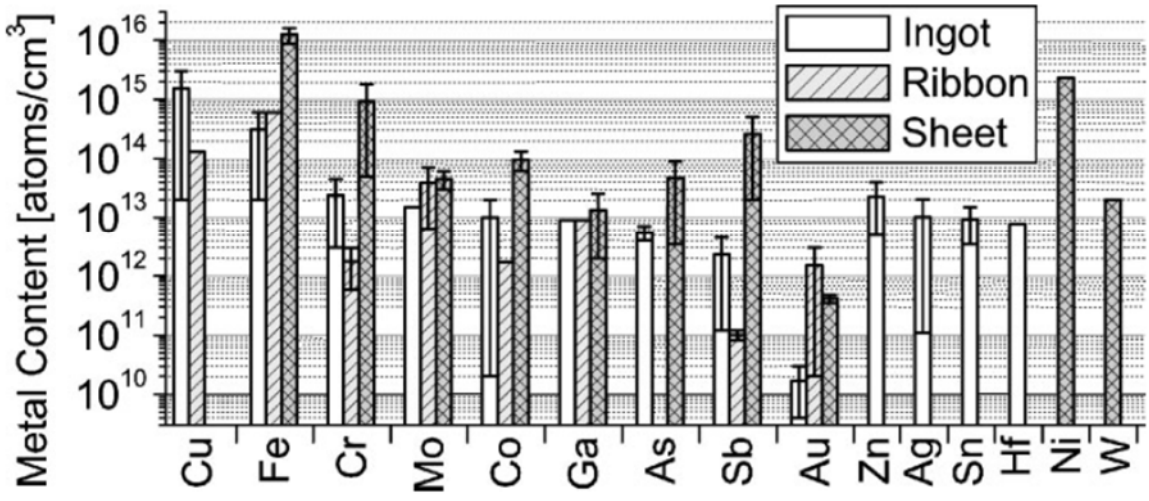

Figure 2.8. Total metal content in ingot-growth, ribbon and sheet in typical multicrystalline silicon materials measured by neutron activation analysis. The missing bars indicate a concentration below detection limit [9].

Among the various metallic impurities in mc-Si material, iron (Fe) is the most harmful and ubiquitous because of its higher concentration and a large electron capture cross section [15, 91]. It is reported that the Fe concentration in a solidified ingot is up to 10^{15} cm^{-3} near the crucible wall due to contamination during ingot growth which reduces to 10^{13}-10^{14} cm^{-3} at the centre of ingot [91]. A small part of total iron concentration (< 1%) is present as in interstitial form whereas most of the metallic impurities are present in precipitate form at grain boundaries and dislocations [92]. Interstitial iron appears as electrically active iron dissolved on interstitial sites, iron-boron (FeB) pairs (usually in boron doped *p*-type wafer) and as α-$FeSi_2$ precipitates. In the following sections, the characteristics of Fe defects and its complexes are reviewed.

2.3.1. Interstitial iron and iron-boron pairs

The concentration of interstitial iron concentration present in multicrystalline silicon depends on the relaxation and segregation during crystallisation process and density of defects such and grain boundaries and dislocations [92]. Interstitial iron (Fe_i) is mobile and forms two main charge states: a neutral and a positively charged state which results in one donor state situated in the lower half of the band gap [94]. At room temperature, Fe is present in interstitial (Fe_i) form or bonded with negatively charged substitutional acceptor boron $(B_s)^-$ forming Fe_iB_s pairs [18]. The kinetics of the reaction is described by the following equation:

$$Fe_i^+ + B_s^- \Leftrightarrow Fe_iB_s \qquad (2.1)$$

The reaction velocity strongly depends on the boron concentration, diffusivity of interstitial iron and storage temperature [95]. Both Fe_i and Fe_iB_s pairs are strong recombination centres and their fundamental recombination properties, namely the defect energy level and the electron and the hole capture cross sections have been determined in several studies as presented in Table 2.1. Any changes in Fe_i and Fe_iB_s concentration affects the carrier lifetime substantially because of having different recombination properties [15].

Table 2.1. Recombination parameters (energy levels, capture cross section for electrons and holes) of interstitial iron (Fe_i) and iron-boron pairs (Fe_iB_s) are published by various authors.

Defect type	Energy, E_T (eV)	Electron capture cross section, σ_n (cm^2)	Hole capture cross section, σ_p (cm^2)	Reference
$[Fe_i]$ donor	$E_v + 0.38$	3.6×10^{-15}	7.0×10^{-17}	Istratov *et al.*, 1999 [18]
	$E_v + 0.39$	3.6×10^{-15}	7.0×10^{-17}	Rein *et al.*, 2005 [15]
Fe_iB_s donor	$E_v + 0.10$	2.0×10^{-14}	1.6×10^{-15}	Istratov *et al.*, 1999 [18]
Fe_iB_s acceptor	$E_c - 0.26$	3.0×10^{-15}	2.5×10^{-15}	Istratov *et al.*, 1999 [30]
	$E_c - 0.26$	2.0×10^{-15}	1.6×10^{-15}	Zoth and Bergholz, 1990 [33]
	$E_c - 0.23$	3.0×10^{-14}	2.0×10^{-15}	Macdonald *el al.*, 2001 [34]
	$E_c - 0.26$	2.0×10^{-15}	5.5×10^{-15}	Rein *et al.*, 2005 [32]

The Fe_iB_s pairs can be dissociated to Fe_i^+ and B_s^- by thermal annealing, or by illumination at room temperature [18]. At lower injection level, the effective lifetime is limited by the concentration of Fe_i whereas Fe_iB_s becomes dominant under higher level injection. An injection dependent lifetime is presented in Figure 2.9 which shows the carrier lifetime varies widely with the dissociation of Fe_iB_s pairs. It is important to note that at the crossover point (2×10^{13} cm^{-3} in Figure 2.9), the carrier lifetime is unchanged for both the Fe_i and Fe_iB_s states. The interstitial iron concentration can be determined based on lifetime changes before and after dissociation. This is used heavily in this thesis and is explained in detail in Chapter 3.

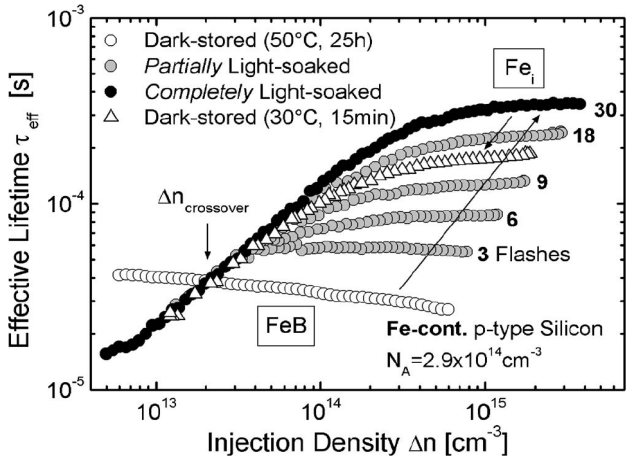

Figure 2.9. The effect of light soaking on the injection-dependent carrier lifetime in an iron-contaminated boron-doped *p*-type silicon sample [15]. The lifetime increases with increasing number of flashes at higher injection level due to dissociation of FeB pairs. The crossover point indicates no change in lifetime for FeB and Fe_i states.

In order to re-associate the Fe_iB_s pairs, the sample is kept in dark conditions at room temperature. The time required for a sample to reach equilibrium FeB concentration depends on acceptor and interstitial iron concentrations [96]. The bulk iron concentration at any time after Fe_iB_s pairs dissociation can be measured according to [97]:

$$[Fe_i]_t = \left([Fe_i]_0 - [Fe_i]_{eq}\right)\exp\left[-1.3\times10^{-3} t N_A^{2/3} \times \exp\left(-\frac{0.68\text{eV}}{k_B T}\right)\right] + [Fe_i]_{eq} \quad (2.2)$$

where $[Fe_i]_0$ and $[Fe_i]_{eq}$ are the initial and equilibrium bulk iron concentration respectively, N_A is the material's acceptor concentration, t is the time from dissociation, k_B is the Boltzmann constant and activation energy of 0.68 eV. The equilibrium iron concentration after a long time from dissociation of Fe_iB_s pairs can be calculated as [97]:

$$[Fe_i]_{eq} = \frac{[Fe_i]_0}{\left[1+N_A 10^{-23}\exp\left(\frac{E_b}{k_B T}\right)\right]\left[1+\exp\left(\frac{E_F - 0.39\,\text{eV}}{k_B T}\right)\right]} \quad (2.3)$$

where E_b is the binding energy of Fe_iB_s pairs discussed in the following section, E_F is the Fermi level which can be determined by [97]:

$$E_F = \frac{E_g}{2} + kT\ln\left(\frac{N_A}{n_i}\right) \quad (2.4)$$

where E_g is the band gap (for silicon material 1.125 eV at room temperature 25 °C) and n_i is the intrinsic carrier concentration.

The recombination activity due to interstitial iron and its effect on carrier lifetime depends upon the dissociation and reformation of Fe_iB_s pairs under illumination, as explained previously. The kinetics of Fe_iB_s dissociation and reformation has been studied in Ref. [18, 98-100]. The formation and dissociation reactions are determined by three energies which are equilibrium binding energy (E_b), the diffusion barrier of Fe_i (E_m) and dissociation energy (E_{diss}), as illustrated in Figure 2.10 [18]. E_{diss} is the potential barrier of the Fe_iB_s pairs annihilation process (~1.20 eV [18]), E_b corresponds to the binding energy between of Fe_i and B_s (0.58 eV to 0.65 eV [18]) and E_m corresponds to the energy Fe_i^+ needs to overcome the diffusion barrier of crystal field (0.64 eV [100]). It is important to note that $E_{diss} < E_m + E_b$, which is reported as a result of Coulomb attraction between Fe_i^+ and B_s^- [100]. The dissociation rate of Fe_iB_s pairs which is calculated in the literature [98] is directly proportional to the square of the carrier generation rate and the inverse square of the Fe_iB_s concentration. The reformation of Fe_i and B_s to Fe_iB_s pairs is limited by the migration energy of Fe_i^+ which is the activation energy of formation of Fe_iB_s pairs [100].

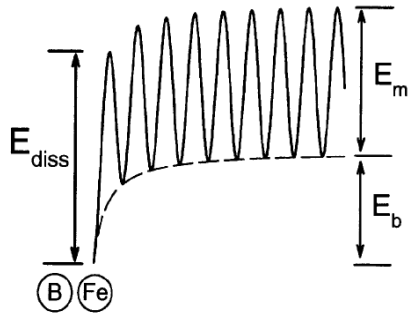

Figure 2.10. An energy diagram of the Fe_iB_s interaction in silicon E_{diss} is the dissociation energy and E_b is the binding energy and E_m is the formation energy [18].

2.4. Recombination in multicrystalline silicon

Carrier lifetime in crystalline silicon material falls into two primary categories: (i) recombination lifetime and (ii) generation lifetime. Generation refers to the creation of excess electron-hole pairs by thermal excitation or absorption of photons. Generation lifetime is a paucity of carriers, as in the space-charge region and the device tries to attain equilibrium [101]. The recombination lifetime is the inverse process of the generation, decaying of generated excess carriers as a result of recombination. The recombination lifetime can be measured by the recombination rate and the excess carrier density as:

$$\tau = \frac{\Delta n}{U} \tag{2.5}$$

where Δn is the excess carrier concentration and U is the recombination rate. The recombination lifetime of minority carrier in crystalline silicon is based on following major recombination mechanisms:

(a) Radiative (band-to-band) recombination.

(b) Coulomb-enhanced Auger recombination.

(c) Recombination through bulk defects (Shockley-Read-Hall).

(d) Surface recombination.

The parameterisation of the above recombination mechanisms is described in the following sections.

2.4.1. Radiative (band-to-band) recombination

Radiative recombination is an intrinsic process which involves falls of free electrons directly from the conduction band and recombination with free holes in the valence band. The excess energy is liberated in the form of a photon [102]. An illustration of the radiative recombination process is shown in Figure 2.11. The photoluminescence imaging technique exploits band-to-band recombination to quantify carrier lifetime (discussed in Chapter 3). The band-to-band recombination lifetime in a *p*-type silicon material can be expressed by:

$$\tau_{\text{radiative}} = \frac{1}{B\left(N_A + n_0 + \Delta n\right)} \tag{2.6}$$

where B is the band-to-band recombination coefficient, N_A is the doping concentration, n_0 is the electron concentration at equilibrium and Δn is the injection level. A detailed calculation of temperature dependence of band-to-band recombination coefficient is reported in [103, 104]. At room temperature (24 °C), the B value for silicon is measured as 4.75×10^{-15} cm^3s^{-1} [104].

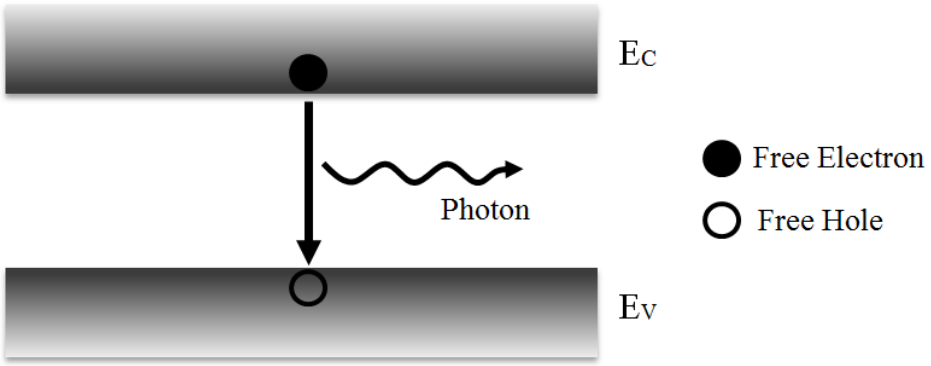

Figure 2.11. Schematic diagram of the radiative recombination process. A free electron from the conduction band recombines with a hole in the valence band and releases a photon.

Radiative recombination usually dominates in direct band structure materials [105] where the extrema of the valence and conduction band are aligned in *k*-space. In silicon material which has an indirect band gap, as illustrated in Figure 2.12, radiative recombination mechanism is weak compared to other recombination processes.

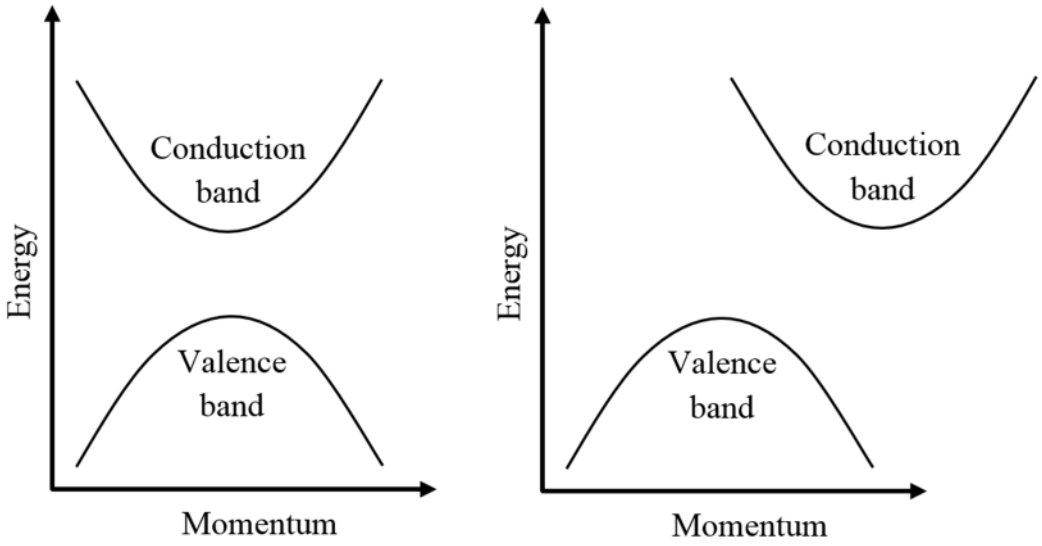

Figure 2.12. Schematic diagram of band structure (a) direct band gap (*e.g.* CdTe) (b) indirect band gap (*e.g.* silicon).

2.4.2. Coulomb-enhanced Auger recombination

Auger recombination is another intrinsic process and dominates usually only for highly doped silicon or at high injection levels. It is a three-particle interaction where a conduction band electron and a valence band hole recombine, with the excess energy being transferred to a third free electron or hole [106]. A schematic diagram of the Coulomb-enhanced Auger recombination process is illustrated in Figure 2.13. The expression for Auger recombination lifetime for *p*-type and *n*-type silicon under low ($\tau_{\text{Auger.li}}$) and high injection ($\tau_{\text{Auger.hi}}$) level are as follows:

p-type silicon

$$\tau_{\text{Auger.li}} = \frac{1}{C_p N_A^2} \text{ and } \tau_{\text{Auger.hi}} = \frac{1}{(C_n + C_p)\Delta n^2} \tag{2.7}$$

n-type silicon

$$\tau_{\text{Auger.li}} = \frac{1}{C_n N_D^2} \text{ and } \tau_{\text{Auger.hi}} = \frac{1}{(C_n + C_p)\Delta p^2} \tag{2.8}$$

where C_p (9.9×10^{-32} cm^6s^{-1}) and C_n (2.8×10^{-31} cm^6s^{-1}) are the Auger coefficient for holes and electrons respectively [107], N_A and N_D are the doping concentration in *p* and *n*-type silicon respectively, Δn and Δp are an excess concentration of electron and hole respectively.

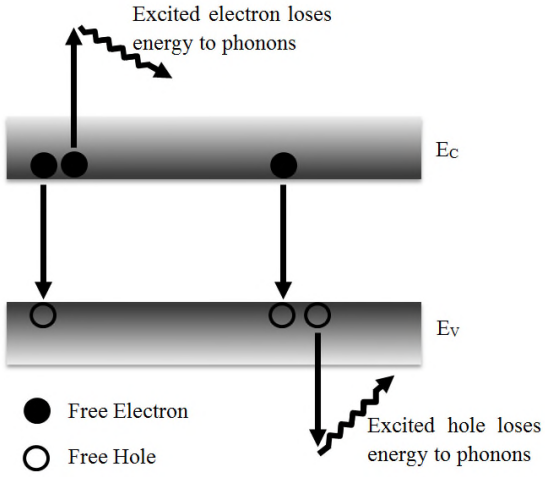

Figure 2.13. Schematic diagram of the Auger recombination mechanism. Solid and open circles represent free electrons and holes in the conduction and valence band, respectively. The excess energy transfer to an electron in the conduction band (left) and to a hole in the valence band (right).

The Auger recombination process is enhanced by Coulombic interaction between electrons and holes [108, 109]. Coulomb-enhanced Auger recombination lifetime is parameterised as [106]:

$$\tau_{\text{CE-Auger}} = \frac{\Delta n}{np(1.8\times10^{-24} n_0^{0.65} + 6\times10^{-25} N_A^{0.65} + 3\times10^{-27}\Delta n^{0.8})} \tag{2.9}$$

where n and p are the concentration of electrons and holes respectively. This process occurs simultaneously with the band-to-band recombination process. In an updated study performed by Richter *et al.* [110], a general parameterisation for intrinsic recombination (combination of radiative and Coulomb-enhanced Auger recombination) was reported as:

$$\tau_{\text{int.}} = \frac{\Delta n}{(np - n_{\text{i.eff}}^2)(2.5\times10^{-31} g_{\text{eeh}} n_0 + 8.5\times10^{-32} g_{\text{ehh}} p_0 + 3\times10^{-29}\Delta n^{0.92} + B_{\text{rel}} B_{\text{low}})} \tag{2.10}$$

where $n_{\text{i.eff}}$ is the effective intrinsic carrier concentration, n_0 and p_0 are the equilibrium density for electrons and holes respectively, B_{rel} is the relative radiative recombination coefficient, B_{low} is the radiative recombination coefficient for lowly doped and lowly injected silicon (4.73×10^{-15} $\text{cm}^{-3}\text{s}^{-1}$), g_{eeh} and g_{ehh} are the enhancement factors. Note constants have the same dimensions as Auger coefficient (cm^6s^{-1}). The effective intrinsic carrier concentration $n_{\text{i.eff}}$, which is given by the following relation:

$$n_{\text{i,eff}} = n_{\text{i}} e^{\beta \Delta E_{\text{g}}/2} \tag{2.11}$$

where n_{i} is the intrinsic carrier concentration, ΔE_{g} is the bandgap narrowing. The inverse thermal energy β is calculated as:

$$\beta = \frac{1}{kT} \tag{2.12}$$

where k is the Boltzmann constant (8.62×10^{-5} eVK^{-1}) and T is the absolute temperature. The intrinsic carrier concentration can be calculated as [111]:

$$n_{\text{i}}^2 = N_C N_V \exp\left(-\frac{E_{\text{g}}}{2kT}\right) \tag{2.13}$$

where N_C and N_V are the densities of states in the conduction and valence respectively, E_{g} is the band gap of silicon.

In Equation 2.10, empirical CE-Auger enhancement factors can be calculated as:

$$g_{\text{eeh}}(N_D)=1+13\left[1-\tanh\left(\left(\frac{N_D}{3.3\times10^{17}}\right)^{0.66}\right)\right] \tag{2.14}$$

and

$$g_{\text{ehh}}(N_A)=1+7.5\left[1-\tanh\left(\left(\frac{N_A}{7.0\times10^{17}}\right)^{0.63}\right)\right] \tag{2.15}$$

2.4.3. Recombination through defects (Shockley-Read-Hall)

Crystallographic defects and impurities present in semiconductors create discrete energy level within the band gap. Recombination of electron-hole pairs can occur through these trap levels as shown in Figure 2.14. Shockley and Read [112] and Hall [113] first derived a theory of the dynamics of the recombination through defects within band gap based on statistical considerations. The assumption made in the statistical derivation are summarised in [114] are:

(i) The semiconductor is non-degenerate.

(ii) All the defects levels have the same energy level.

(iii) The energy position of the defects is independent of charging properties.

(iv) The relaxation time of the captured charge carriers by the defects are much smaller compared to their emission time.

(v) The impurity concentration is negligibly smaller than the background doping.

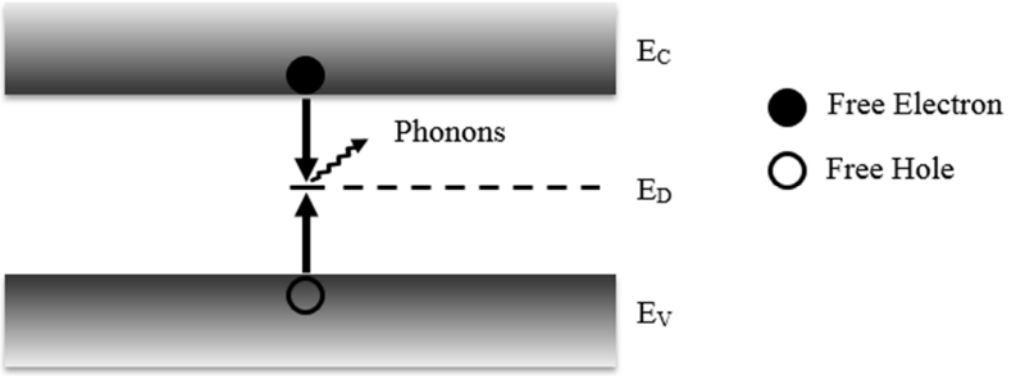

Figure 2.14. Schematic diagram of possible SRH recombination pathway via defects. Defects create energy state in the band gap. A free electron from conduction band relaxes to the defect and combined with a hole.

By considering the single energy level trap defects, the net recombination rate can be expressed by:

$$R = \frac{(np - n_i^2)}{\tau_{p0}(n + n_1) + \tau_{n0}(p + p_1)} \tag{2.16}$$

where τ_{n0} and τ_{p0} are capture time constant for electrons and holes respectively, n_1 and p_1 are SRH densities for electrons and hole respectively, n_i is intrinsic carrier concentration, n and p are concentrations of electrons and holes respectively.

These trap levels form stepping stones where an electron falls from the conduction band. Shockley-Read-Hall (SRH) statistics are a way of quantifying recombination from crystallographic defects, metallic impurities which created discrete energy level within the band gap. *P*-type silicon material contains some other defects including oxygen related defects particularly precipitate, boron-oxygen complexes (in boron doped silicon). SRH statistics for oxide precipitates and associated defects and their impact on carrier lifetime is studied in Murphy *et al.* [115-117]. The boron-oxygen (B_iO_i) complexes are formed under illumination or the injection of minority carriers via a *p-n* junction [118]. It is also reported that B_iO_i defects are electrically active and degrade minority solar cell efficiency (relative) up to 10% [118]. However, these defects can be disregarded by breaking up by using pre-annealing in complete darkness for 10 min at 200 ^oC [119].

The SRH lifetime due to a defect in *p*-type material is given by [112, 113]:

$$\tau_{SRH} = \frac{\tau_{n_0}\left(N_A + p_1 + \Delta n\right) + \tau_{p_0}\left(n_0 + n_1 + \Delta n\right)}{N_A + n_0 + \Delta n} \tag{2.17}$$

The SRH densities are given by:

$$n_1 = N_C \exp\left(-\frac{E_C - E_T}{k_B T}\right) \tag{2.18}$$

and

$$p_1 = N_V \exp\left(-\frac{E_T - E_V}{k_B T}\right) \tag{2.19}$$

Here, N_C (2.86×10^{19} cm^{-3}) and N_V (3.10×10^{19} cm^{-3}) [114] are the effective densities of states at the conduction band and the valence band edges, whose energy position is given

by E_C and E_V. E_T is the energy level of the iron defect and values from previous research are given in Table 2.1.

The capture time constant of electrons (τ_{n0}) and holes (τ_{p0}) respectively are given by the following equations:

$$\tau_{n0} = \frac{1}{[D]\sigma_n v_{th}} \tag{2.20}$$

and

$$\tau_{p0} = \frac{1}{[D]\sigma_p v_{th}} \tag{2.21}$$

where [D] is a concentration of defect, v_{th} is the thermal velocity (2×10^7 cms^{-1}). The capture cross-sections of electrons (σ_n) and holes (σ_p) vary with the state of iron (as given in Table 2.1). An injection dependent τ_{Fei} and τ_{FeB} is illustrated in Figure 2.15 for a p-type sample with a doping level of N_A = 2×10^{15} cm^{-3} where lifetime varies widely with the state of iron defects except the crossover point. Lifetime changes based on defect states is widely used to determine an interstitial iron concentration in silicon material (the detailed method is discussed in Chapter 3). It can be seen that below the crossover point Fe_i defects dominate lifetime whereas FeB becomes lifetime dominating after the crossover point.

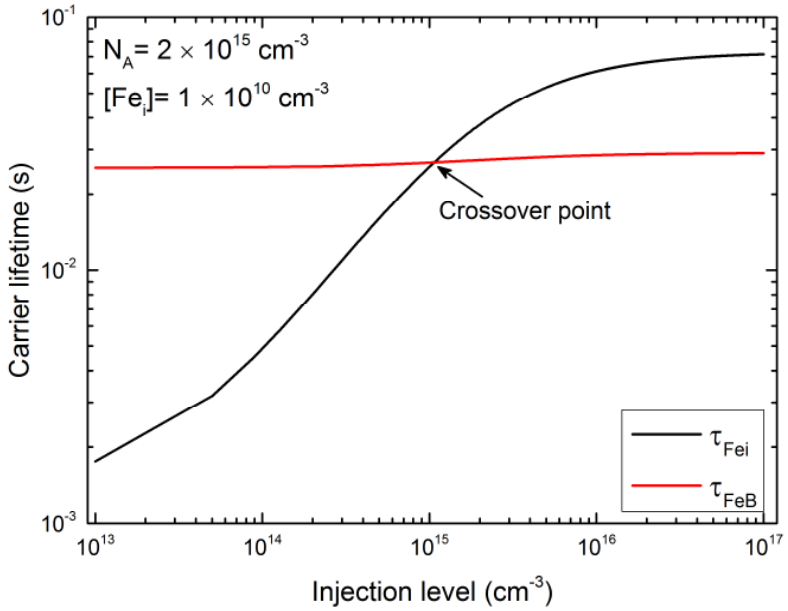

Figure 2.15. An illustration of SRH recombination lifetime as a function of injection level in p-type silicon material with iron in the Fe_i and FeB state. The crossover point indicates no change in carrier lifetime at an injection level.

2.4.4. Surface recombination

The presence of defects at the surface produces energy levels within the bandgap known as surface states which act as recombination centres. These defects are occupied either by an electron or by a hole and interact with the conduction and the valence band. Surface recombination depends on dangling bond or surface state density, as presented in Figure 2.16. The surface recombination lifetime can be expressed as:

$$\tau_{surface} = \frac{W}{2S} \tag{2.22}$$

where W is the thickness of the samples and S is the surface recombination velocity which can be defined as the rate of recombination through surface defects. Dielectric films are used to passivate surface defects and thus to reduce surface recombination [120-123]. A most recent study by R. S. Bonilla *et al*. [124] reported a very low surface recombination velocity of 0.1 cm/s using a triple layer dielectric of low-temperature PECVD a-Si/SiO_x/SiN_x. In this thesis, iodine-ethanol (I-E) and PECVD silicon nitride (SiN_x) passivation techniques are used which are reviewed in Section 2.7.

Figure 2.16. Schematic diagram of surface recombination process through surface defects. Free electrons from conduction band recombine with holes in valence band via the defect energy levels produced by dangling bonds.

2.5. Effective lifetime

The effective minority carrier lifetime depends on all the recombination processes discussed in the above sections, which may occur simultaneously. If the processes are independent, the total recombination rate is the sum of the individual recombination process, and can be expressed as:

$$U_{\text{total}} = U_{\text{Radiative}} + U_{\text{Auger}} + U_{\text{SRH}} + U_{\text{Surface}} \tag{2.23}$$

The effective lifetime (usually referred as minority carrier lifetime) can be calculated by using the Equation 2.5:

$$\frac{1}{\tau_{\text{eff}}} = \frac{1}{\tau_{\text{SRH}}} + \frac{1}{\tau_{\text{Auger}}} + \frac{1}{\tau_{\text{Radiative}}} + \frac{1}{\tau_{\text{Surface}}} \tag{2.24}$$

An example of the effective lifetime for a *p*-type sample with a doping density $N_A = 2 \times 10^{15}$ cm^{-3} is illustrated in Figure 2.17. SRH lifetime is modelled with iron in the Fe_i state using the parameters in Table 2.1 and defect density level of 1×10^{10} cm^{-3}. As multicrystalline silicon wafers usually have a relatively large number of defects and a high concentration of metallic impurities, surface recombination can be considered as negligible if a good passivation scheme such as a-Si/SiO_x/SiN_x is used [124]. It is clearly seen that at lower injection level (< 10^{14} cm^{-3}), the effective lifetime is generally limited by SRH recombination. At intermediate injection levels, other recombination mechanisms (Auger and Band-to-Band) start limiting effective lifetime. At high injection level (> 10^{16} cm^{-3}), the effective lifetime is limited by Auger recombination. It is important to note that effective lifetime is a directly measurable parameter using a lifetime tester (discussed in Chapter 3) and an indicator of solar cell efficiency made from the material studied [125].

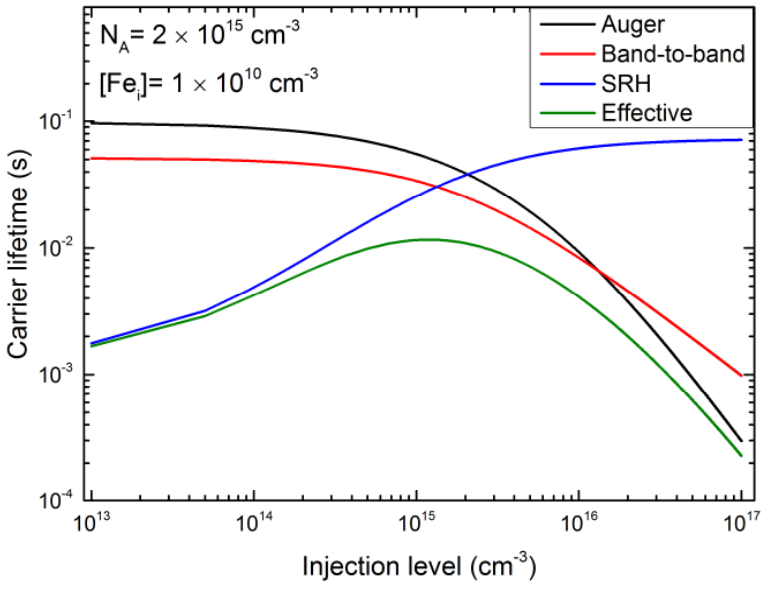

Figure 2.17. Modelling of lifetime for radiative recombination, Auger recombination, SRH recombination and an effective lifetime. A *p*-type boron doped ($N_A = 2\times10^{15}$ cm^{-3}) and iron concentration of 1×10^{10} cm^{-3} is used for this modelling. The parameters used in this modelling are described in the above sections.

2.6. Gettering in multicrystalline silicon

Among the various transition metals, iron (Fe) is the most harmful impurities in multicrystalline silicon which degrades solar cell performance substantially as discussed in previous sections. Its effects can be minimised by engineering of metallic impurities using a controlled thermal annealing process which widely known as 'gettering' in silicon photovoltaics. The fundamental concept of gettering in silicon material is illustrated in Figure 2.18 which mainly involves (a) release of impurities from their original state and become mobile (b) diffuse through the bulk material and (c) capture of impurities at the gettering sites [21]. Gettering processes are classified into two major categories namely *internal* and *external* [19, 20, 44]. The thermodynamic properties of iron in different *external* gettering and low-temperature (≤ 600 °C) *internal* gettering techniques are overviewed in the following sections.

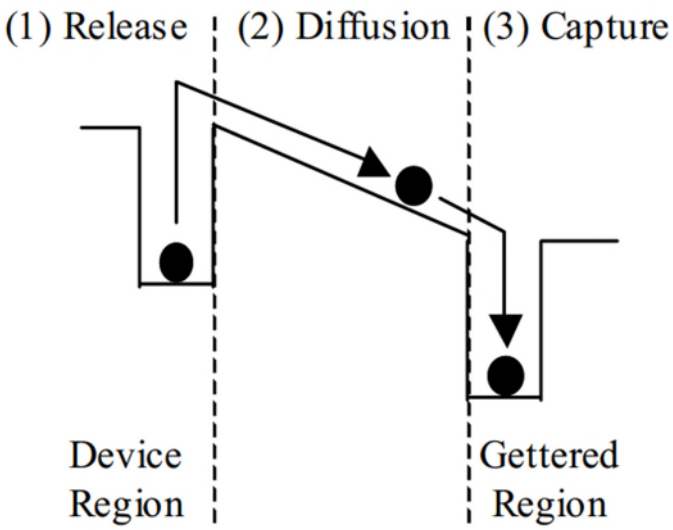

Figure 2.18. Fundamental concept of impurity gettering processes. Solid circles represent of impurities and arrows indicate pathways in gettering process [21].

2.6.1. The behaviour of iron with thermal annealing

The gettering process is based on the underlying physics associated with relaxation and segregation [31, 126]. The effectiveness of a gettering process is usually governed by solubility, diffusivity, segregation coefficient, the peak temperature and subsequent cooling rate. The solubility is the maximum concentration of an impurity which can be dissolved at thermal equilibrium with respect to the substrate material. The solubility of

iron as a function of temperature is reviewed in Istratov *et al.* [18] who summarised the solubility in intrinsic silicon in the temperature range 800 °C to 1200 °C with the following expression:

$$S = \left(8.4^{+5.4}_{-3.4}\right) \times 10^{25} \exp\left(-\frac{2.86 \pm 0.05\text{eV}}{k_B T}\right) \text{cm}^{-3} \tag{2.25}$$

Since *internal* gettering processes are often conducted at temperatures below 800 °C (discussed in Section 2.6.3), it is important to know iron solubility at lower temperatures. Recently, the solubility of iron at temperature range 600 °C to 800 °C was studied by Murphy and Falster [127] who found the following expression:

$$S = 1.3 \times 10^{21} \exp\left(-\frac{1.8\text{eV}}{k_B T}\right) \text{cm}^{-3} \tag{2.26}$$

In the same study, it is also reported that below 600 °C the solubility is approximately independent of temperature as shown in Figure 2.19 and the pre-annealing at higher temperature gives a lower value of iron concentration. The impact of pre-annealing in the temperature range 500 °C to 750 °C on the iron gettering kinetics was investigated in a later paper by Murphy and Falster [128]. Another study on solubility of interstitial metallic impurities in silicon was performed by Myers, Seibt, and Schröter who reported concentration at below the eutectic temperature (as presented in Figure 2.20) [31]. As the solubility is low at ≤ 500 °C, it is therefore not necessary to conduct low-temperature annealing (≤ 500 °C) in a very clean condition from the perspective of additional iron concentration.

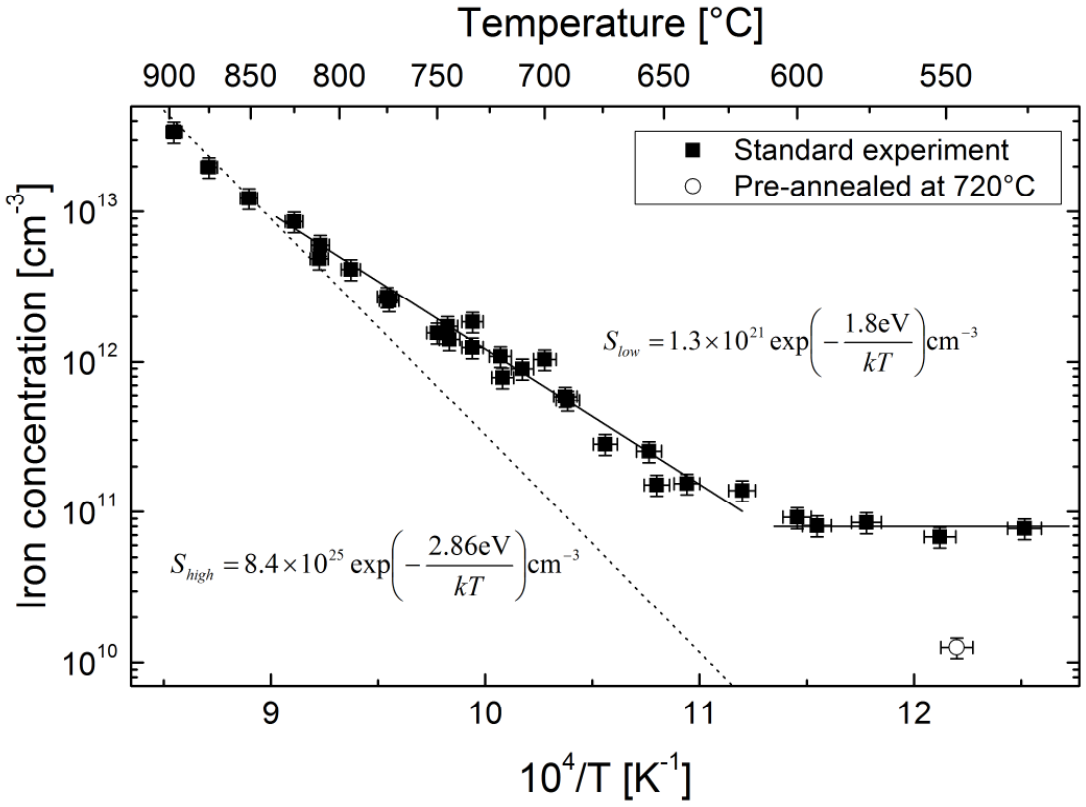

Figure 2.19. Interstitial iron concentration in Czochralski silicon samples annealed at a range of temperature reported in Ref. [127]. The dotted line represents the solubility of interstitial iron at high temperature from Istratov *et al*. [18].

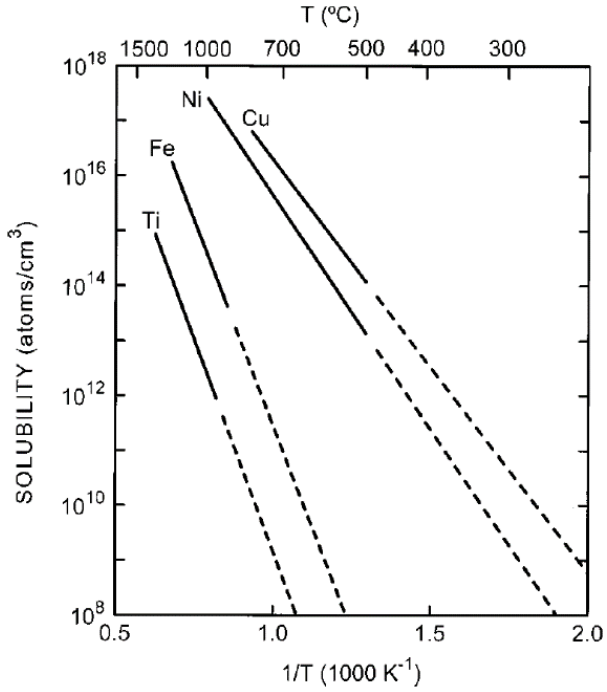

Figure 2.20. Solubilities of different transition metal in silicon as a function of temperature. The solid line represents experimental data and dashed lines are extrapolated [31].

At room temperature, most of the interstitial iron pairs with negatively charge boron (in *p*-type silicon), and these pairs dissociate at temperatures above approximately 100 °C. The diffusivity of interstitial iron is, therefore, one of the key parameters which defines the amount of time needs to reach gettering sites during thermal annealing process and also the size of the contaminated or depleted area after diffusion at a certain temperature. The diffusion of interstitial iron is consolidated by following expression given by Istratov *et al.* [18]:

$$D(Fe_i) = \left(1.0^{+0.8}_{-0.4}\right) \times 10^{-3} \exp\left(-\frac{0.67\text{eV}}{k_B T}\right) \text{cm}^2\text{s}^{-1} \qquad (2.27)$$

In a relaxation gettering process, iron forms precipitate at crystallographic defects with decreasing solid solubility which occurs upon cooling from high temperature. In as-received wafers, more than 90% of the total iron is present in the precipitate form [92] and the size and density of precipitates depend on ingot cooling rate and the density of structural defects. This also indicates the variation in precipitation properties with ingot height as reported in Fenning *et al.* [43]. In the same study, the gettering efficiency is investigated in relation to iron precipitation at different height positions of a mc-Si ingot. It is reported that in highly contaminated samples ($> 1 \times 10^{14}$ cm^{-3}) most of the precipitates remain in the bulk even after *external* gettering with phosphorus. In a study performed using Cz samples by Murphy and Falster [128], a faster reduction in iron concentration when iron silicide phase is present on the surfaces is reported. However, it is important to note that precipitates present after gettering can be dissolved partially during a subsequent high-temperature step which increases interstitial iron concentration as reported in Ref. [129]. Furthermore, a high-temperature process can dissolve precipitates present at structural defects and contaminate the intragranular regions [130]. It is, therefore, possible to find a way to reduce overall bulk iron concentration using low-temperature annealing.

The segregation gettering process occurs during a thermal annealing process in which metallic impurities are extracted from the bulk region using a region with higher solubility. Note that this process does not depend on supersaturation and therefore a lower iron concentration can be achieved compared to the relaxation process. Segregation processes could also occur at the defective regions in multicrystalline silicon material such as grain boundaries and dislocations where the lattice is distorted compared to the

regions with a perfect crystal structure [126]. The *external* gettering processes discussed in the following section is mainly based on the segregation principle.

2.6.2. External gettering

In order to improve minority carrier lifetime in silicon, *external* gettering processes are widely used where metallic impurities are extracted from the bulk by forming a layer with higher solubility at the outer surfaces. Two gettering processes such as phosphorus diffusion gettering (PDG) [19, 30, 39, 131], and aluminium gettering (AlG) [19, 132] are widely used in silicon photovoltaics. As well as being useful for gettering these steps are part of a standard solar cell device fabrication process.

2.6.2.1 Phosphorus gettering

In *p*-type silicon material (usually boron doped) PDG is used to form a thin (~ 0.5 μm) layer of highly phosphorus doped emitter (referred to as n^+) at temperatures above 800 °C. The solubility of metallic impurities is higher in the emitter compared to the bulk region and, so impurities are driven towards the layer by a concentration gradient [19]. As crystallographic defects in multicrystalline materials such as dislocations and GBs determines the efficacy of the PDG process [133], wafers or regions with lower dislocation densities show higher lifetime improvement with minimal or no change in the lifetime found in the highly dislocated area [35]. However, applying an extended low-temperature annealing step at 650 °C after PDG (similar to a low-temperature internal gettering process) can increase the segregation coefficient and hence reduce iron concentration above 99.9% compared to the standard PDG process [131]. A simulation tool, Impurity-to-Efficiency (I2E), is developed by Hofstetter *et al*. [134, 135] which can optimise the time-temperature profile of a PDG process whereas the interaction between defects is not considered.

2.6.2.2 Aluminium gettering

Silicon photovoltaics usually use a thin aluminium layer (≥ 1 μm) to create back electrode and to form a back surface field of Al-Si binary alloy by annealing above the eutectic temperature (≥ 577 °C) [20, 24]. The efficiency of the aluminium gettering process depends on the segregation coefficient and can be quantified by means of a

segregation coefficient, which is the ratio of the metal concentration in the Al: Si melt and silicon while in thermodynamic equilibrium [19, 22]. The segregation coefficient for iron in AlG measured by using deep level transient spectroscopy (DLTS) is found 4×10^4 to 2.5×10^5 at temperatures from 950 °C to 1100 °C [132]. Like PDG process, AlG process can also remove > 99.9% of iron present in as-received condition [131] but it strongly depends on annealing temperature-time profile. Plekhanov *et al.* [136] suggested a process starting at a high temperature followed by a multiple step ramp-down processes to achieve highest AlG efficiency, but the effect of crystallographic defects is not clearly explained. Krenckel *et al.* studied the interaction of interstitial iron and GBs in aluminium gettering and found high lifetime in regions adjacent to the GBs where the thermodynamic behaviour and the effect of dislocations are not clearly explained [52].

2.6.3. Internal gettering

Some researchers have focused on improving minority carrier lifetime in multicrystalline silicon materials without incorporating an additional layer on the surface and explicitly gettering at defective regions in the bulk material [36, 41, 44, 48-50]. This is known as *internal* gettering. This technique involves diffusion of metallic impurities to defective regions such as dislocations, grain boundaries, or precipitates during thermal annealing. Buonassisi *et al.* [9] showed interstitial iron is internally gettered at grain boundaries and dislocation clusters but the efficacy of the gettering process depends on spatial density and microstructure. Other defects such as oxide precipitates also act as a gettering site of impurities but their effectiveness becomes insignificant while another gettering process such as PDG is involved [117]. More recent studies show that surface passivation with silicon nitride (most widely used in silicon photovoltaics) affects the *internal* gettering of interstitial iron in multicrystalline silicon [137, 138]. It is, therefore, important to investigate the effect of *internal* gettering at different stages of solar cell process such as in as-received wafers, after phosphorus diffused emitter formation and after the solar cell fabrication process.

Low-temperature *internal* gettering in as-grown multicrystalline silicon substrates in the absence of phosphorus diffused emitter was studied in Ref. [36, 49]. Krain *et al.* [36] studied interstitial iron concentration in mc-Si at a temperature range of 300 °C to 500 °C and reported an exponential decay in interstitial iron concentration by more than one order of magnitude, as shown in Figure 2.21. They state the decay in interstitial iron

concentration is consistent with iron diffusion to crystallographic defects. Nevertheless, Krain *et al.* [36] do not report the changes in bulk lifetime and kinetics of interaction of crystallographic defects. Furthermore, they used silicon nitride dielectric to passivate their surfaces which is well known for having a high concentration of hydrogen. It is likely that the results were influenced by hydrogenation of interstitial iron as found by Karzel *et al.* in Figure 2.22 [137].

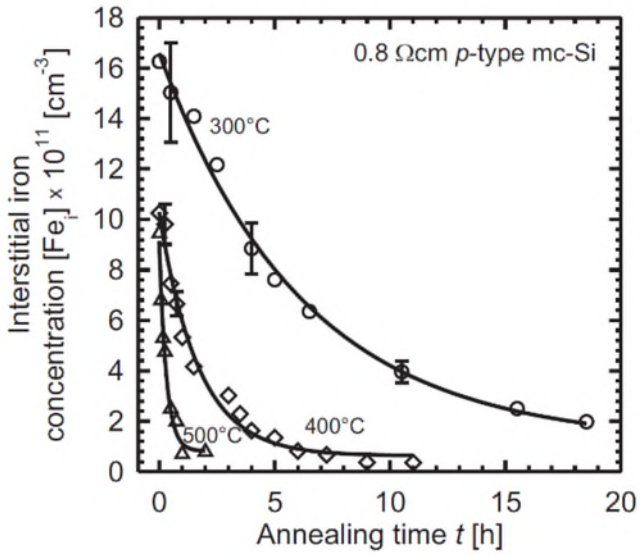

Figure 2.21. The evolution of interstitial iron concentration in mc-Si as a function of cumulative annealing time and temperature using silicon nitride passivation. The solid lines represent a fitting of data set by using an exponential decay function [36].

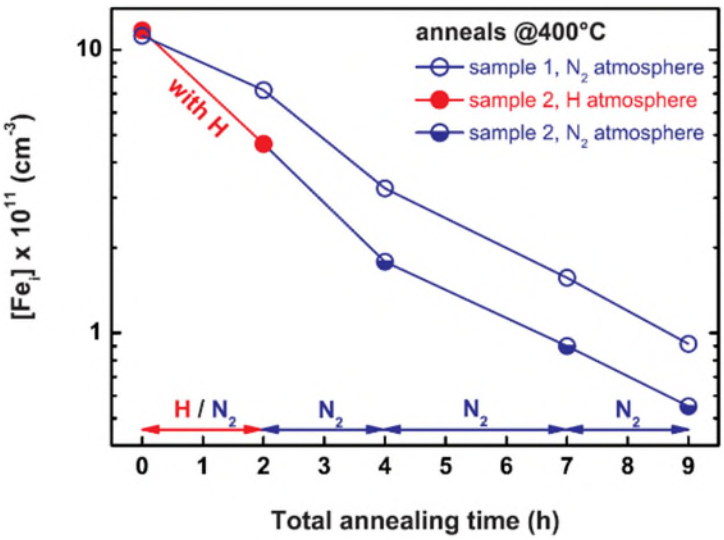

Figure 2.22. Change in interstitial iron concentration ([Fe_i]) upon annealing at 400 °C. In the first two hours of annealing sample 1 and 2 were annealed under nitrogen and hydrogen ambient, respectively and followed by subsequent annealing under nitrogen [137].

To avoid the possible incorporation of hydrogen into the bulk material and formation of Fe-H complex, Liu *et al.* [49] studied *internal* gettering at temperatures from 400 °C to 700 °C as shown in Figure 2.23. A high-temperature (1000 °C) oxidation process was used to passivate the surfaces prior to thermal annealing and the kinetics of the changes in interstitial iron concentration were reported. Although they avoid the possible bulk hydrogenation complexity, the high-temperature oxidation process has dissolved metal precipitates and redistributed impurities during the subsequent cooling step. It is also not known how low-temperature *internal* gettering affects carrier lifetime in samples from different height positions in a commercially grown mc-Si ingot, with change expected due to different dislocation densities at the different heights (see Section 4.5).

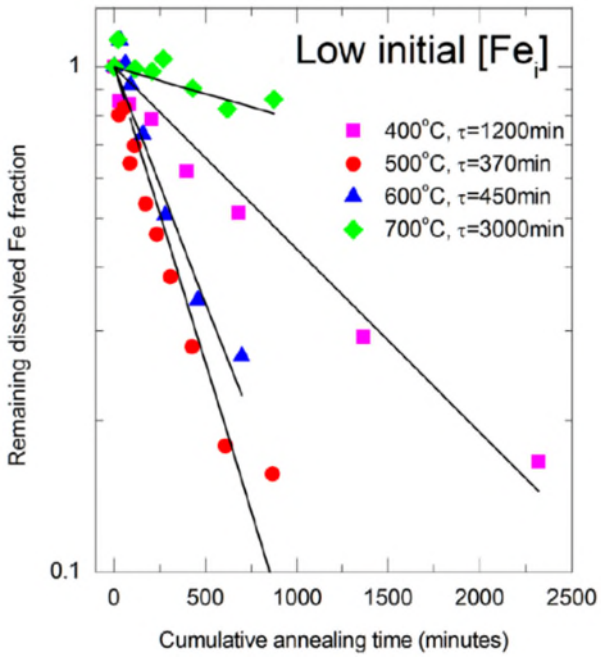

Figure 2.23. Remaining dissolved interstitial iron fraction of the annealing time in four sister samples using oxide passivation with an initial interstitial iron concentration of around 3×10^{12} cm^{-3}. Samples were annealed at 400 °C, 500 °C, 600 °C and 700 °C [49].

Internal gettering in mc-Si substrates after phosphorus diffused emitter formation was studied by Boulfrad *et al*. [48] who reported an improvement in bottom samples (‘red’ zone of the ingot) by applying an annealing at 550 °C after a pre-annealing at ≥ 950 °C. It is also reported that applying PDG can reduce iron further compared to low-temperature annealing only and high concentration of oxygen in the bottom part of the ingot could be a limiting factor for nucleation and precipitation of dissolved metal impurities. However, it is noted that applying a high-temperature pre-annealing step dissolve metallic

precipitate and thus, change the as-grown state. Furthermore, the exact mechanism of precipitates formations around oxide precipitates is not reported.

The impact of low-temperature annealing after solar cell fabrication process was studied by Rinio *et al*. [51], who reported an improvement of 0.5% absolute cell efficiency by annealing at 575 °C, as shown in Figure 2.24. Another *internal* gettering study on mc-Si solar cells was performed by Pickett and Buonassisi [50], who reported an efficiency improvement upon annealing at 500 °C. In both the studies [50, 51], the reason for the efficiency improvement is likely to be a combination of *internal* gettering of defects, *external* gettering into the phosphorus diffused emitter and hydrogenation from silicon nitride passivation. Rinio *et al*. [51] suggested that low-temperature annealing has minimal impact on efficiency improvement compared to *external* gettering but the role of hydrogenation is not reported.

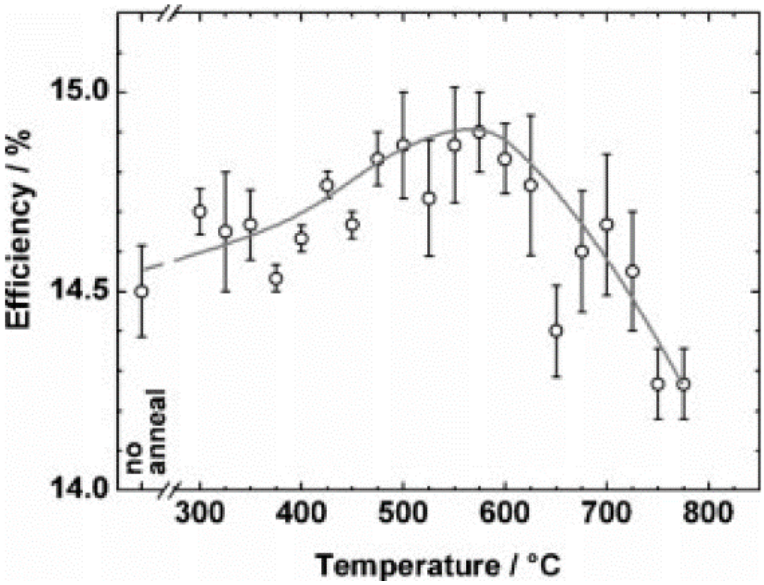

Figure 2.24. Efficiency of multicrystalline silicon solar cells from middle part of the ingot after annealing at different temperatures for 90 min. The annealing was performed after a phosphorus diffusion process [51].

2.7. Surface passivation

Surface defects in silicon materials can be passivated by either field effect passivation or chemical passivation. Different dielectric passivation methods such as PECVD silicon nitride (SiN_x), silicon oxide (SiO_x), aluminium oxide (Al_2O_3), amorphous silicon (a-Si: H) are well established [139-144]. Silicon PV industries commonly use PECVD silicon

nitride passivation in the standard cell processing, which requires a relatively high-temperature process [122, 145]. To avoid an additional thermal effect, chemical passivation such as ethanolic iodine solutions are used to measure bulk lifetime in silicon materials at room temperature [146-148]. In this thesis, a temporary iodine-ethanol (I-E) chemical passivation and PECVD silicon nitride are used. A detail of these two methods is discussed in the following sections.

2.7.1. Iodine-ethanol passivation

Iodine-ethanol solution is a temporary and removable chemical passivation method. Several researchers studied I-E passivation [146, 147, 149]. Stephens and Green studied 0.08 molar of I-E solution which reported that I-E passivation can be superior to the thermally grown oxide passivation method [146]. The effectiveness of this passivation method strongly depends on surface preparation prior to the passivation [147, 150]. Figure 2.25 shows that lifetime can be improved in samples without native oxide by twofold compared to samples with native oxide.

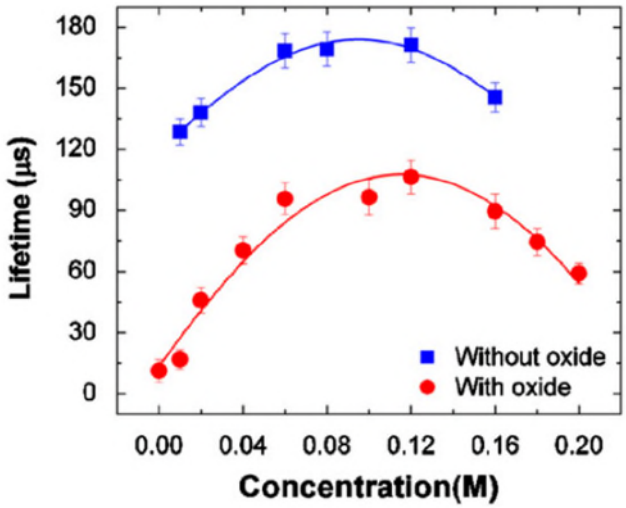

Figure 2.25. A comparison in measured minority carrier lifetime as a function of iodine concentration (molar) for the samples with and without native oxide. The lifetimes were measured at an injection level of 1.2×10^{13} cm^{-3} using a microwave photoconductance decay system (μ-PCD) [147].

Comparative studies between I-E passivation and dielectric passivations were performed by Pollock *et al.* [149] and Sopori *et al.* [151]. Pollock *et al.* [149] reported that I-E passivation is suitable for multicrystalline materials as it is a room temperature process and does not make any change in the bulk materials. However, I-E passivation is

not suitable for a long-term as its effectiveness degrades rapidly with the post-passivation time. Sopori *et al*. [151] reported a very high initial lifetime (22 ms) using I-E passivation for FZ single crystal sample but observed a substantial degradation after few minutes of passivation process. In the same study, it is also reported that I-E solution leaves residues on the silicon surfaces during lifetime measurement and suggested an etch off a thin layer from the surfaces for repetitive lifetime measurement [151]. In another study by Sopori *et al*. [152] investigated the I-E passivation mechanism and influence of a bias light on its effectiveness, which reported that induced light has a strong influence in I-E passivation for samples with a lifetime in the range of 50 to 400 μs. Note that, in this thesis, most of the samples have initial carrier lifetime less than 50 μs (discussed in Chapter 4).

2.7.2. PECVD silicon nitride passivation

Silicon nitride (SiN_x) dielectric layer grown by plasma-enhanced chemical vapour deposition (PECVD) is well established in silicon PV industry [122]. The deposition process uses silane (SiH_4) and ammonia (NH_3)/nitrogen (N_2) gases in a quartz tube where they are dissociated into NH_x and SiH_x species by plasma. This deposition process requires a temperature in the range of 300-400 °C for few minutes (~10 min) [139, 141]. The properties of silicon nitride passivation depend on a number of factors including the ratio of the gases, total gas flow, chamber pressure, substrate temperature [139]. Unlike the I-E passivation, silicon nitride passivation is stable in cell processing [139].

Silicon nitride passivates surface by attachment of hydrogen atoms with dangling bonds, which reduces recombination due to the presence of surface defects substantially. Soppe *et al*. [139] reported surface recombination velocity (SRV) < 30 cm/s using a direct plasma technique. Schmidt *et al*. [153] have reported a very low SRV < 10 cm/s using silicon nitride deposition by direct plasma. Aberle and Hezel studied surface passivation using a remote plasma technique, which reported a surface recombination velocity of 4 cm/s [122]. Silicon nitride films can also passivate the bulk defects during deposition and/or in subsequent thermal annealing [139]. Several authors suggested that that hydrogen atoms can diffuse through bulk defects and interact with them [154-158]. The physical mechanism of bulk defects passivation by hydrogen is not well understood. One possible reason is that both ionized hydrogen and interstitial iron have similar positive charge. Theoretical modelling of interaction between interstitial iron and hydrogen is

studied by Sanati, Szwacki and Estreicher [159] which reported no passivation of interstitial iron due to hydrogen. In a recent study by Karzel *et al*. [137] reported that hydrogen atoms form complexes with metallic impurities such as iron. Most recently, Liu *et al*. [160] have reported that silicon nitride films act as a gettering site for iron upon thermal annealing. It is evident that silicon nitride passivation changes the bulk defects which need to be excluded in low-temperature annealing study.

2.8. Aims and objectives

This thesis aims to improve carrier lifetime in a commercially grown multicrystalline silicon material by applying low-temperature annealing (≤ 500 °C). It also aims to develop a scientific understanding regarding the interaction between metallic impurities and other defects in mc-Si. Since solubilities of metallic impurities are very low at these temperatures (as shown in Figure 2.20), it is not necessary to conduct these experiment under a very clean environment. In order to achieve these aims, bulk lifetime, bulk interstitial iron concentration, the spatial distributions of lifetime and interstitial iron concentration maps are measured and analysed. The following novel experiments are performed to achieve the above aims:

1. To study the distribution of key material properties such as minority carrier lifetime, interstitial iron concentration, dislocation density in samples from different height positions of an edge block in a commercially-grown mc-Si ingot. This lifetime study is different from Bothe *et al.* [161] as a temporary liquid iodine-ethanol passivation is used and extended to a distribution of metallic impurities and crystallographic defects. Primary analysis is not only to show a distribution of different properties but also make a comparative analysis of the changes in low-temperature *internal* gettering (Chapter 4).
2. To perform a low temperature (≤ 500 °C) *internal* gettering on sister samples sourced from four different height positions of an ingot. This work is far more comprehensive and better designed than the experiment in Krain *et al*. [36] and Liu and Macdonald [49]. To avoid the possible bulk hydrogenation sourcing from silicon nitride passivation, a temporary chemical solution of iodine-ethanol is used at room temperature (detail in Chapter 3). This is a different method to dissociate the effect of temperature in iron gettering at crystal defects from other influential factors such as hydrogenation. As no pre-thermal treatment is used, the changes in low-temperature

annealing are directly comparable with the as-grown state (the results are discussed in Chapter 5). This work is published as paper [53].

3. To investigate the role of surface passivation in low-temperature (≤ 500 °C) *internal* gettering. In this work, a comprehensive study is performed in an adjacent of samples from different ingot height positions (as in Chapter 5), as the starting lifetime, interstitial iron concentration and microstructure (particularly the density of grown-in dislocations) varies widely. Sister samples from each location are passivated with PECVD SiN_x and subjected to the same thermal treatment in Chapter 5 and the data are compared to assess the impact of possible hydrogenation from the SiN_x film on the *internal* gettering behaviour. The details are discussed in Chapter 6. This work has been published as paper [54].

4. To investigate the effect of low-temperature (≤ 500 °C) *internal* gettering after a standard phosphorus diffusion gettering with a sheet resistance ~55 Ω/sq. Samples sourced from four different height positions are used for PDG in collaboration with the University of Konstanz, Germany. Sister samples from every height position are annealed at 300 °C to 500 °C. The results are compared to investigate whether low-temperature *internal* gettering is able to improve bulk carrier lifetime after phosphorus diffusion gettering or not (discussed in Chapter 7).

5. To investigate the effect of phosphorus diffused emitter in low-temperature *internal* gettering at 400 °C. This experiment is performed on two sister samples sourced from the same height positions used in Chapter 5 and Chapter 6. Emitters are removed from one set of samples prior to thermal annealing. The results are compared in samples with and without emitter in annealing steps (discussed in Chapter 7).

6. To evaluate the lifetime improvement obtained in Chapter 5 by low-temperature *internal* gettering in as-grown samples in a standard solar cell fabrication process. Two samples sourced from the bottom part of the ingot are used. A sample is annealed at 400 °C prior to phosphorus diffusion gettering. Both samples are subjected to a PDG process and a subsequent low-temperature gettering at 400 °C and the results are compared (discussed in Chapter 7).

The experimental methods used in this thesis are described in the next Chapter.

Chapter 3 Experimental methods

3.1. Introduction

As discussed in Chapter 2, gettering (*external* or *internal*) processes can be applied to improve bulk carrier lifetime in silicon. In this thesis, a comprehensive study into low-temperature *internal* gettering (≤ 500 °C) processes have been performed on multicrystalline silicon wafers sourced from different height positions of a commercially grown ingot. This Chapter discusses the design of the experiments and gives details of different process sequences including sample selection, surface preparation, and different passivation schemes. Furthermore, different characterisation techniques used to measure bulk resistivity, bulk minority carrier lifetime, spatial distribution of lifetime, bulk interstitial iron concentration and spatial distribution of interstitial iron concentration are described.

3.2. Design of experiment

Low-temperature *internal* gettering processes can usually be performed at three different stages in the photovoltaic cell production cycle such as to as-grown wafers, after emitter formation and after completion of the solar cell fabrication process. An illustration of a process sequence from silicon raw materials to PV system and different experiments performed in this thesis is presented in Figure 3.1. Firstly, a comprehensive experiment (1a) on low-temperature *internal* gettering was performed on as-grown multicrystalline silicon samples using a temporary chemical surface passivation (results are discussed in Chapter 5). In order to investigate the effect of different passivation schemes on low-temperature *internal* gettering including possible hydrogenation effects from the silicon nitride dielectric layers, experiment 1b was designed (discussed in Chapter 6). Another

set of experiments (2a, 2b and 2c) on samples after phosphorus diffused emitter formation was designed to investigate whether low-temperature *internal* gettering can improve lifetime even after PDG process. Furthermore, *external* gettering of metallic impurities to phosphorus diffused layers and to silicon nitride passivation layers in low-temperature annealing was investigated.

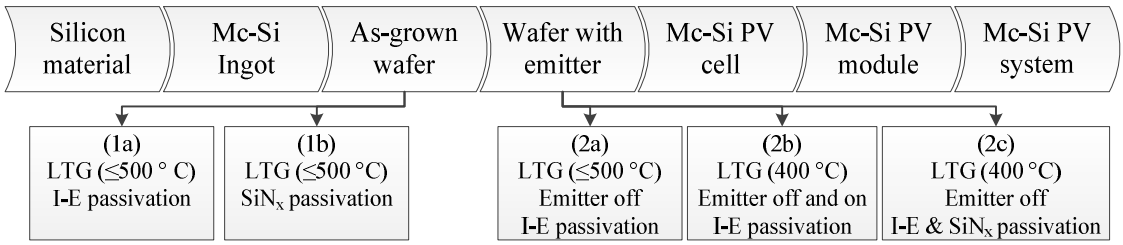

Figure 3.1. Process sequence from raw silicon material to multicrystalline silicon photovoltaic system. Illustration of the major experiments performed on as-grown and after phosphorus diffused emitter formation in this thesis.

3.3. Sample selection

Samples were sourced from an edge block of a commercially grown multicrystalline silicon (mc-Si) ingot (cross section: 624 mm × 624 mm) supplied by a mc-Si wafer manufacturer. The neighbouring (sister) wafers came from four different height positions of the block (bottom (B), bottom middle (MB), top middle (MT) and top (T)) with a surface area of 156 mm × 156 mm. The distributions of wafer properties such thickness, bulk resistivity were measured, as discussed in Section 3.4. It is noted that these wafers were cut using a diamond wire so the surface structure is slightly shiny and ridged which is different from usual wafers used in mc-Si photovoltaics. In order to make experimental samples, the neighbouring wafers were laser cut into 39 mm × 39 mm by using a 34 ns, 355 nm neodymium yttrium-aluminium-garnet (Nd: YAG) (E-series) laser micromachining system fitted with high-resolution computer numerical control (CNC) stages from Oxford Lasers. The sister samples were numbered by a diamond scribe according to a brick position in the ingot, height position in the brick and chronological order in every position. The selection process from cast ingot to experimental samples is illustrated in Figure 3.2 (i) and (ii).

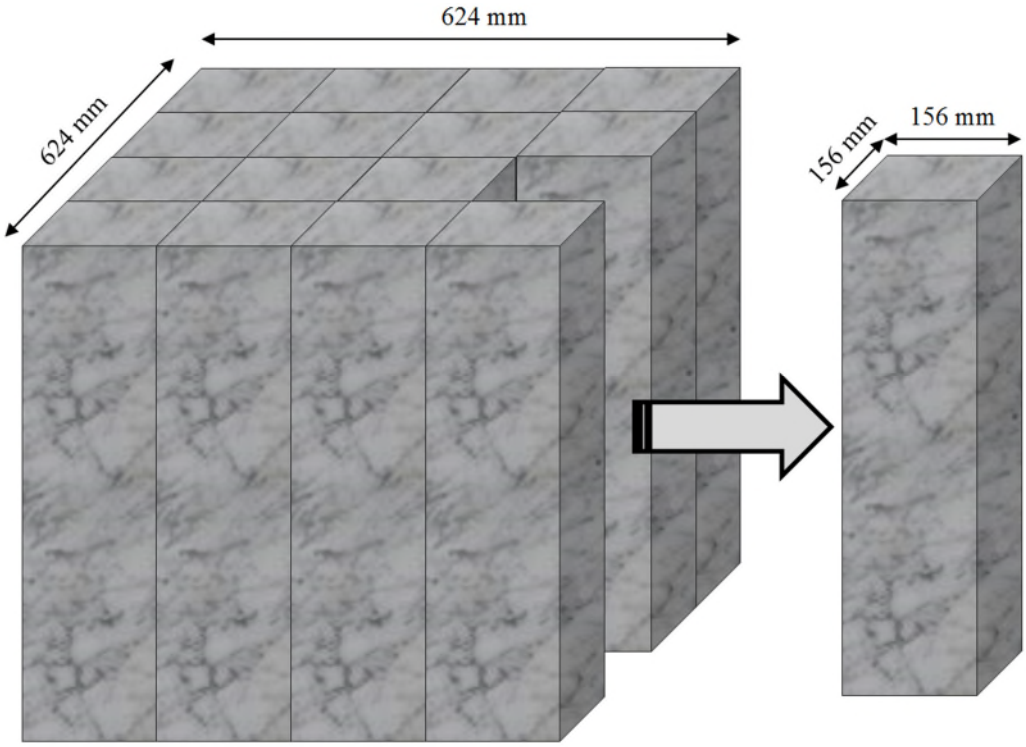

(i)

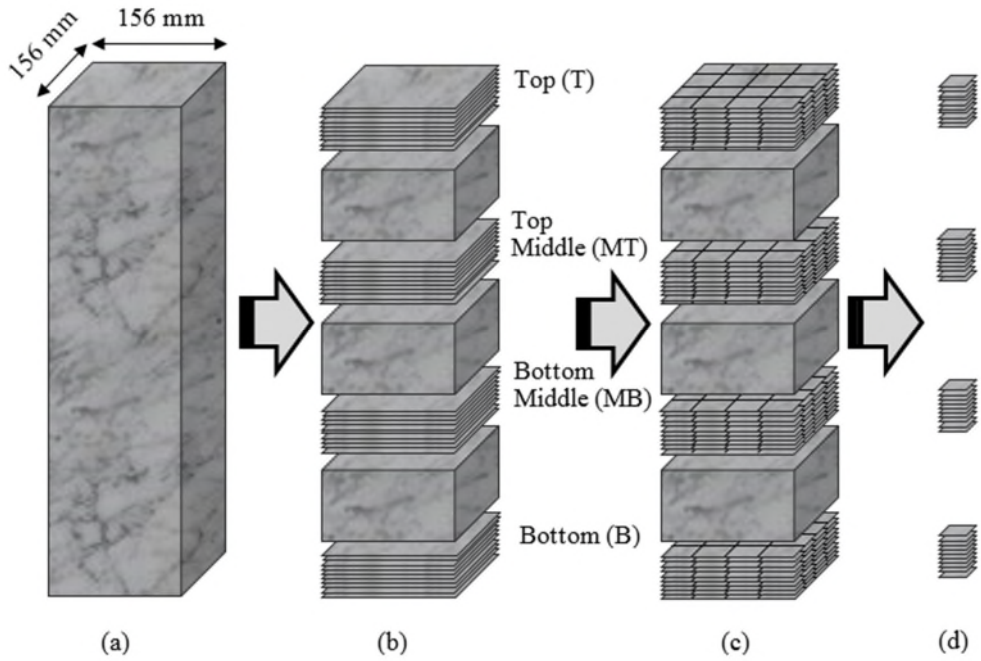

(ii)

Figure 3.2. Illustrations of sample selection: (i) a block from the edge of a commercially grown ingot (ii) 10 sister wafers (156 mm × 156 mm) from four different height positions (b) wafers after laser cutting (c) and experimental samples (39 mm × 39 mm).

3.4. Thickness and bulk resistivity measurement

The thickness of as-received sister samples was measured by using a slide calliper with a precision of 0.01 mm. A distribution of thickness and a statistical box plot of as-received values and after a chemical polishing for samples from different height positions is presented in Figure 3.3. It shows that the data clusters fit with the statistical analysis. The average thickness in all four height positions varies marginally from 205 μm to 210 μm. It is noted that the final thickness after removing saw damage by a wet chemical etching process is substantially lower than the primary thickness, used in the bulk lifetime measurement.

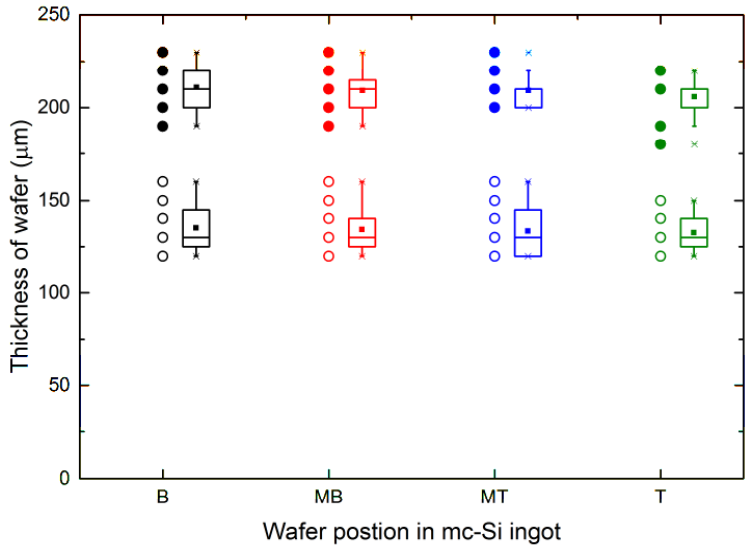

Figure 3.3. Distribution of measured thickness (± 10 μm) of as-received (solid circles) and after chemical polishing (open circles) of 10 sister wafers from four different height positions of the mc-Si brick. To the right of each data cluster, the open box represents the 25th and 75th percentile and median. The solid rectangular point in the open box represents the mean of data cluster.

The bulk resistivity was measured by a four-point-probe resistivity meter made by Jandel Engineering Limited. An RM300 test unit was used to measure bulk resistivity in combination with four-point-probe equipment as shown in Figure 3.4a and Figure 3.4b. The probe head contains four probes with a spacing (s) of 1 mm. Its height needs to be adjusted manually according to the thickness of the experimental sample to ensure a proper contact. An operating lever was used to place the probe head down to complete

cycle between the probes and samples. A current was supplied between the two outside probes and the corresponding voltage was measured across the other two probes, illustrated in Figure 3.4b.

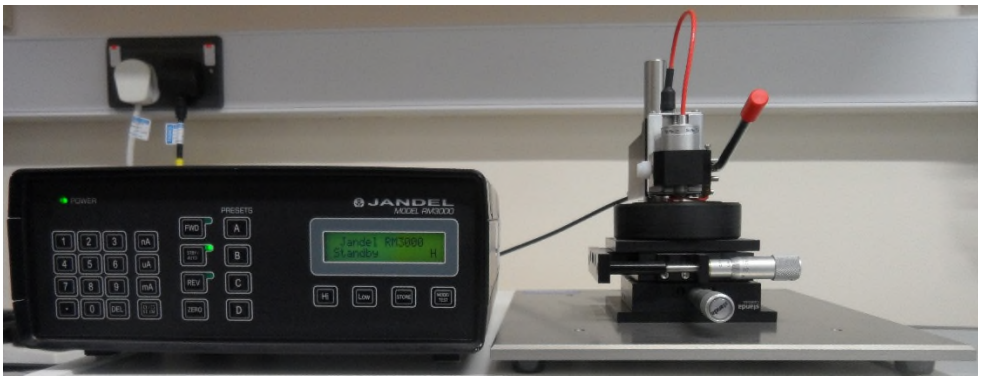

(a)

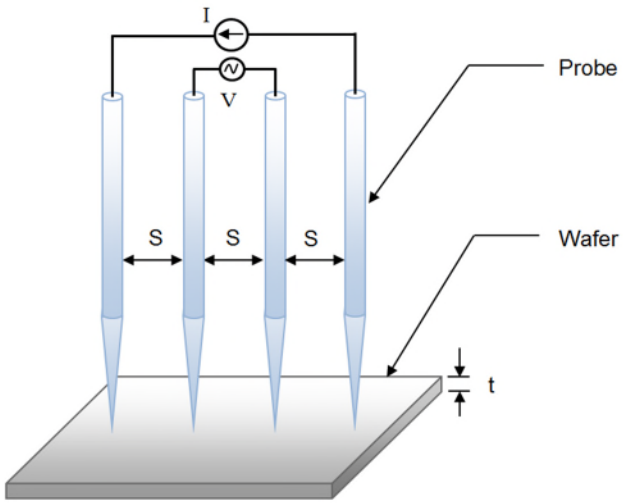

(b)

Figure 3.4. (a) The four-point probe resistivity meter used in this work (b) illustration of the fundamental working principle. The probe spacing s = 0.1 cm.

Bulk resistivity for wafers and films can be expressed as:

$$\rho = R_s \times t \tag{3.1}$$

where t is the thickness of the sample (cm) and R_s is the sheet resistance of the wafer (Ω cm) which can be calculated as [162]:

$$R_s = \left(\frac{\pi}{\ln 2}\right) \times \frac{V}{I} \tag{3.2}$$

where I is the test current (A) and V is the measured voltage (V). Using Equation 3.1 and 3.2, the bulk resistivity can be calculated as [162]:

$$\rho = 4.532 \times \frac{V}{I} \times t \times C_1 \tag{3.3}$$

where C_1 is the correction factor depends on the ratio of samples thickness (t) and probe spacing (s) for wafers (sheet) and ratio of diameter to probe spacing for circular samples is presented in Table 3.1.

Correction factors for rectangular sample thickness, t		Correction factors for circular sample diameter, d	
t/s	$C_1(t/s)$	d/s	$C_2(d/s)$
0.3	1.0000	10	4.1712
0.4	0.9995	20	4.4364
0.5	0.9974	30	4.4892
0.6	0.9919	40	4.5080
0.7	0.9816	50	4.5167
0.8	0.9662	60	4.5215
0.9	0.9459	70	4.5244
1.0	0.9215	80	4.5262
1.2	0.8643	90	4.5275
1.4	0.8026	100	4.5284
1.6	0.7419	200	4.5314
1.8	0.6852	∞	4.5320
2.0	0.6337		

Table 3.1. Calibration constant used to measure bulk resistivity for sheet/film and circular sample by using the four-point-probe resistivity meter [162].

Bulk resistivity (volume) for the samples in Figure 3.3 was measured by applying a forward bias current of 100 μA. A distribution of data cluster and corresponding statistical box plot is presented in Figure 3.5. Although the distributions show a deviation from the mean value, they have a good agreement with statistical box plot at every height position in the ingot. The average bulk resistivity (volume) is highest at the bottom part of the ingot 7.5 Ω cm and it decreases to 4.75 Ω cm at the top part of the ingot. It is noted that the measured sheet resistivity by four-point-probe is ~1 Ω cm which is similar to the resistivity range supplied by the wafer manufacturer which varies from 0.7 Ω cm to 1.1 Ω cm from top to bottom in the brick. The bulk resistivity was measured at five different points in the samples and a slight variation was found. The average bulk resistivity was used for lifetime measurements.

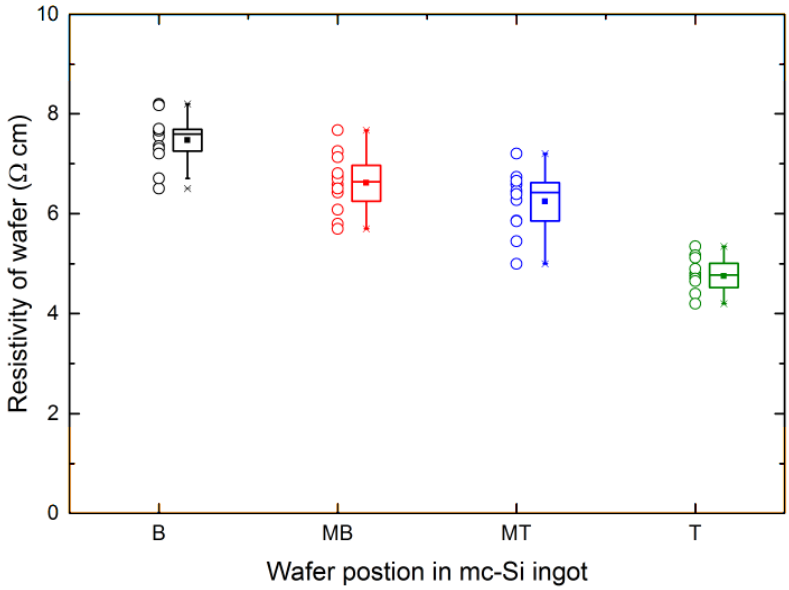

Figure 3.5. Distribution of resistivity (volume) (with an error limit up to ± 0.7 Ω cm) of sister wafers measured by the four-point-probe resistivity meter for samples at four different height positions in a mc-Si ingot. To the right of each data cluster, the open box represents the 25th and 75th percentile and median. The solid rectangular point in the open box represents the mean of data cluster.

3.5. Surface structure and etching

After sample selection and primary characterisation of material properties including thickness and bulk resistivity, samples' surfaces were examined under a microscope and different chemical solutions to remove saw damage were investigated. In this section, surface structures of as-received samples, a detailed process of different chemical polishing techniques and their effect on surface morphology are discussed. Furthermore, the method used to determine the dislocation density distribution is discussed.

3.5.1. As-received wafers

As stated in the previous section that a diamond cutter was used to slice the ingot into wafers and therefore, wafers have a higher degree of surface roughness than the usual wafers used in the silicon photovoltaic industry. The surface structures of as-received samples were examined with a ContourGT-X optical surface-profiling system which can detect in a range from a fraction of 1 nm up to approximately 10 mm in height. Figure

3.6a and Figure 3.6b show a 3D profile of 10 mm × 10 mm surface area and a line profile (marked with a white dashed line in Figure 3.6a) respectively. It can be seen that surface ridges are widely spread over the surface area with ± 12 μm height variation with respect to the reference line (0 μm).

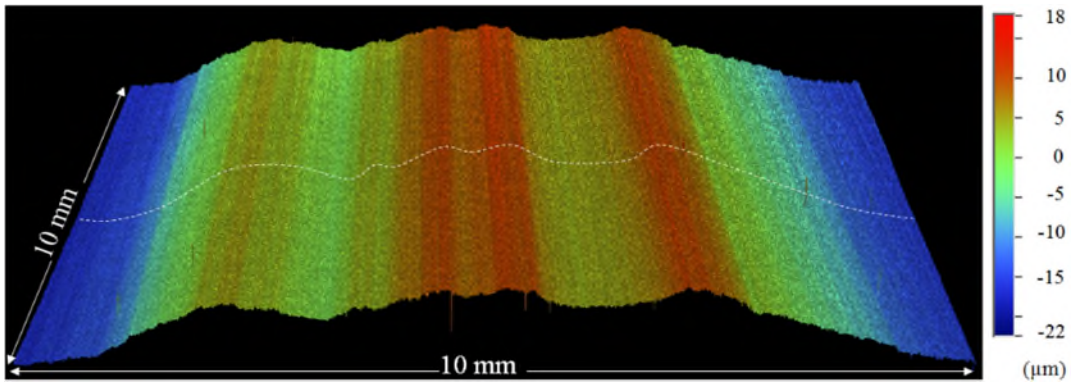

(a)

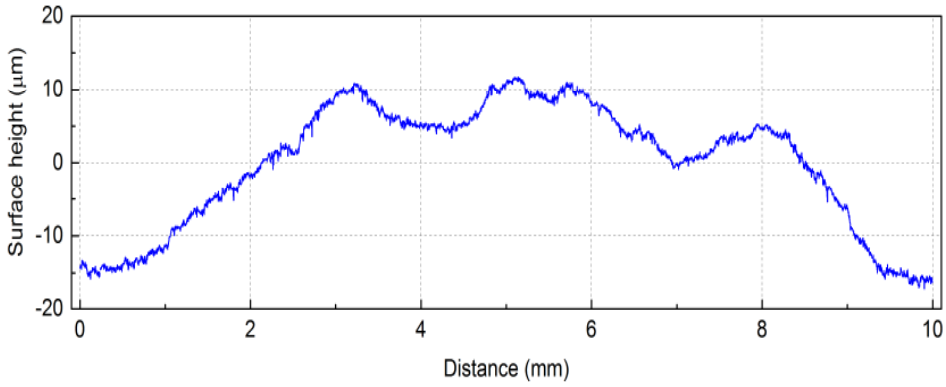

(b)

Figure 3.6. Illustration of a surface profile of a typical part of an as-received mc-Si wafer (a) 3D image of a surface area of 10 mm × 10 mm (b) line scan of surface height along the marked white line in Figure (a).

Although, the surfaces exhibit non-uniformly distributed ridges, the most important thing is to examine the surface structure at the microscopic level as this may affect the effectiveness of surface passivation and thus bulk lifetime measurement. The surface roughness of an as-received mc-Si sample was examined with different levels of magnification under an XL30 ESEM scanning electron microscope. Images are shown in Figure 3.7. It was seen that surfaces are heavily damaged as in Figure 3.7b and distributed randomly. Chemical polishing was used to remove saw damages created during wafer

dicing process and to reduce overall surface waviness, as discussed in the following sections.

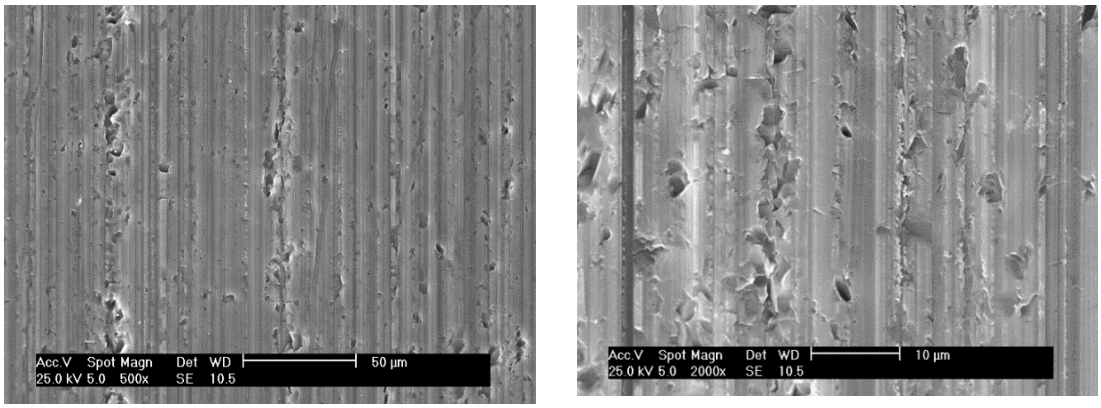

(a) (b)

Figure 3.7. The surface structure of an as-received mc-Si sample under an XL30 ESEM Scanning electron microscope at different magnifications (a) 500x (b) 2000x.

3.5.2. Planar etching

As-received samples contain deep saw damage which needed to be removed to create a uniform surface. In multicrystalline silicon photovoltaics, wet chemical techniques are used to texture surface to reduce reflection from the surfaces and to improve light trapping properties [163, 164]. Anisotropic etching using an alkaline solution such sodium hydroxide (NaOH), potassium hydroxide (KOH) or tetramethylammonium hydroxide (TMAH) is well established for single crystal silicon [165, 166]. However, this is not suitable for multicrystalline silicon materials as they contain grains with different crystal orientations. It is, therefore, necessary to use an isotropic etching technique which is independent of crystal orientations. In this work, both wet etching approaches (alkaline and acidic) were investigated. It is noted that the purpose of the etching process is not to texture the surface to improve light trapping but to create a uniform polished or semi-polished surface for characterisation, particularly lifetime imaging. In the following sections, brief details of the reaction processes and surface morphologies are discussed.

3.5.2.1 Alkaline etching by TMAH

In order to remove saw damage from the surface, a TMAH (25%) solution was investigated. A multicrystalline silicon sample was dipped in 10% of TMAH solution at

80 °C temperature for 10 min and followed by an RCA cleaning (detail is described in Section 3.5.4) and nitrogen drying. A general reaction mechanism of silicon in an alkaline solution can be given by:

$$Si + 2H_2O + 2OH \rightarrow \left[SiO_2(OH)_2\right]^{-2} + 2H_2 \quad (3.4)$$

It was noted that the reaction rate strongly depends on solution temperature and process time. A thickness of 10-15 μm was etched off from each side of the sample, which was estimated by:

$$t_{\text{etch-off}} = \frac{m_i - m_f}{2 \times A \times \rho} \quad (3.5)$$

where m_i is the initial mass, m_f is the mass after chemical etching measured using a mass balance with a precision of 0.001 g, A is the surface area, ρ is the density of silicon (taken as 2.3290 g/cm^3 [167]).

The surface morphologies after etching were investigated under the same SEM at low (250x) and high (2000x) magnification as shown in Figure 3.8a and Figure 3.8b which show that surface structure varies with crystal orientation. To avoid the dependency on crystal orientation, this etching technique was not used further in this thesis.

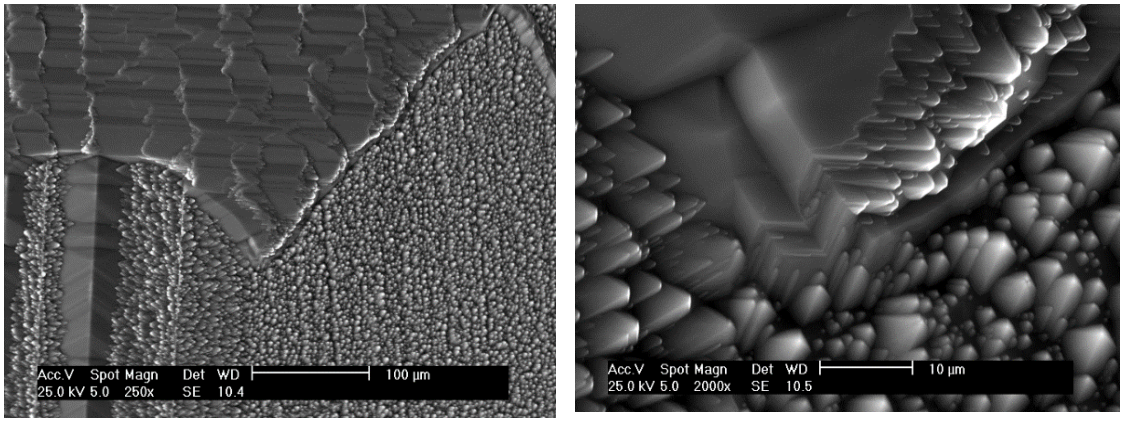

(a) (b)

Figure 3.8. The surface structure of a mc-Si sample after etching with a TMAH alkaline solution in a SEM at (a) 250x (b) 2000x magnification.

3.5.2.2 Acidic etching

The anisotropic etching process using an alkaline solution is not suitable for multicrystalline silicon material to have a uniform surface as discussed in the previous

section. Therefore, an isotropic etching technique using an acidic solution comprising hydrofluoric acid (HF (50%)), nitric acid (HNO_3 (69%)) and acetic acid (CH_3COOH (100%)) was used. HF and HNO_3 mixtures are widely used in silicon photovoltaics for etching silicon in which HNO_3 oxidise the surface and HF removes silicon dioxides [168]. CH_3COOH acts as a controller of the etching rate [169]. The fundamental reaction mechanism is according to:

$$3Si + 4HNO_3 + 18HF \rightarrow 3H_2SiF_6 + 4NO + 8H_2O \quad (3.6)$$

Several key factors including solution composition, reaction mechanism, temperature, etching rate, agitation, batch size were investigated. A suitable composition of the mixture was estimated according to an iso-etch-rate contour at room temperature (25 °C) as in Figure 3.9 [170] in which curve lines represent constant etching rate (× 25.4 μm/min). A ratio of HF: HNO_3: CH_3COOH = 24:58:18 was used in this thesis where the reaction rate is ~78.7 μm/min (~3.1× 25.4 μm/min) as pointed by the intersection of red lines in the iso-etch contour. Samples were etched for 60 s at room temperature which removed approximately 30 μm of material from both sides. It was noted that surface morphology strongly depends on agitation of solution during the etching process and batch size in a solution. The samples were agitated vertically to avoid etch pit formation and a fresh solution was made after etching every three samples. After etching, the samples were RCA cleaned and followed by nitrogen drying. The surface structure after performing the etching process was investigated, as discussed below.

The surface profile was measured by a contactless ContourGT-X optical surface-profiling system and profiles are shown in Figure 3.10a and Figure 3.10b. The ridge height in as-received samples ($\pm$ 15 μm) (illustrated in Figure 3.6) was decreased substantially to $\pm$ 5 μm after performing the etching process. The surface morphology was examined in the SEM and planarity was observed as shown in Figure 3.11a and 3.11b. Furthermore, unlike the TMAH etching process, the isotropic etching process creates uniform planar surfaces without being dependent on crystal orientations.

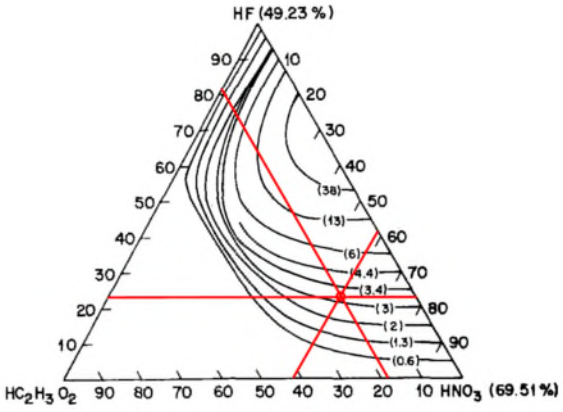

Figure 3.9. Curves of a constant rate of changes of silicon material (× 25.4 μm/min) as a function of etchant composition (weight percent in the system HF:49.23%, HNO_3:69.51% and CH_3COOH:100%). The red colour lines represent the composition of three acids in solution and the intersection (circle) represents approximate reaction rate [170].

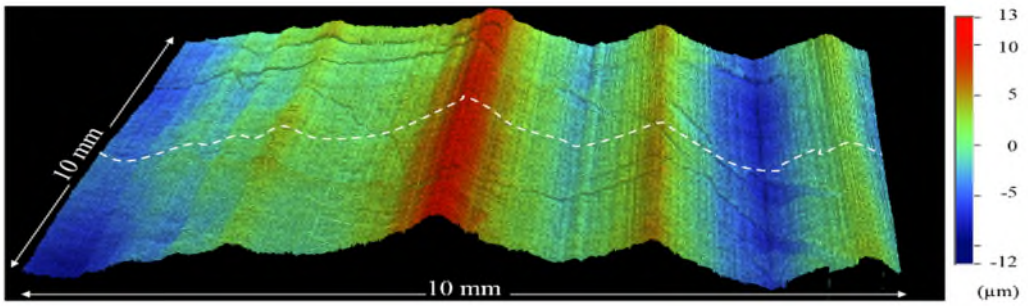

(a)

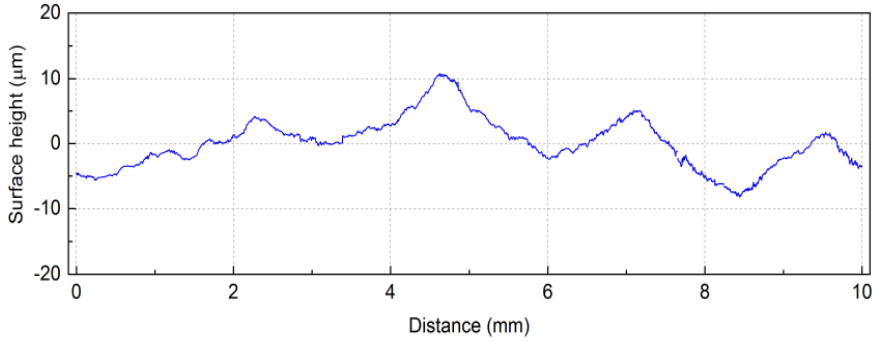

(b)

Figure 3.10. An example of the surface profile of a multicrystalline silicon wafer after chemical polishing with isotropic etching (HF: HNO_3: CH_3COOH = 24:58:18) (a) 3D image of a surface area of 10 mm × 10 mm (b) line scan of surface height along the white marked line in Figure (a).

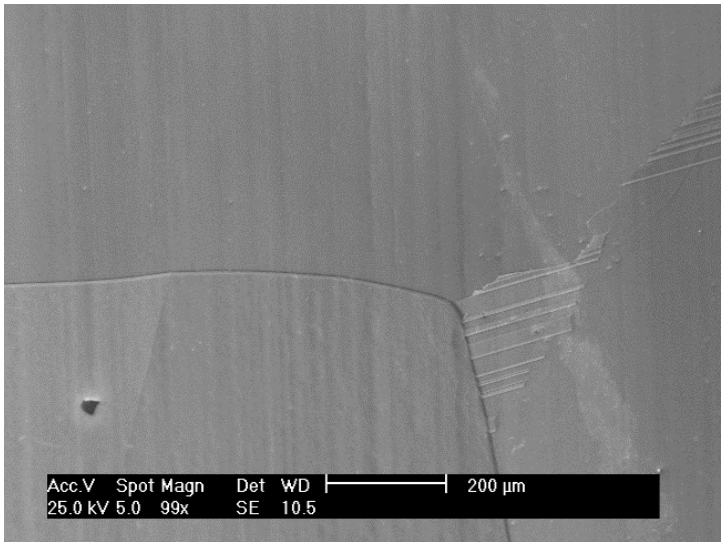

(a)

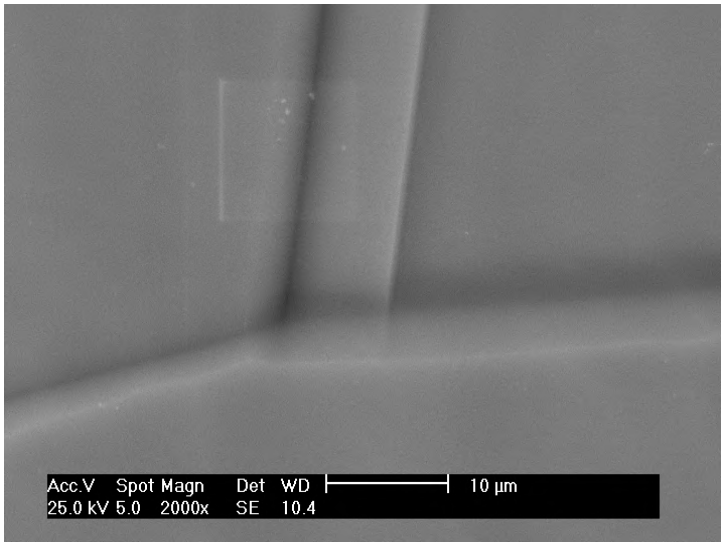

(b)

Figure 3.11. The surface structure of a multicrystalline silicon wafer after polishing by isotropic etching (HF: HNO_3: CH_3COOH = 24:58:18) under SEM with a magnification of (a) 99x (b) 2000x. The surface 'waviness' is clearly visible in the first image (a). The lines in both the images are grain boundaries.

3.5.2.3 Emitter removal

A series of low-temperature *internal* gettering experiments were performed on samples after phosphorus diffusion gettering. To reveal the bulk lifetime, emitters were removed using an acidic solution comprising HNO_3 (69%): CH_3COOH (100%): HF

(50%) in the ratio of 10:5:2 at room temperature for 35 s and followed by an RCA cleaning. A thickness of ~5 μm was etched off from every side.

3.5.3. Defect-revealing etching and dislocation mapping

Dislocations can increase recombination activity and reduce device performance by introducing recombination centres, as discussed in Chapter 2. Usually, dislocations in multicrystalline silicon wafers are not visible after planar etching as demonstrated by Figure 3.11. Several wet chemicals etches like Secco [171] and Sopori [172] are well established to reveal dislocations. Although Secco is a rapid and effective etch, it was not used here because of a safety concern over potassium dichromate ($K_2Cr_2O_7$). In this thesis, dislocations were revealed after saw damage removal. Two defect etching solutions were investigated. Firstly, an experiment was performed with a micropit delineation etchant (MD1) comprising HF (50%), HNO_3 (69%) and CH_3COOH (100%) in the ratio of 1: 4: 95 at room temperature [173]. It was observed that the etching is extremely slow. More than 40 h was required to confirm the findings in Ref. [173]. Furthermore, the etch pit diameter was estimated as less than 5 μm. Dislocation density was counted by using microscopic images in the image processing software ImageJ. However, this approach requires high-resolution images. A large number of image files needs to be run to make a dislocation density of a large area *e.g.* 39 mm × 39 mm which is extremely time-consuming exercise. To resolve this issue, a rapid dislocation density mapping technique developed by Needleman *et al.* [174] was implemented. A summary of the major processing sequences used is shown in Figure 3.12 and discussed in the following sections.

To reveal dislocations, a Sopori etch comprising HF (50%): CH_3COOH (100%): HNO_3 (69%) = 36: 20: 2 was used at room temperature for 90 s with a vertical agitation. To remove the stain layer created by Sopori etch, samples were dipped in a solution of HNO_3 (69%): HF (50%) = 9:1 for 2 s and followed by an RCA cleaning. Etch pits were characterised under an XL30 ESEM scanning electron microscope and results are shown in Figure 3.13a and 3.13b. It can be seen that dislocation density is not uniform throughout the samples. In relatively high defect-containing regions, dislocations etch pits appear to be lined up as reported in Ref. [175]. The average etch pit diameter was estimated as ≥ 5

μm, as shown in Figure 3.13b which is necessary for sufficient contrast in scanned images.

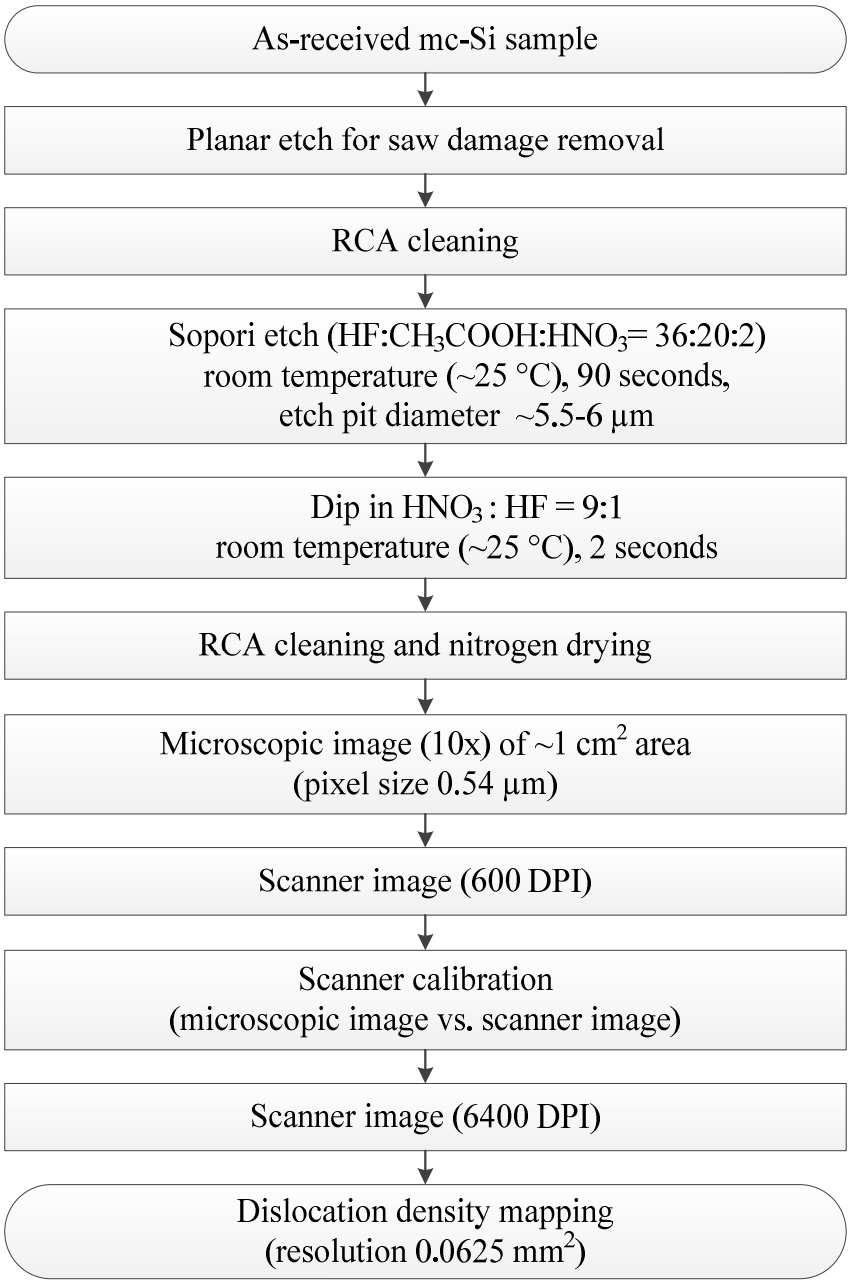

Figure 3.12. Process sequence to measure dislocation density in a multicrystalline silicon sample revealed by a Sopori etch. The counting algorithm developed by Needleman *et al.* was used to determine dislocation density [174].

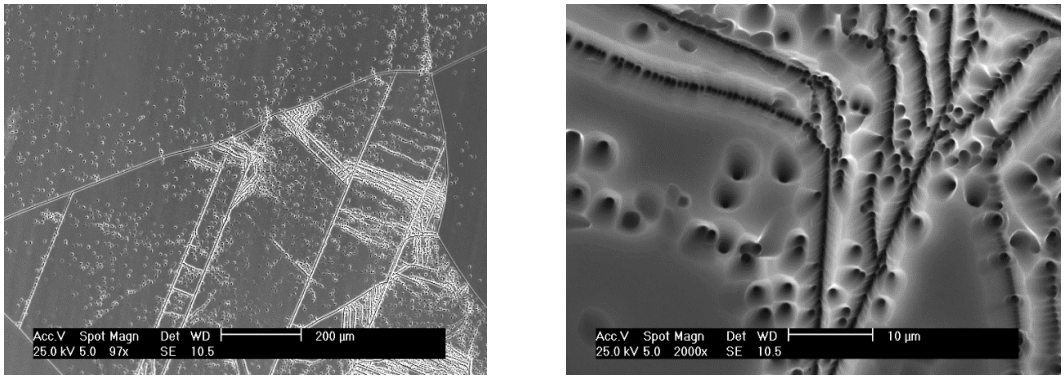

(a) (b)

Figure 3.13. Microscopic images of dislocation density of a multicrystalline silicon sample used in this thesis under a magnification of (a) 97x (b) 2000x. The solid straight lines represent grain boundaries in both the images.

An Epson Perfection V-800 Photo Scanner was used to scan the etched sample. To calibrate the scanning images, an etched sample was scanned with a resolution of 600 dots per inch (DPI) as shown in Figure 3.14a. A microscopic image under a magnification of 10x was obtained of a small rectangular region (marked by dashed in Figure 3.14a) from a Zeiss optical microscope (automated stage control with integrated software and automated image stitching). Scanned and microscopic images of the same region were then used into respective Matlab codes (freely available online at http://pv.mit.edu/dlcounting/) and a calibration curve was generated between scanner and microscope output. The number of white pixels from the inverted scanner image was plotted against dislocation density obtained from the microscope image, as presented in Figure 3.14b. The data cluster shows a linear agreement from which calibration parameters such as intercept (-1.19) and slope (2.13×10^{-4} pixel.cm^2) were estimated. After performing the calibration process, etched samples were scanned with a higher resolution of 6400 DPI to obtain accurate measurements. Dislocation density maps were generated using the counting algorithm in Ref. [174] with a pixel area of 0.0625 mm^2 using the calibration scaling factors, as shown in Figure 3.14c.

It is noted that there are some technical limitations of this mapping technique. Firstly, etch pits diameters must be greater than 5 μm. Secondly, due to the overlapping of dislocation in defect cluster, the maximum measurable dislocation density is ~ 4×10^6 cm^{-2}. Finally, since the technique is based on surface images, any surface defects such as regions with twin boundaries give very high dislocation density which is not an actual representation of bulk defects.

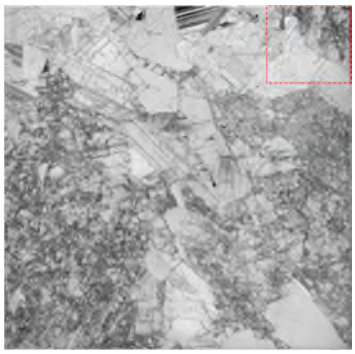

(a)

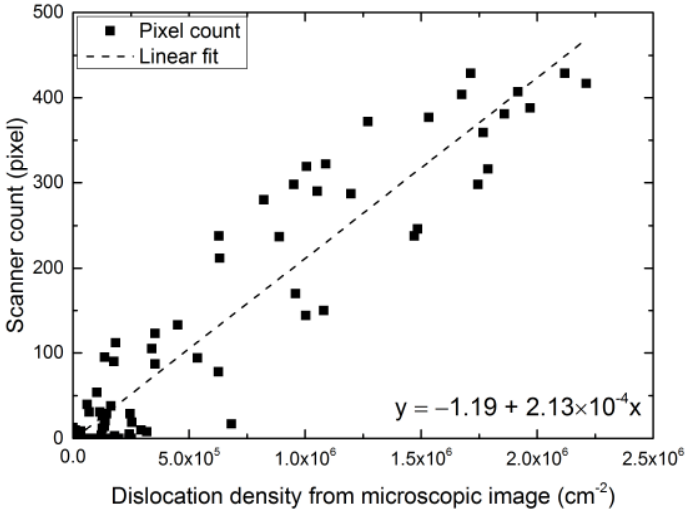

(b)

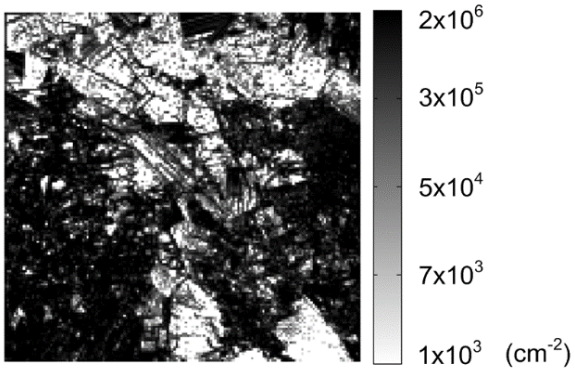

(c)

Figure 3.14. (a) Scanned image of a multicrystalline silicon sample (39 mm × 39 mm) with a 600 DPI; (b) calibration of the scanned image (dotted box in Figure a) from an optical microscope image (10x). The dashed line represents a linear fit of the data cluster; (c) dislocation density mapping using the counting algorithm of the sample in Figure a.

3.5.4. RCA cleaning

A standard RCA cleaning method was used heavily in this thesis. The cleaning procedure is summarised as follows:

- Dip in a solution of ammonium hydroxide (28 to 30%), hydrogen peroxide (31%) and deionized (DI) water in the ratio 1:1:5 for 10 mins at 75 to 85 °C ('RCA 1').
- Dip in DI water for 1 min at room temperature followed by a rinse in DI water (resistivity 18.2 MΩ cm) at room temperature (~25 °C) for 3 mins.
- Dip in 2% hydrofluoric solution (50%) at room temperature (~25 °C) for 1 min.
- Dip in a solution of hydrochloric acid (37%), hydrogen peroxide (31%) and deionized water mixed in the ratio 1:1:5 for 10 mins at 75 to 85 °C ('RCA 2').
- Dip in DI water for 1 min at room temperature and followed by a rinse in DI water (resistivity 18.2 MΩ cm) at room temperature (~25 °C) for 5 mins.
- Dry in nitrogen.

A fresh solution was made for every two cycles of cleaning. Samples were then placed in boxes to avoid unwanted contamination from the atmosphere.

3.6. Surface passivation

In silicon photovoltaics, passivation is one of the most important manufacturing steps to reduce optical loss and surface recombination velocity. In this thesis, after removing saw damage by using isotropic etching, samples were passivated with different surface passivation techniques. As discussed in Chapter 2, silicon nitride passivation is widely used but it is widely believed to have an effect on bulk lifetime. To mitigate such complexity and to limit the possible effect of bulk hydrogenation, a temporary chemical solution of iodine-ethanol passivation process was used in this thesis. To investigate the possible bulk hydrogenation effect, a set of samples was also passivated with silicon nitride and compared with the iodine-ethanol passivation. In the following section surface passivation techniques used in this thesis are discussed.

3.6.1. Iodine-ethanol

A temporary chemical solution of iodine-ethanol was heavily used in this thesis. It is noted that this method strongly depends on the wafer surface preparation (particularly cleaning) prior to surface passivation. The major process sequences of I-E surface passivation are shown in Figure 3.15a. Samples were RCA cleaned and were then dipped in 10% HF solution to remove native oxide (which affects lifetime substantially [147]),

followed by a methanol dip. Samples were dried in nitrogen and immediately placed in transparent polythene bags. A 0.1 M solution of iodine (≥ 99.8% purity, supplied by Fisher Scientific) and ethanol (≥ 99.8% purity, supplied by Sigma-Aldrich) was made and a few drops of solution were added at room temperature to form a thin uniform layer on both surfaces. The excess solution and air bubbles were squeezed out prior to sealing. An example of a 39 mm × 39 mm multicrystalline silicon sample after completion of I-E passivation is shown in Figure 3.15b. As the I-E passivation technique suffers from a lack of stability [176], characterisation of a sample was performed within 4-5 minutes after completion of the surface passivation process. The repeatability of lifetime measurement using I-E passivation and effect of illumination on passivation quality were investigated, as discussed in the following sections. To avoid residue formation on the surfaces, samples were removed from the polythene bag immediately after characterisation and dipped in a methanol, followed by an RCA cleaning. The samples were examined under an optical microscope to check any surface changes due to I-E passivation, particularly residue formation. No residue was observed in this work. A fresh solution was made to passivate samples after every thermal annealing step.

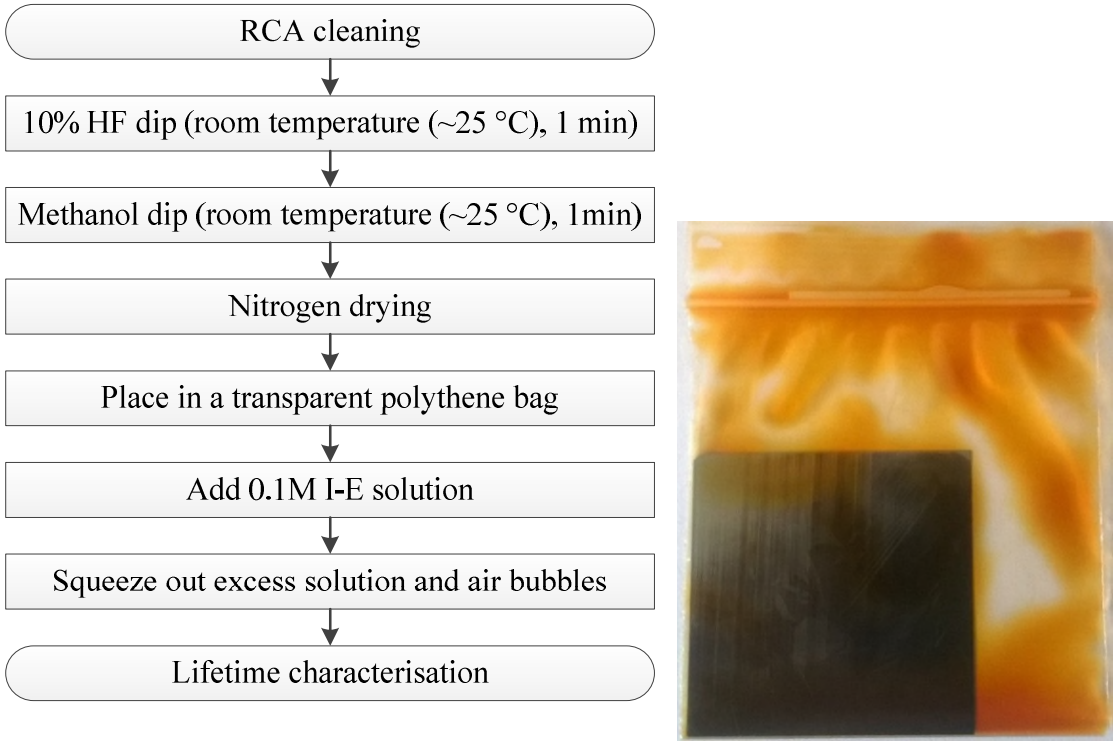

(a) (b)

Figure 3.15. (a) Process sequence used in I-E passivation process (b) an illustration of a mc-Si sample (39 mm × 39 mm) passivated with an I-E solution.

In this thesis, one of the key experiments is to determine interstitial iron concentration in which samples were illuminated to dissociate iron-boron pairs (details discussed in Section 3.9.1). It is, therefore, important to know the effect of illumination on surface passivation quality and change is bulk lifetime after illumination. A control experiment was performed with a chemically polished *n*-type (phosphorus doped) mc-Si sample with a thickness of 190 μm and 7.2 Ω cm bulk resistivity. As the sample is phosphorus doped, it is free from iron-boron complexes which usually dissociate under illumination and degradation related to boron-oxygen complexes. The sample was RCA cleaned and passivated with I-E solution by following the process sequence in Figure 3.15a. Bulk lifetime was measured using a Sinton WCT-120 lifetime tool (detail in Section 3.8.1). The sample was illuminated by more than 50 consecutive intense flashes (~30 suns) of light with a ~10 μs decay constant and lifetime was measured immediately and compared as shown in Figure 3.16. For an example, at an injection level of 1×10^{15} cm^{-3} lifetimes are 16.3 μs and 17.6 μs measured before and after flashing respectively. This change is not significant as the lifetime is assumed to be accurate to ± 4.3 % [177].

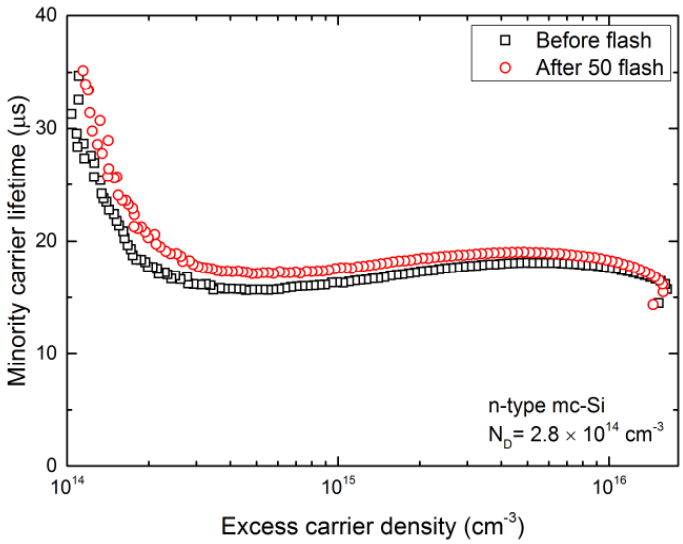

Figure 3.16. Comparison in an injection dependent minority carrier lifetime for *n*-type mc-Si samples at before and after an illumination with 50 consecutive intense flashes.

In order to investigate the repeatability issue with I-E passivation, a *p*-type (boron doped [B] = 1.9×10^{15} cm^{-3}) FZ polished sample with a thickness of 190 μm and bulk resistivity 7.4 Ω cm was used. Note that FZ sample contains a very low concentration of oxygen, so the effects related to boron-oxygen complexes is lower. The sample was RCA cleaned and passivated with an I-E solution and bulk lifetime was measured immediately.

The passivation was removed and cleaned afterwards as discussed in the previous section. The sample was kept in the dark for more than 36 h to re-associate iron-boron pairs and re-passivated with a freshly made solution and lifetime was measured. This cycle was repeated three times and lifetimes are compared in Figure 3.17. The measured lifetimes are 304, 339, 317 and 328 μs which are within the mean value 322 μs ± 4.3%. These results indicate that lifetime is reproducible with I-E passivation.

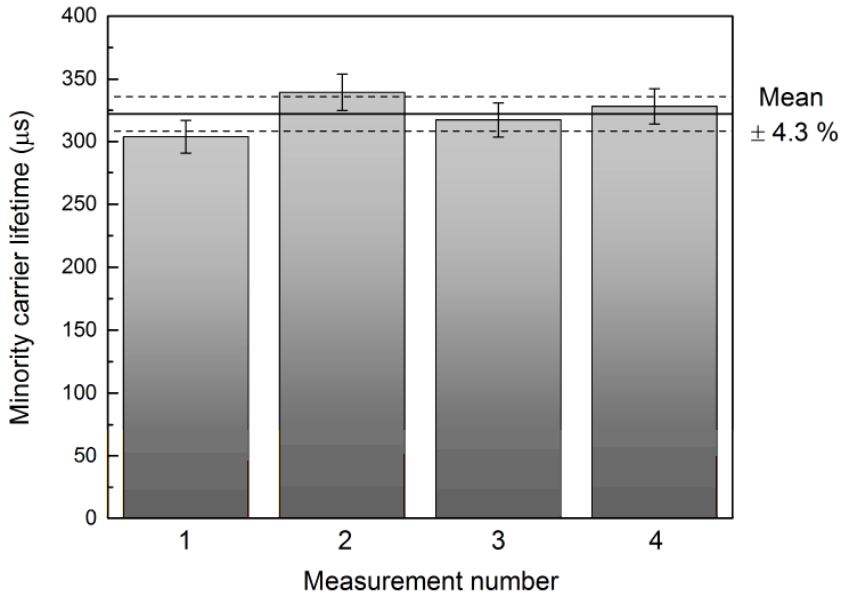

Figure 3.17. A repeatability study of minority carrier lifetime measured for a *p*-type (boron doped) float zone single crystal sample with I-E passivation. Lifetime is measured at an injection level of 1×10^{15} cm^{-3} with iron in the FeB state.

3.6.2. Silicon nitride

To investigate the bulk hydrogenation effect, a batch of multicrystalline silicon samples was passivated by remote plasma-enhanced chemical vapour deposition (PECVD) at 375 °C for approximately 10 mins by ISFH in Germany [178]. Similar to the other samples used in I-E passivation, saw damage was removed from using isotropic etching and followed by RCA cleaning. The samples were dipped in a HF solution to remove native oxide prior to silicon nitride (SiN_x) deposition. A thickness of 70 nm SiN_x with a refractive index of 2.4 was grown on both sides of the samples at a temperature ~375 °C. Samples are characterised by bulk lifetime and spatial distribution of lifetime and low-temperature *internal* gettering was performed.

3.7. Thermal annealing

To perform low-temperature *internal* gettering at ≤ 500 °C, sister samples from every height position in the ingot were annealed under nitrogen ambient in a Carbolite tube furnace (maximum rated temperature 1200 °C) with 60 cm length and 6.1 cm diameter. A K-type thermocouple was used to measure the temperature at the centre of the tube where the samples were placed and set points on the control panel were calibrated for 300, 400 and 500 °C. At a given temperature, samples from all height positions were subjected to identical annealing and cooling treatments, as annealing and removal were performed simultaneously in a quartz boat. Samples were air cooled rapidly to room temperature. The cooling rate was measured using a temperature gun which was estimated as less than 10 s to cool down to room temperature (~ 25 °C). Samples were RCA cleaned and kept in dark prior to characterisation.

3.8. Characterisation

In this thesis, multicrystalline silicon samples were characterised by bulk carrier lifetime and by the spatial distribution of lifetime. Bulk interstitial iron concentrations and spatially resolved maps were calculated based on the lifetime changes before and after dissociation of iron boron pairs. Bulk lifetime was measured by quasi-steady-state photoconductance (QSS-PC) by a Sinton lifetime tester and lifetime images were acquired using a photoluminescence (PL) imaging tool. In the following sections, the characterisation techniques are discussed.

3.8.1. Bulk lifetime measurement

Injection dependent bulk lifetime spectroscopy is one of the most important characterisation techniques used in silicon photovoltaics. A contactless photoconductance technique was developed by Sinton and Cuevas [179]. This technique is based on the recombination of excess carriers generated by an optical flash. A Sinton WCT-120 lifetime tester with a 1.4 cm diameter detection region was used in this work and is shown in Figure 3.18. It can measure carrier lifetime from 0.1 μs to several ms over a range of injection levels (10^{12} to 10^{17} cm^{-3}). In this thesis, an injection level 1×10^{15} cm^{-3} was used

as this is far from the crossover point and it mitigates the effect of carrier trapping. The system comprises a flash lamp which generates excess carriers in the silicon wafers and therefore increases its photoconductance (σ_L), given by [179]:

$$\Delta\sigma_L = qW(\mu_n\Delta n + \mu_p\Delta p) \tag{3.7}$$

where q is the elemental charge, W is the sample thickness, μ_n and μ_p are the electron-hole mobilities, Δn and Δp are average densities of excess electron and holes respectively. Since every absorbed photon generates one electron-hole pair, so that $\Delta n = \Delta p$, Equation 3.7 becomes:

$$\Delta\sigma_L = qW(\mu_n + \mu_p)\Delta n \tag{3.8}$$

And therefore:

$$\Delta n = \frac{\Delta\sigma_L}{qW(\mu_n + \mu_p)} \tag{3.9}$$

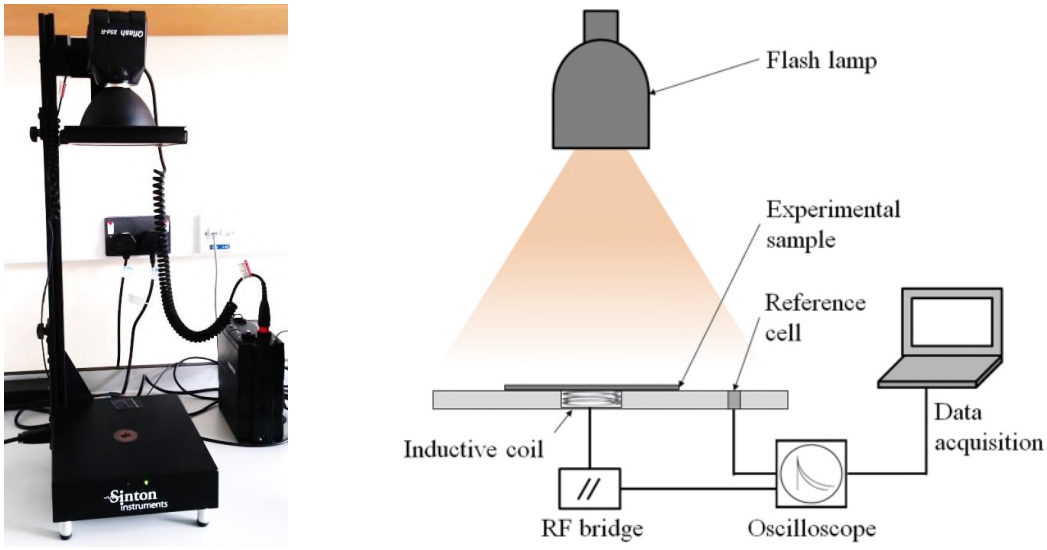

(a) (b)

Figure 3.18. Lifetime tester to measure injection dependent bulk lifetime (a) a WCT-120 tool from Sinton Instruments (b) schematic diagram of the configuration.

It is noted that Equations 3.8 and 3.9 are only applicable where in the absence of trapping of minority carriers [180, 181]. As μ_n and μ_p are functions of excess carrier density, an iterative method is required to measure average excess carrier density and

therefore the change is photoconductance. A reference solar cell is used to determine the time dependence of the excess photoconductance in the silicon wafer.

Two main techniques transient photoconductance decay (PCD) and quasi-steady-state photoconductance (QSS-PC) are usually used to measure bulk lifetime. The effective carrier lifetime can be expressed as [114]:

$$\tau_{eff} = \frac{\Delta n(t)}{U(t)} = \frac{\Delta n(t)}{G(t) - R(t)} \tag{3.10}$$

where U is the net recombination rate, G is the photogeneration rate and R is the recombination rate. R can be expressed as [114]:

$$R(t) = \frac{d\Delta n(t)}{dt} \tag{3.11}$$

Equation 3.10 becomes as [114]:

$$\tau_{eff} = \frac{\Delta n(t)}{G(t) - \frac{d\Delta n(t)}{dt}} \tag{3.12}$$

In the transient method, the sample is exposed to a sharp pulse of illumination and the excess carrier density is determined in the absence of illumination. The carrier generation between light impulse and photoconductance decay is zero ($G \equiv 0$); Equation 3.12 can be written as:

$$\tau_{eff} = \frac{\Delta n(t)}{-\frac{d\Delta n(t)}{dt}} \tag{3.13}$$

It is noted that transient method is used for a sample with high carrier lifetime (> 200 μs). For a sample with relatively low carrier lifetime (< 200 μs), a quasi-steady-state method is used. It is noted that lifetime is significantly lower than the decay time of the illumination source. As in steady state $\frac{d\Delta n(t)}{dt} = 0$, the Equation 3.12 can be written as:

$$\tau_{eff} = \frac{\Delta n(t)}{G(t)} \tag{3.14}$$

In most cases in this thesis, carrier lifetime is below 100 μs and therefore QSS-PC mode is used to measure bulk lifetime. The optical constant is a fraction of photogeneration

compared to 38 mA/cm^2 and varies with dielectric layer properties (thickness and refractive index) and wafer thickness [182]. In this thesis, optical constants used for SiN_x passivation scheme is 0.9 whereas it is assumed as 0.8 for I-E passivation scheme (between bare silicon and silicon nitride passivated silicon). Note that optical constant within ±5% accuracy does not affect lifetime substantially. As the PL imaging tool does not contain an integrated lifetime measurement system, lifetime at low injection level (equivalent to excitation in the PL imaging tool) was used to make a calibrated lifetime image (discussed in Section 3.8.3)

3.8.2. Trapping of minority carriers

It is well known that multicrystalline silicon material contains minority carrier traps which are associated with a rise in lifetime at low injection levels [181]. In this thesis, trapping effects were observed in some cases where lifetime increases abnormally at low injection level. Since the lifetime images were made at low injection level (discussed in the following section), corrections to the data are applied to mitigate trapping. A 'Bias Light' correction factor was used as suggested by Macdonald *et al.* [183]. A value was chosen near the low end of the range 0.2 Suns and increased until the in the regions where the trapping was prominent reaches a minimum. In most cases, a bias light value of 0.3 to 0.5 Suns gives satisfactory results. It was noted that any lifetime at an injection level below the bias point carrier density was considered as a measurement artefact.

3.8.3. Photoluminescence imaging

Photoluminescence (PL) imaging is a contactless and robust method to measure spatially resolved lifetime and thus to identify defective regions in a sample [184, 185]. This technique is very effective in multicrystalline silicon as the material properties vary widely (vertically and laterally in an ingot). It is based on photon emission from band-to-band recombination of electrons from the conduction band with the holes in the valence band (as discussed in Chapter 2), generated by an external excitation. A PL imaging tool (LIS-L1) supplied by BT Imaging was used in this thesis, is shown in Figure 3.19a. It contains a ring of light emitting diodes (LEDs) with a wavelength of 650 nm to excite the sample and a silicon charge-coupled device (CCD) imaging sensor to capture emitted photons from the sample. PL imaging can be made in two different magnifications in the

same system used. In standard magnification (lower), the tool can produce an image of an area of 165 mm × 165 mm with a resolution of ~160 μm. Under high magnification, the pixel size decreases to 23 μm. In this thesis, standard magnification was used in most cases as the experimental sample size is 39 mm × 39 mm. A schematic diagram of a configuration of the PL imaging tool and an example of a calibrated lifetime image is illustrated in Figure 3.19b.

(a)

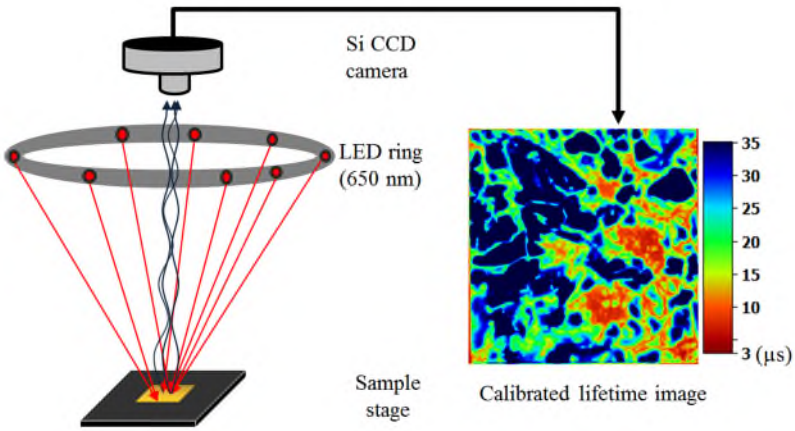

(b)

Figure 3.19. (a) A photoluminescence imaging tool (LIS-L1) from BT Imaging and (b) schematic diagram of working principle of the PL imaging tool at Warwick. Experimental sample is excited by an LED array with an emission wavelength of 650 nm. Photons emitted by radiative recombination are captured by a silicon charge-coupled device (CCD) imaging sensor. Lifetime imaging was determined using the PL imaging and bulk lifetime from the Sinton QSS-PC tool.

The PL tool at Warwick is designed based on photon flux which varies linearly with the percentage in the power supply as shown in Figure 3.20a. At 100% LED power, the maximum photon flux in our system is 3.56×10^{17} $cm^{-2}s^{-1}$. As the PL imaging tool does not contain a lifetime measurement system, it requires integration with the Sinton QSS-PC tool to make spatial lifetime images. To measure a calibrated lifetime image, excitation in the PL imaging tool needs to be calibrated in term of 'Suns' unit (1 sun equivalent to standard illumination at AM1.5 or 1000 W/m^2). A relationship between the photon flux and equivalent Suns is shown in Figure 3.20b. The highest illumination is equivalent to 1.42 Suns at 100 % power in LEDs, decrease linearly with the LED power.

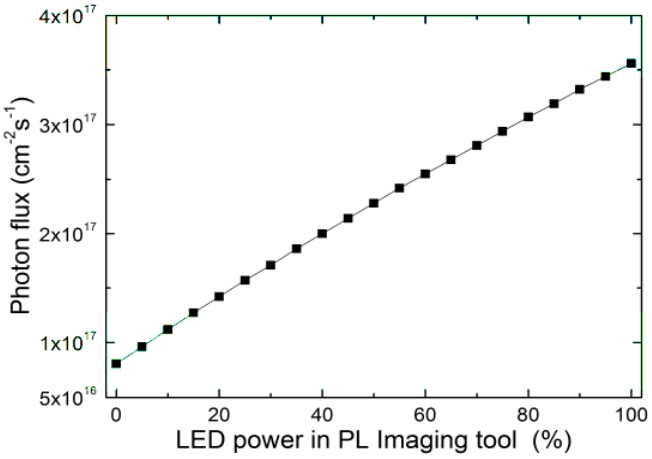

(a)

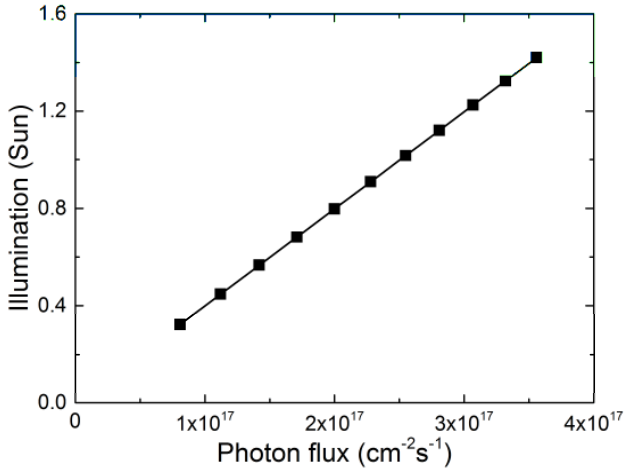

(b)

Figure 3.20. (a) Photon flux as a function of LED power in the PL imaging tool at Warwick. (b) The relationship between photon flux (a function of LED power) and illumination in Suns.

The photoluminescence signal intensity generated by the sample depends on bulk lifetime and the quality of surface passivation used [186]. For a *p*-type silicon sample, the PL intensity can be expressed as [185]:

$$I_{PL} = C.B.\Delta n(\Delta n + N_A) \tag{3.15}$$

where C is a calibration constant with varies from one sample to next due to optical effects (a brief process of determining C value is discussed in the following section), B is the radiative recombination coefficient, Δn is the excess carrier concentration and N_A is the doping density. Since the coil diameter in the Sinton tool used in this work is 1.4 cm, an area of 1.4 cm × 1.4 cm was set as a field of view (FoV) in the PL imaging tool. As the properties vary widely in multicrystalline silicon material, samples must be aligned in both the tools to have an accurate calibration factor which was done by using two jigs. The tool produces an image of excess carrier density by using the Equation 3.15 with an arbitrary C value. The software estimates the calibration constant based on a comparison of average excess carrier density in the region of FoV area ($\Delta n_{\text{PL Imaging}}$) and the excess carrier density estimated from the Sinton tool (Δn_{Sinton}). As the PL imaging tool operates under steady state condition, the Δn_{Sinton} can be calculated by [125]:

$$\Delta n = \tau_{\text{eff}} \times G \tag{3.16}$$

where τ_{eff} is the effective lifetime estimated from injection dependent lifetime graph from the Sinton tool at the corresponding illumination (Suns) used in the PL imaging tool and G is the average generation rate which is calculated by [125]:

$$G = \frac{IN_{\text{ph}}(1-R)}{W} \tag{3.17}$$

where I is the light intensity (Suns), N_{ph} is the incident photon flux ($\text{cm}^{-2}\text{s}^{-1}$), R is the reflectance factor from the front surface at the 650 nm wavelength (%) and W is the wafer thickness (μm). After estimating the calibration constant, the PL imaging tool produces a Δn image of the entire sample and thus an effective lifetime images using the Equation 3.16. A flow chart of making lifetime images is shown in Figure 3.21. The exposure time and illumination intensity affect the measurement substantially, as discussed in the following section.

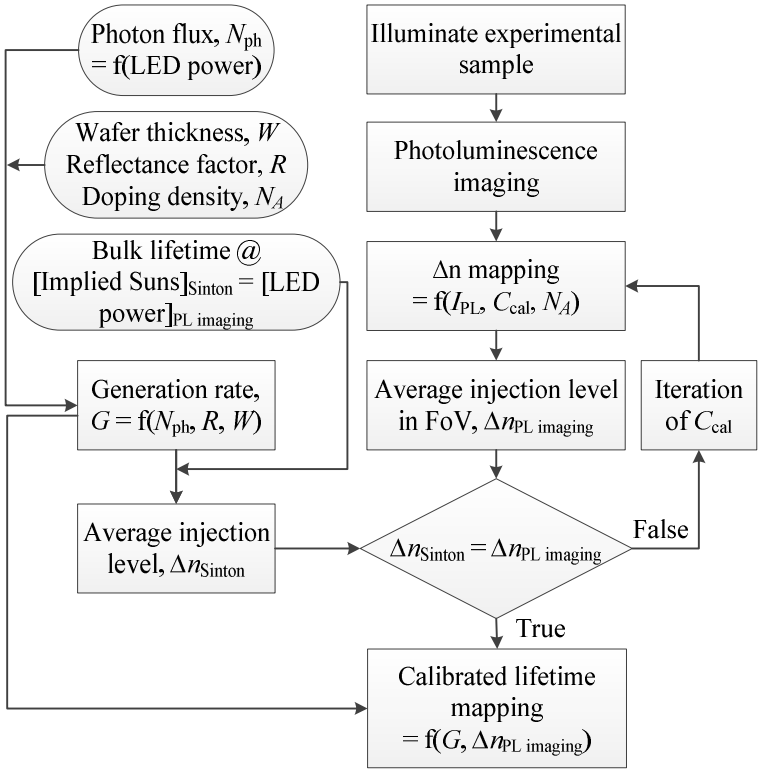

Figure 3.21. Process sequence in the PL imaging tool for determining a calibrated lifetime image.

To estimate exposure time and illumination intensity, a controlled experiment was performed with three chemically polished Cz single crystal silicon samples with a doping density ranging from 1.1×10^{15} to 1.3×10^{15} cm^{-3}. Samples were passivated with silicon nitride. Bulk lifetimes were measured as 12, 46 and 103 μs at an illumination level of 1.42 Suns (equivalent to 100 % LED power in the PL imaging tool) respectively using the Sinton QSS-PC tool. Calibrated lifetime images were made with varying exposure time (0 to 20 s) at 100% LED power. The average PL count, injection level and average lifetime were estimated in the region of FoV and were compared.

As the PL intensity is proportional to the rate of radiative recombination (discussed in the previous section), the longer exposure time incident more photon and a result of higher radiative recombination rate. PL count usually increases with exposure time in the samples as shown in Figure 3.22. It is noted that PL signal can be estimated ranging from 1,000 to 60,000 counts and therefore the sample with relatively high lifetime (103 μs) exhibits a plateau after an exposure for 8 s. Since the PL imaging is carried out under steady state conditions, the injection level exhibits a constant value with exposure time in all three samples, as shown in Figure 3.23. Similarly, the average carrier lifetime (with

the iron in FeB state) in the FoV regions remain unchanged, as shown in Figure 3.24 with exposure time. In this thesis, an exposure time ranging from 1 to 5 s was used depending on starting bulk lifetime value. It is noted that a longer exposure time in an iron contaminated sample dissociates more iron-boron pairs which could result in different lifetime mapping as is discussed in more details in the following section. However, for multicrystalline silicon samples, an exposure time less than 1 s was not found to be sufficient to obtain minimum average PL signal count (1,000) in as-received samples. In the samples after phosphorus diffused emitter formation, an exposure time of 1 s can produce a PL image with sufficient contrast.

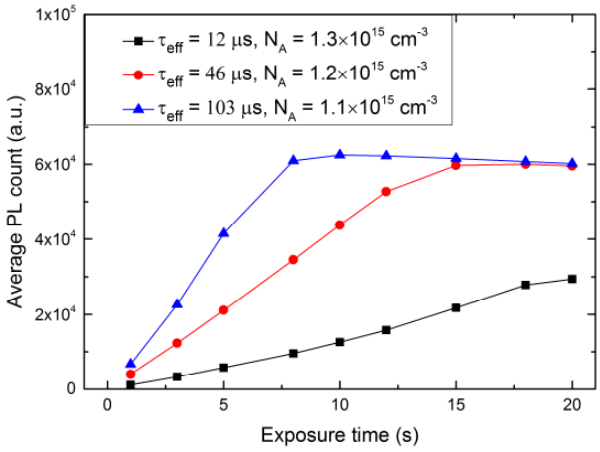

Figure 3.22. Variation in PL count as a function of exposure time in the PL imaging tool at 100 % power (1.42 Suns) in the LED array for three *p*-type (boron doped) Cz single crystal samples. The average PL count range is 1,000 to 60,000.

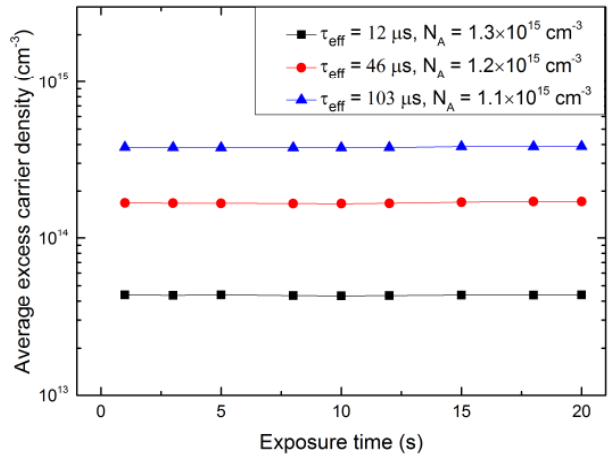

Figure 3.23. Variation in average injection level as a function of exposure time in the PL imaging tool at 100 % power (1.42 Suns) in the LED array for three *p*-type (boron doped) Cz single crystal samples.

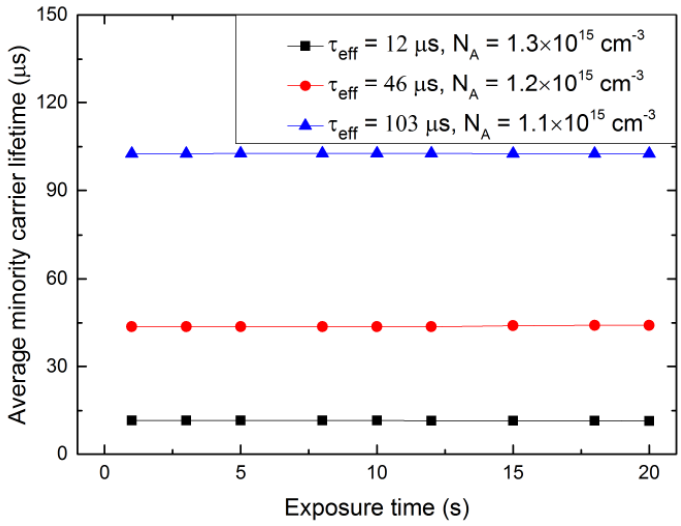

Figure 3.24. Variation in average carrier lifetime as a function of exposure time in the PL imaging tool at 100 % power (1.42 Suns) in the LED array for three *p*-type (boron doped) Cz single crystal samples.

In order to estimate illumination intensity and the corresponding effect on lifetime imaging, a controlled experiment was performed on a silicon nitride passivated Cz single crystal silicon sample with a doping level of 1.2×10^{15} cm^{-3} and bulk interstitial iron concentration of 1.8×10^{11} cm^{-3}. Lifetime was initially measured with iron in FeB state with Sinton tool. The sample was exposed for 5 s with varying power from 1 to 100% in the LED light and measured bulk lifetime after every step. Finally, the sample was illuminated with 50 consecutive intense flashes of light to dissociate iron-boron pairs and measured lifetime immediately. The injection dependent lifetimes are compared and shown in Figure 3.25. At a high injection level (for example 1×10^{15} cm^{-3}), it can be seen that lifetime increases after an exposure with higher LED power which is attributed to dissociation of iron-boron pairs. The corresponding percentage of dissociated iron-boron pairs is estimated based on interstitial iron concentration at every level (a detailed method is discussed in Section 3.9) is shown in Figure 3.26. It is shown that the percentage of FeB dissociation is ~5% after illumination at 1% LED power and it increases linearly to ~74% at 100 % LED power. In this thesis, 10% LED power (equivalent to 0.447 Suns) was used in all measurements where the estimated dissociation of iron-boron pairs is approximately 10%. Although lower LED power reduces FeB pair dissociation, it gives lower PL signal count than the minimum limit (1,000 counts) and cannot be used in samples with lower bulk lifetime. At 0.447 Suns illumination, mc-Si samples show an injection level ranging from 1×10^{13} to 1×10^{14} cm^{-3} which are usually below the

crossover point. In some cases, bulk lifetime measurement was corrected by a 'Bias Light' factor due to avoid minority carrier trapping effects.

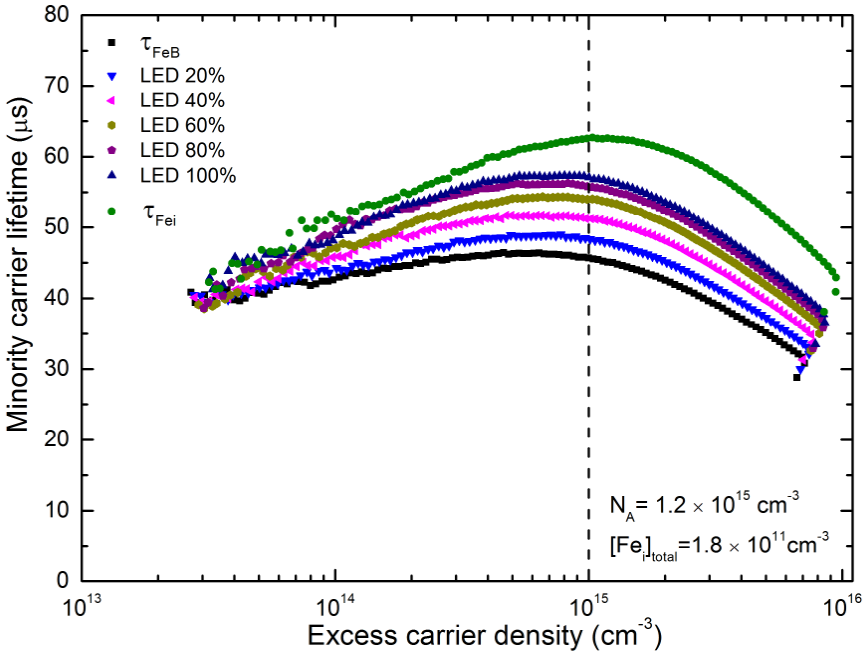

Figure 3.25. Change in injection dependent lifetime in QSS-PC after illumination at different power in the LED array in the PL imaging tool with an exposure time of 5 s for a Cz single crystal sample with a thickness of 690 μm. The vertical dotted line represents lifetime at an injection level of 1×10^{15} cm^{-3}.

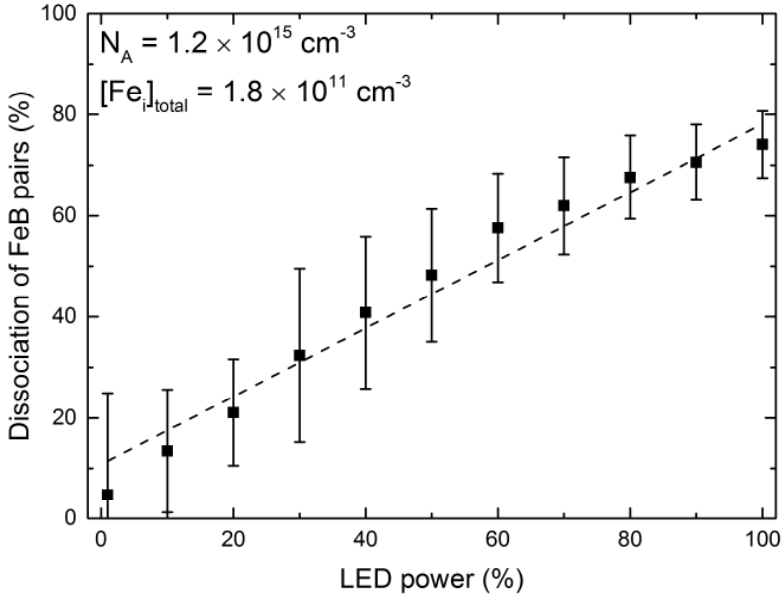

Figure 3.26. Dissociation of iron-boron pairs in the same Cz single crystal sample after exposure at different power in the LED array for 5 s in the PL imaging tool in Figure 3.25. Interstitial iron concentration is calculated at an injection level of 1×10^{15} cm^{-3}.

3.9. Interstitial iron concentration

Iron is one of the most harmful and ubiquitous impurities which degrade carrier lifetime substantially as discussed in Chapter 2. Most of the iron in mc-Si is in precipitate form and only a small percentage (< 1%) is in the form of interstitial iron (Fe_i) and iron-boron pairs. In this thesis, mc-Si wafers were characterised in terms of changing bulk interstitial iron concentration and spatial distribution in as-received state and after every thermal annealing step. The measurement technique used in this thesis is discussed in the following section.

3.9.1. Bulk interstitial iron concentration

Zoth and Bergholz developed a technique to determine interstitial iron concentration using the changes in carrier lifetime (or, equivalent diffusion length) before and after dissociation of FeB pairs at constant generation rate [187]. This technique assumes that all recombination processes except SRH due to FeB and Fe_i remain unchanged in the FeB dissociation process. The interstitial iron concentration is determined using the following expression [187]:

$$[\mathrm{Fe_i}] = C\left(\frac{1}{\tau_{\mathrm{Fe_i}}} - \frac{1}{\tau_{\mathrm{FeB}}}\right) \tag{3.18}$$

where τ_{FeB} and $\tau_{\mathrm{Fe_i}}$ are lifetime before and after dissociation of FeB pairs, C is the prefactor. The advantage of this measuring technique is that other recombination mechanisms cancel out. The *C* values can be estimated from the known recombination parameter of FeB, Fe_i and the doping concentration as reported by Macdonald *et al.* [96]. Since the value of *C* is injection dependent, rapid change in Δn can create a substantial error in Fe_i concentration. Murphy *et al.* [188] have suggested another method of interstitial iron concentration measurement using SRH statistics which was used in this thesis. The modelling equation is expressed by:

$$\left[\frac{1}{\tau_{\mathrm{Fe_i}}} - \frac{1}{\tau_{\mathrm{FeB}}}\right]_{\mathrm{SRH\,model}} = \left[\frac{1}{(\tau_{\mathrm{eff}})_{\mathrm{Fe_i}}} - \frac{1}{(\tau_{\mathrm{eff}})_{\mathrm{FeB}}}\right]_{\mathrm{measured}} \tag{3.19}$$

where $(\tau_{\text{eff}})_{\text{Fe}_i}$ and $(\tau_{\text{eff}})_{\text{FeB}}$ are measured effective lifetime with the iron in Fe_i and FeB state respectively, can be expressed by:

$$\frac{1}{(\tau_{\text{eff}})_{\text{Fe}_i}} = \frac{1}{(\tau_{\text{SRH}})_{\text{Fe}_i}} + \frac{1}{\tau_{\text{Auger}}} + \frac{1}{\tau_{\text{Radiative}}} + \frac{1}{\tau_{\text{Surface}}} \tag{3.20}$$

and

$$\frac{1}{(\tau_{\text{eff}})_{\text{FeB}}} = \frac{1}{(\tau_{\text{SRH}})_{\text{FeB}}} + \frac{1}{\tau_{\text{Auger}}} + \frac{1}{\tau_{\text{Radiative}}} + \frac{1}{\tau_{\text{Surface}}} \tag{3.21}$$

FeB pairs were dissociated by more than 50 consecutive intense flashes of light with a ~10 μs decay constant and $(\tau_{\text{eff}})_{\text{Fe}_i}$ was measured immediately. It is noted that other recombination processes (except SRH) are assumed to be unchanged during dissociation of iron boron pairs. Note that sample was aligned in the measurement before and after dissociation of FeB pairs. Using the SRH statistics equations (as explained in Chapter 2), lifetime can be expressed as:

$$\left[\frac{1}{\tau_{\text{Fe}_i}}\right]_{\text{SRH model}} = \frac{[Fe_i]}{\frac{1}{(N_A + n_0 + \Delta n)}\left[\frac{(N_A + p_1^{Fe_i} + \Delta n)}{\sigma_n^{Fe_i} v_{th}} + \frac{(n_1^{Fe_i} + n_0 + \Delta n)}{\sigma_p^{Fe_i} v_{th}}\right]} \tag{3.22}$$

and

$$\left[\frac{1}{\tau_{\text{FeB}}}\right]_{\text{SRH model}} == \frac{[Fe_{FeB}]}{\frac{1}{(N_A + n_0 + \Delta n)}\left[\frac{(N_A + p_1^{FeB} + \Delta n)}{\sigma_n^{FeB} v_{th}} + \frac{(n_1^{FeB} + n_0 + \Delta n)}{\sigma_p^{FeB} v_{th}}\right]} \tag{3.23}$$

where $[Fe_i]$ and $[Fe_{FeB}]$ are the concentration of interstitial iron and iron-boron pairs respectively. In this work, SRH parameters were chosen from the study of Rein and Glunz [15]. $[\text{Fe}_i]$ was measured using the Equation 3.19 to 3.23 at an injection level of $\Delta n = 1 \times 10^{15}$ cm $^{-3}$.

The uncertainty in iron concentration was estimated by using a quadrature error method, based on a $\pm$ 4.3% error in lifetime measurement. It can be expressed by:

$$\text{Uncertainty in iron concentration} = \frac{\Delta[\text{Fe}_i]}{2} \tag{3.24}$$

where

$$\Delta[Fe_i] = \sqrt{\left([Fe_i] - [Fe_i]_{min}\right)^2 + \left([Fe_i]_{max} - [Fe_i]\right)^2} \quad (3.25)$$

$[Fe_i]$ was calculated based on directly measured lifetime by the Sinton tool. The minimum possible interstitial iron concentration ($[Fe_i]_{min}$) and maximum possible interstitial iron concentration ($[Fe_i]_{max}$) was estimated by the extrema ± 4.3% error in lifetime, can be expressed by:

$[Fe_i]_{min}$:

$$\left[\frac{1}{\tau_{Fe_i}} - \frac{1}{\tau_{FeB}}\right]_{SRHmodel} = \left[\frac{1}{((\tau_{eff})_{Fe_i})_{min}} - \frac{1}{((\tau_{eff})_{FeB})_{max}}\right]_{measured} \quad (3.26)$$

$[Fe_i]_{max}$:

$$\left[\frac{1}{\tau_{Fe_i}} - \frac{1}{\tau_{FeB}}\right]_{SRHmodel} = \left[\frac{1}{((\tau_{eff})_{Fe_i})_{max}} - \frac{1}{((\tau_{eff})_{FeB})_{min}}\right]_{measured} \quad (3.27)$$

The uncertainty in iron concentration measurement varies widely depending on doping, bulk lifetime in Fe_i and FeB states. In some cases, the error bar was estimated to be very large particularly when iron concentration is close or lower than the detection limit. At the detection limit, the effective lifetime with iron in the interstitial state can exceed that when iron is in FeB pair form.

3.9.2. Spatial mapping of interstitial iron concentration

The spatial distribution of interstitial iron concentration was made using the SRH model described in the above section based on lifetime changes at every independent pixel as suggested by Macdonald *et al.* [189]. A relatively lower injection level (far below than the crossover point) was used to minimise dissociation of iron boron pair by excitation in the PL imaging tool. The PL imaging tool generates text files of a lifetime and excess carrier density before and after iron-boron pairs dissociation. A Matlab code was made to model interstitial iron concentration distribution which works only for the same size of matrix arrays of lifetimes and excess carrier density. It is important to note that sample's position has to be aligned in lifetime measurement in FeB and Fe_i states.

Any misalignment could lead a substantial error. As discussed in Section 3.8.3, lifetime was measured under the same generation rate before and after dissociation of iron boron pairs, therefore, injection level varies in every pixel. As the iron concentration measurement technique requires the same injection level for a lifetime with FeB and Fe_i state, there is some uncertainty in interstitial iron mapping.

The local carrier lifetime and injection measurement using PL are usually affected by lateral carrier diffusion (known as 'smearing' effect) when the minority carrier diffusion length is comparable with pixel size. Due to this effect, regions with higher lifetime exhibit relatively lower value and vice versa which strongly depends on a lifetime in the bulk [190]. Phang *et al.* suggested a continuity equation to minimise the lateral diffusion effects [191]. However, in this thesis smearing effect was not considered as substantial due to using samples with lower bulk lifetime (< 50 μs in most cases) and larger pixel size (~160 μm) in the lifetime imaging.

3.10. Summary

In this Chapter, the experimental methods used in this thesis are described. All the as-received samples were polished chemically for saw damage removal. Dislocation density, initial lifetime measurement with iodine-ethanol and silicon nitride passivation are applied in Chapter 4. Low-temperature annealing with iodine-ethanol and silicon nitride passivation schemes are applied in Chapter 5 and Chapter 6, respectively. Low-temperature gettering on phosphorus diffused samples is applied in Chapter 7.

Chapter 4 Properties of as-grown multicrystalline silicon

4.1. Introduction

Cast multicrystalline silicon ingots contain large densities of structural defects such as grain boundaries and dislocations [59, 74, 192]. They also contain a high density of metallic impurities in the form of both point-like defects and precipitates [9, 13, 14]. Structural defects are particularly recombination active and degrade minority carrier lifetime substantially when decorated by metallic impurities as discussed in Chapter 2 [84]. It is also discussed in Chapter 2 that metallic impurities and structural defects concentrations vary widely over ingot height position in an as-grown mc-Si ingot made by directional solidification. Minority carrier lifetime typically is highest in the middle and the lowest at the top and bottom part of the ingot [161, 193]. Since the top of the ingot solidifies last, it usually has the highest density of dislocations [66, 72] and has a relatively high impurity content from impurities remaining in the melt [194, 195]. Due to impurity diffusion from the crucible, the bottom of the ingot [194, 195] and the edges [196] also have relatively high impurity contents. Extrema at the bottom and top of ingots are sometimes referred to as “red zones” when their lifetime is too low for the use in solar cells.

In this thesis, samples from four different height positions top (T), top middle (MT), bottom middle (MB) and bottom (B) of a commercially grown mc-Si ingot were used. The selection procedure of sister samples (39 mm × 39 mm) from every height position is illustrated in Figure 3.2 in Chapter 3. After primary characterisation in terms of

thickness and bulk resistivity in sister samples, the saw damage was removed by using a planar etch solution (as presented in Section 3.5.2). Samples were passivated with a temporary iodine-ethanol passivation at room temperature and with silicon nitride passivation scheme (SiN_x) (discussed in Section 3.6). Bulk lifetimes were measured by the Sinton lifetime tester and bulk interstitial iron concentrations were calculated. Photoluminescence images were made and interstitial iron concentration maps were produced using the method described in Section 3.8.3 and 3.9 in Chapter 3. Dislocations were revealed with a defect-revealing etch ('Sopori' etch) and distribution mapping was made following the described method in Section 3.5.3. In this Chapter, different material properties including bulk minority carrier lifetime, bulk interstitial iron concentration, dislocation densities and photoluminescence images at all four height positions are presented and discussed. The primary aim of this Chapter is to present a detailed characterisation of the starting material. This underpins the data in the subsequent Chapters which aim to develop processes to improve material properties.

4.2. Distribution of bulk lifetime in as-grown mc-Si ingot

4.2.1. Carrier lifetime with iodine-ethanol passivation

Figure 4.1 shows the distribution of measured bulk carrier lifetime at an injection level 1×10^{15} cm^{-3} with iron in the FeB state for as-grown sister samples sourced from the four different height positions. A statistical box plot is also presented for every data cluster at every height position. The average lifetime is presented by a solid rectangular box. The lifetime varies significantly with the height position. It can be seen that the samples from the bottom and the top of the ingot exhibit the lowest average lifetime which are 5.6 μs and 12.4 μs respectively. The bottom middle and top middle wafers have the maximum average lifetimes of 44 μs and 28 μs, respectively. Neighbouring samples at every height position have very similar carrier lifetimes. Although data cluster at a height position exhibits an agreement with statistical box plot, samples from the middle of ingot exhibit a relatively wider distribution than the samples from the bottom and top. The variation among sister wafers could be attributed to a difference in a number of factors including surface preparation, I-E passivation, the concentration of metallic impurities and structural defects. However, the average carrier lifetime distribution over the ingot height

position shows a consistency with the finding of other studies [161, 193]. It is important to note that improving material quality particularly, minority carrier lifetime, in the samples from the bottom and top part of the ingot ('red zone') is a technologically important. Low-temperature internal gettering technique is used to improve bulk lifetime and the results are presented in Chapter 5.

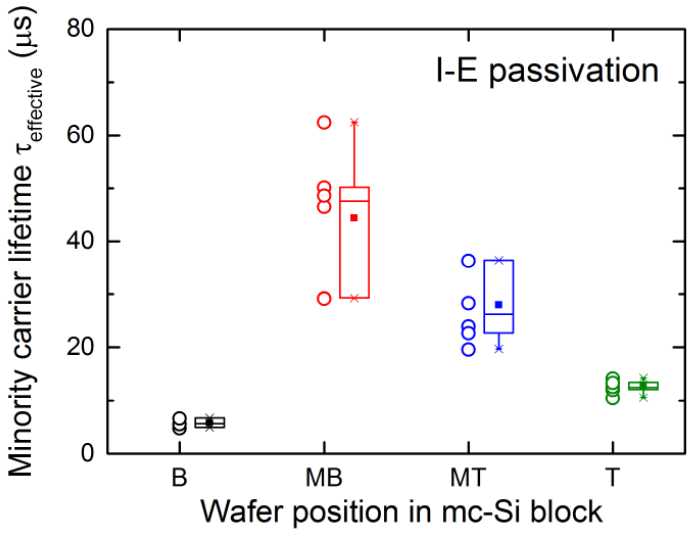

Figure 4.1. Distribution of the bulk minority carrier lifetime (with iron in the FeB state) at an injection level of 1×10^{15} cm^{-3} measured with the iodine-ethanol passivation in as-grown mc-Si sister samples from different height positions in the ingot. To the right of each data cluster, the open box represents the 25^{th} and 75^{th} percentiles and the median. The solid rectangular point within the box is the mean.

4.2.2. Carrier lifetime with silicon nitride passivation

Figure 4.2 shows the distribution of as-grown bulk minority carrier lifetime with the silicon nitride (SiN_x) passivation scheme for mc-Si samples from four different height positions in the ingot. Details of the silicon nitride passivation process are discussed in Section 3.6. Note that these samples are sourced from adjacent (not sister) locations of the samples used in Figure 4.1. The overall trend in lifetime distribution is the same as in Figure 4.1. Samples from the bottom and top part of the ingot have the lowest average carrier lifetimes of 7.7 μs and 17.4 μs, respectively. The maximum average lifetime (114.2 μs) is found in the bottom middle part of the ingot. The samples from top middle part show average lifetime between the bottom middle and top part of the ingot (46 μs). In order to improve lifetime particularly in the low-lifetime samples from the bottom and

top part of the ingot, samples were subjected to low-temperature gettering which is discussed in Chapter 6 and the results are compared with I-E passivation scheme in Chapter 5.

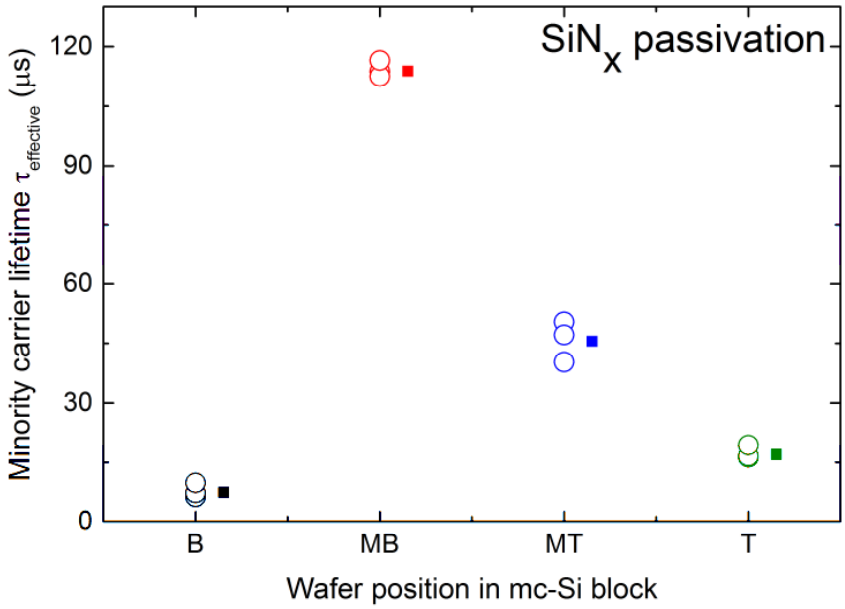

Figure 4.2. Distribution of the bulk minority carrier lifetime with iron in the FeB state at an injection level of 1×10^{15} cm^{-3} measured with silicon nitride (SiN_x) passivation in as-grown mc-Si sister samples from different height positions in the ingot. To the right of each data cluster, the solid rectangular point is the mean.

4.3. Distribution of interstitial iron concentration in as-grown mc-Si ingot

4.3.1. Interstitial iron concentration with iodine-ethanol passivation

The distribution of interstitial iron concentration in the bulk is presented in Figure 4.3. Neighbouring samples at every height position have very similar concentrations. The samples from the centre part of the ingot show a relatively wider distribution than the samples from the extrema of the ingot. The average interstitial iron concentration is highest at the bottom of the ingot 2.9×10^{12} cm^{-3}, and fairly high at the top of the ingot 1.0×10^{12} cm^{-3}. In the middle of the ingot, the average interstitial iron is relatively low. In the bottom middle and top middle samples, the average values are 2.0×10^{11} cm^{-3} and 3.0×10^{11} cm^{-3}, respectively. This trend is well understood. The increase towards the top

of the ingot is because it is last to solidify and the low segregation coefficient of iron means the melt's iron concentration increases with time [195]. The high value at the bottom of the ingot is due to in-diffusion from the crucible [194]. In general, the interstitial iron concentration distribution shows an inverse relationship with the lifetime distribution. As the metallic impurities are recombination active, samples with relatively higher iron concentration (in the bottom part of the ingot) show lower carrier lifetime. In the same way, the centre part of the ingot has lower interstitial iron concentration and therefore, higher bulk lifetime. This indicates that mitigating interstitial iron concentration could lead a substantial increase in lifetime. As the bottom samples have more than one order of magnitude higher bulk iron concentration, it is important to reduce iron concentration and thus improve production yield in silicon photovoltaics. The evolution of interstitial iron concentration in low-temperature gettering using these samples are discussed in Chapter 5.

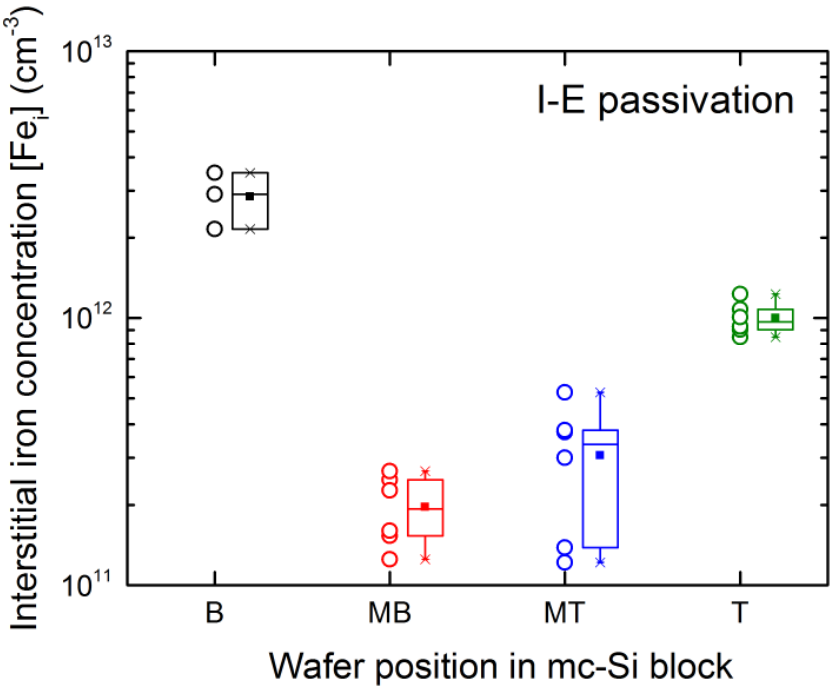

Figure 4.3. Distribution of the bulk interstitial iron concentration measured at an injection level of 1×10^{15} cm^{-3} using iodine-ethanol passivation in as-grown mc-Si sister samples from different ingot positions. To the right of each data cluster, the open box represents the 25th and 75th percentiles and the median. The solid rectangular point within the box is the mean.

4.3.2. Interstitial iron concentration with silicon nitride passivation

Figure 4.4 shows the as-grown bulk interstitial iron concentration using silicon nitride (SiN_x) passivation for mc-Si samples sourced from four different height positions in the ingot. The highest average interstitial iron concentration (2.2×10^{12} cm^{-3}) was found in samples from the bottom part of the ingot. The average iron concentration decreases with height position and substantially lower in bottom middle (5×10^{10} cm^{-3}) and top middle (1.4×10^{11} cm^{-3}) part of the ingot. At the top of the ingot, the average iron concentration is fairly high (6.6×10^{11} cm^{-3}). A comparison in as-grown average iron concentration with I-E passivation scheme is discussed in the following sections. In order to reduce interstitial iron concentrations, these samples are subjected to low-temperature gettering and the effect of silicon nitride passivation scheme is investigated (discussed in Chapter 6).

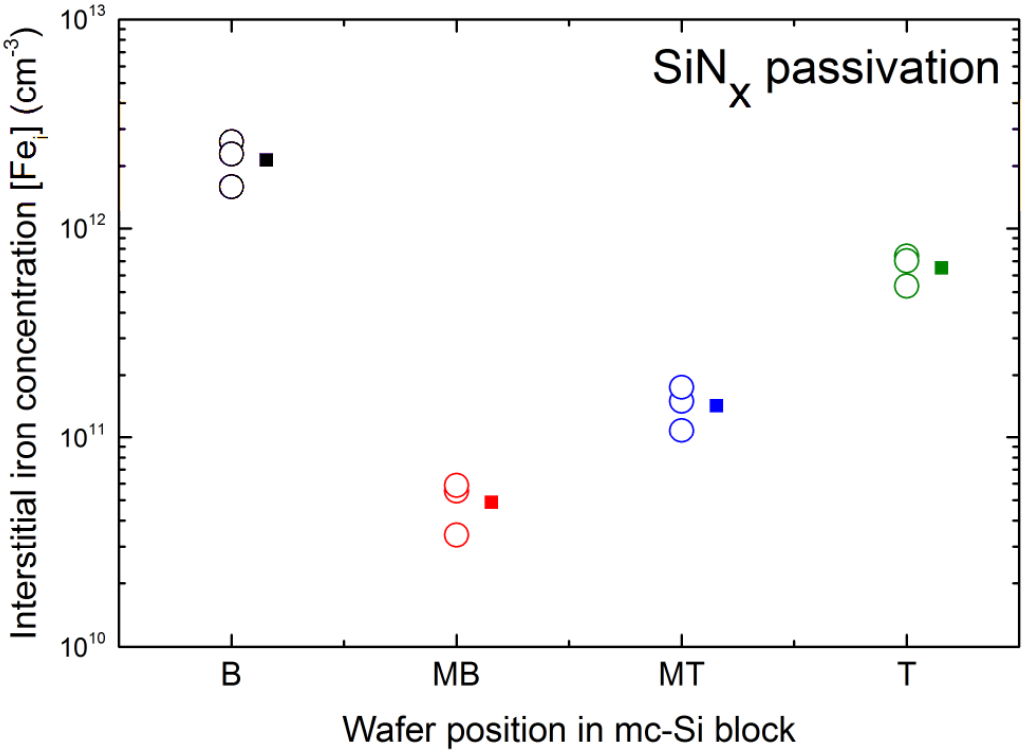

Figure 4.4. Distribution of the interstitial iron concentration measured at an injection level of 1×10^{15} cm^{-3} using silicon nitride (SiN_x) passivation in as-grown mc-Si sister samples from different ingot positions. To the right of each data cluster, the solid rectangular point is the mean.

4.4. Iodine-ethanol versus silicon nitride passivation in as-grown state

A comparison in as-grown average bulk minority carrier lifetime and average bulk interstitial iron concentration for samples with I-E and SiN_x passivation schemes are shown in Figures 4.5 and 4.6, respectively. The average as-grown lifetimes with SiN_x passivation are considerably higher than with I-E passivation, particularly in high-lifetime samples from the middle part of the ingot. For example, the average lifetime in the bottom middle sample is 114.2 μs with SiN_x compared to 44.3 μs with I-E passivation scheme. Although the adjacent set of samples are used for this study, a small difference in lifetime due to slightly different microstructures might occur. The difference in surface recombination velocity between I-E and SiN_x passivation could also affect the initial lifetime values. A comparative study in lifetime improvement with I-E and SiN_x passivation is presented and discussed in Chapter 6.

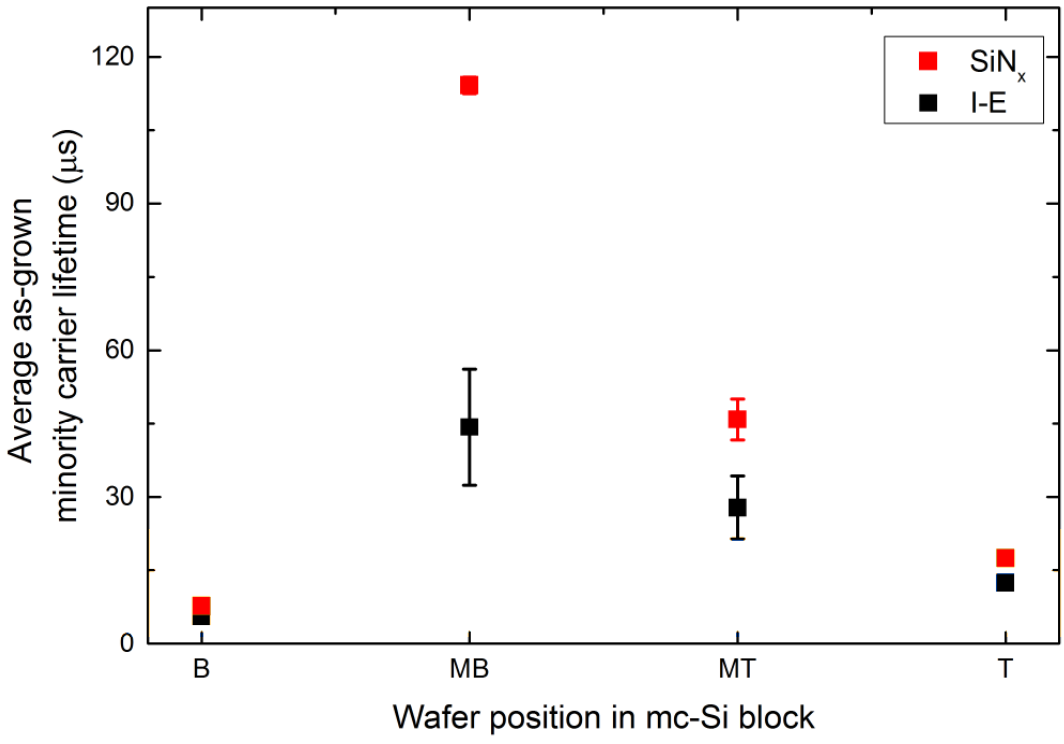

Figure 4.5. Comparison in the average bulk minority carrier lifetime with iron in the FeB state for the I-E and SiN_x passivated mc-Si samples used in Figures 4.1 and 4.2, respectively. The lifetimes were measured at an injection level of 1×10^{15} cm^{-3}. The bars represent the standard deviation of each data cluster from Figures 4.1 and 4.2.

Figure 4.6 shows the average as-grown interstitial iron concentration strongly depends on the choice of passivation scheme. Samples with silicon nitride passivation show considerably lower iron concentration compared to I-E passivation scheme. This finding is consistent with the study of Karzel *et al*. [137] which used quinhydrone-methanol solution (similar to our I-E passivation). In the bottom and top part of the ingot, samples with SiN_x passivation have fairly lower interstitial iron concentration than the samples with I-E passivation. The difference is found more substantial in high-lifetime samples from the centre part of the ingot. In the bottom middle samples, the average interstitial iron concentration with SiN_x is 5×10^{10} cm^{-3} compared to 2×10^{11} cm^{-3} with I-E passivation. It is important to note that I-E was performed at room temperature whereas SiN_x passivation was made by remote PECVD at 375 °C for ~10 min. Furthermore, SiN_x is well known for a high concentration of hydrogen [178, 197] which could diffuse to the bulk material during the deposition process and affect as-grown interstitial iron concentration values. A comparative analysis of the effects of SiN_x and I-E passivation in low-temperature gettering is discussed in Chapter 6.

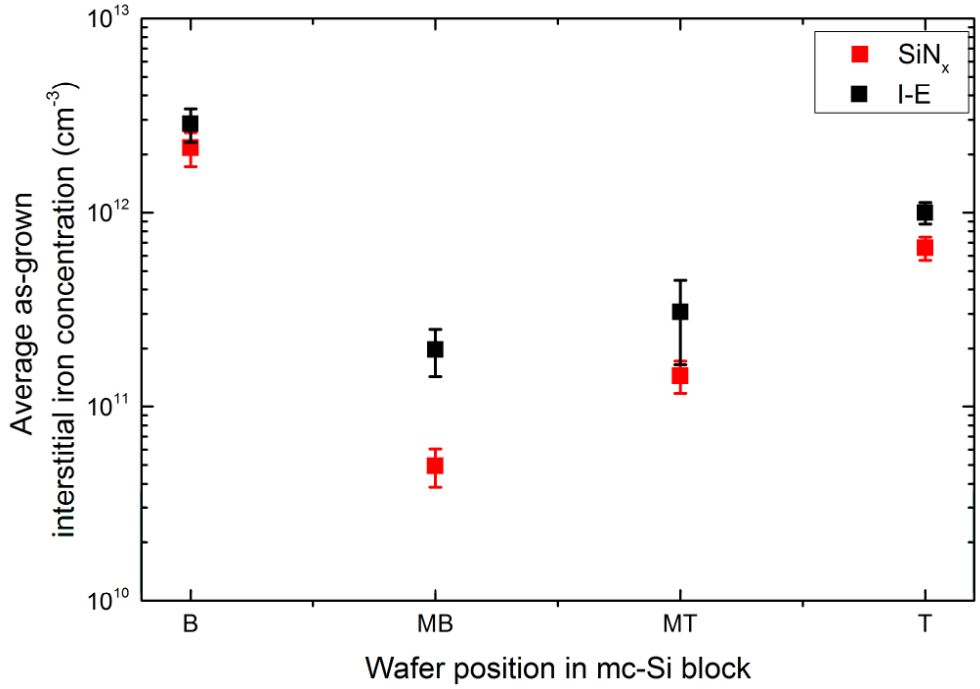

Figure 4.6. Comparison of the average bulk interstitial iron concentrations for the I-E and SiN_x passivated mc-Si samples used in Figures 4.3 and 4.4, respectively. The lifetimes were measured at an injection level of 1×10^{15} cm^{-3}. The bars represent the standard deviation of each data cluster from Figures 4.3 and 4.4.

4.5. Microstructural characterisation

Figure 4.7 summarises the microstructural properties of different samples sourced from the top, top middle, bottom middle and bottom position of the ingot. Figure 4.7(a) shows scanned optical images of the samples with 6400 dots per inch (DPI) after preferential etching. These images are analysed using the dislocation counting algorithm [174] to give the dislocation area density maps in Figure 4.7(b). The upper limit of dislocation area density is ~ 2×10^6 cm^{-2}, as around this value dislocation etch pits overlap and are not separable. Furthermore, any other black regions in the optical images (*e.g.* twin boundaries in MB sample) are presented as regions with very high dislocation density. Figure 4.7(a) and 4.7(b) show that samples from different heights of the ingot have clearly different microstructures. Samples from the bottom of the ingot have the lowest number etch pits and relatively more areas with a low dislocation density. The number of etch pit increases with the height positions. Samples from the top of the ingot have the highest number of etch pits and relatively few areas with a low dislocation density. The samples from the bottom middle exhibit a similar trend to the bottom sample. On the other hand, the top middle samples also have a large number of etch pit which is similar to the top samples. The distribution of the dislocation density in these maps is also plotted graphically in Figure 4.8.

Figure 4.7(c) shows PL images of the same samples (prior to the preferential etch). Different scales are maintained to show the microstructural features in samples with substantially different lifetimes. The magnitude of the local PL signal presented in Figure 4.7(c) is dependent upon the local minority carrier lifetime. The PL images are consistent with the bulk lifetime measurements in Figure 4.1, with the average PL intensity lowest at the bottom of the ingot, highest in the middle and somewhere in between at the top.

The scanned optical images in Figure 4.7(a) show a reasonably high concentration of twin boundaries in samples extracted from all heights of the ingot. It is interesting to identify twinned regions in Figure 4.7(a) and inspect the same regions in Figure 4.7(c). It is clear that the twin boundaries do not substantially affect the PL signal, which means they do not exhibit detectable recombination activity. The PL images show that the recombination activity arises principally in regions with high concentrations of dislocations and from some, but not all, grain boundary types. The PL images also

demonstrate that twin boundaries, which can clearly be seen in Figure 4.7(a), do not give rise to PL contrast in as-grown mc-Si. This is consistent with other reports which show twin boundaries to have very low (or perhaps no) recombination activity [64, 65, 72].

The histogram of dislocation density at different height position in ingot is shown in Figure 4.8. Samples from the bottom and bottom middle of the ingot have the most regions with very low ($< 2 \times 10^5$ cm^{-2}) dislocation densities, and the frequency distribution falls off with increasing density. Samples from the top and top middle have more even distributions of dislocation densities and have many more regions with high dislocation density than the samples from lower in the ingot. These observations are consistent with those of Ryningen *et al.* [66] who trace dislocation clusters from the top of the block downwards, and those of Stokkan who found an increase in dislocation density towards the top of the ingot [72]. The regions of high dislocation density generally give rise to lower PL signals and have lower carrier lifetime than low dislocation density regions, as shown in Figure 4.7(c). This is as expected from many previous studies (*e.g.* Ref. [35]). It is noted that a reasonably high frequency of regions with apparently higher dislocation density ($> 2 \times 10^6$ cm^{-2}) is observed in all four height positions, and this can be attributed at least partially to how the twin boundaries are analysed by the dislocation counting algorithm as noted above.

These results indicate that dislocation densities are not directly dominating the variation in bulk lifetime in the as-grown ingot. In the wafers from the bottom of the ingot has a relatively low density of dislocations but it has the lowest starting carrier lifetime (5.6 μs) of any of the regions investigated (Figure 4.1). This is at least partially due to the relatively high concentration of interstitial iron which acts as a recombination centre in the bulk (Figure 4.3). Wafers with relatively high concentrations of interstitial iron are likely to be affected by low-temperature annealing at 300 °C to 500 °C as interstitial iron diffuses fairly rapidly at these temperatures. A comprehensive study on low-temperature *internal* gettering in as-grown samples is discussed in Chapter 5. The improvement in bulk lifetime is also investigated in terms of interaction between dislocation densities and metallic impurities.

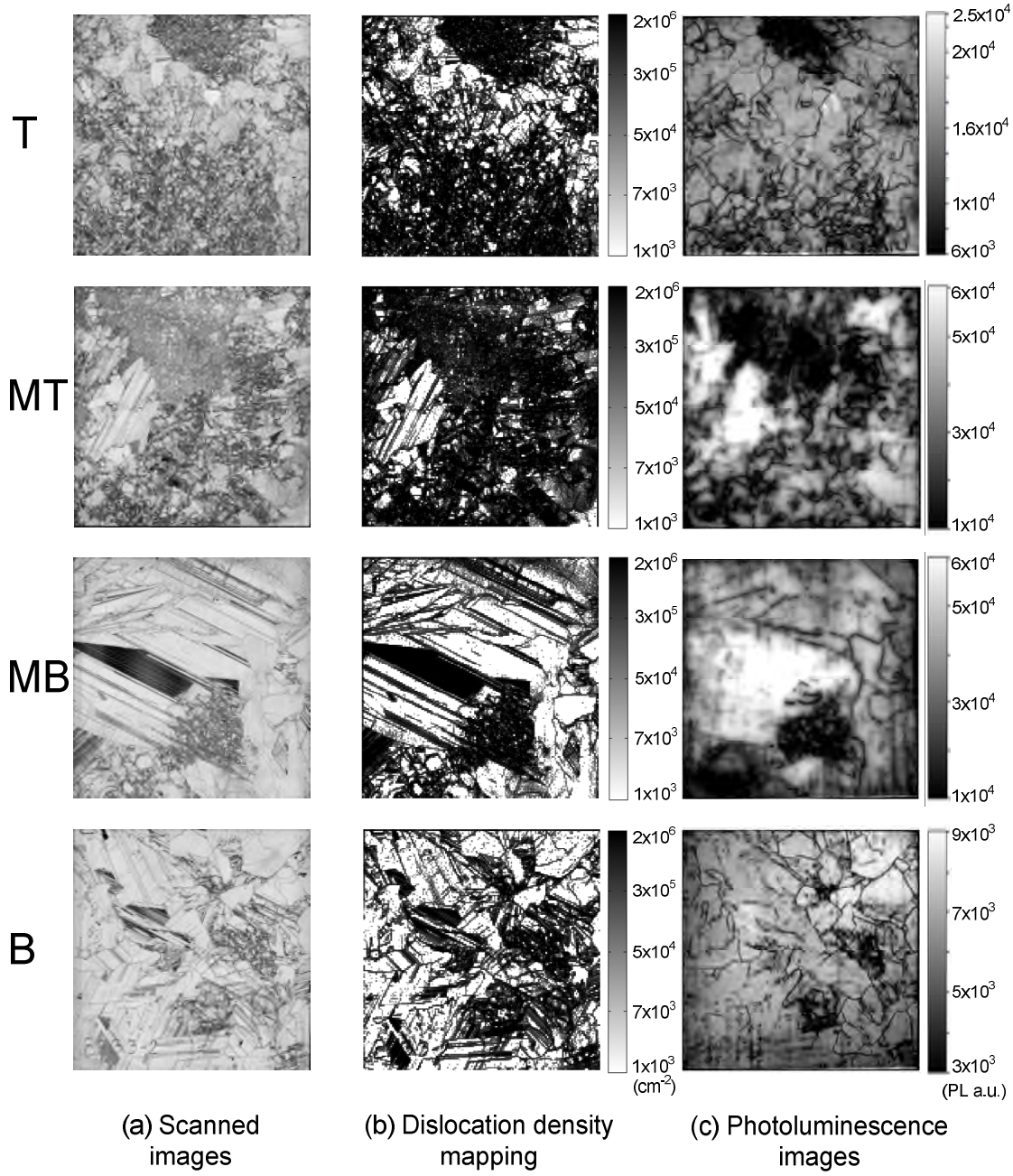

Figure 4.7. The first column (a) shows optically scanned images of Sopori etched samples (39 mm × 39 mm) from the different height positions. The second column (b) shows the corresponding dislocation density maps. The third column (c) shows the corresponding PL images of the as-received corresponding samples (before Sopori etching). Different scales are used in (c) to show clearly microstructural features in samples with substantially different lifetimes. Sister samples are used in low-temperature gettering study with I-E passivation as discussed in Chapter 5.

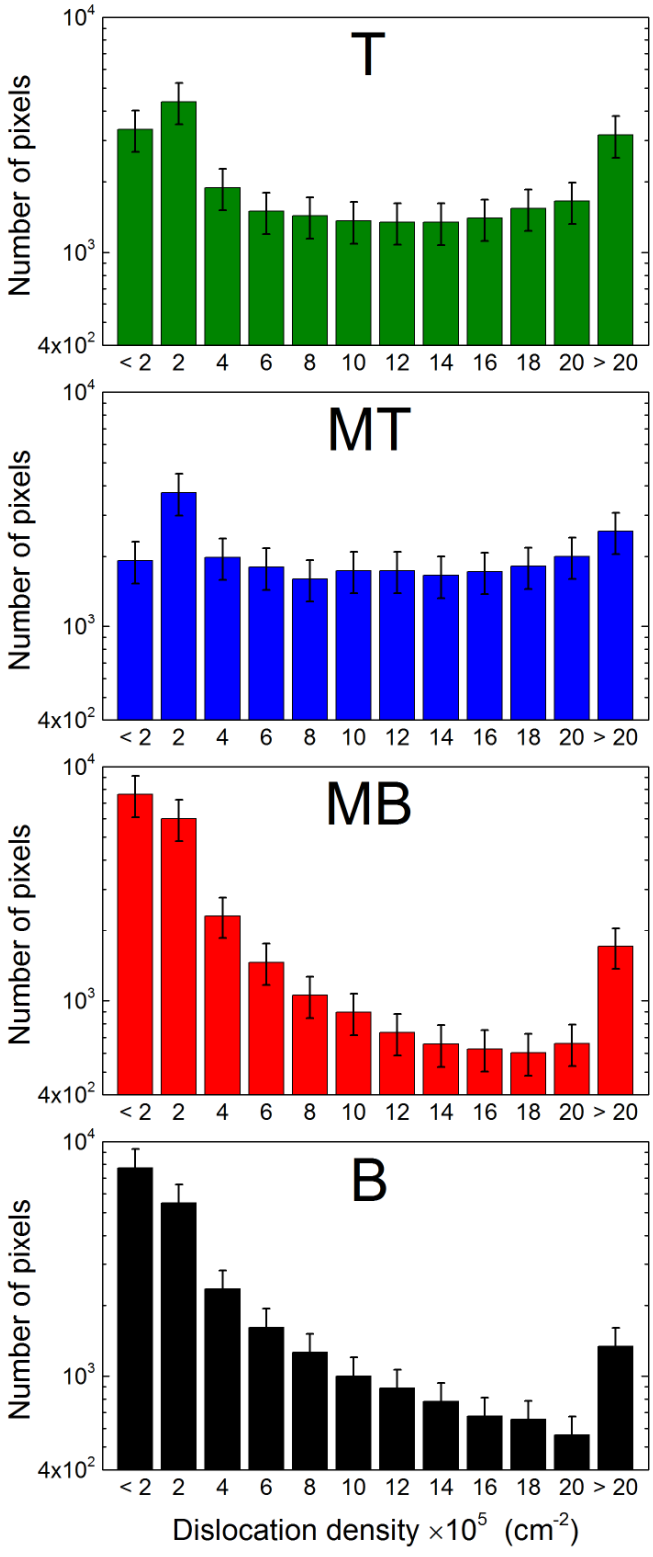

Figure 4.8. A frequency distribution of dislocation densities for samples sourced from the four different height positions from the Figure 4.7. A bin width of 2×10^5 cm^{-2} and 20% error bar are considered in distribution analysis. Sister samples are used for low-temperature gettering study as discussed in Chapter 5.

4.6. Summary

In summary, this Chapter presents an initial characterisation of bulk minority carrier lifetime and bulk interstitial iron concentration in as-grown samples sourced from four different height positions in a commercially mc-Si ingot. These samples are used for low-temperature internal gettering in this thesis (Chapter 5 and Chapter 6). A temporary iodine-ethanol and silicon nitride passivation schemes are used. Samples from the bottom of ingot have the lowest lifetime and the highest bulk interstitial iron concentration. The centre parts of the ingot show relatively high lifetime and the lowest interstitial iron concentration. The top part of ingot shows lifetime and interstitial iron concentration at somewhere between the bottom and centre of the ingot. Although trends in lifetime and interstitial iron concentration distributions are the same with both passivation schemes, samples with silicon nitride passivation show higher average lifetimes and lower average interstitial iron concentrations compared to those with iodine-ethanol passivation. The discrepancy in as-grown lifetime and interstitial iron concentration between SiN_x and I-E and their evolution with low-temperature gettering is discussed further in Chapter 6.

This Chapter also presents a distribution of dislocation density and photoluminescence images for different samples. The bottom and bottom middle show relatively low dislocation density. The top and top middle part show a large area with high dislocation density ~2 $\times 10^6$ cm^{-2} where etch pits overlap and not separable. The average PL signal found at different height positions is consistent with the measured bulk lifetime distribution. Twin boundaries are found at every height position. These do not show recombination activity.

Chapter 5 Low-temperature gettering to improve lifetime in as-received wafers

5.1. Introduction

As reviewed previously in Chapter 2, minority carrier lifetime is the key materials parameter for multicrystalline silicon (mc-Si) solar cell substrates. Lifetime in mc-Si is limited by recombination associated with metallic impurities in many forms, including point-like defects, precipitates and impurities bound to or precipitated at structural defects such as dislocations or grain boundaries. Some metallic impurities, such as interstitial iron, are sufficiently mobile that they can be redistributed by annealing at low temperatures. Controlling defects in mc-Si is a key to optimising the efficiency of mc-Si solar cells.

Iron, which is one of the most harmful and ubiquitous impurities, can be present in cast mc-Si in concentrations of 10^{14} to 10^{15} cm^{-3} [18, 195, 198]. Most of this iron is tied up in a relatively small number of precipitates, and the bulk iron concentration in the form of interstitial iron (Fe_i) or iron-boron (FeB) pairs can be orders of magnitude lower [195]. Engineering the distribution of impurities, such as iron, is the key to optimisation of lifetime [199]. Gettering processes are used to redistribute metallic impurities into locations and configurations in which they are less detrimental to lifetime. Extensive research into *external* gettering using near-surface phosphorus, boron or aluminium has

been performed (*e.g.* Ref. [20, 40, 131, 132]). Targeted *external* gettering approaches exist for particularly low lifetime wafers, such as saw damage gettering [200] and extended gettering based on slower cooling rates [201]. *Internal* gettering, in which impurities are redistributed within the bulk of the material, has also been used in mc-Si [36, 41, 48, 49]. *Internal* gettering can occur unintentionally in mc-Si during cooling after high-temperature cell processing steps. It can also take place in intentionally designed thermal processes.

Low-temperature (≤ 600 °C) annealing has been proposed as a way of improving the properties of silicon [36, 48-51, 202, 203] as many of the key impurities are sufficiently mobile at such temperatures that they can be redistributed. At low temperatures, the solubility of impurities such as iron is low [127, 128], so in principle, there is no need to conduct such processes in very clean conditions. Low-temperature annealing has empirically been found to improve solar cell efficiency, with Pickett and Buonassisi finding an improvement at 500 °C [50] and Rinio *et al.* finding the biggest improvement at 575 °C [51]. The mechanism by which cell efficiencies are improved is not well established, with the improvement likely to be a combined effect of *external* gettering, *internal* gettering and bulk passivation. It is also not known how different parts of the ingot with different defect distributions respond to low-temperature processes.

Other researchers have investigated the effects of low-temperature annealing at the substrate level [36, 48, 49]. In considering the results of these studies, it is vital to consider the details of the experimental conditions used, as these strongly affect the conclusions drawn. Krain *et al*. reported a reduction in interstitial bulk iron concentration by more than one order of magnitude after annealing silicon nitride surface passivated samples at 300 °C to 500 °C [36]. The activation energy for the interstitial iron reduction process was similar to that for diffusion of interstitial iron. Krain *et al.* however do not report the change in average bulk lifetime, nor do they appear to control the effect of wafer microstructure. It is possible that the low-temperature annealing performed in their work was influenced by bulk hydrogenation from the silicon nitride film [49, 137, 138, 204]. This can have the effect of passivating bulk defects [205], and it is also possible that hydrogen interacts with iron [137, 206]. Liu and Macdonald have studied *internal* gettering at 400 °C to 700 °C in samples surface passivated by a high-temperature (1000 °C) dry oxidation [49]. Although this is likely to have minimised hydrogenation, it will

have had the effect of redistributing metallic impurities from their as-grown state. A study by Boulfrad *et al.* reported a lifetime improvement in bottom red zone material by applying annealing at 550 °C after a high-temperature pre-annealing step (≥ 950 °C) [48]. The high-temperature pre-treatment will have dissolved metallic precipitates [130], and thus the as-grown state will have also been modified. In summary, whilst low-temperature annealing has been shown to have beneficial effects, detailed understanding of its effects on unmodified as-grown mc-Si in isolation from other effects such as bulk hydrogenation is currently lacking.

In this Chapter, results from a systematic set of low-temperature annealing experiments on as-received mc-Si wafers sourced from four different height positions of a commercially grown ingot are presented. Samples are passivated temporarily with an iodine-ethanol (I-E) chemical solution [147] to avoid possible bulk hydrogenation and thermal annealing during passivation. Sister samples from every height position are annealed at low temperatures (300 °C to 500 °C) for a wide range of time periods. At each time step, samples are re-passivated with a freshly made I-E solution and the lifetime and interstitial iron distribution are re-measured with QSS-PC lifetime measurements and also photoluminescence (PL) imaging. It is therefore believed that the effect of low-temperature annealing on lifetime (as well as interstitial iron concentration) is free from possible bulk hydrogenation effects. The results presented here, therefore, isolate more uncontrolled variables than previous studies [36, 48, 49] and enable the thermal effects only to be studied.

5.2. Experimental methods

Wafers (156 mm × 156 mm) were sourced from four different height positions (top (T), top middle (MT), bottom middle (MB), bottom (B)) of an edge block from a commercially-grown boron doped mc-Si ingot. Neighbouring wafers from all the positions were laser cut into 39 mm × 39 mm samples. The selection of samples used is illustrated in Figure 3.2 in Chapter 3. Samples were initially ~200 μm thick, with resistivities in the range 7.5 Ω cm to 11.5 Ω cm.

Samples were chemically polished with a planar etch solution as discussed in Section 3.5.2 in Chapter 3. After saw damage removal, samples (125 μm to 150 μm thick) were

passivated with the 0.1M I-E solution at room temperature and lifetimes were measured at an injection level of 1×10^{15} cm^{-3} by quasi-steady-state photoconductance (QSS-PC) [179] using a Sinton WCT-120 lifetime tester. Bulk interstitial iron concentrations were also calculated by following the methods discussed in Section 3.9.1 in Chapter 3. For interstitial iron calculations, lifetime data from QSS-PC at an injection level of $\Delta n = 1 \times 10^{15}$ cm^{-3} were used, as this is not at the cross-over point [15, 96] and to avoid trapping issues which are prevalent at lower injections [181]. For all the samples, measured lifetimes are assumed to be accurate to ± 4.3% [177].

The spatial distribution of lifetime was measured with iron in the FeB and Fe_i state using a BT Imaging LIS-L1 PL imaging system with a 1.1×10^{17} $cm^{-2}s^{-1}$ photon flux with an exposure time of 5 s. Excitation is achieved using an LED array with an emission wavelength of 650 nm and detection is with a silicon CCD. PL images were calibrated in terms of lifetime by a QSS-PC measurement made at the centre of the same sample [184]. For the conditions used here, the pixel width and height is ~160 μm. Lifetime measurements were made within a few minutes of initial surface passivation as the quality degrades rapidly. After the final measurement, the samples were subjected to a methanol dip followed by RCA cleaning to remove iodine related residues.

The spatial distribution of the interstitial iron concentration was calculated using the model (discussed in Section 3.9.2 in Chapter 3) based on lifetime changes at every pixel as reported in Macdonald *et al*. [189]. The injection level used for interstitial iron mapping was different for every pixel and generally was much lower than for the QSS-PC calculations to prevent unwanted dissociation of FeB pairs during measurement.

Three sister samples with near-identical microstructures from every height position were selected for annealing at 300 °C, 400 °C and 500 °C. Samples were annealed in a fused silica tube furnace (60 cm length, 6.1 cm diameter) under nitrogen ambient. For a given temperature, samples from all height positions were subjected to identical annealing and cooling treatments, as annealing and removal were performed simultaneously. Cooling was always fast and it is estimated that the samples were at room temperature in ~ 10 s. After each annealing treatment samples were again subjected to RCA cleaning and were stored in the dark for ≥ 36 h to ensure complete re-association of FeB defects [97]. Samples were then passivated with a freshly made I-E solution and lifetime was

measured. A summary of the major processing and characterisation sequences used is shown in Figure 5.1.

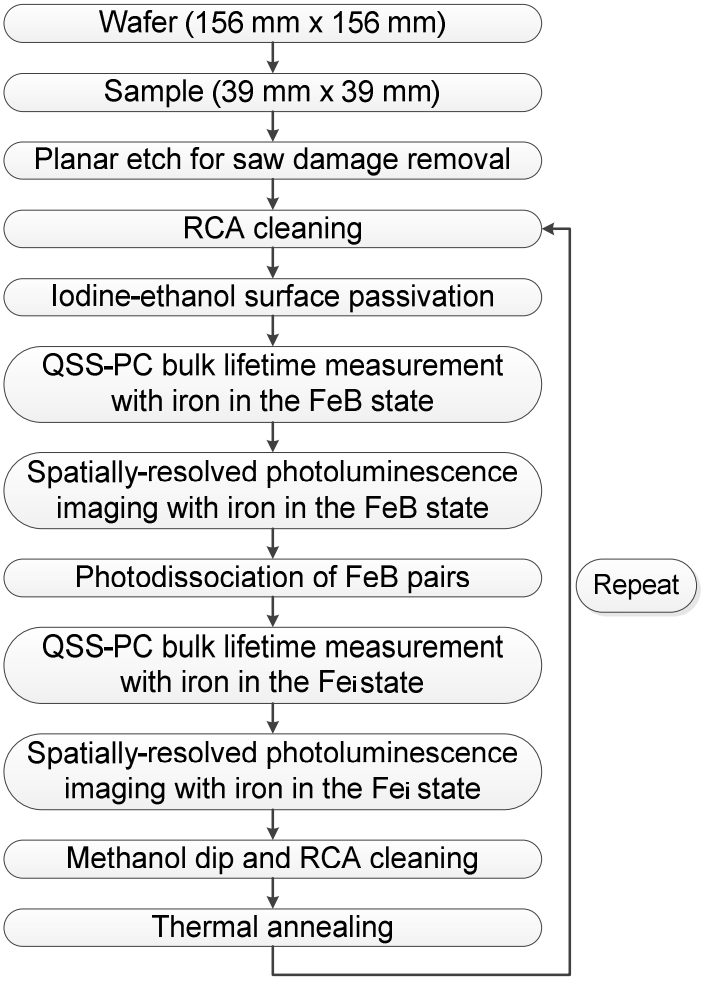

Figure 5.1. The processing and characterisation sequence for the low-temperature annealing experiments. Details of every process step are described in Chapter 3.

5.3. Results

In this Chapter, the effects of low-temperature annealing using a temporary iodine-ethanol solution are investigated. Samples were annealed in the absence of a dielectric layer on their surfaces, so any changes in lifetimes can be attributed to the thermal effect only. Note that the initial characterisation of these samples is presented and discussed in Sections 4.2.1 and 4.3.1 in Chapter 4. In the following sections, the key findings of low-temperature annealing are discussed in the context of the height position in the ingot.

5.3.1. Bulk minority carrier lime in low-temperature annealing

5.3.1.1 Lifetime with iron in the FeB state

Figure 5.2 shows the evolution of carrier lifetime with iron in the FeB state (τ_{FeB}) at an injection level of 1×10^{15} cm^{-3} for all three annealing temperatures as a function of cumulative time. Note that the maximum cumulative annealing time was chosen based on the trend of lifetime improvement observed. The overall effects of the annealing on lifetime are also summarised in Table 5.1. The samples from the bottom part of the ingot have the lowest average bulk lifetime (5.7 ± 0.9 μs) in the as-received state, represented by the dashed line in every graph. Lifetime is improved substantially for all three annealing temperatures. Although lifetime increases in all three cases, the effect of low-temperature annealing is not straightforward. Lifetime improvement is not found to be systematic with annealing temperature. The bottom samples exhibit the most straightforward time dependence compared to the samples from other parts of the ingot (discussed in Section 5.5). The largest improvement is found at 400 °C when 35 h of cumulative annealing increases the lifetime from 5.5 μs to 38.7 μs which is a remarkable improvement for such a simple process. Annealing at 300 °C and 500 °C gives ultimate improvements by a factor of ~ 6 and ~ 4. It is interesting to note that lifetime decreases from 6.6 μs to 5.7 μs upon annealing at 500 °C in the first 10 h but longer-term annealing gives a recovery.

In the samples from the centre part of the ingot (bottom middle and top middle), as-received lifetime is relatively high compared to the bottom and top parts of the ingot. The average lifetimes are 44 μs and 28 μs for MB and MT samples, respectively. Both the MB and MT samples exhibit similar behaviour when subjected to low-temperature annealing. In general, lifetime is improved slightly in annealing at 300 °C, whereas no overall improvement is observed upon annealing at 400 °C and 500 °C. The largest improvement from 50 μs to 66 μs is observed upon annealing at 300 °C for 53 h in the bottom middle sample. It is important to note that lifetime reduces substantially in primary annealing steps at 400 °C and 500 °C. For example, lifetime reduces from 48 μs to 5 μs after 7.5 h of cumulative time period at 500 °C for the bottom middle sample. At both temperatures, lifetime recovers after the longest annealing period. There is a lot of

scatter in the data, and it is unclear whether substantial stable improvements are ever realised at 400 °C and 500 °C.

The samples from the top part of the ingot have fairly high average as-received lifetime ~12.5 μs compared to the bottom samples. Top wafers respond differently to low-temperature annealing compared to bottom wafers perhaps due to the different grown-in dislocation density (Figure 4.7). Note that the sample annealed at 300 °C was broken after 43 h of the cumulative annealing period and therefore no data points are available after this step. Lifetime decreases after the primary annealing step in all three cases. However, lifetime is ultimately improved in all the three annealing temperatures. The largest improvement in lifetime is observed of a factor of ~2 upon annealing at 400 °C for 35 h. The time dependence in lifetime improvement is more complicated in top wafers than the bottom wafers. These data are discussed in detail in Section 5.5.1.

5.3.1.2 Lifetime with iron in the Fe_i state

Figure 5.3 shows the evolution in lifetime with iron in the Fe_i state (τ_{Fei}) as a function of cumulative annealing time. The measured τ_{Fei} (at an injection level of 1×10^{15} cm^{-3}) is generally higher than the measured lifetime with iron in the FeB state. The trend in τ_{Fei} changes is similar to those of τ_{FeB} (Figure 5.2) in all three annealing temperatures for samples from four height positions. In the bottom samples, lifetime (τ_{Fei}) is improved upon annealing at three temperatures. In the best case, τ_{Fei} increases from 10.8 μs to 48.3 μs upon annealing at 400 °C for 35 h. In samples from the centre part of the ingot, lifetime is improved slightly upon annealing at 300 °C. Annealing in 400 °C and 500 °C, lifetime reduces abruptly after primary annealing but they do not exhibit an overall improvement in the bottom middle and top middle sample. In the top samples, τ_{Fei} is decreased in primary annealing steps and is improved ultimately in longer term annealing. These data are discussed in detail in Section 5.5.1.

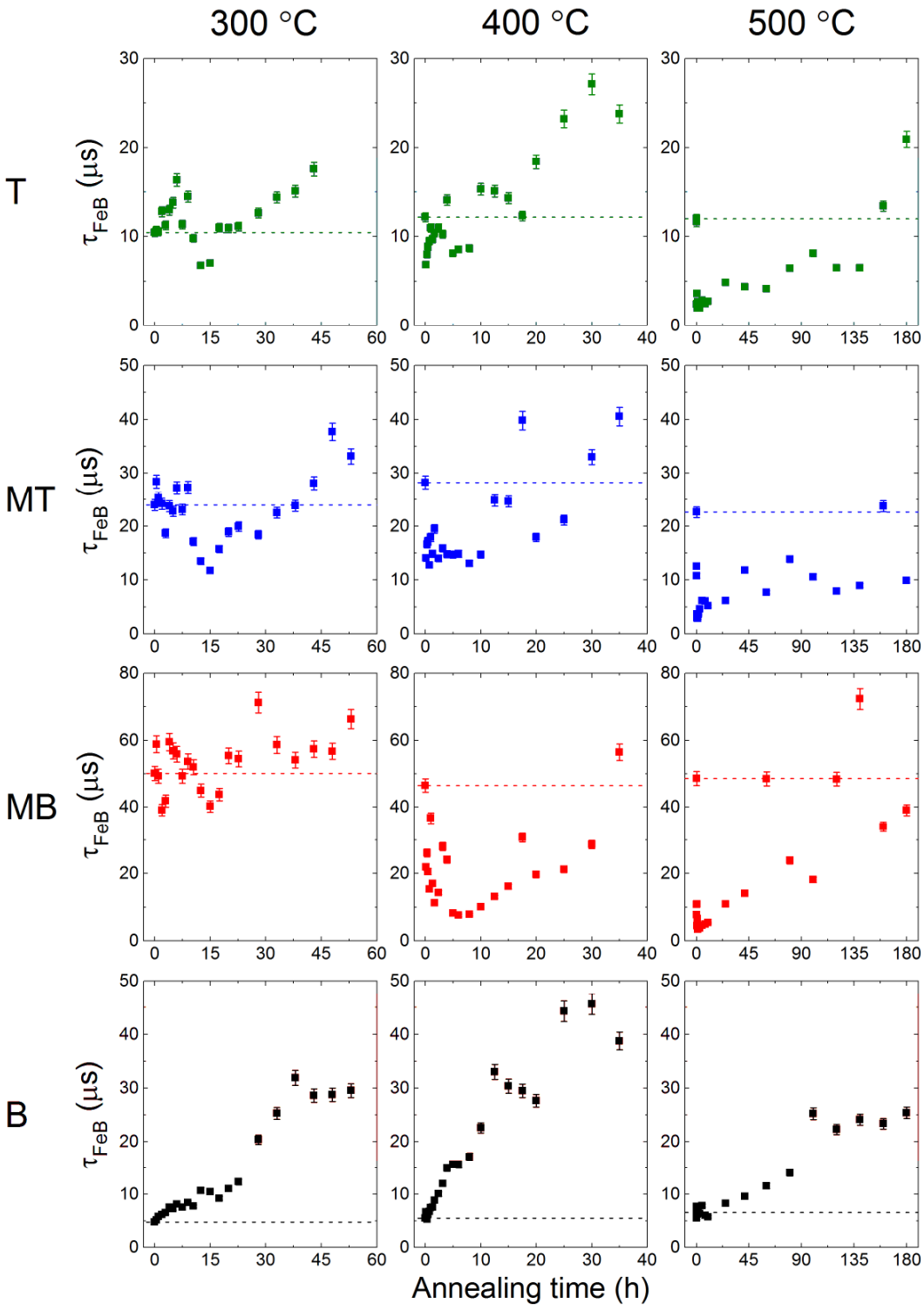

Figure 5.2. Measured minority carrier lifetime with iron in the FeB state (τ_{FeB}) an injection level of 1×10^{15} cm^{-3} for samples from the bottom (B), bottom middle (MB), top middle (MT) and top (T) of the mc-Si ingot. Sister samples were annealed at 300 °C, 400 °C and 500 °C for the cumulative annealing time plotted. The dashed lines represent the as-grown values.

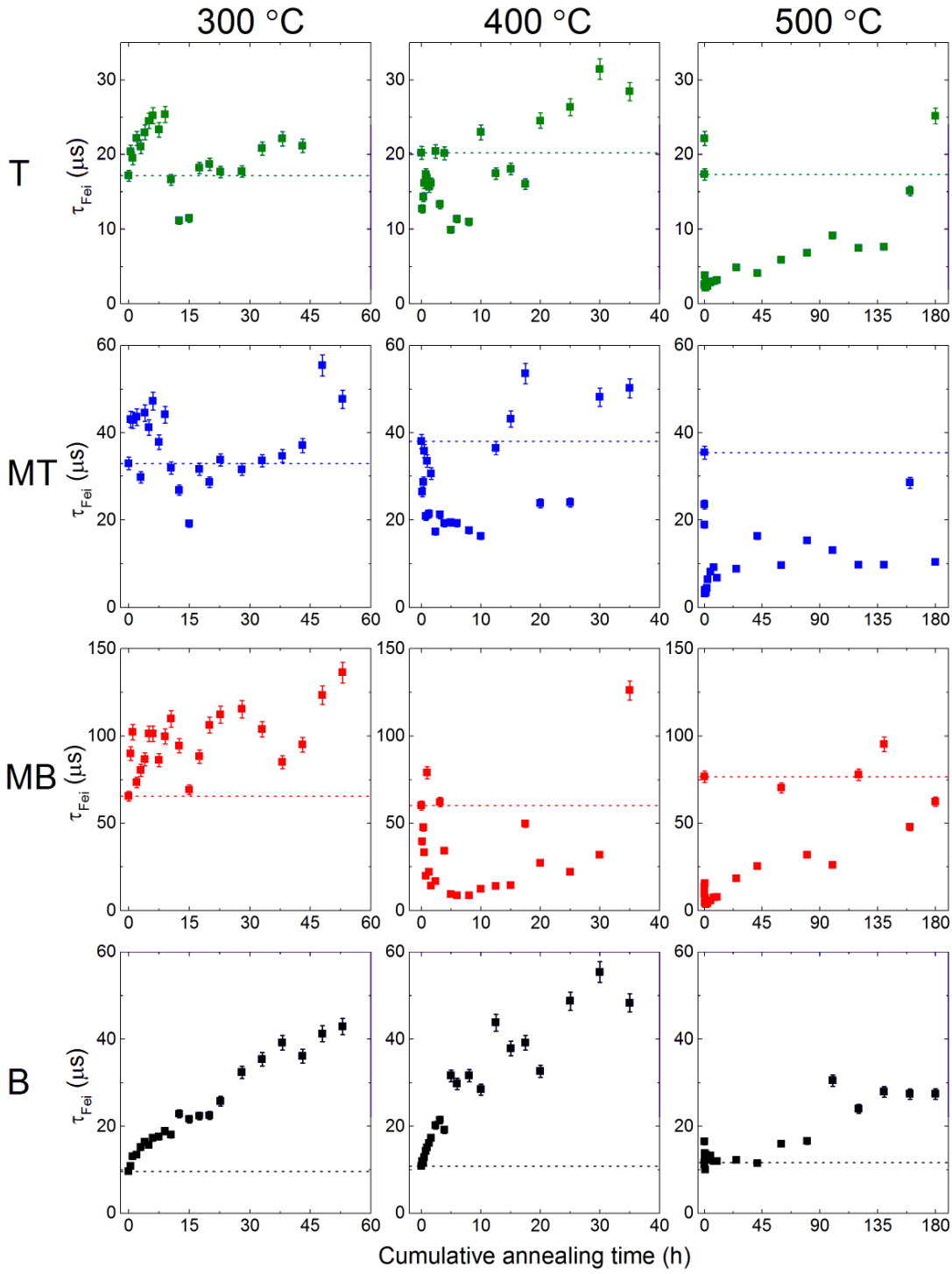

Figure 5.3. Measured minority carrier lifetime with iron in the Fe_i state (τ_{Fei}) an injection level of 1×10^{15} cm^{-3} for samples from the bottom (B), bottom middle (MB), top middle (MT) and top (T) of the mc-Si ingot. Sister samples were annealed at 300 °C, 400 °C and 500 °C for the cumulative annealing time plotted. The dashed lines represent the as-grown values.

5.3.2. Bulk interstitial iron concentration in low-temperature annealing

Figure 5.4 shows evolution in the average interstitial iron concentration as a function of cumulative annealing time at 300 °C, 400 °C and 500 °C temperatures for samples sourced from four different height positions. The distribution of as-received interstitial iron concentration in these samples using iodine-ethanol passivation is discussed in Section 4.3.1 in Chapter 4. The as-received interstitial iron concentrations are represented by dashed lines in Figure 5.4 to show the relative changes at low-temperature annealing. It is noted that error bars (calculation described in Section 3.9.1) are relatively big at low interstitial iron concentrations as they are close to the detection limits.

The bottom samples have the highest average as-received bulk interstitial iron concentrations ($2.9 \pm 0.7 \times 10^{12}$ cm^{-3}) compared to other parts of the ingot. The bulk interstitial iron concentration generally falls with annealing time in all three cases. In annealing at 300 °C, the interstitial iron decays approximately exponentially from 3.5×10^{12} cm^{-3} to 3.5×10^{11} cm^{-3} after 53 h. Annealing at 400 °C and 500 °C, interstitial iron concentrations surprisingly increases slightly in the primary steps. In annealing at 400 °C, there is a slight initial increase in the bulk iron concentration followed by an approximately exponential decay from 2.8×10^{12} cm^{-3} to 2.6×10^{11} cm^{-3} after 35 h. The largest reduction is 2.2 order of magnitude, observed upon annealing at 500 °C for 180 h. It is interesting to note that, the average bulk interstitial iron concentration increases from 2.1×10^{12} cm^{-3} to 2.9×10^{12} cm^{-3} after first 10 h of annealing at 500 °C. However, it decreases to 9.6×10^{10} cm^{-3} after 180 h of cumulative annealing time.

The samples from the centre part of the ingot have the lowest average interstitial iron concentration in the as-received state compared to the bottom and top part of the ingot. The average interstitial iron concentration of the as-received bottom middle and top middle samples are 2.0×10^{11} cm^{-3} and 4.0×10^{11} cm^{-3}, respectively. At 300 °C, interstitial iron concentration increases slightly in primary annealing step and remains unchanged in further annealing steps in both the bottom middle and top middle samples. At 400 °C and 500 °C, primary annealing step increases interstitial iron concentration substantially. The worst scenario is in the bottom middle sample where interstitial iron concentration increases from 5.1×10^{11} cm^{-3} to 2.8×10^{12} cm^{-3} upon annealing at 500 °C for 1 h of the

cumulative time. Although it recovers after longer term annealing, no overall improvement is observed compared to the as-received state upon annealing at both 400 °C and 500 °C temperatures. These data are discussed in detail later.

In the top samples, the average as-received interstitial iron concentration is 1.0×10^{12} cm^{-3}, fairly low compared to the bottom samples. After primary annealing steps, interstitial iron concentration increases in all three annealing temperatures and recovers in further steps. In the best scenario, the average interstitial iron concentration reduces from 1.0×10^{12} cm^{-3} to 2.1×10^{11} cm^{-3} upon annealing at 400 °C for 35 h. Annealing at 500 °C, interstitial iron concentration increases from ~8.0×10^{11} cm^{-3} to 3.0×10^{12} cm^{-3} after 27.5 h of the cumulative time. The trend in interstitial iron concentration reduction upon annealing at 500 °C is scattered and not clear. However, after the last annealing step (total 180 h cumulative annealing time) interstitial iron concentration ultimately reduces to ~2.5×10^{11} cm^{-3}. These data are discussed in detail in Sections 5.5.1 and 5.5.2.

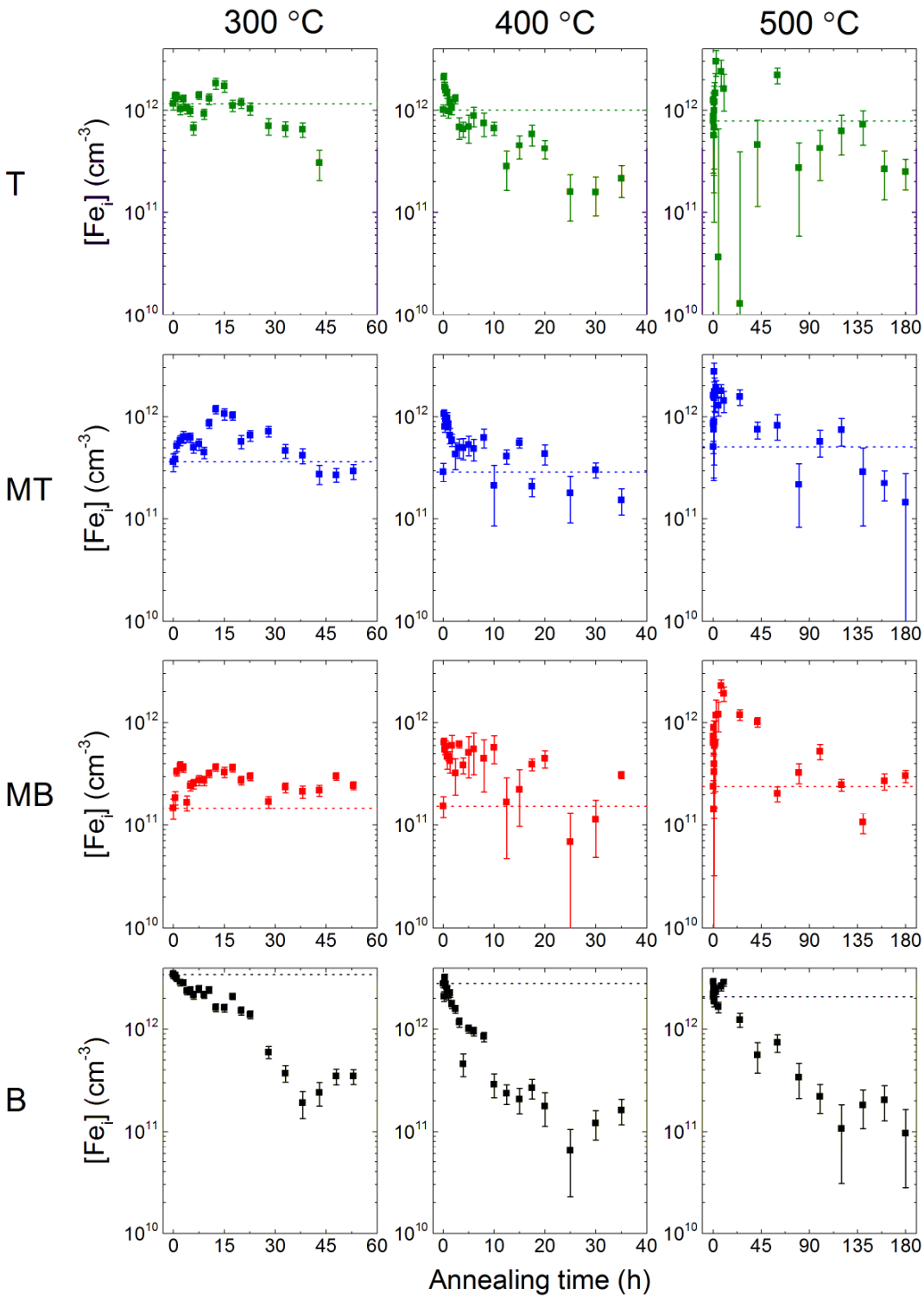

Figure 5.4. Interstitial iron concentration ([Fe_i]) estimated an injection level of 1×10^{15} cm^{-3} for samples from the bottom (B), bottom middle (MB), top middle (MT) and top (T) of the mc-Si ingot. Sister samples were annealed at 300 °C, 400 °C and 500 °C for the cumulative annealing time plotted. The dashed lines represent the as-grown values.

5.3.3. Spatial distribution of carrier lifetime

Spatially resolved lifetime images with iron in the FeB and Fe_i states were acquired at each processing step for every sample annealed at 300 °C, 400 °C or 500 °C. The evolution of the spatially resolved lifetime with iron in the FeB state in the bottom, bottom middle, top middle and top samples at certain time steps are shown in Figures 5.5, 5.6, 5.7 and 5.8, respectively. These Figures also show the spatial distribution of dislocation density (discussed in Chapter 4) of sister sample from every height position. The same scale is maintained for all images to show changes over the annealing period at different temperatures and at different height positions. Note that the values of lifetime plotted are, in general, lower than those from QSS-PC used in Figure 5.2, to avoid unwanted dissociation of FeB pairs by the PL imaging measurement.

In the bottom as-grown samples (Figure 5.5), lifetimes are initially low in the bulks of the grains and very low at certain grain boundaries. With increasing cumulative annealing time the lifetime improves, particularly in the bulks of the grains in all three annealing temperatures. The largest overall improvement is observed upon annealing at 400 °C for 35 h. The grain boundaries and regions with crystallographic defects become worse upon annealing in the all three cases. Note that pixel size in the lifetime images is ~160 µm × 160 µm which reduces the contrast of some grain boundaries.

In the bottom middle samples (Figure 5.6), initial lifetime is relatively high in the bulk grain regions and very low at the grain boundaries and defect clusters. The initial annealing reduces lifetime throughout the wafer particularly upon annealing at 400 °C and 500 °C. In the worst case, the average lifetime is reduced to less than 10 μs upon annealing at 500 °C for 0.08 h. Lifetime then begins to recover in regions in the bulk grain regions. It is interesting to note that some grain boundaries become visible after longer term annealing at 500 °C.

The top middle samples (Figure 5.7) exhibit the similar behaviour of the bottom middle samples. In general, the top middle samples have more crystallographic defective regions compared to the bottom middle samples. Note that the top middle sample annealed at 300 °C was partially broken after 10.5 h of the cumulative time and therefore no images are available after this step. Lifetime in the as-received state is high in some grains but substantially low in defective regions. The initial annealing reduces lifetime throughout

the wafer, particularly at 500 °C. Lifetime then begins to recover in some of the bulk regions. The biggest overall improvement is observed after annealing at 400 °C for 35 h. Like the bottom middle samples, many grain boundaries also appear to be visible after the longest annealing cumulative annealing time (180 h) at 500 °C.

The spatial distribution of lifetime in the as-received top samples (Figure 5.8) is very similar to the bottom samples. The top samples have more crystallographic defects compared the bottom samples. The spatial distribution of dislocation density shows the top sample has the largest average dislocation. In the as-received state, lifetime is low throughout the samples. In annealing at 300 °C, lifetime increases slightly after initial annealing steps. Lifetime is ultimately improved in grain regions after 43 h of annealing (sample was broken after this step). In annealing at 400 °C and 500 °C, lifetime reduces substantially throughout the samples. In both the cases, lifetime recovers with further annealing in most of the bulk grains and the defective regions become worse upon annealing.

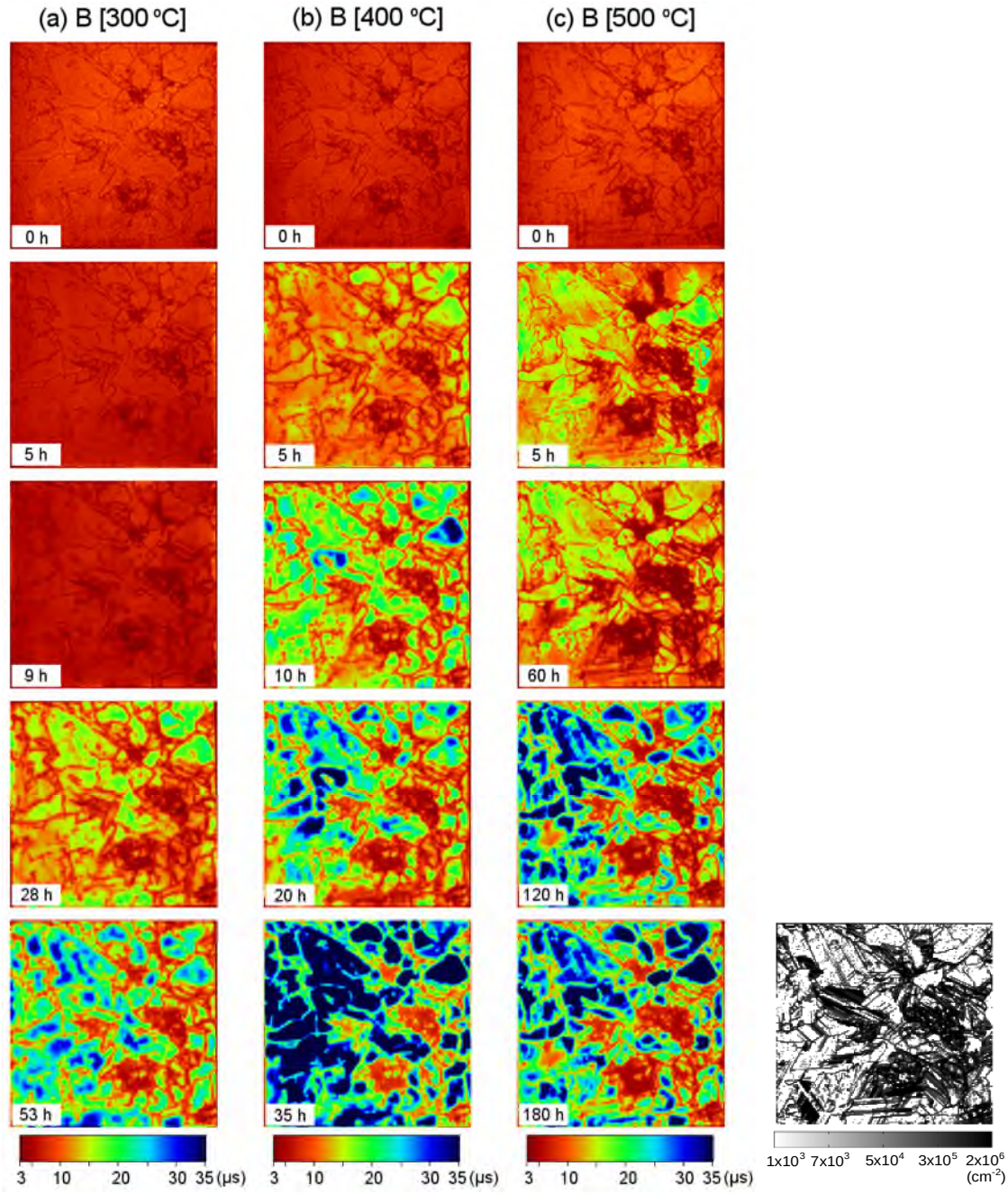

Figure 5.5. Spatial distribution of minority carrier lifetime with iron in the FeB state in mc-Si samples (39 mm × 39 mm) from the bottom part of the ingot. Sister samples were annealed at 300 °C, 400 °C and 500 °C. A map of dislocation density of a sister sample is presented in the right column.

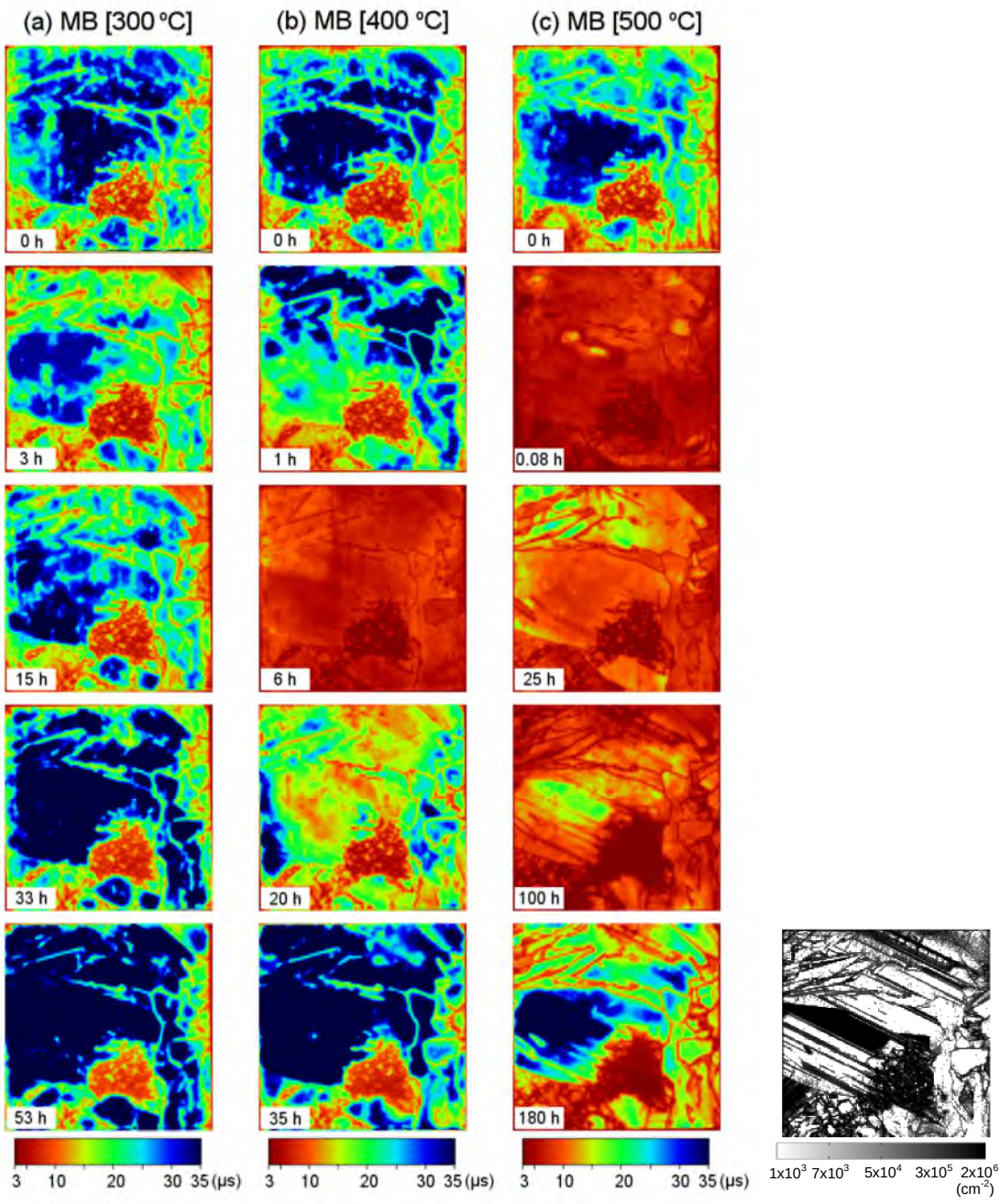

Figure 5.6. Spatial distribution of lifetime with iron in the FeB state in mc-Si samples (39 mm × 39 mm) from the bottom middle part of the ingot. Sister samples were annealed at 300 °C, 400 °C and 500 °C. A map of dislocation density of a sister sample is presented in the right column.

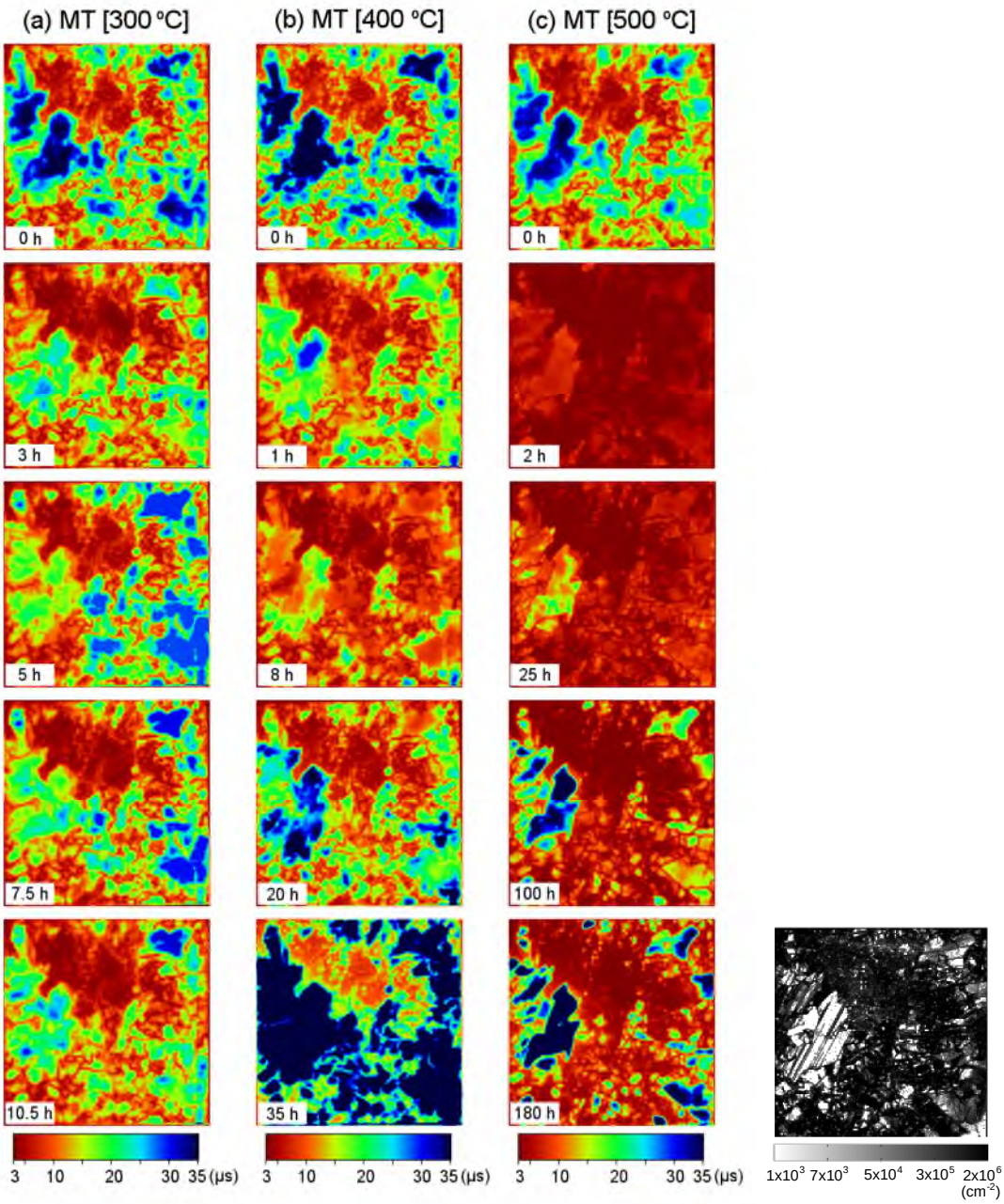

Figure 5.7. Spatial distribution of minority carrier lifetime with iron in the FeB state in the top middle samples (39 mm × 39 mm). Sister samples were annealed at 300 °C, 400 °C and 500 °C. A map of dislocation density of a sister sample is presented in the right column.

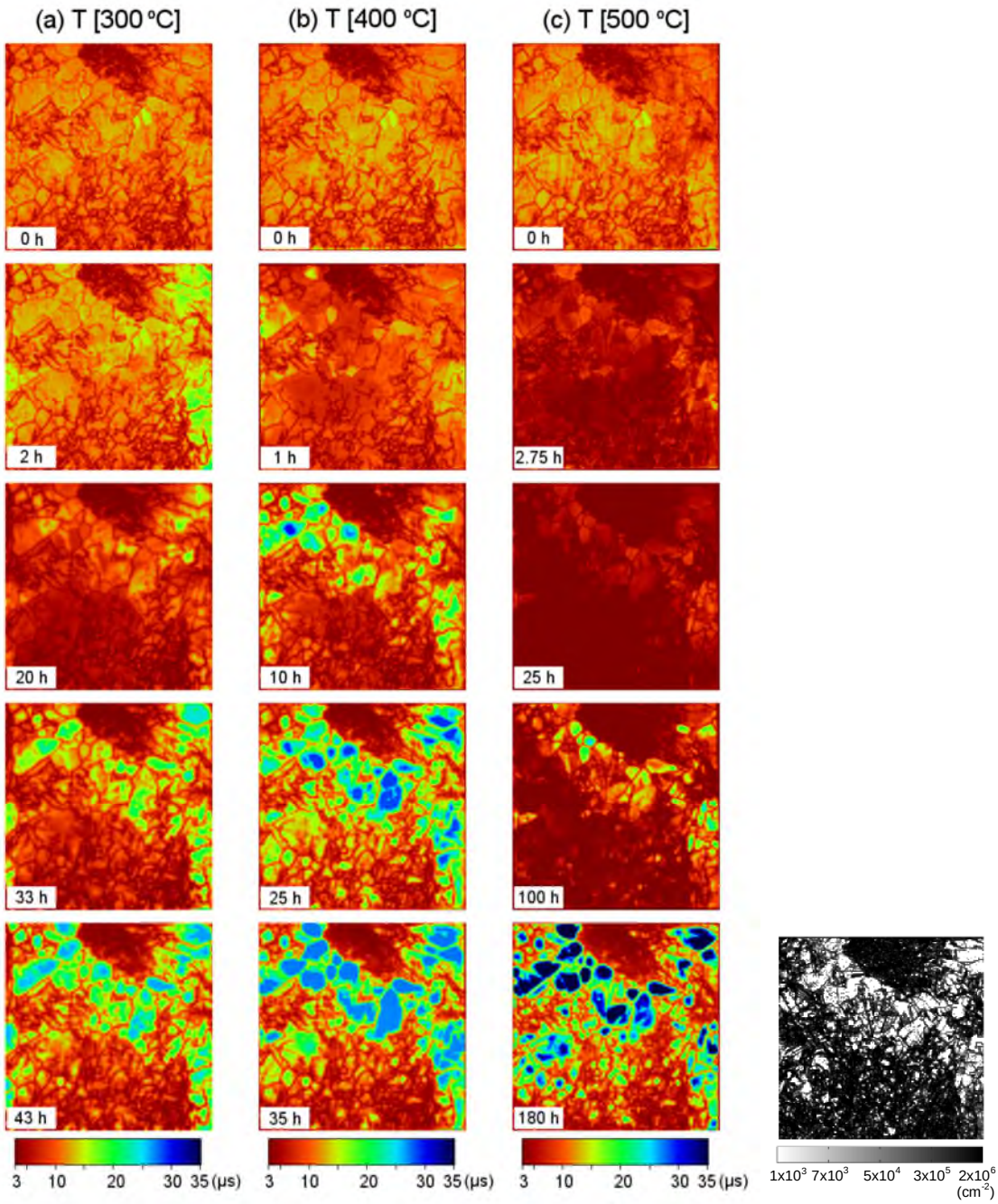

Figure 5.8. Spatial distribution of minority carrier lifetime with iron in the FeB state in the top samples (39 mm × 39 mm). Sister samples were annealed at 300 °C, 400 °C and 500 °C. A map of dislocation density of a sister sample is presented in the right column.

5.3.4. Spatial distribution of interstitial iron concentration

Interstitial iron concentration mapping technique is based on lifetime changes before and after dissociation of FeB pairs in every pixel (~160 μm) (discussed in Section 3.9.2 in Chapter 3). Interstitial iron concentration maps were made after every annealing step

in all three annealing temperatures for samples from four height positions. The interstitial iron concentrations change substantially upon annealing and are presented in Figures 5.9, 5.10, 5.11 and 5.12 for the bottom, bottom middle, top middle and top samples, respectively. The same logarithmic scale is maintained in all cases to enable a fair comparison.

Figure 5.9 shows the evolution of the interstitial iron distribution, estimated from the lifetime images presented in Figure 5.5. The bottom samples have the highest interstitial iron concentration > 10^{12} cm^{-3}, distributed throughout the samples. Low-temperature annealing changes the interstitial iron concentration distribution substantially. In most of the bulk grain regions, the interstitial iron concentration decreases to ≤ 10^{10} cm^{-3} upon annealing at all three temperatures. The best result is found in the sample annealed at 500 °C for 180 h. A few bulk grains show slightly high iron concentration.

Figure 5.10 shows the changes in interstitial iron concentration distribution in the bottom middle samples upon annealing at 300 °C to 500 °C. The as-received states have relatively low interstitial iron concentration (≤ 10^{11} cm^{-3}) in most of the bulk grain regions. The annealing appears to have caused higher interstitial iron concentrations in all three annealing temperatures compared the as-grown state. The worst case is upon annealing at 500 °C where interstitial iron concentration increases to ≥ 10^{12} cm^{-3} throughout the sample. Longer annealing steps reduce to ~10^{11} cm^{-3} in some grain regions. Furthermore, annealing increases recombination associated with certain grain boundary types.

Figure 5.11 shows the changes in interstitial iron concentration distribution in the top middle samples, which is similar compared the bottom middle samples. Note that the top middle samples have relatively high dislocation density compared the bottom middle samples. In the as-received state, interstitial iron concentration is ≤ 10^{11} cm^{-3} in some bulk grain regions and ≥ 10^{12} cm^{-3} in the defective regions. Low-temperature annealing shows both decreases and increases in the interstitial iron concentrations. Annealing at 300 °C and 400 °C, interstitial iron concentration reduces with annealing time. The largest reduction is observed upon annealing at 400 °C where most of the bulk grain regions have an interstitial iron concentration of ≤ 5.0 × 10^{10} cm^{-3} and defective regions (with high dislocation density) have a concentration of ≥ 1.0 × 10^{12} cm^{-3}. Interstitial iron concentration increases throughout the sample after primary annealing steps at 500 °C.

Longer annealing reduces the interstitial iron concentration to ~1.0×10^{10} cm^{-3} in a few bulk grain regions only, but most of the regions remain unchanged (> 1.0×10^{12} cm^{-3}).

Figure 5.12 shows the spatial distribution of interstitial iron concentration in as-received states and changes in low-temperature annealing for the top samples. In as-received states, interstitial iron concentration is ≥ 1×10^{12} cm^{-3} throughout the samples. The interstitial iron concentration reduces substantially (≤ 5×10^{10} cm^{-3}) in most of the bulk regions upon annealing at 300 °C and 400 °C. The defective regions show a very high interstitial iron concentration of ≥ 10^{12} cm^{-3} after the longest cumulative annealing time. In annealing at 500 °C, interstitial iron concentration remains almost unchanged in first 80 h of cumulative time and recovers in some grain regions in further annealing steps. These maps and relations with crystallographic defects (*e.g.* dislocation) are discussed in detail in Section 5.5.

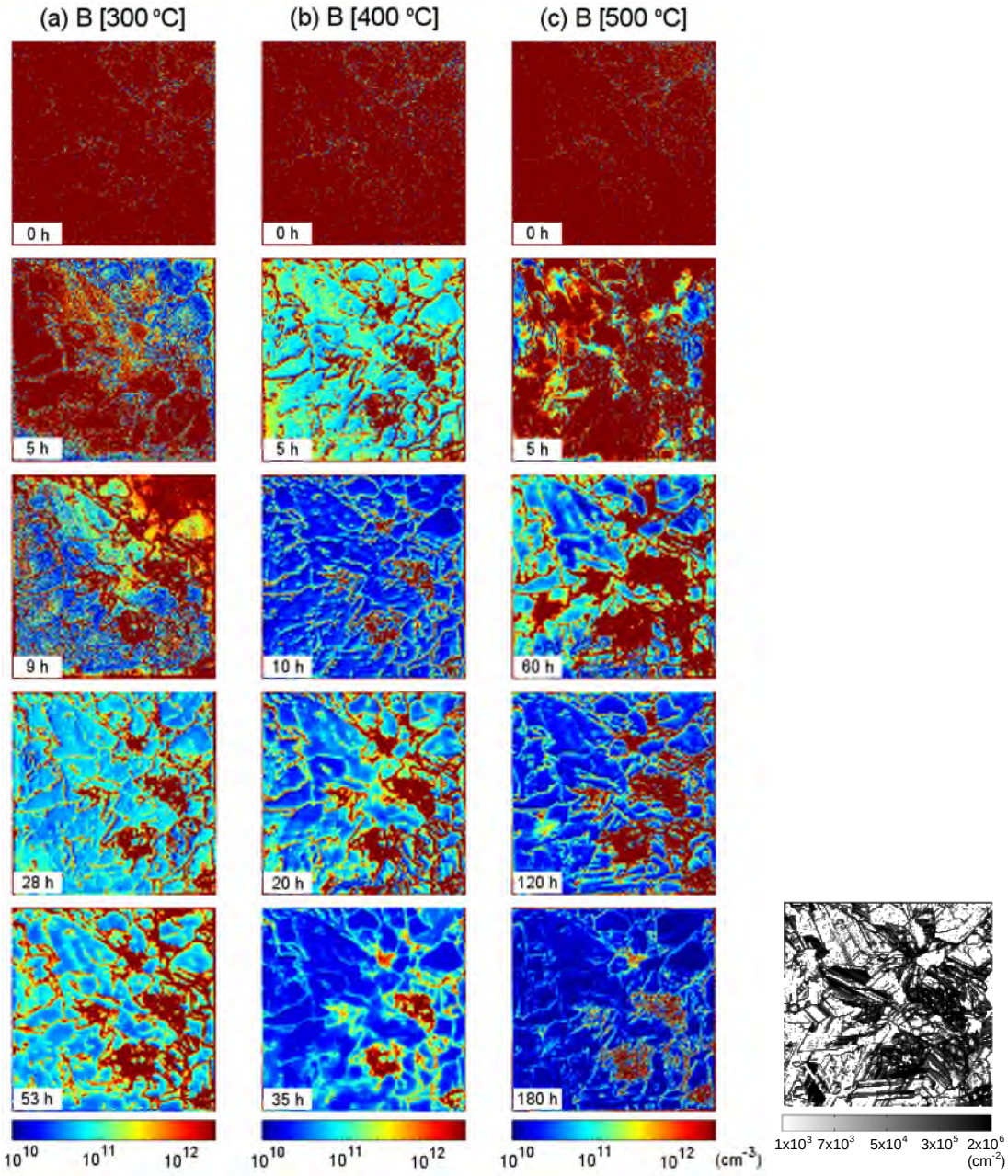

Figure 5.9. Spatial distribution of interstitial iron concentration in the same bottom samples (39 mm × 39 mm) used in Figure 5.5. Samples annealed at the temperatures and cumulative times shown. A map of dislocation density of a sister sample is presented in the right column.

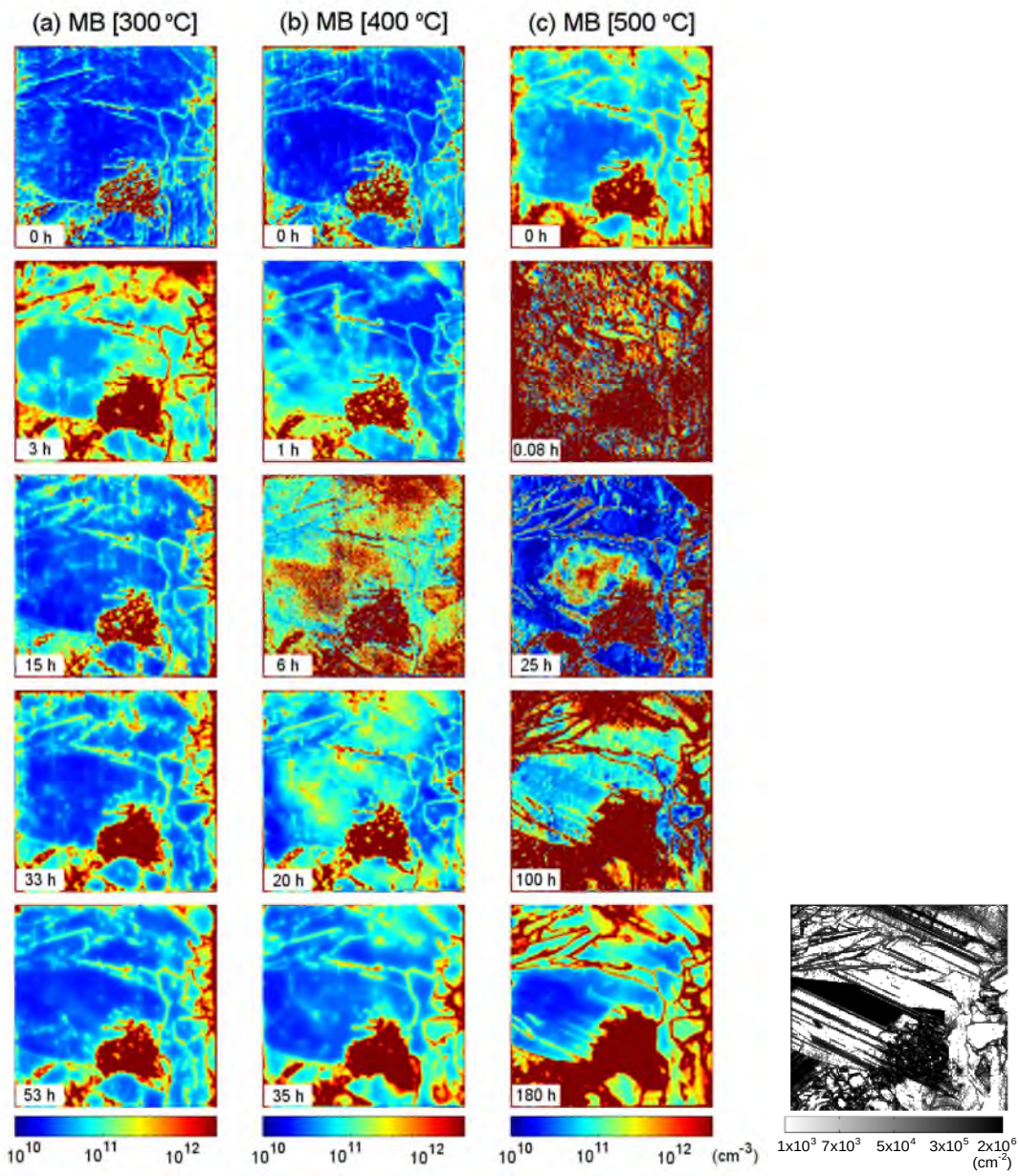

Figure 5.10. Spatial distribution of interstitial iron concentration in the same bottom middle samples (39 mm × 39 mm) used in Figure 5.6. Samples annealed at the temperatures and cumulative times shown. A map of dislocation density of a sister sample is presented in the right column.

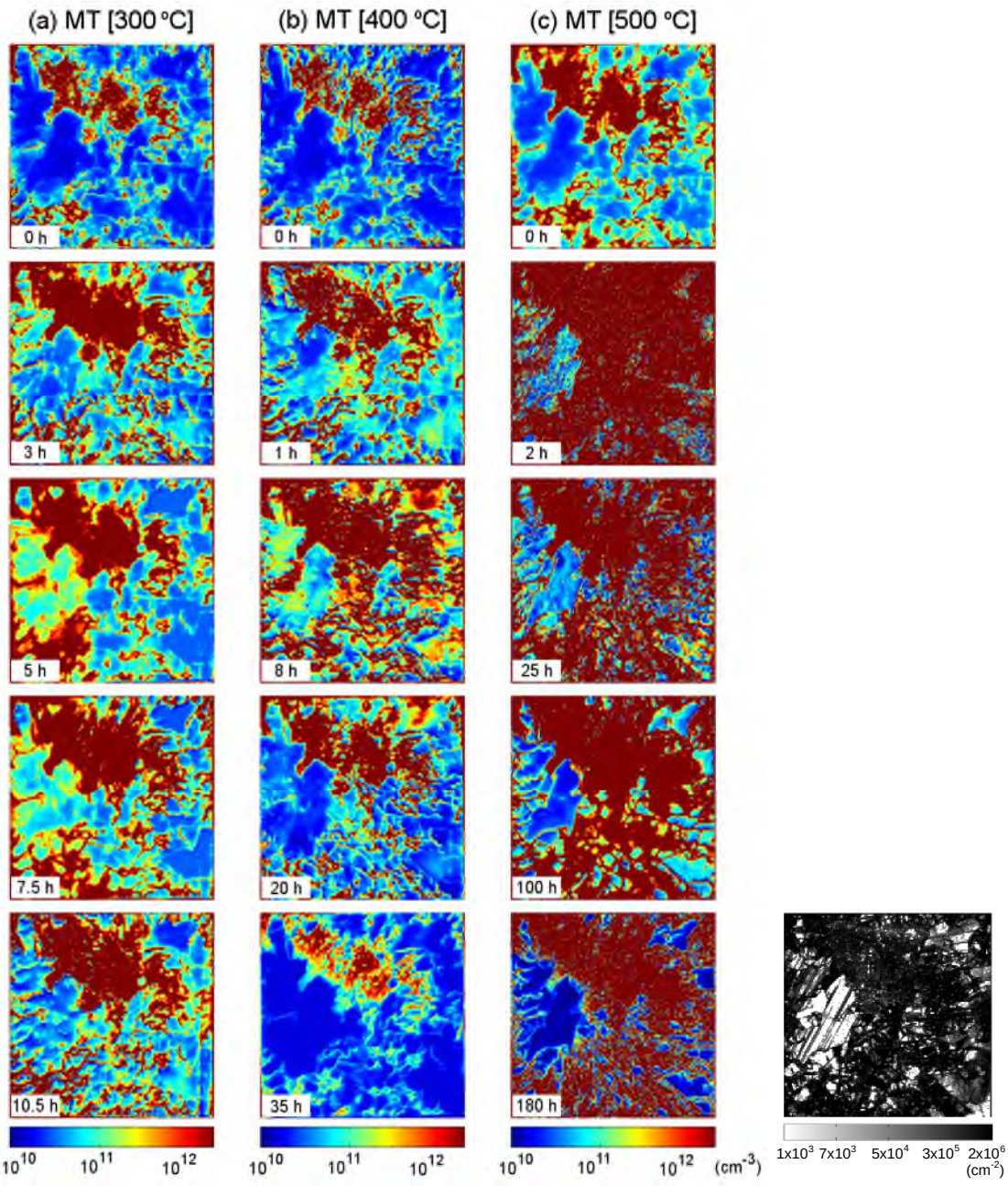

Figure 5.11. Spatial distribution of interstitial iron concentration in the same top middle samples (39 mm × 39 mm) used in Figure 5.7. Samples annealed at the temperatures and cumulative times shown. A map of dislocation density of a sister sample is presented in the right column.

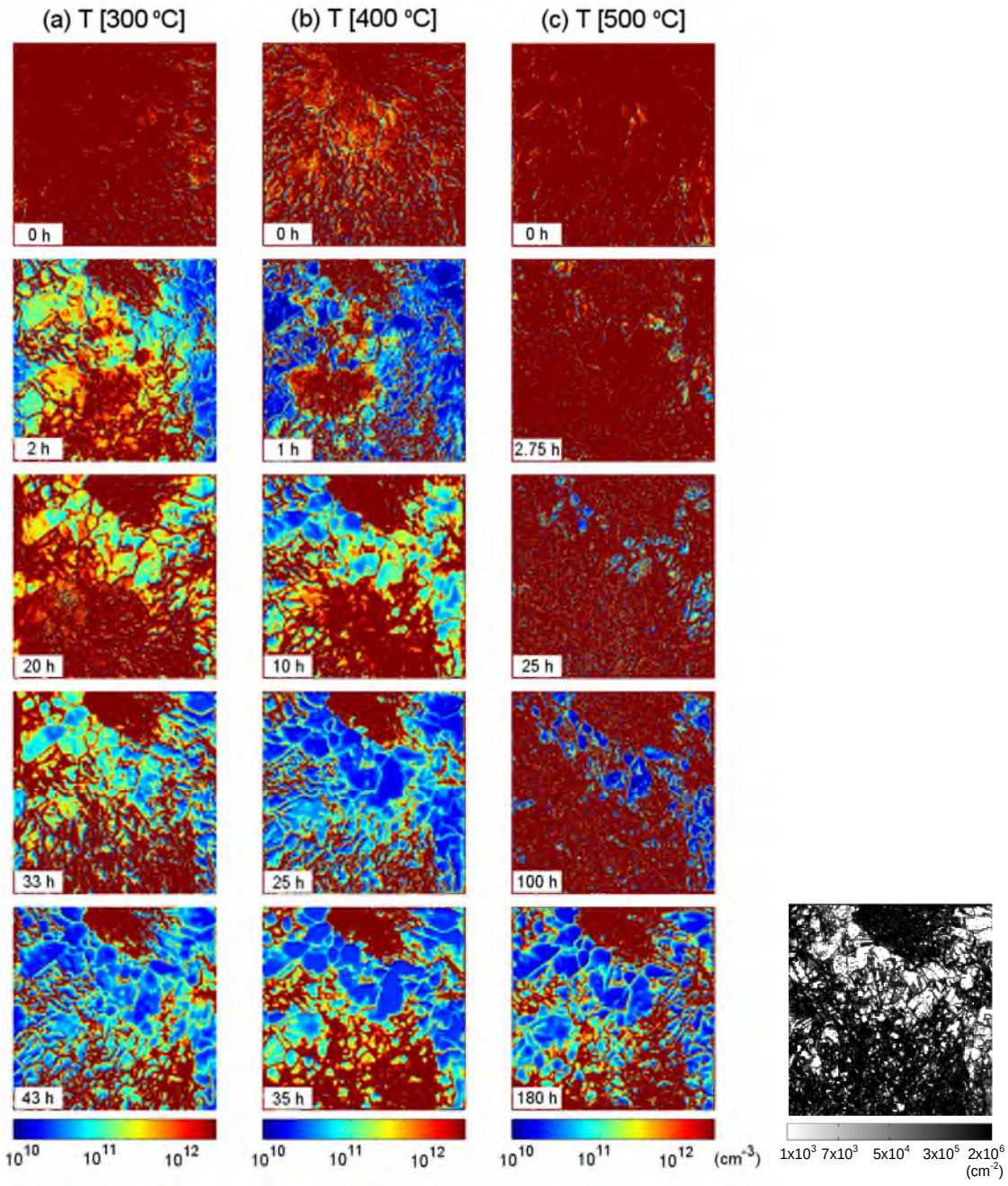

Figure 5.12. Spatial distribution of interstitial iron concentration in the same top samples (39 mm × 39 mm) used in Figure 5.8. Samples annealed at the temperatures and cumulative times shown. A map of dislocation density of a sister sample is presented in the right column.

5.4. Analysis

5.4.1. Correlation of lifetime and interstitial iron changes

The correlation between lifetime change and interstitial iron concentration change may provide evidence for the origin of the lifetime change. Every as-received sample was characterised by bulk lifetime before any annealing, $\tau_{FeB}(0)$, as well as by the as-grown interstitial iron concentration $[Fe_i](0)$. At each cumulative annealing time, *t*, the bulk lifetime with iron in the FeB state, $\tau_{FeB}(t)$, and the interstitial iron concentration, $[Fe_i](t)$ are measured. If the lifetime changes occur solely due to changes in interstitial iron concentrations, it might be expected that the change in normalised recombination rate correlates with the change in normalised interstitial iron concentration according to:

$$\frac{\frac{1}{\tau_{FeB}(t)} - \frac{1}{\tau_{FeB}(0)}}{\frac{1}{\tau_{FeB}(0)}} = A\left(\frac{[Fe_i](t) - [Fe_i](0)}{[Fe_i](0)}\right) \qquad (5.1)$$

where *A* is a proportionality constant.

Figure 5.13 shows plots for the wafers from the bottom, bottom middle, top middle and top parts of the ingot in accordance with Equation 5.1. The diagonal dashed lines represent 1:1 correlation between the normalised recombination rate change and the normalised interstitial iron concentration change. At all temperatures investigated, there is a good 1:1 correlation for samples from the bottom of the ingot. This means that the lifetime change in bottom wafers can be explained mainly by the removal of interstitial iron from the bulk. The error bars for annealing at 500 °C are relatively bigger than the other annealing temperatures and slightly deviate from the 1:1 line. For bottom middle samples, lifetime changes which occur upon low-temperature annealing do not appear to correlate in a simple way with the change in interstitial iron concentration. The correlation is particularly poor for annealing at 500 °C. The same is probably also true at 300 °C and 400 °C, although the change due to defects other than interstitial iron is smaller at these temperatures. The correlation for the top middle samples shows a similar behaviour of the bottom middle samples where it is very poor at 500 °C and shows a scattered relationship. In annealing at 300 °C and 400 °C, the top middle samples show a fairly good relationship. In the top samples, a mixed correlation is observed for all three

annealing temperatures. For annealing at 300 °C and 400 °C, there is a quite good correlation between changes in lifetimes and interstitial iron concentrations. Annealing at 500 °C does show a poor correlation.

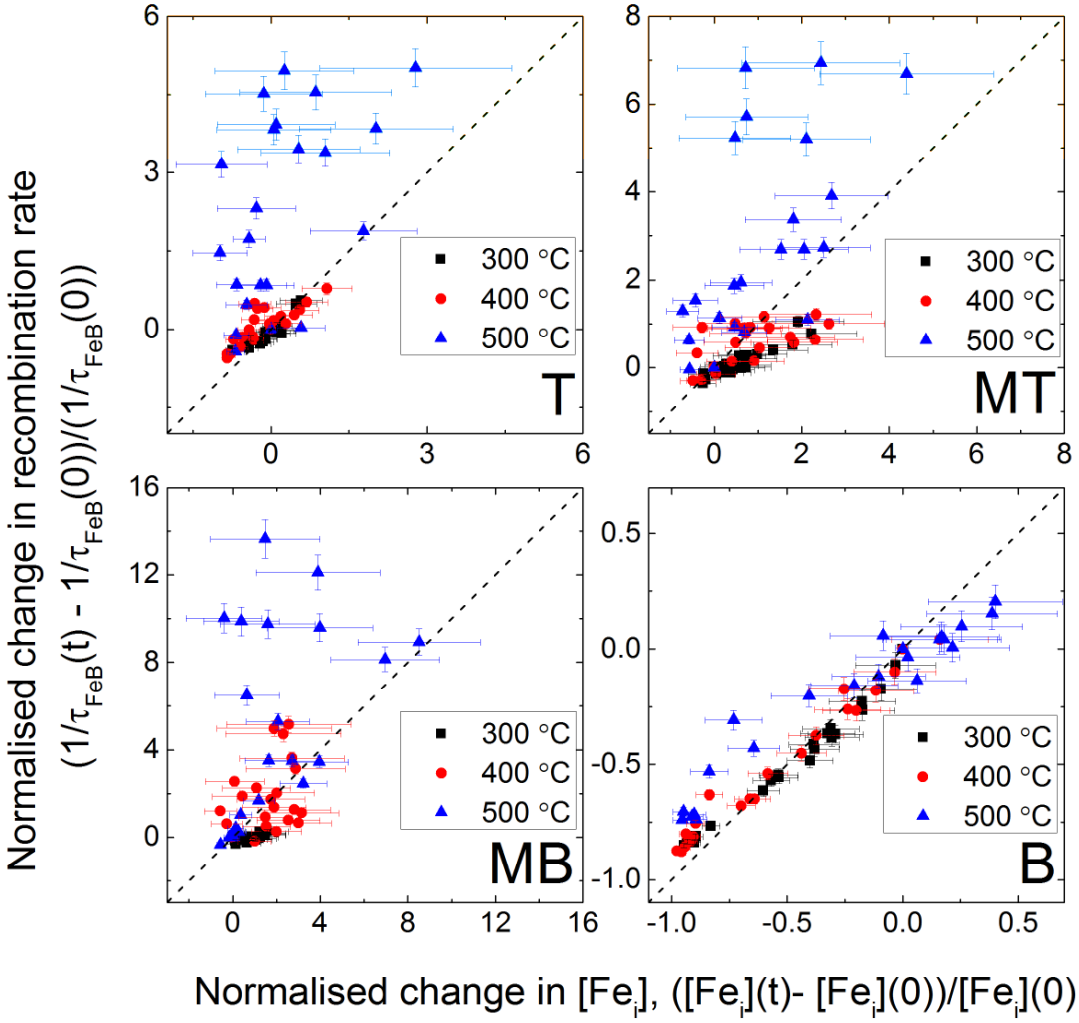

Figure 5.13. Change in recombination rate normalised by as-grown recombination rate versus change in bulk iron concentration normalised by as-grown bulk iron concentration according to Equation 5.1 for samples from the top (T), top middle (MT), bottom middle (MB) and bottom (B) part of the ingot. The dashed lines represent a 1:1 relationship.

5.4.2. Correlation of interstitial iron changes and dislocation density

The spatial distribution of interstitial iron concentration maps is produced at every annealing step. Low-temperature annealing changes interstitial iron concentration distribution substantially in samples from every height position, as presented in previous sections. Dislocation density distribution maps were produced from sister samples from

every height position (presented in Chapter 4 and Figures 5.5 to 5.12). The change in interstitial iron concentration is calculated according to:

$$\Delta[Fe_i] = \left([Fe_i](t) - [Fe_i](0)\right), \tag{5.2}$$

where $[Fe_i](t)$ and $[Fe_i](0)$ are the concentrations after the final annealing step and as-received state, respectively. A correlation between the change in interstitial iron concentration upon annealing at 400 °C and dislocation density is made according to Equation 5.3 and presented in Figure 5.14 for samples from four height positions:

$$\Delta[Fe_i] = A[D], \tag{5.3}$$

where $[D]$ is dislocation density and A is the proportionality constant. For this analysis, results from the annealing at 400 °C are chosen as the largest lifetime improvement is observed (Figure 5.2). Interstitial iron concentration changes have a reasonably good correlation with dislocation density. In general, regions with high dislocation density show relatively high interstitial iron concentration after low-temperature annealing for samples from every height position of the ingot. These data are discussed detail in Section 5.5.

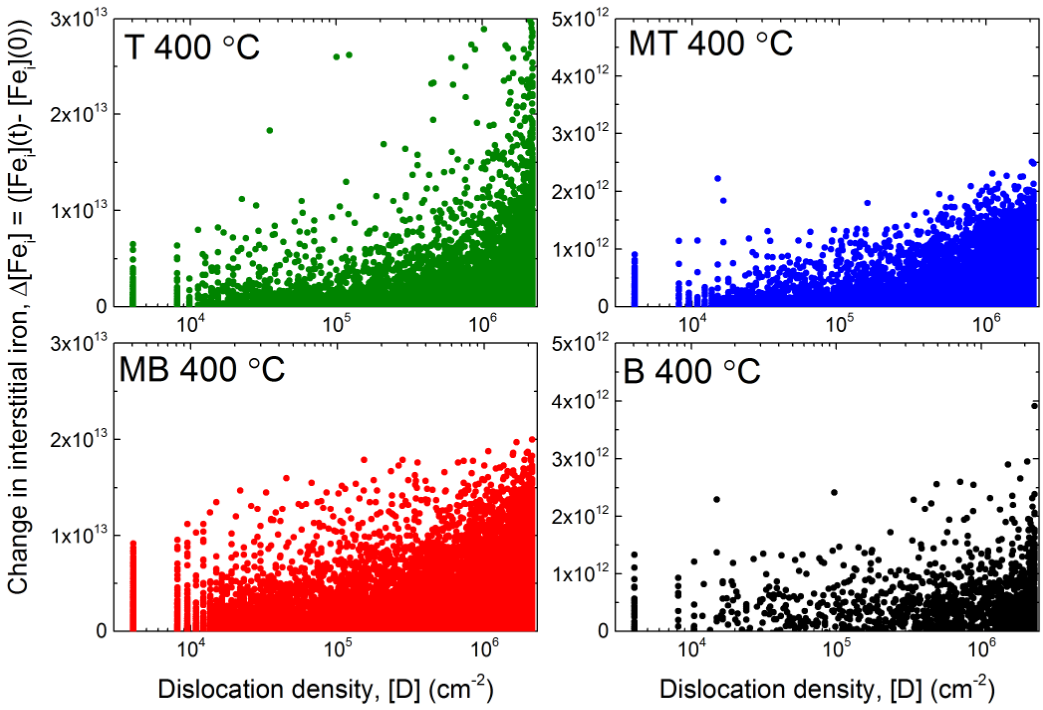

Figure 5.14. Relationship between the change in interstitial iron concentration and dislocation density for samples from four different height positions in the ingot. Samples were annealed at 400 °C for 35 h.

Table 5.1. Summary of starting and final lifetimes and interstitial iron concentration, and their relative values after the final annealing stage. The red or green shading respectively represent a deterioration or improvement in bulk carrier lifetime, or an increase or decrease in the interstitial iron concentration.

Ingot position	Annealing temperature (°C)	Total annealing time (h)	As-grown		After longest time annealing		Improvement in bulk lifetime $\frac{\tau_{FeB}(t_{max})}{\tau_{FeB}(0)}$	Reduction in interstitial iron concentration $\frac{[Fe_i](0)}{[Fe_i](t_{max})}$
			$\tau_{FeB}(0)$ (μs)	$[Fe_i](0)$ ($\times 10^{11}$ cm^{-3})	$\tau_{FeB}(t_{max})$ (μs)	$[Fe_i](t_{max})$ ($\times 10^{11}$ cm^{-3})		
T	300	43	10.4	11.6	17.5	3.0	1.7	3.8
	400	35	12.1	10.1	23.8	2.1	2.0	4.8
	500	180	12.0	7.9	20.9	2.5	1.8	3.2
MT	300	53	24.0	3.7	33.1	3.0	1.4	1.2
	400	35	28.2	2.9	40.5	1.5	1.4	1.9
	500	180	22.6	5.1	9.86	1.4	0.44	3.5
MB	300	53	50.1	1.5	66.4	2.5	1.3	0.60
	400	35	46.5	1.6	56.4	3.1	1.2	0.50
	500	180	48.6	2.4	39.1	3.0	0.80	0.79
B	300	53	4.76	35.0	29.5	3.5	6.2	10.1
	400	35	5.52	28.0	38.7	1.6	7.0	17.3
	500	180	6.61	20.8	25.4	0.96	3.8	21.6

5.5. Discussion

5.5.1. Effect of low-temperature annealing

This study relies on re-passivation at each processing stage using a temporary chemical solution and annealing without surface passivation. Therefore, bulk lifetime values in Chapter 5 are probably not influenced by hydrogenation or changes in surface passivation quality. Previous low-temperature annealing studies tend to report interstitial iron concentration [36, 50], cell efficiency [50, 51], or lifetimes after high-temperature processing [48, 49]. Whilst these all suggest beneficial effects in certain circumstances, this study focuses, for the first time, on the thermal effect of low-temperature annealing on lifetime in as-grown mc-Si. The key findings are discussed in the context of the height position in the ingot.

5.5.1.1 Bottom wafers

The average lifetime in bottom wafers was increased by annealing at all temperatures investigated, as shown in Figure 5.2 and Figure 5.3 and Table 5.1. The largest improvement is at 400 °C when 35 h of cumulative annealing increases the lifetime to ~7 times the as-received value. Annealing at 300 °C and 500 °C gives ultimate improvements of ~ 6 and ~ 4 times.

Figure 5.4 shows an ultimate reduction in the average interstitial iron concentration in bottom wafers. At 300 °C, the iron decays approximately exponentially. At 400 °C, there is a slight initial increase in bulk iron concentration followed by a decay, and at 500 °C, the bulk iron concentration increases for a period before it starts to decay. The annealing time dependence of the interstitial iron concentration is discussed in Section 5.5.3. Figure 5.13 shows the correlation between normalised changes in recombination rate (reciprocal lifetime) and normalised change in interstitial iron concentration, according to Equation 5.1. At all temperatures investigated, there is a good correlation for wafers from the bottom of the ingot. This means that the lifetime change in bottom wafers can be explained mainly by the removal of interstitial iron from the bulk.

Figure 5.5 shows the evolution of the spatially resolved lifetime in the bottom samples annealed at all three temperatures and spatial distribution of dislocation density. In as-

grown samples, the lifetime is initially low in the bulks of the grains and very low at certain grain boundaries and in the vicinity of dislocation clusters. With increasing cumulative annealing time the lifetime improves, particularly in the bulks of the grains. Figure 5.9 also shows substantial changes in the interstitial iron distribution which occur during annealing of the same samples. Initially, the interstitial iron concentration is $>10^{12}$ cm^{-3} throughout the wafer, whereas after 35 h of cumulative annealing it is reduced to be of order 10^{10} cm^{-3} in many regions, with a few regions remaining with higher concentration. The evolution of the spatial distribution of interstitial iron is broadly similar to the observations of Liu and Macdonald [49]. The absence of any *external* gettering layer means it is likely that interstitial iron is gettered to internal features, such as iron-containing precipitates, grain boundaries and dislocations. The kinetics do not exclude the possibility of interstitial iron gettering to the samples' surfaces, although previous work in single crystal silicon suggests this is unlikely [128]. Figure 5.14 shows that an increase in interstitial iron concentration at regions with high dislocation density ($> 10^4$ cm^{-2}) upon annealing at 400 °C for 35 h. In the bulk regions with low dislocation density ($\leq 10^4$ cm^{-2}), the interstitial iron concentration decreases upon annealing compared to the as-received states. This indicates gettering of interstitial iron to the region with high dislocation density upon low-temperature annealing.

5.5.1.2 Middle wafers

Data for the bottom middle (MB) and top middle (MT) samples are discussed together as similar effects are observed in both sample types. In most cases, annealing samples from the middle of the block initially result in a lifetime reduction (Figure 5.2 and 5.3). There is also an initial increase in the interstitial iron concentration (Figure 5.4). With further annealing the lifetime recovers and the interstitial iron concentration reduces. Given sufficient time there are small ultimate lifetime improvements at 300 °C and 400 °C. Annealing at 500 °C results in a very abrupt initial reduction in lifetime. There is a lot of scatter in the data, and it is unclear whether substantial stable improvements are ever realised at 500 °C. In middle wafers, the impact of low-temperature annealing (without bulk hydrogenation effects) at best results in marginal improvements; at worst the lifetime is reduced substantially if the samples are not annealed for sufficient time.

The evolution of the spatial distribution of lifetime in the bottom middle and top middle samples at all three temperatures are shown in Figure 5.6 and Figure 5.7,

respectively. These Figures also show the spatial distribution of dislocation density (presented in Chapter 4). The initial annealing reduces lifetime throughout the wafer. Lifetime then begins to recover in regions where the dislocation density is low. The average lifetime after the last annealing step is lower than the as-grown lifetime. It is notable that the low lifetime regions within the high dislocation-containing areas are much more diffuse (less sharp) after annealing than before. The evolution of interstitial iron concentration distribution in the bottom middle and top middle samples at all three temperatures are shown in Figure 5.10 and Figure 5.11, respectively. The annealing appears to have caused higher interstitial iron concentrations in regions with high dislocation densities than in the as-grown state. The relationship in Figure 5.14 also shows the change in interstitial iron concentration is high in regions with high dislocation density ($> 10^4$ cm^{-2}). Annealing increases recombination associated with certain grain boundary types. Some (but not all) boundary types which exhibited no, or very little, detectable recombination contrast in the as-grown state exhibit stronger recombination contrast. This is presumably because they have gettered impurities from the bulk. This observation is consistent with electron beam induced current (EBIC) studies of Chen *et al.*, which found increased EBIC contrast in samples subjected to slow cooling [65], which will have had similar effects to low-temperature annealing.

For middle samples, lifetime changes which occur upon low-temperature annealing do not appear to correlate in a simple way with the change in interstitial iron concentration (Figure 5.13). The correlation is particularly poor at 500 °C, which was also the case for top samples. Although annealing at 500 °C does affect the interstitial iron concentration (Figure 5.4), it can be concluded that annealing at this temperature must also affect the concentration of another defect or other defects. The same is probably also true at 300 °C and 400 °C, although the change due to defects other than interstitial iron is smaller at these temperatures.

5.5.1.3 Top wafers

Top wafers respond differently to low-temperature annealing compared to bottom wafers. Although lifetime is ultimately increased for all temperatures used, the magnitude of the improvement and also the final lifetime is lower than in annealed bottom wafers (Figure 5.2 and Figure 5.3 and Table 5.1). The largest improvement in lifetime is a factor of ~ 2 occurs upon annealing at 400 °C for 35 h.

The annealing time dependence of lifetime is more complicated in the top wafers compared the bottom wafers. Annealing at 500 °C, lifetime falls substantially from ~ 12 μs to ~ 2 μs within 15 minutes. This is accompanied by a substantial initial increase in interstitial iron concentration to a peak of ~ 3×10^{12} cm^{-3}. The initial impact of the annealing appears to be to release interstitial iron into the bulk from somewhere else in the material, as discussed in Section 5.5.2.

The spatial distribution of lifetime and interstitial iron concentration for the top samples annealed at 300 °, 400 °C and 500 °C are presented in Figure 5.8 and Figure 5.12, respectively. After 1 h of annealing, the lifetime generally decreases slightly, but it recovers and improves with further annealing. The initial decrease in lifetime appears to be due to a lowering of lifetime in the bulk of the grains. This does not correlate with the interstitial iron map which shows the interstitial iron concentration to fall in most parts of the material. This suggests that reconfiguration of a defect other than interstitial iron is responsible for the initial lifetime reduction. With the exception of this initial decrease, for top samples annealed at 300 °C and 400 °C, there is however a quite good correlation between lifetime change and interstitial iron change (Figure 5.13). Lifetime improvements brought on by low-temperature annealing at these temperatures are therefore most likely due to reconfiguration of interstitial iron into a state or complex in which it is less recombination active. The correlation between the change in interstitial iron and dislocation density (Figure 5.14) suggests that interstitial iron is likely to be gettered at regions with high dislocation density (> 10^4 cm^{-2}). The lifetime changes in top samples at 500 °C do not, in general, correlate with the interstitial iron changes in a simple way. This could mean that another impurity is involved at this temperature, or that iron is present in a different state.

It is instructive to compare the lifetime maps with the top dislocation density maps in Figure 5.8. Parts of the sample with relatively low dislocation densities undergo a much larger lifetime improvement upon annealing than those with higher densities. In fact, the regions with very high dislocation densities are found to get slightly worse after annealing. This shows that impurities, including interstitial iron, are internally gettered to regions with high dislocation densities. This is to be expected as dislocations provide low energy sites for the segregation of impurities such as iron [192] and similar results are found after phosphorus diffusion gettering at higher temperatures [35]. The different

response between the top and bottom wafers is therefore probably due to their different microstructures (Figures 5.5 and 5.8). The top wafers have a higher dislocation density on average, and so impurities can segregate to or precipitate at relatively more sites. This gives rise to more recombination sites than in the bottom, in which there are fewer dislocations and hence fewer sites for iron decoration or precipitation. Figure 5.14 shows that the interstitial iron concentration is relatively high in regions with high dislocations ($> 10^4$ cm^{-2}). As suggested by Boulfrad *et al.* [48], it could also be the case that the higher oxygen concentration in the bottom wafers due to the segregation coefficient being greater than unity causes oxide precipitates to form upon low-temperature annealing and act as trapping sites for iron [47, 116]. This explanation is speculative, however.

5.5.2. Interstitial iron increases upon annealing

One of the most surprising findings is that low-temperature annealing causes an initial increase in the interstitial iron concentration. This is surprising because the levels of interstitial iron are supersaturated [18, 127, 128] and hence there is a driving force for iron to come out of solid solution, rather than to enter it. Such an increase did not appear to be observed by Krain *et al.* [36], nor Liu and Macdonald [49]. Iron "bleeding" from iron silicide precipitates in mc-Si material is a well-known phenomenon at processing temperatures ≥ 800 °C [45, 136], and is explained by the increased solid solubility of interstitial iron relative to iron silicide at high temperatures causing the bulk concentration of the interstitial iron to increase. Low-temperature solubility data are not available, but extrapolation of high temperature solubility data for ≥ 800 °C gives ~ 2×10^7 cm^{-3} at 500 °C, and extrapolation of medium temperature solubility data at 600 °C to 800 °C [18, 127, 128] gives ~ 2×10^9 cm^{-3} at 500 °C. The interstitial iron concentration in this experiment increases to ~ 3×10^{12} cm^{-3} at 500 °C, which is at least three (and possibly more than five) orders of magnitude higher than extrapolated solubility trends. It is therefore concluded that the mechanism of iron release at low temperatures is not the same as at high temperatures.

Analysis of the interstitial iron release is most feasible in bottom middle samples, because of their relatively low as-grown concentrations. Peak concentrations of 3.8×10^{11} cm^{-3} at 300 °C, 6.4×10^{11} cm^{-3} at 400 °C, and 2.3×10^{12} cm^{-3} at 500 °C were measured (Figure 5.4). The initial release of interstitial iron into the bulk is, therefore, temperature

dependent, which suggests the involvement of a solubility driven process with respect to a different iron-containing phase or state than for the higher temperature solubility data. As annealing continues, the interstitial iron released is then transformed into a state which is not interstitial iron.

Whilst this experiment is demonstrated that mc-Si can be improved substantially by low-temperature annealing, it is perhaps surprising that the improvement is not even greater. The steady state interstitial iron concentrations after the maximum annealing time (given in Table 5.1) are orders of magnitude higher than extrapolations of the solubility data with respect to an iron silicide phase [18, 127, 128]. It is surprising that this remaining supersaturated interstitial iron is not gettered to iron-containing precipitates, or that new precipitates are nucleated. Understanding how this interstitial iron is apparently trapped in the bulk is an important topic which requires further scientific study.

To investigate possible contamination during the annealing step as a possible alternative explanation for interstitial iron increases, a control experiment was performed using a float-zone *p*-type single crystal silicon sample under an annealing process used in this thesis. The annealing temperature and time were chosen based on the worst scenario in this Chapter where a bottom middle sample was annealed at 500 °C for 7.5 hours and iron concentration was increased by ~1 order of magnitude. At the starting, the experimental sample (*p*-type FZ) has an interstitial iron concentration of 1.6×10^{10} cm^{-3} which decreases to 4×10^{9} cm^{-3} after the annealing process, as presented in Figure 5.15. Note that the final interstitial iron concentration is very close to detection limit and therefore, it has a large error bar. This indicates that the change in the bottom middle, top middle and top samples during low-temperature thermal annealing are independent of the contamination from the annealing tube furnace. This is not surprising, given the low solubility [31, 127] but this was an important possible explanation to check. However, placing a control sample throughout the entire process can provide a better explanation particularly lifetime changes in the middle samples.

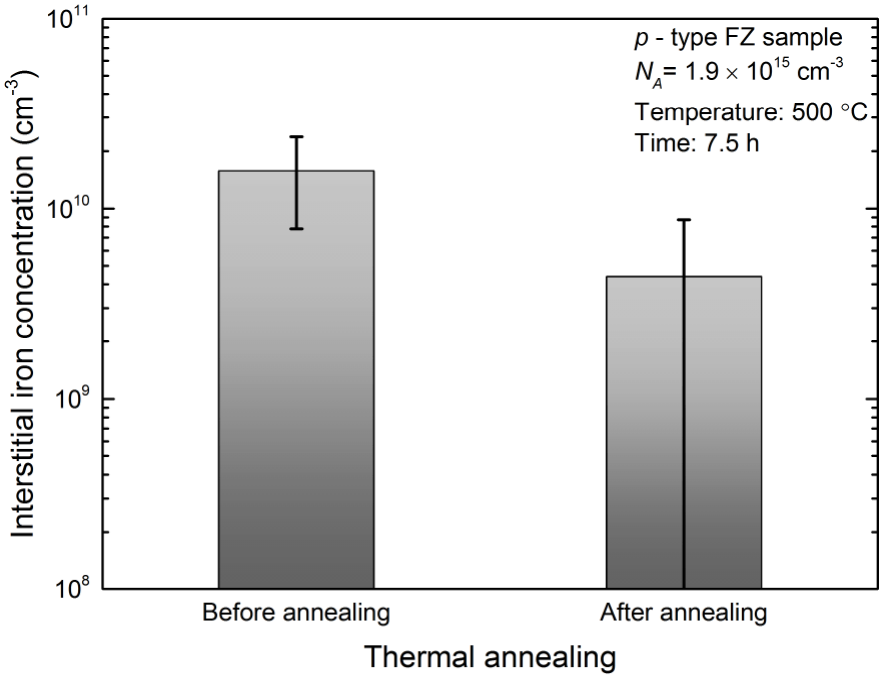

Figure 5.15. A comparison of interstitial iron concentration before and after thermal annealing at 500 °C for 7.5 h on a *p*-type FZ single crystal sample to check for possible furnace contamination.

5.5.3. Kinetics of interstitial iron concentration reduction

The interstitial iron concentration in samples from most of the block did not behave as might be expected from the studies of Krain *et al.* [36], and Liu and Macdonald [49] which found the interstitial iron concentration generally to reduce. However, samples from the bottom of the wafer did show a reduction in interstitial iron concentration. An approximately exponential decay in interstitial iron concentration can be parameterised using:

$$[Fe_i](t) = [Fe_i](t_{max}) + \left([Fe_i](0) - [Fe_i](t_{max})\right)\exp\left(-\frac{t}{\tau_{decay}}\right) \qquad (5.4)$$

where $[Fe_i](t)$ is the iron concentration after cumulative annealing time *t*, $[Fe_i](t_{max})$ is the steady-state iron concentration reached after the maximum cumulative annealing time, $[Fe_i](0)$ is the starting interstitial iron concentration and τ_{decay} is the time constant for the decay in interstitial iron concentration. Overlooking any initial iron increases, fitting the bottom data in Figure 5.4 gives τ_{decay} values of 14 h at 300 °C, 4.0 h at 400 °C and 45 h at 500 °C.

Krain *et al.* found the iron reduction to be dependent on annealing temperature in a way consistent with the temperature dependence of the diffusion coefficient of interstitial iron [36]. Given an activation energy for diffusion of 0.67 eV [18], the diffusivities at 400 °C and 500 °C are respectively expected to be ~ 7.5 times and ~33 times higher than at 300 °C. The values of τ_{decay} are ~ 3.5 times smaller at 400 °C than at 300 °C, and ~ 3.2 larger at 500 °C than at 300 °C. The results in bottom samples are therefore not consistent with the interstitial iron reduction process being controlled only by diffusion of interstitial iron. In samples from other locations, the relationship is even less clear.

Liu and Macdonald also fitted time constants to their interstitial iron decay data, which like this study was performed using sister wafers [49]. For their samples with a starting interstitial iron concentration of 3×10^{12} cm^{-3} (similar to the bottom samples but taken from a similar block position to the bottom middle samples in this thesis) they found values of ~ 20 h at 400 °C, ~ 6.2 h at 500 °C, ~ 7.6 h at 600 °C, and ~ 50.2 h at 700 °C. The absolute values of time constant cannot be compared to these works, due to different microstructures. However, it is noted that Liu and Macdonald also found the rate of iron decay initially to increase with increasing temperature, then to slow down as temperature increased further.

Two key differences between the methodology used in this work and that used by Krain *et al.* [36] may account for the substantial differences between the results. Firstly, they used silicon nitride passivation, which is thought by some to introduce hydrogen into the bulk of the material [137, 138]. A study by Karzel *et al.* compared the effects of a temporary liquid surface passivation scheme (similar, but not identical, to this work) with silicon nitride surface passivation, and found that iron diffusion was affected by the presence of hydrogen from the silicon nitride [137]. Liu and Macdonald found a strong dependence on iron precipitation rate on surface passivation type which they attribute to hydrogen incorporation [49]. Secondly, Krain *et al.* state their samples came from different parts of the ingot [36]. In this work, it is shown that the location within the ingot makes a substantial difference to the behaviour of the interstitial iron concentration, due to substantially different microstructures at the different ingot positions (Figure 5.4 and Section 4.5 in Chapter 4). It is therefore very difficult to assess the impact of microstructure in their work. In summary, this work and that of Liu and Macdonald [49] shows that low-temperature *internal* gettering of interstitial iron is significantly more

complicated than the diffusion-limited model Krain *et al.* [36]. As well as diffusion, the concentration of bulk interstitial iron is influenced by the release of interstitial iron into, and capture of interstitial out of, the bulk.

5.6. Conclusions

A comprehensive study was performed into the effect of low temperature (300 °C to 500 °C) annealing on lifetime and interstitial iron concentration in mc-Si. Sister wafers were sourced from four different height positions with differing microstructures characterised by their dislocation distributions. A temporary liquid iodine-ethanol room temperature passivation scheme was used to minimise unintentional hydrogenation and any thermal effects due to the passivation process, so this experiment shows the effect of thermal processing only.

The results show, for the first time, that low-temperature annealing can dramatically improve the carrier lifetime in multicrystalline silicon materials. Relatively poor samples from the bottom of the block were improved substantially, and the improvement in lifetime correlated with reductions in interstitial iron concentration. The best results were achieved at 400 °C, at which lifetime was increased from 5.5 μs to 38.7 μs by annealing for ~35 h. Smaller improvements were also realised in top wafers, with lifetime increasing from 12.1 μs to 23.8 μs under the same conditions. The smaller improvement in top wafers is attributed to the higher concentration of recombination-active dislocations. The benefit of low-temperature annealing on good wafers from the middle of the block was found to be marginal, with substantial reductions in lifetime initially occurring at 400 °C and 500 °C, followed by a slow recovery.

This work shows that the effect of low-temperature annealing on interstitial iron concentration is much more complicated than found in previous work by Krain *et al.* using silicon nitride passivated samples [36]. Annealing at 300 °C to 500 °C was found initially to release of interstitial iron into the bulk in many cases. It is found that the interstitial iron concentration decay is not determined only by the diffusion of interstitial iron. The lack of correlation with interstitial iron in some cases shows that other defects can also play a role.

In summary, the experiments in this Chapter is demonstrated that low-temperature annealing improves the lifetime mc-Si used in photovoltaics. It has the potential to be a relatively low-cost process for improving red zone wafers, thus enabling the use of more contaminated feedstocks and reducing wastage. Although the annealing times required are fairly long, the conditions required are not dissimilar to those used in the production of some commodity glass products. The key to successful implementation is adding the low-temperature gettering at the correct stage in the production process, as junction formation, surface passivation and firing steps may all affect the distribution of metallic impurities. The effect of different surface passivation schemes in low-temperature annealing is discussed in next Chapter, in an initial attempt to reconcile the findings with those of Krain *et al*. [36].

Chapter 6 Effect of passivation on low-temperature gettering

6.1. Introduction

Low-temperature gettering (≤ 500 °C) using iodine-ethanol passivation in as-grown samples from four different height positions of a mc-Si ingot is discussed in Chapter 5. It has been shown low-temperature annealing in the absence of a dielectric surface passivation film can improve lifetime in relatively poor mc-Si wafers from the bottom and top of ingot by redistribution of impurities. Also, despite the interstitial iron being massively supersaturated at the temperatures used [128], the interstitial iron concentration did not always reduce. In many cases, the impact of low-temperature annealing was to increase the measured interstitial iron concentration, and the interstitial iron changes in sister samples with near identical microstructures did not exhibit a simple temperature-dependence behaviour. The findings were in stark contrast to a previous similar study by Krain *et al*. which used silicon nitride surface passivation on samples from different height positions of the block [36]. In their study, a systematic reduction in the interstitial iron concentration was found and the activation energy for this process was consistent with that for the diffusion of interstitial iron [18]. Part of the change is believed to arise from *internal* gettering of metallic impurities, but additional effects result from the process used to passivate the surfaces for lifetime measurement. This Chapter aims to address this apparent conflict and to further the understanding of the initial lifetime reduction.

Why might the surface passivation treatment be a relevant issue for low-temperature gettering? Silicon nitride (SiN_x) films deposited by plasma-enhanced chemical vapour deposition (PECVD) at temperatures around 300 °C to 425 °C are hydrogen rich [178, 197]. There is clear direct evidence for hydrogen entering the bulk from SiN_x films after annealing at temperatures considerably higher than the deposition temperature. For instance, very short (~1 min) post-deposition annealing at 750 °C gives rise to the formation of platinum-hydrogen complexes [197] and deuterium trapped at oxide precipitates is detected by secondary ion mass spectrometry (SIMS) in samples with deuterated SiN_x fired at 800 °C [204]. At lower temperatures, direct evidence of bulk hydrogenation is difficult to obtain due to the lower concentrations involved. However, if hydrogenation does also occur at these temperatures, it could affect both lifetime and *internal* gettering of interstitial iron. Furthermore, the possibility of *external* gettering during the long low-temperature annealing procedure should not be excluded. Rinio *et al.*'s study on partially-processed cells concluded that *external* gettering to the emitter was responsible for most of the improvement observed [51]. A recent study by Liu *et al.* has also found iron to be segregated evenly within PECVD SiN_x films on the surface of iron-contaminated single-crystal silicon which has been annealed at 700 °C [160].

Several studies using photoconductance lifetime methods have found that the low-temperature behaviour of iron in silicon depends on the surface passivation scheme used [49, 137, 138, 207]. It is frequently suggested, although not explicitly proven, that this is due to hydrogenation of the bulk from the dielectric. Liu *et al.* compare the effects of SiO_2, Al_2O_3 and SiN_x passivation on the iron concentration decay kinetics, and find the decay kinetics depend on passivation type [49, 138]. Their results suggest that no or very little hydrogenation occurs from the SiO_2, some hydrogen in-diffuses from the Al_2O_3 and substantial hydrogenation occurs from the SiN_x. Other results reported by Karzel *et al.* compare a room temperature quinhydrone-methanol treatment with SiN_x, with the latter introducing hydrogen into the bulk which influences the behaviour of interstitial iron [137]. Hydrogenation control in mc-Si is very important, and recent work has shown that it is possible to manipulate the hydrogen charge state [205, 207] as a route to higher lifetimes in PV substrates.

In this Chapter, a comprehensive study which aims to assess the role of surface passivation on low-temperature annealing experiments for samples from different height positions in a mc-Si ingot is presented and discussed. Sister samples from each location are passivated with PECVD SiN_x and annealed 300 °C to 500 °C. The starting lifetime

and the interstitial iron concentration of the samples used in this study are discussed in Chapter 4. Lifetime and interstitial iron concentration are measured at every annealing step with bulk lifetime measurements and with photoluminescence (PL) imaging. Secondary ion mass spectrometry (SIMS) is used to measure the iron distribution in the SiN_x films in certain samples after annealing. The data are compared with the low-temperature gettering using a temporary iodine-ethanol passivation scheme discussed in Chapter 5 to assess the impact of possible hydrogenation from and gettering to the SiN_x film.

6.2. Experimental methods

6.2.1. Sample selection

Samples were chosen from four different height positions, as shown in Figure 3.2 in Chapter 3. Resistivities were in the range of 4.8 Ω cm to 11.5 Ω cm. A single crystal Cz silicon wafer with a resistivity of 8 Ω cm and a thickness of 740 μm was used for control purposes. Adjacent samples from every height position were polished using a planar etch solution (described in Section 3.5.2 in Chapter 3), passivated with PECVD silicon nitride and iodine-ethanol, respectively. The details of passivation processes are described in Section 3.6 in Chapter 3. Sister samples from subsequent wafers with near-identical microstructures were selected for annealing at different temperatures. Dislocation density maps for I-E passivated samples have been discussed previously in Chapters 4 and 5 and also published in Ref. [53]. The dislocation density distributions are typical of those found in mc-Si, being highest at the top, and lowest at the bottom [53].

6.2.2. Surface passivation and lifetime measurement

Lifetime and interstitial iron concentration were measured at every annealing step by following the method described in Sections 3.8 and 3.9 in Chapter 3, respectively. For some purposes in this Chapter, the effective lifetime due to recombination other than FeB pairs in the bulk (τ_{other}) was used which is determined according to:

$$\tau_{other} = \left(\frac{1}{\tau_{effective}} - \frac{1}{\tau_{FeB}} \right)^{-1} \quad (6.1)$$

where $\tau_{effective}$ is the effective lifetime with the iron in FeB states, τ_{FeB} (the lifetime due to recombination at FeB pairs) at each step using the Shockley-Read-Hall recombination parameters for FeB of Rein and Glunz [15]. The spatially resolved lifetime images with bulk iron in the FeB and Fe_i state were measured using a BT Imaging LIS-L1 PL imaging tool at each annealing step. A detail of the PL imaging tool is described in Section 3.8.3 in Chapter 3. The spatial distributions of interstitial iron concentration were also produced at every annealing step, described in Section 3.9.2 in Chapter 3.

6.2.3. Low-temperature annealing

Three sister samples from every height position were annealed at 300 °C, 400 °C and 500 °C under nitrogen ambient. Silicon nitride passivation remains on the samples during annealing whereas I-E passivation was removed with an RCA prior to the annealing steps. Samples in both the passivation methods were subjected to identical annealing and cooling treatments, as annealing and removal were performed simultaneously. Samples were then stored in the dark for ≥ 36 h to ensure complete re-association of FeB defects [97]. A summary of the process sequence is presented in Figure 6.1.

6.2.4. SIMS iron measurements

After the final annealing step, SIMS was performed through the SiN_x film and into the bulk of the three annealed bottom samples. Measurements were performed by EAG Laboratories (Sunnyvale, CA, USA) on a commercial basis. The measurement depth resolution was < 1.5 nm/step, although the actual resolution was limited by the mixing of bombarded ions during SIMS measurements. Data were collected from a circular area with a diameter of ~ 60 μm. The detection limit for iron was ~ 4×10^{14} cm^{-3}. Silicon was monitored as a marker species with its secondary ion intensity qualitatively measured, which served to distinguish the locations of SiN_x and the Si bulk in the depth profiles. The depth was calibrated using the known thickness of the SiN_x film.

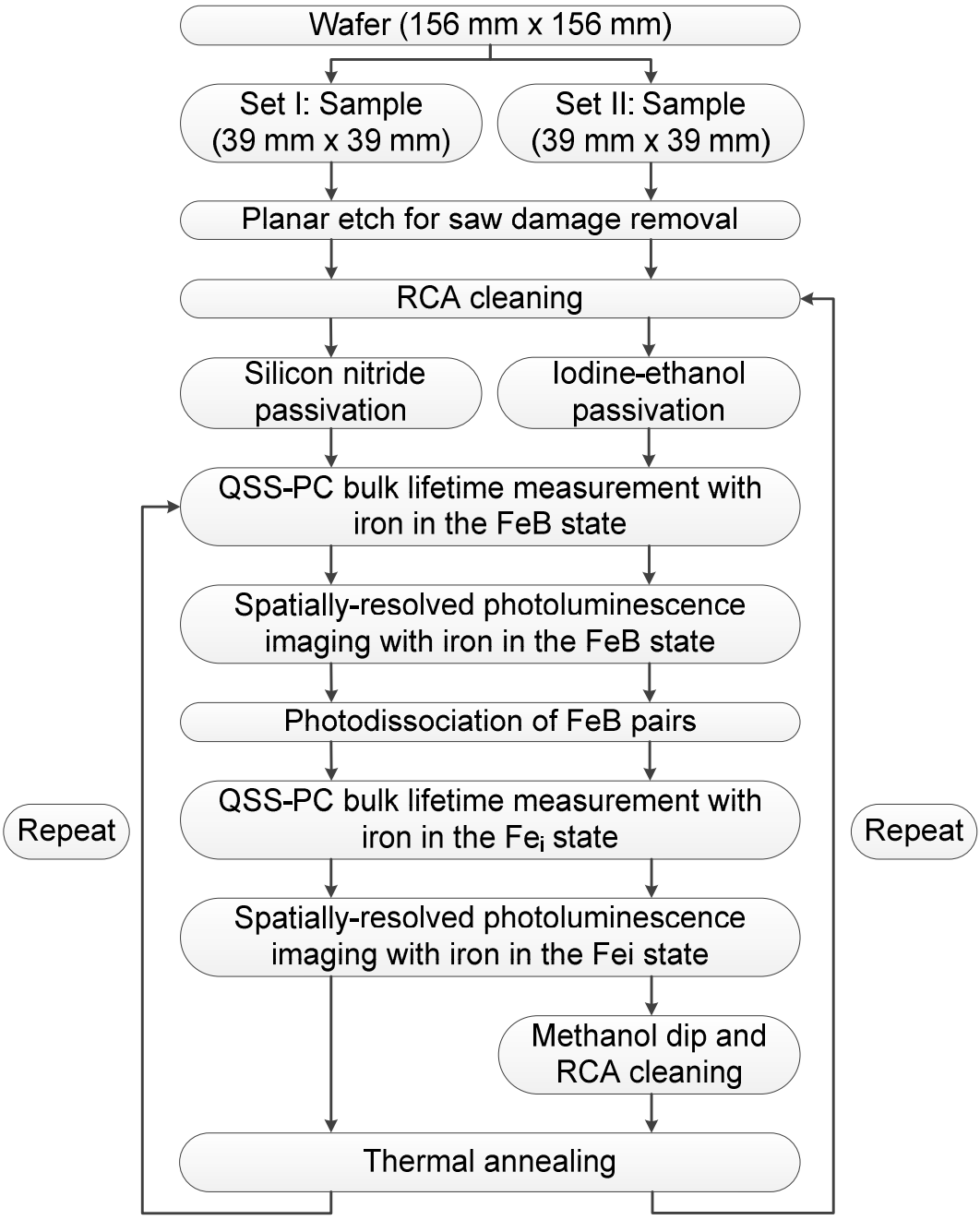

Figure 6.1. The processing and characterisation sequence for the low-temperature gettering experiments. Details of every process step are described in Chapter 3.

6.3. Results

6.3.1. Lifetime in control samples

In this Chapter, low-temperature annealing was performed with silicon nitride (SiN_x) passivation and compared with the results with iodine-ethanol (I-E) passivation which is

discussed in Chapter 5. It is, therefore, important to compare an effective lifetime for SiN_x and I-E passivation in a control sample. Figure 6.2 shows the injection dependence of lifetime in the Cz silicon control samples taken from the same wafer, which has a similar doping level to the mc-Si samples studied. The lifetime at $\Delta n = 1 \times 10^{15}$ cm^{-3} is 433 μs with SiN_x passivation and 528 μs with I-E passivation. On the assumption that the bulk lifetime is same in both samples after passivation, any difference would be due to different surface recombination velocities. Under this assumption, the surface recombination velocity would be 22% higher in the silicon nitride case. It is not possible to give an absolute value for the surface recombination velocity partly because an assumption of near infinite bulk lifetime in the control is not satisfied. Previous work with the same silicon nitride passivation scheme on 670 μm thick samples (similar doping, same injection) gives effective lifetimes up to 3.1 ms [188]. This puts an upper limit on the surface recombination velocity at around 11 cm/s for the silicon nitride scheme used here. A value for iodine-ethanol lower than this would be consistent with the literature [208].

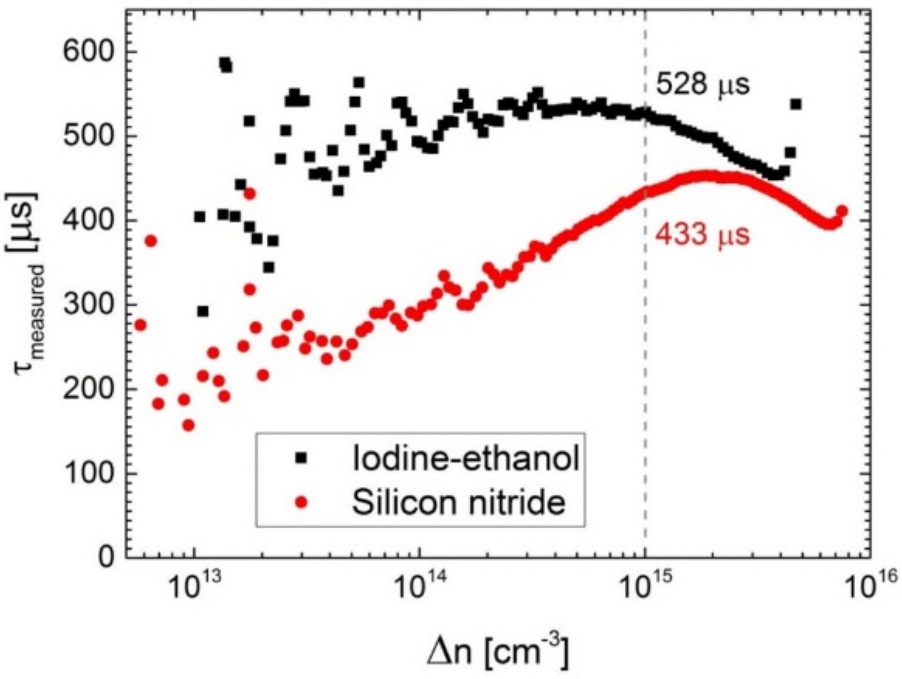

Figure 6.2. Injection-dependent lifetime with iron in the FeB state in samples from the same *p*-type Cz single crystal silicon control wafer (740 μm thick; 1.2×10^{15} cm^{-3} boron) with different passivation schemes. The vertical dashed line and stated values are at $\Delta n = 10^{15}$ cm^{-3}, as used for subsequent measurements on mc-Si.

6.3.2. Bulk lifetime and interstitial iron in SiN_x passivated samples

Bulk lifetime data (with iron in the FeB state) and average interstitial iron concentration for samples from different height positions with SiN_x passivation are plotted as a function of annealing temperature and time in Figure 6.3 and Figure 6.4, respectively. The ultimate effect of low-temperature annealing is also summarised in Table 6.1. Data are presented for sister samples at each position were annealed at either 300 °C, 400 °C or 500 °C for the cumulative annealing time shown. The values of τ_{other} in the as-received samples with both passivation types are also given in Table 6.1. The as-received lifetime and interstitial iron concentrations values vary substantially with ingot height position (discussed in Chapter 4), represented by a horizontal dashed line on each graph, so the effects of annealing are clearly visible. The changes in lifetime and interstitial iron concentration are complex and strongly depend on sample position in the ingot and annealing temperature.

6.3.2.1 Bottom wafers

The as-received bottom samples have lowest average bulk lifetime 7.7 ± 1.8 μs. The changes in the bulk lifetimes are presented in Figure 6.3 (bottom row). Lifetime increases substantially at all three annealing temperatures and exhibits the most straightforward time dependence improvement in lifetime compared to the other parts of the ingot. The largest improvement is a factor of ~ 3.8, observed upon annealing at 500 °C for 60 h. Annealing at 400 °C and 300 °C give an ultimate improvement of ~ 2.7 and ~ 1.6 times, respectively.

The as-received bottom samples exhibit the highest interstitial iron concentration 2.2 × 10^{12} ± 2.9 × 10^{11} cm^{-3}. The evolution of interstitial iron concentration for bottom samples in low-temperature annealing is presented in Figure 6.4 (bottom row). In all three annealing temperatures, the interstitial iron concentration decays approximately exponentially. In annealing at 400 °C and 500 °C, the ultimate reduction in iron concentration is almost ~ 0.6 orders of magnitude compared to the as-received value. Annealing at 300 °C for 33 h gives the largest reduction in iron concentration by ~ 1.3 order of magnitude. A correlation between the change in lifetime and recombination rate is discussed in Section 6.4.

The evolution of the spatial distribution of lifetime and interstitial iron concentration with SiN_x passivation in the bottom sample annealed at 400 °C are presented in Figure 6.7(b) and 6.9(b), respectively. Initial lifetime is low in most of the bulk regions and begins to increase with the annealing time. The regions with relatively high crystallographic defects exhibit overall very little, perhaps no improvement after the longest cumulative annealing period. The interstitial iron concentration is very high (> 10^{12} cm^{-3}) mainly in the defective regions. Interstitial iron concentration decreases to ≤ 10^{10} cm^{-3} in most of the bulk grain regions and defective regions become worse with annealing.

6.3.2.2 Middle wafers

The bottom middle (MB) and top middle (MT) samples with silicon nitride passivation (SiN_x) are discussed together as they exhibit similar behaviour upon low-temperature annealing. The as-received lifetimes are 113 ± 2 μs and 46 ± 5 μs for the bottom middle and top middle samples respectively represented by dashed horizontal lines in Figure 6.3 (second and third rows). Upon annealing at 300 °C, lifetime remains almost unchanged compared to the as-received status in MB sample and increases slightly in the MT sample. The largest improvement in lifetime is observed in both the MB and MT samples annealed at 400 °C. In the MB and MT samples, lifetime increases to ~ 165 μs and ~ 65 μs respectively in the first ~ 5 h of cumulative annealing period and remain almost constant upon further annealing.

The evolution of interstitial iron concentration in low-temperature annealing for the middle samples (MB and MT) is presented in Figure 6.4 (second and third rows). The as-received values are represented as dashed lines on every graph and also discussed in Chapter 4. The interstitial iron concentration decreases substantially upon annealing at 300 °C and 400 °C. The largest reduction is 1.8 orders of magnitude in the MB sample upon annealing at 400 °C. Note that no initial increase in interstitial iron concentration is observed upon annealing at 400 °C. Annealing at 500 °C increases interstitial iron concentration in the primary steps and reduces in longer annealing steps. For example, in the MB sample, interstitial iron concentration increases from 3×10^{10} cm^{-3} to 1.7×10^{11} cm^{-3} in first 1.25 h of annealing at 500 °C and then decreases to 6.9×10^{10} cm^{-3} after 60 h.

However, there is a lot of scatter in the data and it is not clear whether there is an overall reduction in interstitial iron concentration compared to as-received values or not.

The evolution of the spatial distributions of lifetime and interstitial iron concentration at 400 °C for a bottom middle sample (Figure 6.7(d) and 6.9(d)) and a top middle sample (Figure 6.8(d) and 6.10(d)) are shown. In both the samples, lifetime is relatively high in most of the bulk grain regions in the as-received state compared to the samples from extrema of the ingot. Lifetime increases substantially in most of the bulk grains with annealing period in both the samples. The interstitial iron concentration was initially high in most of the regions ($\geq 10^{11}$ cm^{-3}) and decreases with annealing at 400 °C.

6.3.2.3 Top wafers

Figure 6.3 (top row) shows as-received lifetime and changes in a low-temperature annealing with SiN_x passivation for top samples. The average as-received lifetime (16.3 ± 1 μs) is higher than the values in the bottom samples. Annealing at both 300 °C and 400 °C, lifetime improves substantially to ~ 23 μs after the final annealing step. Upon annealing at 500 °C, lifetime decreases abruptly in initial annealing steps and recovers on further annealing. Upon annealing at 500 °C, there is a lot of scatter data and it is unclear whether substantial stable improvements are ever realised. The interstitial iron concentration in Figure 6.4 (top row) decreases upon both the annealing at 300 °C and 400 °C by ~ 1 and ~ 0.4 order of magnitude compared to the as-received values. Upon annealing at 500 ° C, the interstitial iron concentration initially increases from 5×10^{11} cm^{-3} to ~ 9×10^{11} cm^{-3} and reduces with further annealing steps.

Spatially resolved lifetime (with iron in the FeB state) and interstitial iron maps for a top sample annealed at 400 °C are presented in Figure 6.8(b) and 6.10(b), respectively. Initially, lifetime was relatively high in the bulks of some grain regions and low in the grain boundaries and defect cluster regions. Lifetime is likely to be unchanged with annealing time in contrast to the improvement in bulk lifetime. Note that the injection level used in lifetime imaging is lower than the bulk lifetime measurement (Figure 6.4). A relatively small improvement is observed at low injection level (*e.g.* 5×10^{13} cm^{-3}). The interstitial iron concentration is low in the bulk grain regions and high in the grain boundaries and defective regions. Upon annealing at 400 °C for 25 h, interstitial iron

concentration reduces in some grain regions whereas it remains same or increases in the regions with defect cluster.

6.3.3. SiN_x versus I-E passivation in low-temperature annealing

A comprehensive study on low-temperature gettering effect using iodine-ethanol (I-E) for samples from four different height positions is discussed in Chapter 5 and also published as Ref. [53]. Figure 6.5 shows a comparison in lifetime normalised to the starting value for SiN_x and I-E passivated samples is for samples for all height positions annealed at 300 °C, 400 °C or 500 °C for the cumulative time period shown. Figure 6.6 shows the corresponding interstitial iron comparison between SiN_x and I-E passivated samples.

Spatially resolved lifetime images with iron in the form of FeB pairs and interstitial iron concentration maps for the samples annealed at 400 °C from all height positions with SiN_x and I-E passivation are compared for selected annealing times upon annealing at 400 °C. Figures 6.7 and 6.8 show lifetime images with iron in the FeB state. Maps of the interstitial iron concentration distribution for the same conditions are shown in Figures 6.9 and 6.10. These comparisons are discussed details in later sections.

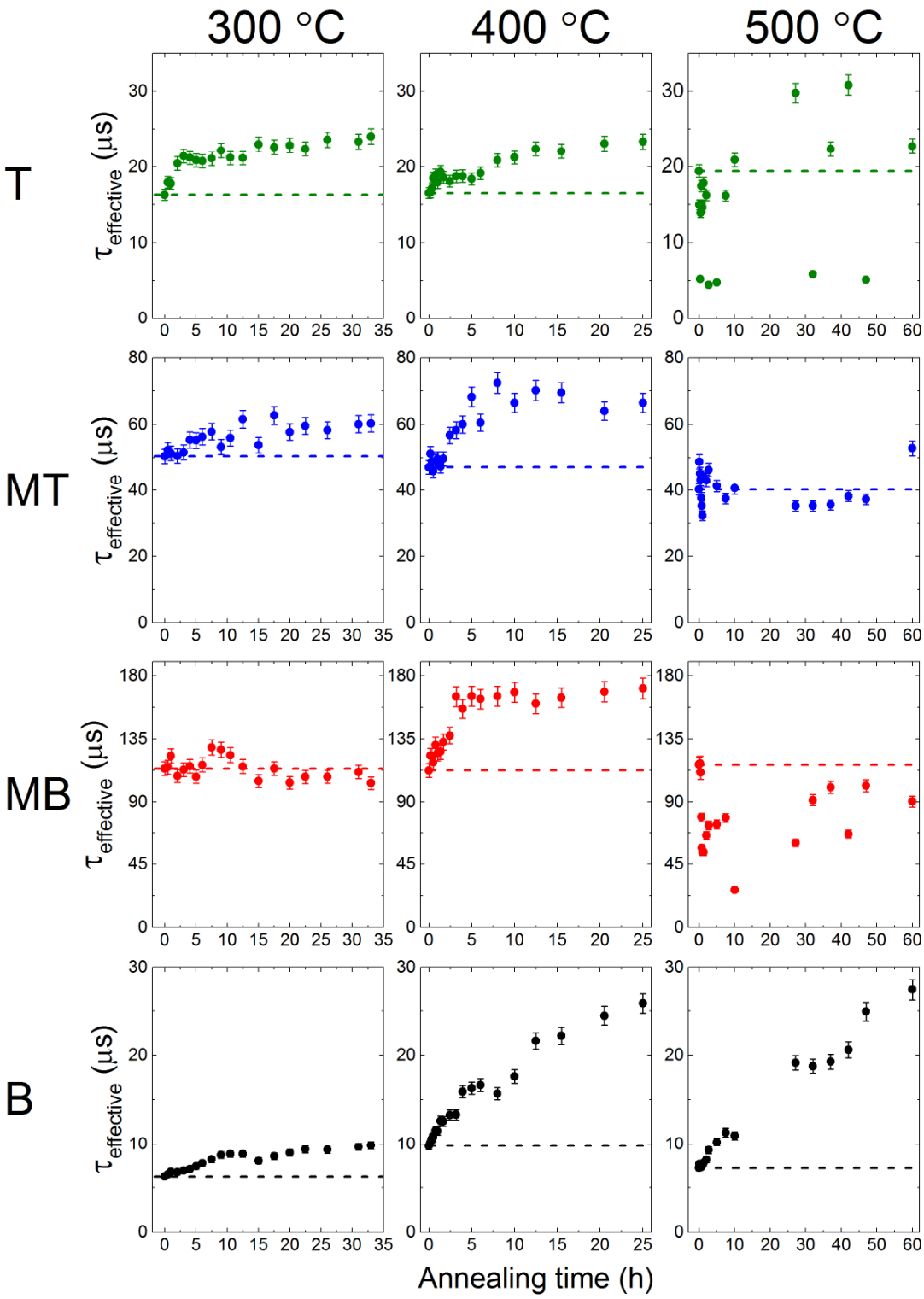

Figure 6.3. Effective carrier lifetime (with iron in the FeB state) in the samples with silicon nitride surface passivation measured by QSS-PC at an injection level of 1×10^{15} cm^{-3}. Samples were sourced from the top (T), top middle (MT), bottom middle (MB) and bottom (B) of the ingot. Sister samples were annealed at 300 °C, 400 °C and 500 °C for the cumulative annealing time plotted. The dashed lines represent the initial values.

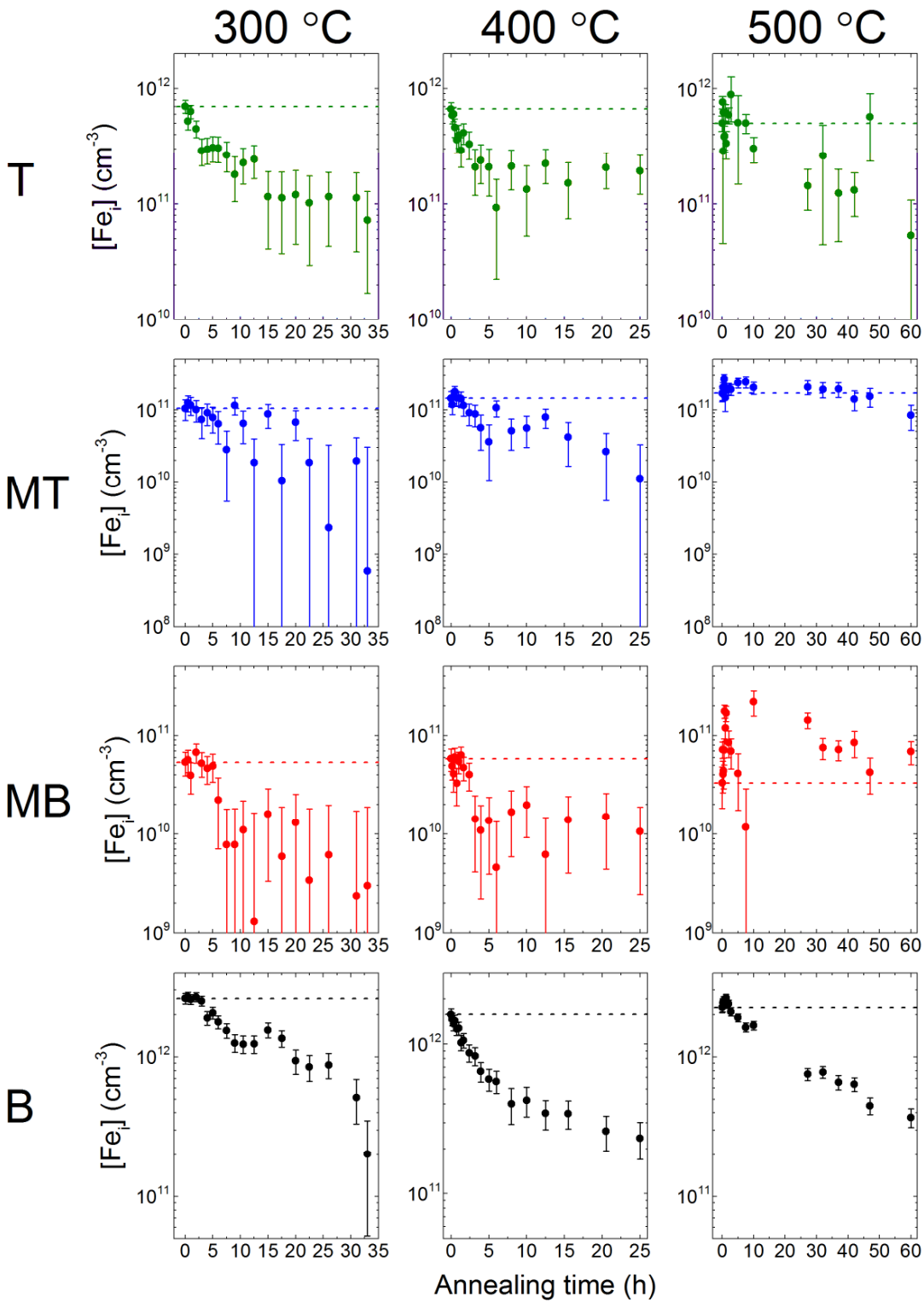

Figure 6.4. Bulk interstitial iron concentration ([Fe_i]) in the samples with silicon nitride (SiN_x) passivation measured at an injection level of 1×10^{15} cm^{-3}. Samples were sourced from the top (T), top middle (MT), bottom middle (MB) and bottom (B) of the ingot. Sister samples were annealed at 300 °C, 400 °C and 500 °C for the cumulative annealing time plotted. The dashed lines represent the initial values.

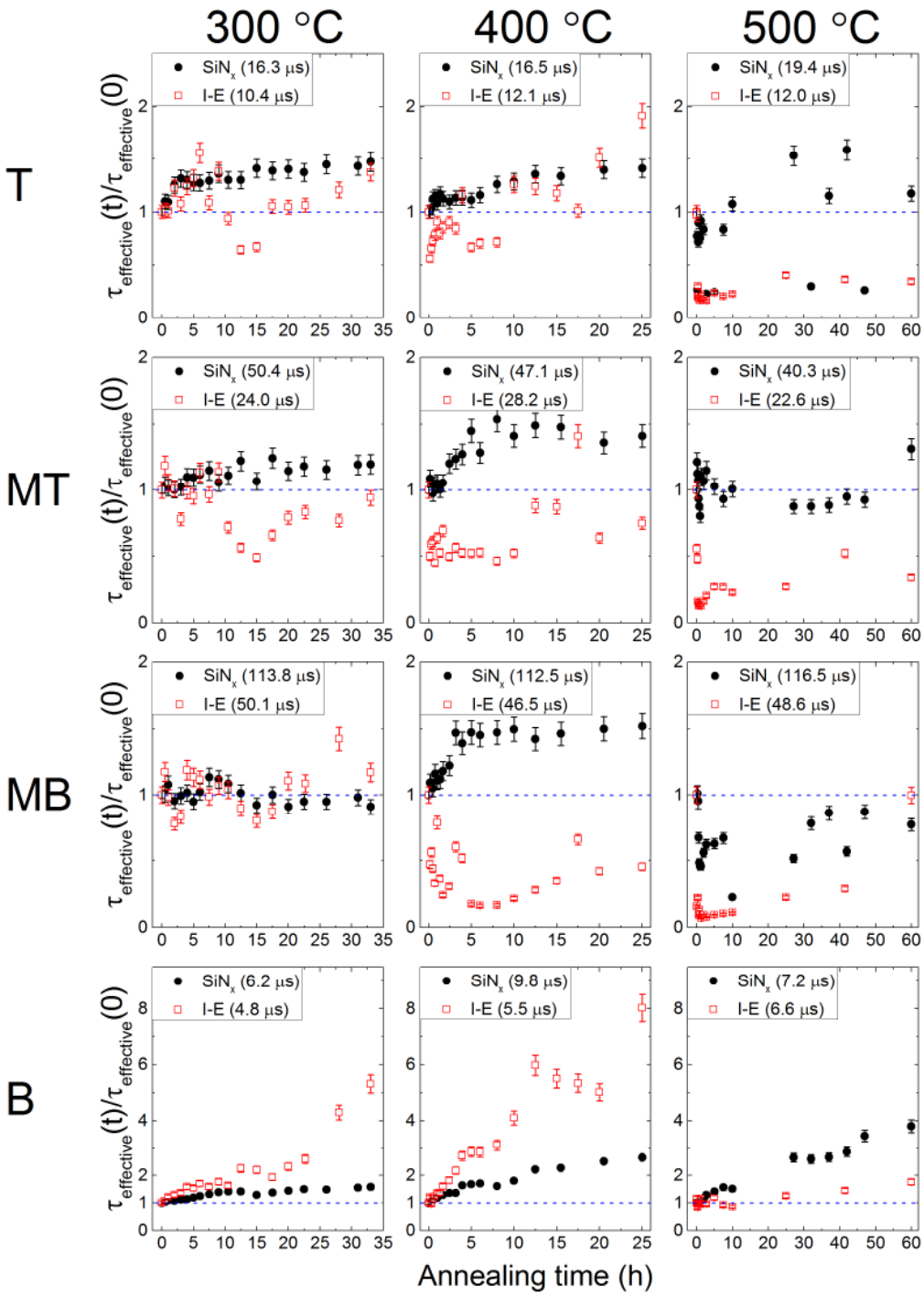

Figure 6.5. Comparison in normalised lifetime with iron in the FeB state for the samples from the top (T), top middle (MT), bottom middle (MB) and bottom (B) of the ingot with silicon nitride (SiN_x) and iodine-ethanol (I-E) passivation. Sister samples from every height positions were annealed at 300 °C, 400 °C and 500 °C for the cumulative annealing time plotted. The lifetimes were measured at an injection level of 1×10^{15} cm^{-3}. The values in the brackets represent the as-grown lifetime. The dashed lines represent the as-grown states.

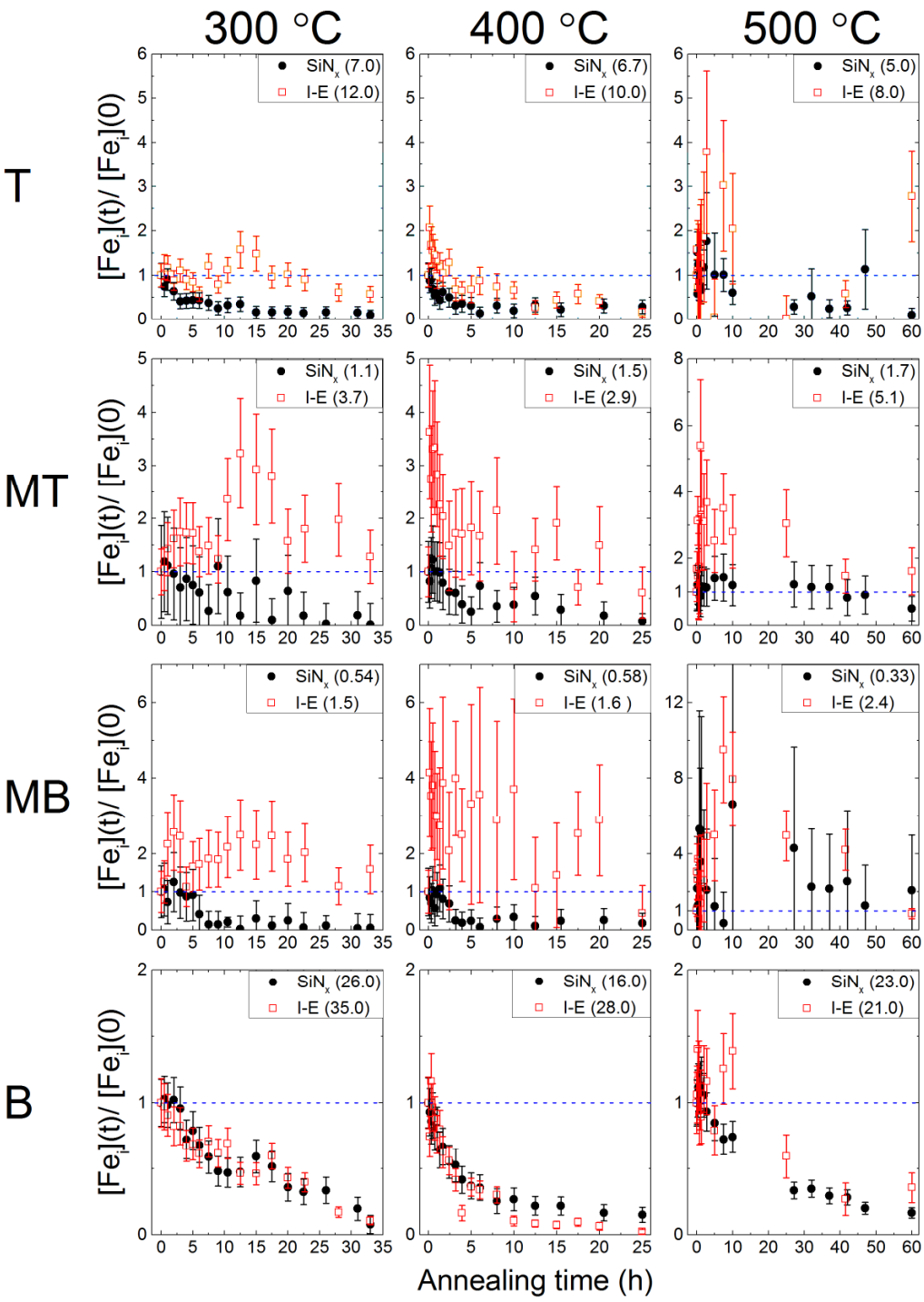

Figure 6.6. Comparison in normalised interstitial iron concentration for samples from the top (T), top middle (MT), bottom middle (MB) and bottom (B) of the ingot with silicon nitride (SiN_x) and iodine-ethanol (I-E) passivation. Sister samples were annealed at 300 °C, 400 °C and 500 °C for the cumulative annealing time plotted. The values in the brackets are the interstitial iron concentrations ($\times 10^{11}$ cm^{-3}) for as-grown samples. The dashed lines represent the starting states.

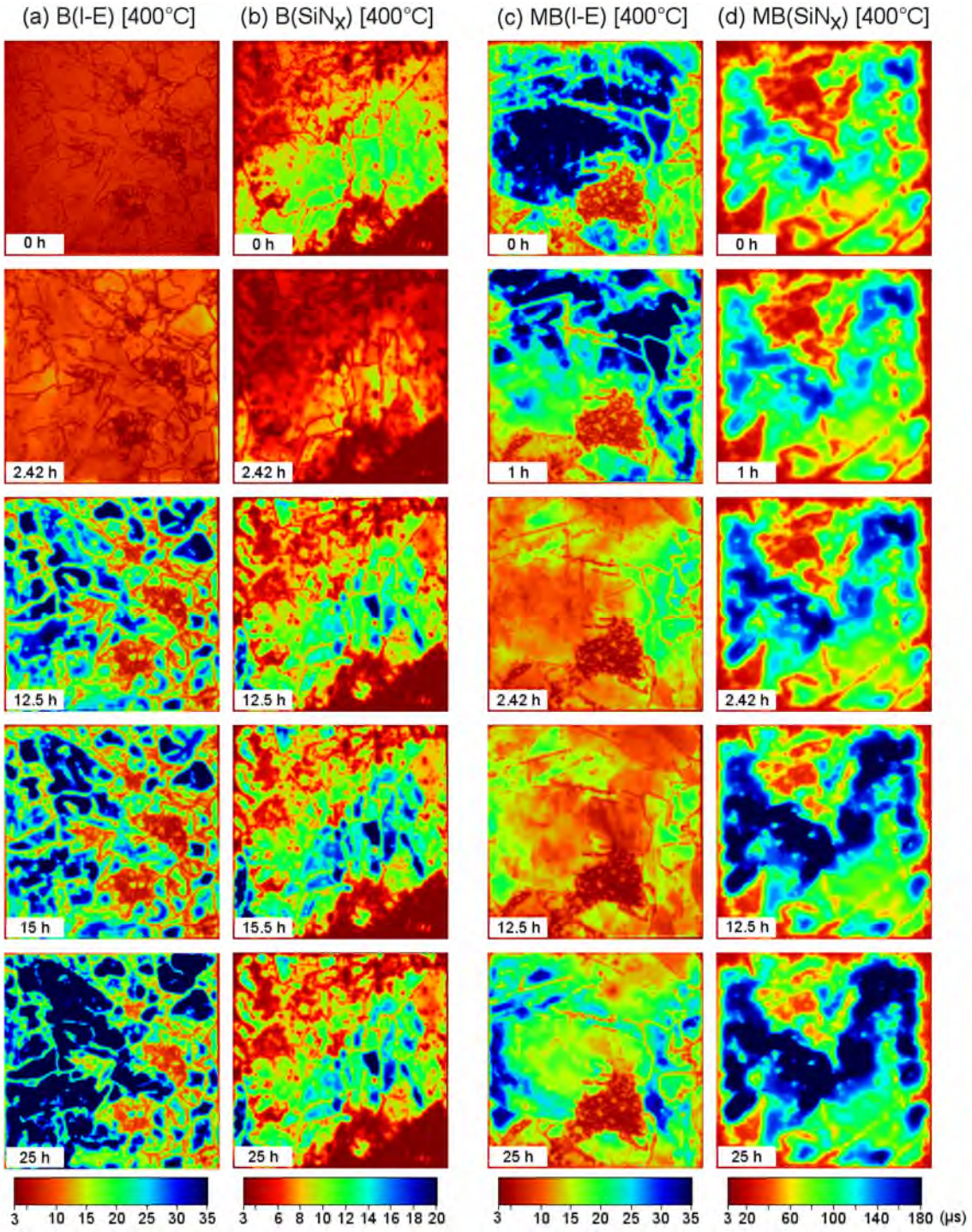

Figure 6.7. Spatial distribution of lifetime with iron in the FeB state in selected samples (39 mm × 39 mm). Samples sourced from the bottom (B) and bottom middle (MB) of a mc-Si block passivated with iodine-ethanol and PECVD SiN_x, respectively. Samples were annealed at the temperatures and cumulative times shown. Figure 6.9 shows corresponding interstitial iron concentration maps.

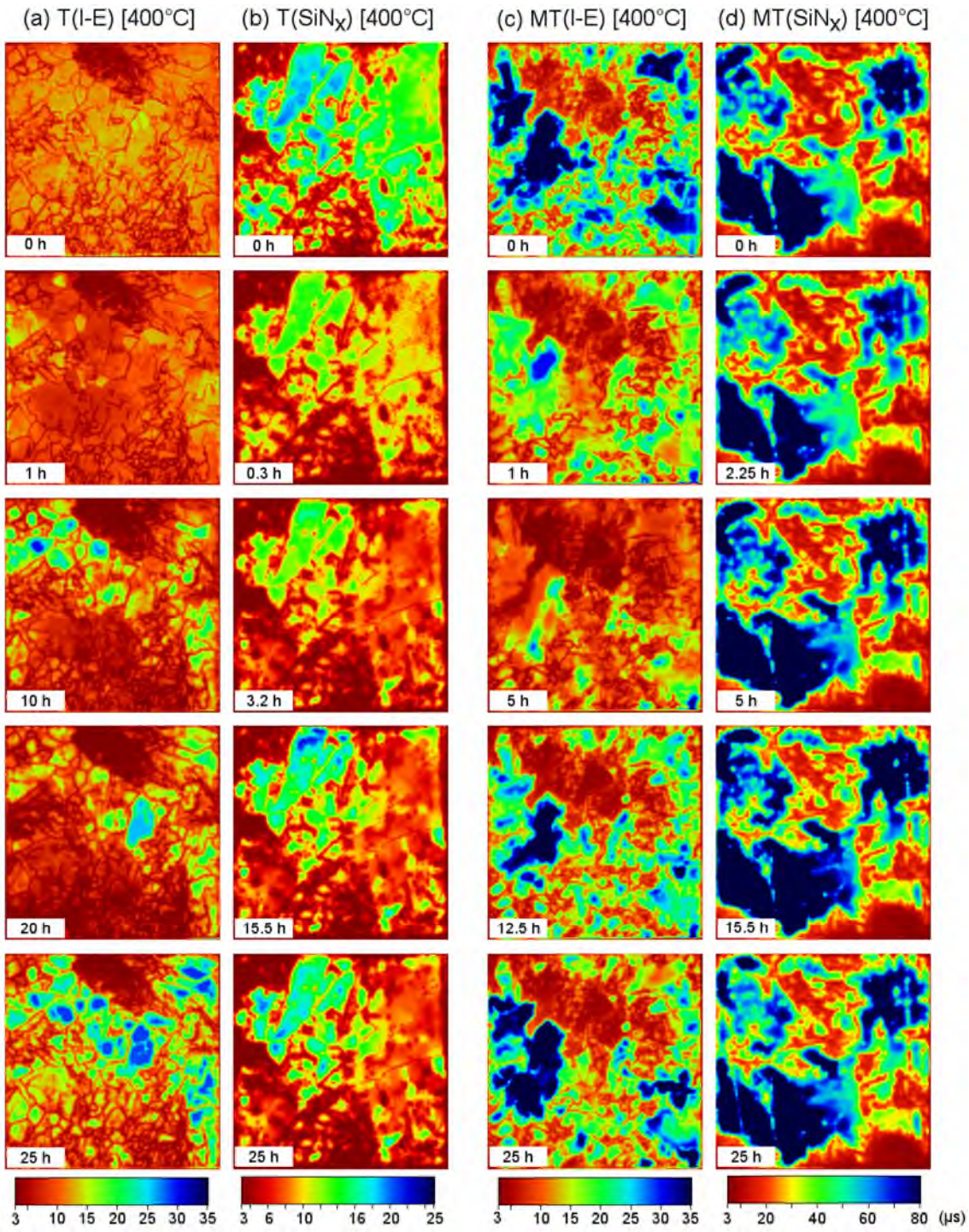

Figure 6.8. Spatial distribution of lifetime with iron in the FeB state in selected samples (39 mm × 39 mm). Samples were annealed at the temperatures and cumulative times shown and were sourced from the top (T) and top middle (MT) of a mc-Si block passivated with iodine-ethanol and PECVD SiN_x respectively. Figure 6.10 shows corresponding interstitial iron concentration maps.

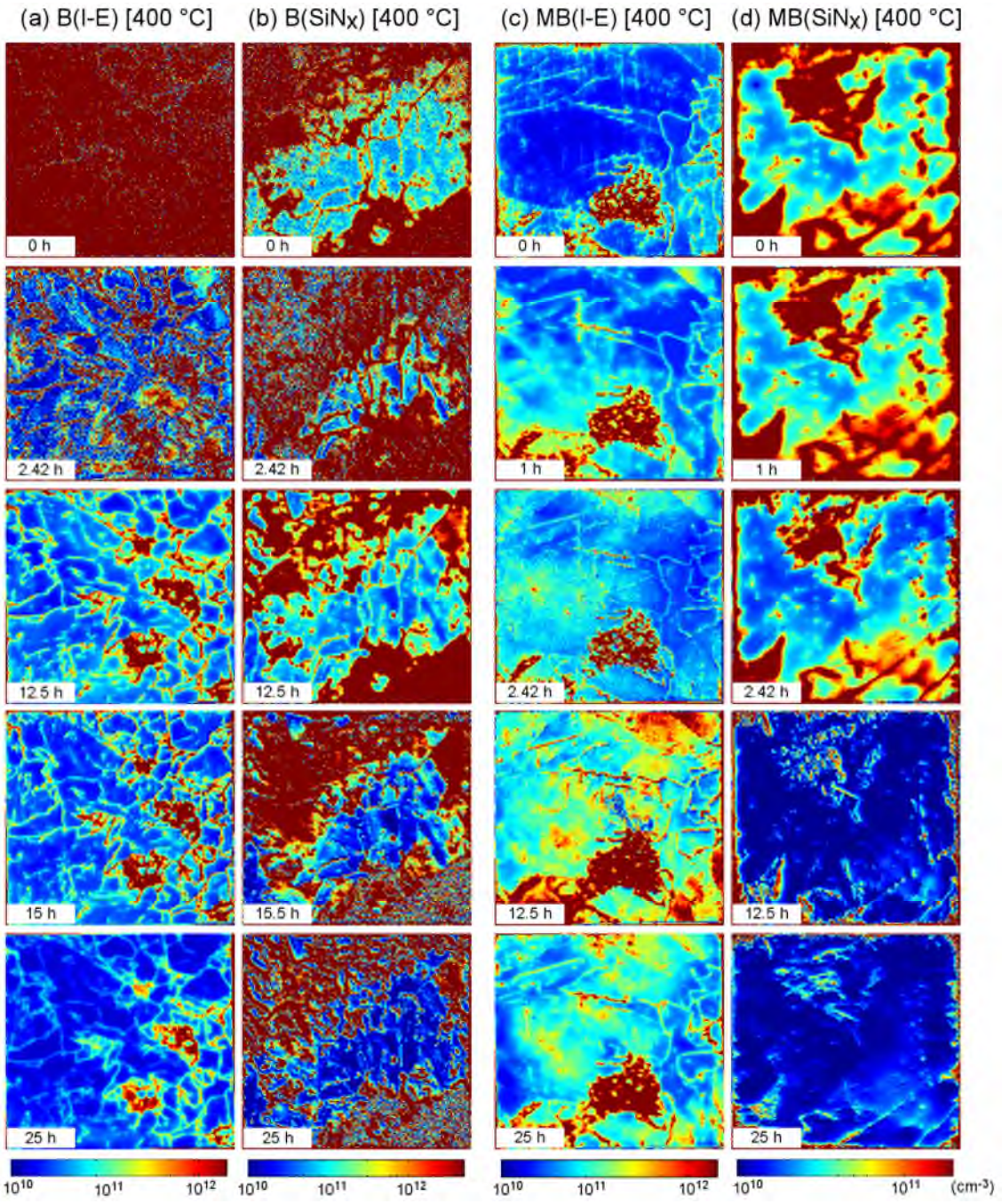

Figure 6.9. Spatial distribution of interstitial iron in the same samples for which lifetime measurements are shown in Figure 6.7. The samples (39 mm × 39 mm) were sourced from the bottom (B) and bottom middle (MB) and were passivated with iodine-ethanol (I-E) or PECVD silicon nitride (SiN_x). Samples were annealed at the temperatures and for the cumulative times shown.

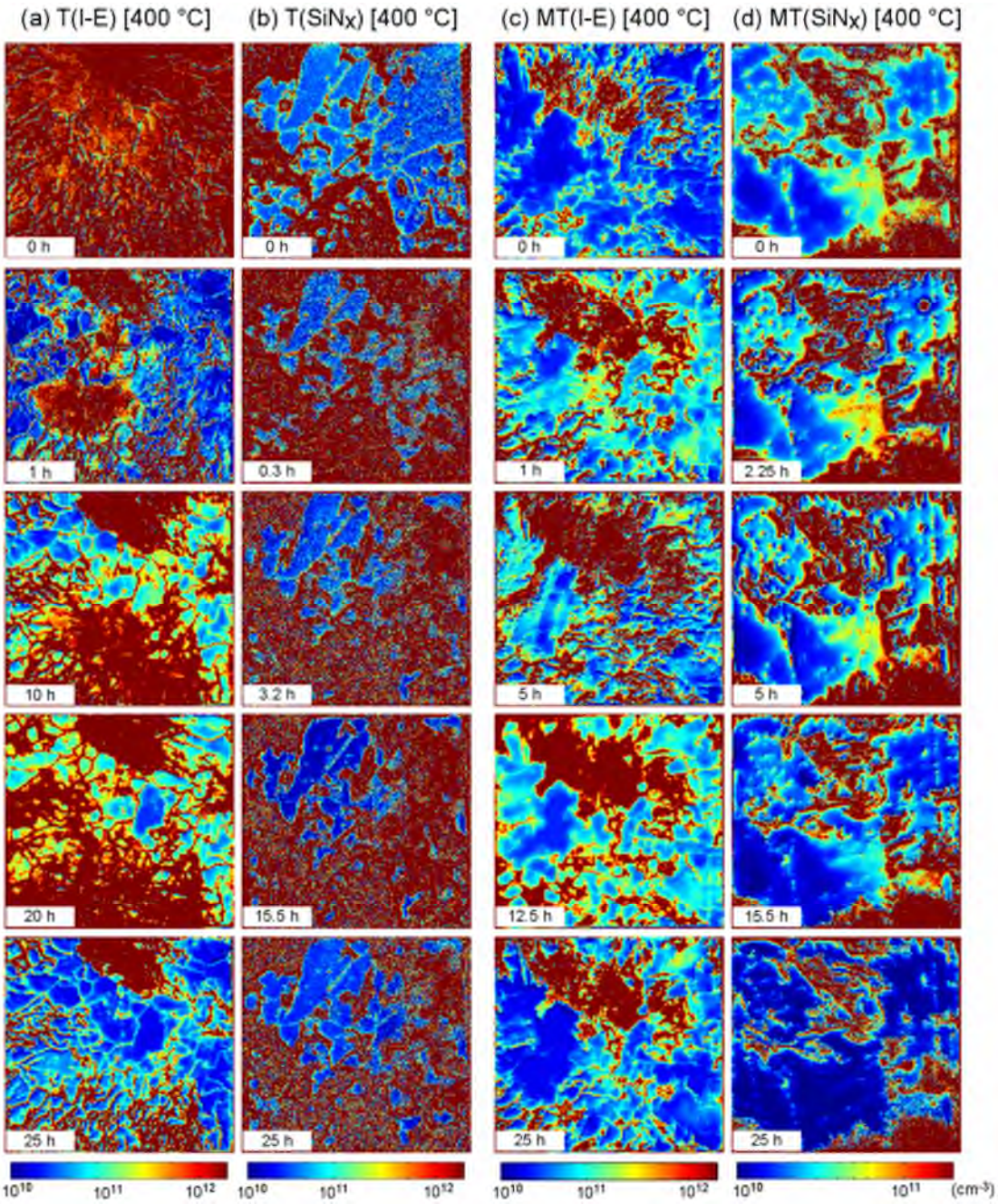

Figure 6.10. Spatial distribution of interstitial iron in the same samples for which lifetime measurements are shown in Figure 6.8. The samples (39 mm × 39 mm) were sourced from the top (T) and top middle (MT) and were passivated with iodine-ethanol (I-E) or PECVD silicon nitride (SiN_x). Samples were annealed at the temperatures and for the cumulative times shown.

6.3.4. SIMS depth profiles

SIMS depth profiles were taken from regions laser cut out of the SiN_x passivated bottom samples annealed for the maximum duration (33 h at 300 °C; 25 h at 400 °C; 60 h at 500 °C) in which there was a large reduction (> 10^{12} cm^{-3}) in interstitial iron compared to the initial value, as illustrated in Figure 6.11. If such a concentration of iron from a 140 μm thick sample is instead distributed in 140 nm of SiN_x (accounting for both sides), the average concentration of iron in the SiN_x would be > 10^{15} cm^{-3}, which would be detectable by SIMS. SIMS is sensitive to total iron, so any non-interstitial iron also gettered from the bulk may also segregate to the SiN_x layer.

Data from the SIMS measurements from SiN_x passivated bottom samples are presented in Figure 6.12. The top plot (a) shows the secondary ion intensity, which was used to estimate the position of the SiN_x film. The bottom plot (b) shows the iron concentration as a function of depth. A thin (~ 20 nm) layer of contamination was found at the surface of each sample and this could have from sample cutting and handling.

Substantial concentrations of iron were always found in the SiN_x film. The concentration was highest nearest the sample surface and reduced with depth into the sample. No spike or dip in iron concentration was observed at the interface between SiN_x and the mc-Si bulk. The concentration of iron in the SiN_x was dependent on the annealing temperature, with average concentrations being 2.0×10^{17} cm^{-3} at 500 °C, 4.0×10^{16} cm^{-3} at 400 °C, and 1.7×10^{16} cm^{-3} at 300 °C. The iron concentration just beneath the mc-Si surface was above the SIMS detection limit in all cases, being very high (> 10^{16} cm^{-3}) in the 500 °C case.

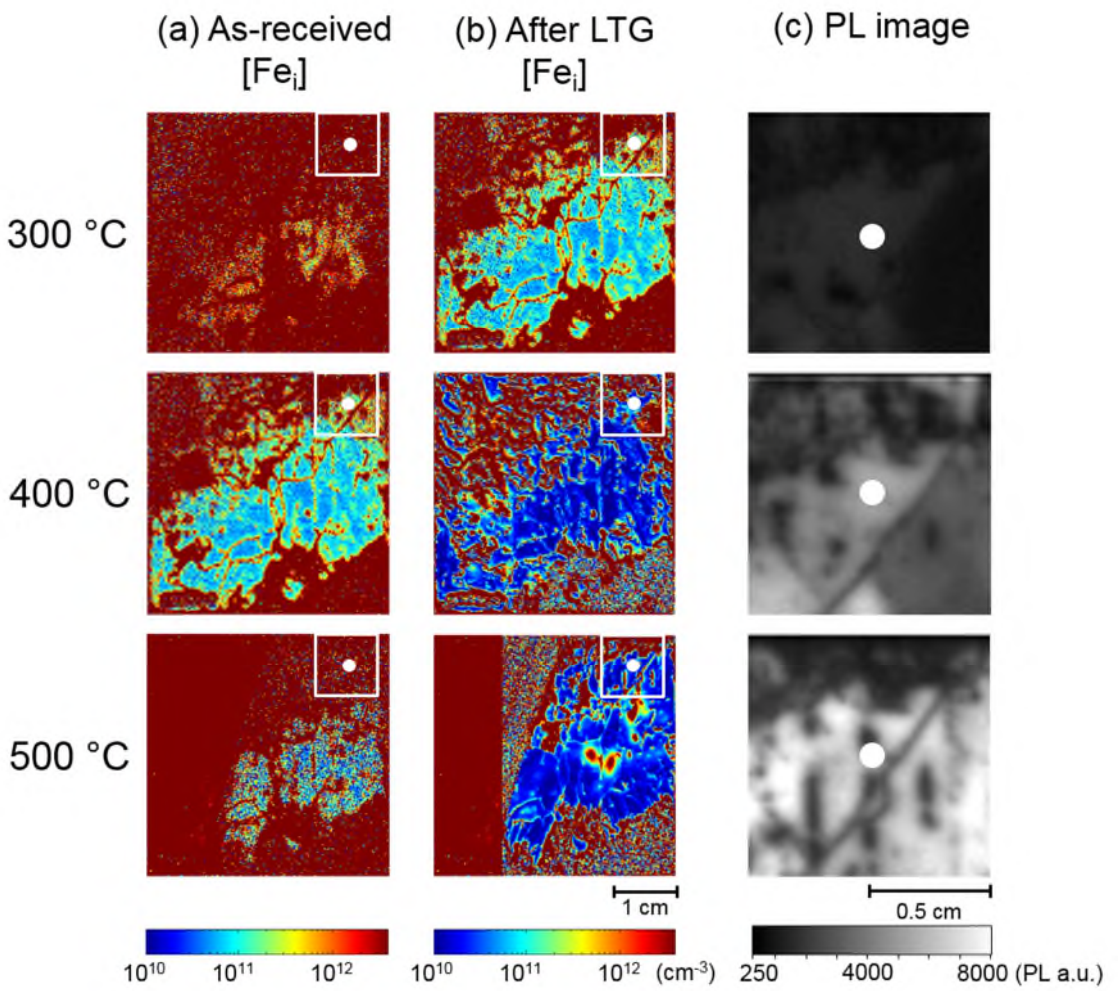

Figure 6.11. Sample section for the SIMS experiment from the bottom samples annealed with silicon nitride passivation at 300 °C, 400 °C and 500 °C temperatures. The first (a) and second (b) columns show the spatial distribution of the interstitial iron in the as-received state and after the final annealing step respectively. The samples (10 mm × 10 mm) positions for SIMS are marked with 'white' rectangular boxes. The 'white' circles indicate the exact locations for SIMS profiles. The right column (c) shows PL images of the experimental samples sent off for SIMS analysis.

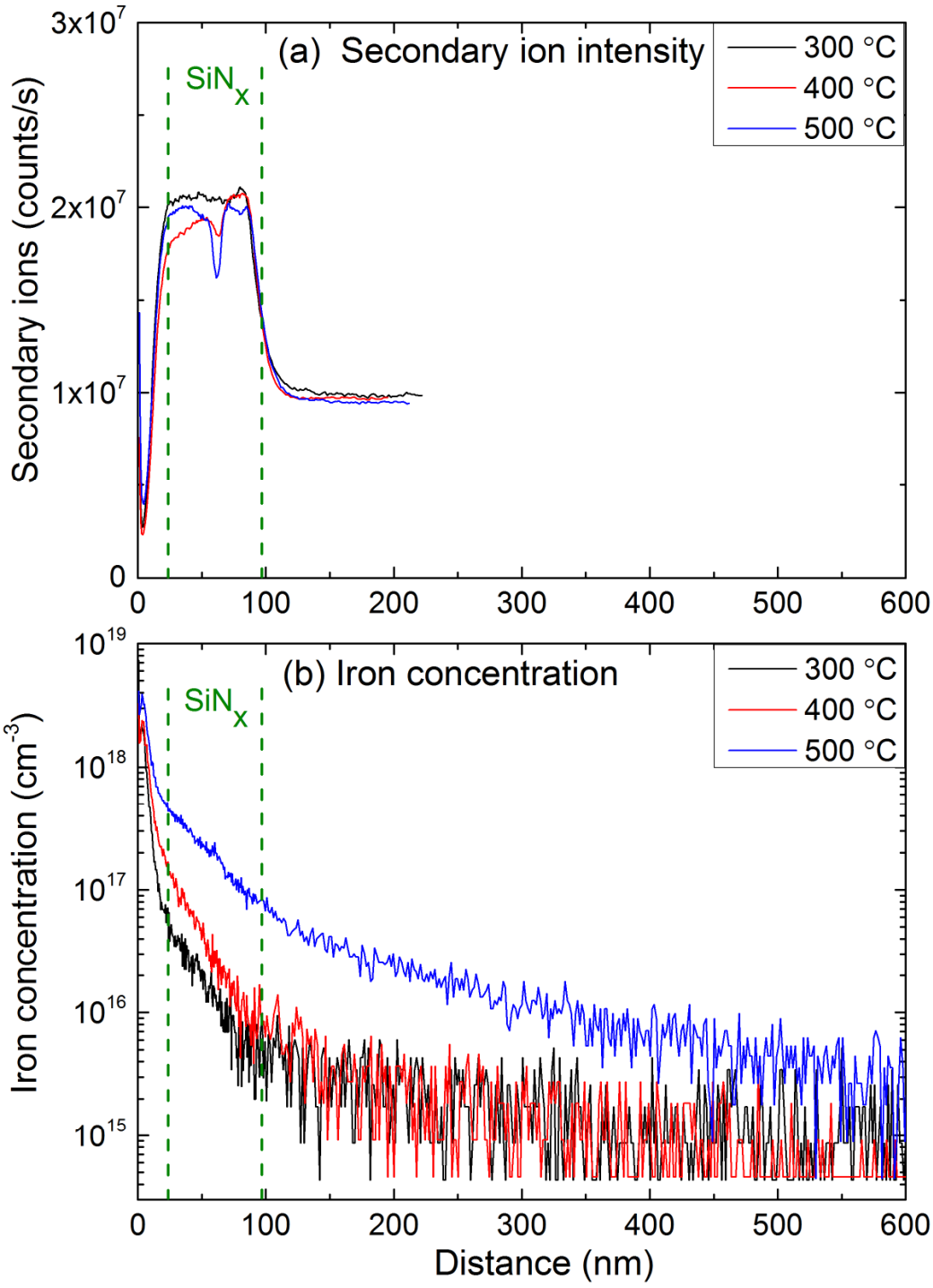

Figure 6.12. SIMS depth profiles from bottom samples annealed with silicon nitride passivation at 300 °C, 400 °C or 500 °C after the final annealing step. The top plot (a) shows the secondary ion intensity which is used to locate the SiN_x film, the approximate extrema of which are marked as vertical dashes. The bottom plot (b) shows the iron concentration measured in the SiN_x film and also the top part of the mc-Si bulk. The detection limit was ~ 4×10^{14} cm^{-3}.

Table 6.1. Summary of starting and final lifetimes and interstitial iron concentration, and their relative values after the final annealing stage. The red or green shading respectively represent deterioration or improvement in bulk carrier lifetime, or an increase or decrease in the interstitial iron concentration.

Ingot position	Annealing temperature (°C)	Total annealing time (h)	As-grown $\tau_{effective}(0)$ (μs)		As-grown $[Fe_i](0)$ ($\times 10^{11}$ cm^{-3})		As-grown $\tau_{other}(0)$ (μs)		Improvement in $\frac{\tau_{effective}(t_{max})}{\tau_{effective}(0)}$		Reduction in $\frac{[Fe_i](0)}{[Fe_i](t_{max})}$	
			SiN_x	I-E	SiN_x	I-E	SiN_x	I-E	SiN_x	I-E	SiN_x	I-E
T	300	33	16.3	10.4	7.0	11.6	29.2	18.5	1.48	1.37	9.66	1.74
	400	25	16.5	12.1	6.7	10.1	28.8	21.9	1.41	1.91	3.45	6.39
	500	60	19.4	12.0	5.0	8.0	31.4	18.3	1.17	0.35	9.34	0.36
MT	300	33	50.4	24.0	1.1	3.7	62.7	34.2	1.20	0.94	10.19	0.78
	400	25	47.1	28.2	1.4	2.9	63.2	39.4	1.41	0.75	12.96	1.65
	500	60	40.3	22.6	1.7	5.1	53.9	37.6	1.31	0.34	2.01	0.62
MB	300	33	113.8	50.1	0.54	1.5	147.3	67.5	0.91	1.17	17.94	0.63
	400	25	112.5	46.5	0.58	1.6	147.5	62.0	1.52	0.46	5.51	0.35
	500	60	116.5	48.6	0.33	2.4	135.9	81.6	0.78	1.00	0.48	1.18
B	300	33	6.4	4.8	26.1	35.0	14.9	10.7	1.58	5.31	12.94	9.41
	400	25	9.8	5.5	15.8	28.0	21.9	12.0	2.65	8.03	6.69	22.95
	500	60	7.2	6.6	22.5	20.8	17.5	12.7	3.80	1.76	6.06	2.81

6.3.5. Correlation of lifetime and interstitial iron changes

The correlations between normalised recombination rate change relative to the as-grown value and normalised change in interstitial iron concentration relative to the as-grown value for sister samples from every height position were made according to the Equation 5.1 (Chapter 5) and presented in Figure 6.13. The diagonal dashed line in every graph represents a 1:1 relationship at three annealing temperatures. Although the bottom wafers exhibit some correlation for all three annealing temperatures, data points slightly deviate from the 1:1 relationship line. The middle parts of the ingot (bottom middle (MB) and top middle (MT)) show a very poor relationship. In the top wafers, samples annealed at 300 °C and 400 °C show a relationship whereas it is very weak at 500 °C.

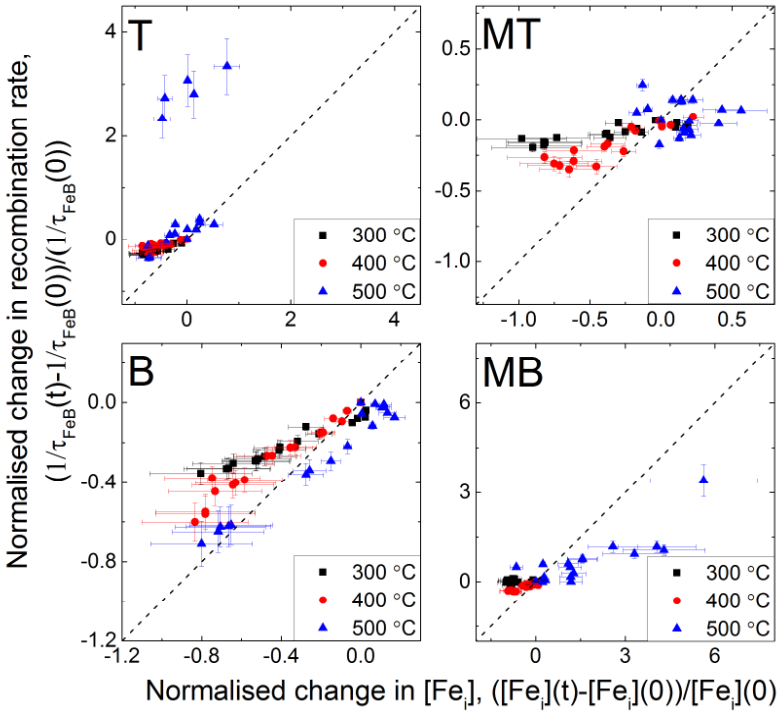

Figure 6.13. Change in recombination rate normalised by as-grown recombination rate versus change in bulk interstitial iron concentration normalised by as-grown bulk interstitial iron concentration according to Equation 5.1 (Chapter 5) for samples from the top (T), top middle (MT), bottom middle (MB) and bottom (B) of the mc-Si block. The dashed lines represent a 1:1 relationship.

A correlation between normalised recombination rate change by the value in the prior annealing step and normalised change in interstitial iron concentration by the value in the prior annealing step were also made according to Equation 6.2 and shown in Figure 6.14.

$$\frac{\frac{1}{\tau_{FeB}(t)}-\frac{1}{\tau_{FeB}(t\text{-}1)}}{\frac{1}{\tau_{FeB}(t)}}=A\left(\frac{[Fe_i](t)-[Fe_i](t\text{-}1)}{[Fe_i](t)}\right) \quad (6.2)$$

As silicon nitride passivation degrades upon annealing at ≥ 500 °C [207], the correlation in Figure 6.14 has relatively lower passivation effect compared to the correlation presented in Figure 6.13. The samples from the bottom part of the ingot show a weak correlation. Samples from other parts of the ingot show a very poor correlation upon annealing all three temperatures investigated.

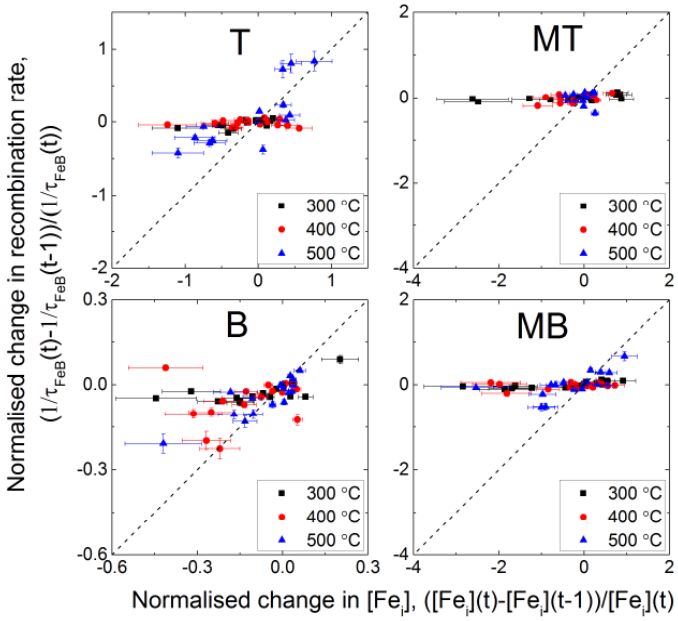

Figure 6.14. Change in recombination rate normalised by recombination rate in the prior annealing step versus change in bulk iron concentration normalised by bulk iron concentration in the prior annealing step according to Equation 6.2 for samples from the top (T), top middle (MT), bottom middle (MB) and bottom (B) of the mc-Si block. The dashed lines represent a 1:1 relationship.

6.4. Discussion

6.4.1. Lifetime changes in SiN_x passivated samples

The results show that long low-temperature annealing can generally improve the lifetime in as-received mc-Si passivated with SiN_x. Figure 6.3 shows the effective lifetime

in SiN_x passivated samples from all four locations in the ingot was increased by annealing at 400 °C. The improvement was particularly significant in the bottom samples which experienced lifetime increases by a factor of ~ 2.7. Annealing SiN_x passivated samples at 300 °C had a smaller positive effect on lifetime in all cases except for the bottom middle samples which were unaffected. The effect of annealing at 500 °C was mixed. The biggest relative improvement (a factor of 3.8) was achieved for the bottom sample upon annealing at 500 °C for 60 h. Annealing at 500 °C for relatively high lifetime bottom middle samples results in a reduction in lifetime, and the trend in the top sample was unclear. Figures 6.13 and 6.14 show the correlation between normalised changes in recombination rate (reciprocal lifetime) and normalised change in interstitial iron concentration. At all temperatures investigated, the wafers from the bottom part of the ingot show a good correlation. This indicates that the lifetime changes in the bottom wafers can partially be attributed to the changes in the interstitial iron concentration in the bulk. The correlations for the middle and top samples do not show a simple relationship. Although annealing at 300 °C and 400 °C reduces interstitial iron concentration, it can be concluded that annealing at these temperatures must also affect the concentration of another defect or other defects.

Only very limited data on the effect of low-temperature annealing on lifetime in SiN_x passivated mc-Si are available in the literature. Liu *et al.* studied the effect of 400 °C annealing on mc-Si achieved a ~ 2.6 times improvement in lifetime in 5.6 h [138], although the actual values of effective lifetime measured were considerably lower than the results presented in this Chapter. The PL images of lifetime reported by Krain *et al.* are also qualitatively consistent with the lifetime images reported in Figure 6.7(b).

6.4.2. Interstitial iron changes in SiN_x passivated samples

In this study, interstitial iron in mc-Si samples is highly supersaturated at the annealing temperatures used. Solubility data at low temperatures (≤ 500 °C) is discussed in Section 5.5.2. The starting interstitial iron concentrations are several orders of magnitude higher than the solubility values. It is not therefore surprising that the interstitial iron concentration in SiN_x passivated mc-Si has a tendency to reduce with annealing at 300 °C and 400 °C (Figure 6.4).

In Chapter 5, low-temperature gettering using I-E passivation was presented and discussed. The results (Chapter 5) were compared to those of Krain *et al.* [36] which are not to be quantitatively consistent, as shown in Figure 6.15. Two possible explanations were proposed for this discrepancy: (i) hydrogenation from their SiN_x affecting the behaviour of interstitial iron; and/ or (ii) that their samples came from different parts of the ingot so have different microstructures. The decay in interstitial iron concentration is clearest in bottom samples as these have the highest concentration, and Figure 6.6 shows that in these samples the decay rates are similar for both passivation schemes used. Thus, it can be concluded that hydrogenation (if it occurs) does not explain the difference between the studies and favours the remaining explanation of microstructural differences between the samples. If this is true then the correlation between the temperature dependence of gettering and iron diffusivity found by Krain *et al.* is likely to have been coincidental. A direct measurement of hydrogen concentration in bulk materials by FTIR or SIMS technique could be a topic for future study.

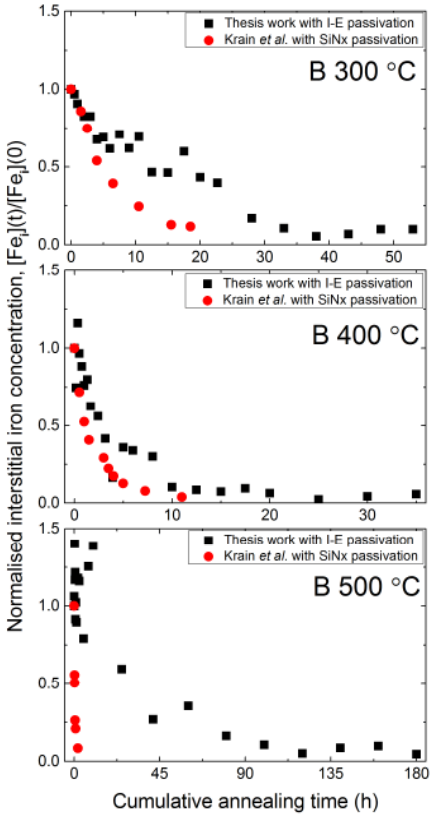

Figure 6.15. Comparison of normalised change in interstitial iron concentration upon low-temperature annealing between the results from the bottom samples with I-E passivation (Chapter 5) and data from Krain *et al.* [36]. Interstitial iron in this thesis and Krain *et al.* were measured at an injection level of 1×10^{15} cm^{-3} and 3×10^{15} cm^{-3}, respectively.

6.4.3. Differences between I-E and SiN_x passivation initial states

Initial lifetimes measured with SiN_x passivation are considerably higher than with I-E passivation (Table 6.1). Distributions of the as-received bulk lifetime for the I-E and SiN_x passivated samples are presented in Chapter 4. Lifetime measurements made on the Cz-Si control sample (Figure 6.2) demonstrate that this is not due to differences in the surface recombination velocity. The comparison samples are from adjacent locations of the same wafers, and whilst small difference from slightly different microstructures might occur, it cannot account for the magnitude of the differences observed. It can, therefore, be concluded that the *bulk* lifetimes are affected by choice of surface passivation technique, and possible reasons for this are discussed in Section 6.4.6.

The starting values of interstitial iron concentration are dependent on the choice of passivation method (Table 6.1) with concentrations usually considerably lower with SiN_x passivation compared to I-E passivation. Distributions of as-received interstitial iron concentration are presented in Chapter 4. This finding is consistent with the study of Karzel *et al.* [137], whose quinhydrone-methanol solution is similar to I-E solution in this thesis, in that it is a room temperature treatment and probably does not introduce hydrogen into the material. Karzel *et al.* offered a possible explanation in terms of hydrogen from SiN_x passivation affect interstitial iron concentration and diffusivity of interstitial iron. Theoretical calculations using molecular-dynamics (MD) simulations suggest hydrogen does not passivate interstitial iron [159], although experimental results suggest that hydrogen may interact with iron under certain conditions [206, 209, 210]. One additional possibility raised by SIMS data (discussed in section 6.4.5) showing iron incorporation into the SiN_x is that interstitial iron is gettered to the SiN_x layer during the passivation treatment which involves 375 °C annealing for ~10 mins. The kinetic feasibility of this can be assessed using a double sided diffusion model according to Equation 6.3 described in Ref. [128] using the established diffusivity for interstitial iron [18], as shown in Figure 6.16.

$$[Fe_i]_{\text{average}} = [Fe_i]_{\text{final}} + ([Fe_i]_{\text{initial}} - [Fe_i]_{\text{final}}) \sum_{\substack{k=1 \\ k\,\text{odd}}}^{\infty} \frac{8}{\pi^2 k^2} \exp\left(-\frac{D_{Fe}\, t\, \pi^2 k^2}{d^2}\right), \qquad (6.3)$$

where $[Fe_i]_{\text{average}}$ is the average iron concentration, $[Fe_i]_{\text{final}}$ is the final iron concentration, $[Fe_i]_{\text{initial}}$ is the initial iron concentration, k is an integer, D_{Fe} is the diffusion coefficient of

iron, *d* is the sample thickness and *t* is anytime. The biggest absolute difference in as-received interstitial iron levels occurs in bottom samples annealed at 400 °C (Table 6.1). Taking the true starting interstitial iron concentration (2.8×10^{12} cm^{-3}) to be that measured with I-E passivation, modelling the interstitial iron diffusion to both surfaces shows that 10 minutes at 375 °C does result in an average bulk interstitial iron concentration (1.58×10^{12} cm^{-3}) similar to that measured with SiN_x. Thus iron gettering to the SiN_x passivation film during the passivation treatment is kinetically viable in this case, and this possibility for the discrepancy between passivation methods is worthy of future investigation. Note that the effect of thermal annealing during silicon nitride deposition technique at 375 °C is found to be different from the low-temperature annealing used in works due to a different annealing atmosphere.

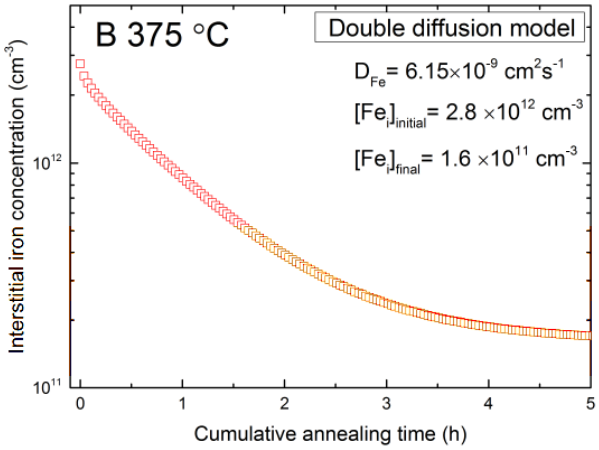

Figure 6.16: Modelling of bulk interstitial iron concentration as a function of cumulative annealing time using the kinetics using a double-side diffusion model according to Equation 6.3 for the bottom samples at an annealing temperature of 375 °C. The initial and final interstitial iron concentration are chosen from the bottom sample annealed at 400 °C for 35 h with I-E passivation.

The difference in starting lifetimes between the I-E and SiN_x passivated samples is not just because of differences in interstitial iron levels. The values of τ_{other} given in Table 6.1 have the lifetime due to recombination at bulk iron factored out and are always substantially higher in the SiN_x case. All it can be claimed for certain is that SiN_x does something different to the bulk lifetime than I-E. The origin of this difference is not clear from this study alone. Possible explanations might include bulk hydrogenation by passivation (which has been directly proven to occur at higher temperatures [197, 204]) or gettering of impurities other than bulk iron to the SiN_x film.

6.4.4. Comparison of annealed I-E and SiN_x passivated samples

A comparison in lifetime (with iron in the FeB state) and bulk interstitial iron concentration for the silicon nitride passivated and iodine-ethanol passivated samples annealed at all three temperatures is presented in Figure 6.5 and Figure 6.6, respectively. The samples from the both the passivations were subjected to the same thermal treatment for the same cumulative period. The lifetimes and iron concentration values are normalised to the as-received values for both SiN_x and I-E passivated samples so that the data can be compared directly.

6.4.4.1 Bottom and top wafers

In the bottom and top samples with both the SiN_x and I-E passivation, the behaviour is quantitatively similar. Bottom samples have a relatively low starting lifetime and relatively high starting interstitial iron concentration experience lifetime improvements and longer-term interstitial iron reductions with both passivation types. The kinetics of the decay in interstitial iron concentration at a given temperature are very similar in samples with both the passivations (Figure 6.5) which suggest the main sink for interstitial iron is the same for both passivation types. This is perhaps surprising that the samples for SiN_x and I-E passivation for a given annealing temperature were not sister, but adjacent, samples so have similar properties by virtue of their ingot location but not near-identical microstructures. Lifetime improvement in the bottom samples annealed at 300 °C and 400 °C is higher with I-E passivated samples than the SiN_x passivated samples. This result indicates that defects other than iron are involved in silicon nitride passivated samples. In the top wafers, lifetime is improved and interstitial iron concentration decayed in samples with both the passivations at 300 °C and 400 °C. The decay rate in iron concentration is slightly higher in SiN_x passivated top samples than the I-E passivated samples. Annealing at 500 °C exhibits a lot of scatter in the data in top samples with both the passivations.

The spatial lifetime distribution images for the bottom and top samples for both the passivations are presented in Figures 6.7(a) and 6.7(b) and 6.8 (a) and 6.8(b), respectively. The corresponding interstitial iron concentration maps are presented in Figures 6.9(a) and 6.9(b) and 6.10(a) and 6.10(b), respectively. Note that a different scale is maintained for SiN_x and I-E passivated samples as they have different as-received values. It can be seen that the size and distribution of grains are different in both the passivated samples. With

both passivation types, the lifetimes increase with annealing and the interstitial iron concentrations decrease. The changes which occur are slow and much slower than if diffusion-limited *internal* gettering of interstitial iron is the only process involved. The gettering process requiring the longest impurity diffusion length would be gettering to the SiN_x film (or surface in the case of I-E passivation), yet if known diffusion coefficients of interstitial iron [18] are used with a two-sided surface diffusion calculation [128] the decay in interstitial iron concentration in the bottom samples would be faster than observed experimentally by a factor of ~ 6 at 300 °C, ~ 15 at 400 °C and ~ 20 at 500 °C, as shown in Figure 6.17. At 500 °C after an initial increase, the decay is slower than at 400 °C, which is indicative of multiple mechanisms of iron gettering occurring.

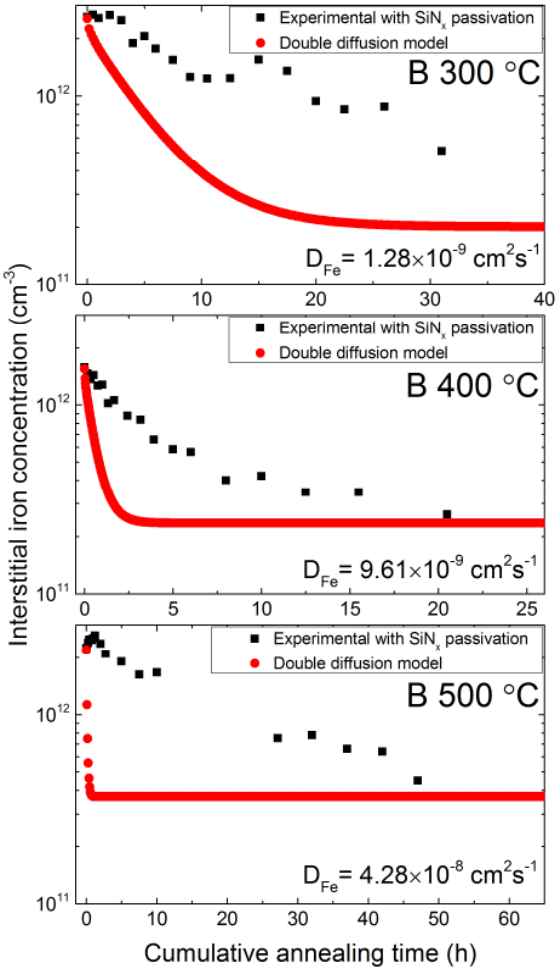

Figure 6.17: Comparison of measured bulk interstitial iron concentration as a function of cumulative annealing time and the kinetics using a double-sided diffusion model for the bottom samples according to Equation 6.3. Samples were passivated with silicon nitride passivation and annealed at 300 °C, 400 °C and 500 °C temperatures.

There are good reasons not to abandon the surface or SiN_x film gettering mechanism in bottom samples entirely, however. Factors in favour include the SIMS data for SiN_x samples, the same interstitial iron decay in non-sister samples, and previous studies which have found iron gettering to free surfaces in single crystal silicon [211, 212]. Trapping of interstitial iron at crystal defects in mc-Si could slow down the effective diffusion process of interstitial iron, and iron release from elsewhere in the material at 500 °C could complicate the kinetics further.

6.4.4.2 Middle wafers

The effect of low-temperature annealing in samples from the middle part of the ingot (MB and MT) show a significant difference between SiN_x and I-E passivated samples. Annealing SiN_x passivated samples at 300 °C or 400 °C has a positive effect on lifetime and decay in interstitial iron concentration, whereas in I-E case the effect is more mixed and can be highly detrimental.

The time dependence of bulk lifetime and interstitial iron concentration for samples from the middle of the ingot is strongly passivation-dependent as shown in Figure 6.5 and Figure 6.6, respectively. The abrupt reduction in lifetime observed in samples with I-E passivation upon annealing at 400 °C and 500 °C [53], was rarely observed in samples with SiN_x passivation. For example, the lifetime in bottom middle sample reduced from 46.5 μs to just 7.6 μs after 6 h of annealing at 400 °C with the I-E passivation, whereas the same treatment with SiN_x passivation increases lifetime from 112 μs to 163 μs. The key difference is in bulk interstitial iron concentration decreases substantially with SiN_x passivated samples whereas it increases with I-E upon annealing at 300 °C and 400 °C. It is therefore concluded that passivation strongly affects the *internal* gettering behaviour.

The spatially resolved lifetime images for the bottom middle and top middle samples annealed at 400 °C with both the SiN_x and I-E passivation are shown in Figure 6.7(c), 6.7(d), 6.8(c) and 6.8(d), respectively. The corresponding interstitial iron concentration maps are shown in Figures 6.9(c) and 6.9(d) and 6.10(c) and 6.10(d), respectively. A decrease in lifetime in I-E passivated samples is clearly visible with I-E but not with SiN_x passivation. Although lifetime recovers with I-E passivation upon further annealing but it is lower in most of the bulk grain regions compared to the as-received values. Furthermore, the lifetime reduction in the sample with I-E passivation is accompanied by

an increase in interstitial iron concentration but this increase is far too small to account for the dramatic lifetime reduction. The samples with SiN_x passivation lifetime improves in both the MB and MT samples at an intermediate stage and remains constant in further annealing. Why does lifetime reduce substantially with I-E but not with SiN_x? One possibility is that bulk passivation from the SiN_x film somehow prevents the formation of the recombination centres which form with I-E passivation. Other possibilities include that fast diffusing impurities are released from locations within the bulk of the material upon initial annealing and are gettered by the SiN_x film but not by a free surface, or that contamination from outside the sample can enter in the I-E case but not in the SiN_x case as the film might act as a diffusion barrier. The complexity of low-temperature gettering is discussed in Section 6.4.6. It is noted that grain structure and densities are slightly different in the I-E and SiN_x passivated samples which might cause a difference in interstitial iron kinetics. The difference in lifetime improvement and interstitial iron concentration reduction upon annealing between SiN_x and I-E passivated samples could be a result of bulk hydrogenation as recent studies by Liu *et al*. [138], Karzel *et al*. [137] and Leonard *et al*. [206] provided evidence for hydrogen interacting with bulk iron. In this study, there is no direct evidence of hydrogen present in the bulk material but SiN_x film has an effect on iron concentration which discussed in details in the following section.

6.4.5. Gettering of iron to SiN_x layers

The effect of SiN_x film in gettering bulk interstitial iron concentration at low-temperature annealing is investigated in this section. A SIMS profile of iron concentration for bottom samples annealed at 300 °C, 400 °C and 500 °C are used to examine the distribution of iron in SiN_x film and the Si wafer substrate.

The SIMS results show a high concentration of iron exists in the SiN_x film after annealing at three temperatures. As in the recent study of Liu *et al.* [160], no peak in iron signal was observed at the interface between the SiN_x and the silicon bulk, which demonstrates the interface itself is not a site for gettering or iron precipitation. The iron profile through the SiN_x is also fairly smooth (no large spikes), which suggests that iron has segregated throughout the SiN_x and does not exist in large precipitates. (The step size

for SIMS depth profiling was < 1.5 nm so large precipitates would be detectable in principle).

The concentrations of iron found in the SiN_x layer are higher than expected if the only source of iron were interstitial iron lost from the bulk. The area selected for SIMS analysis was known from PL imaging experiments to have interstitial iron reductions of up to ~2 × 10^{12} cm^{-3}, so if all this were gettered to the SiN_x the concentration in the SiN_x would be ~2 × 10^{15} cm^{-3}. Figure 6.12 (b) shows substantially higher iron concentrations in the SiN_x than this. The additional iron could come from iron-containing precipitates in the bulk, which in mc-Si are well-known to contain more iron than is dissolved in the bulk [92]. The possibility that some of the iron comes from contamination cannot be ruled out with certainty. It is noted that a possible iron contamination during the annealing process was investigated and discussed in Chapter 5 where no contamination is observed. However, the results in Figure 6.12 show that iron is highly soluble in SiN_x films processed at low temperatures. The absence of any interface effects suggests that iron would enter the SiN_x from the mc-Si bulk material as well as from surface the sample. The recent SIMS study on float-zone silicon by Liu *et al.* [160] compared samples with and without bulk iron contamination, finding much higher concentrations in the SiN_x in the former case. Iron gettering to SiN_x films is, therefore, an important consideration in the processing of SiN_x passivated silicon solar cells.

6.4.6. Complexities of low-temperature gettering in mc-Si

The results of this study and those of others show that low-temperature gettering in mc-Si is a complex problem and cannot be explained by a single gettering mechanism. An interstitial iron diffusion-limited *internal* gettering model (as suggested by Krain *et al.* [36]) does not explain the observations presented Chapter 5 and Chapter 6. Specifically, it cannot explain why the reduction in interstitial iron is so slow, why interstitial iron levels sometimes increase in spite of apparent supersaturation, and why the decays in interstitial iron at 500 °C is slower than at 400 °C. Surface passivation does influence the low-temperature gettering behaviour, but not in a straightforward way. Whilst it is tempting to state hydrogenation from SiN_x is responsible for any differences, there no direct evidence for this. SIMS data in this work and the recent study of Liu *et al.* [160] show that iron is highly soluble in PECVD SiN_x and given the slow decays in this work

(and those of Krain *et al.* [36]) *external* gettering of interstitial iron at low temperatures is a very important consideration. There are however differences between the two passivation schemes (such as why the lifetime in high lifetime middle samples is more stable with SiN_x than with I-E) that *external* gettering of interstitial iron cannot easily explain. Possible hydrogenation from PECVD SiN_x at low temperatures ($\leq$ 500 °C) is an important topic needs further experimentation.

Based on the results presented in Chapter 5 and Chapter 6, it can be concluded that gettering of metallic impurities in low-temperature annealing is not straightforward and could be occurred by multiple mechanisms simultaneously. The following mechanisms must be understood to explain low-temperature gettering in mc-Si:

(i) *Internal* gettering, whereby impurities diffuse to sites in the material (*e.g.* grain boundaries, precipitates or dislocations). The interstitial iron concentration maps in Figure 6.9 and Figure 6.10 shows that iron concentration decreases in the bulk grain regions and increases in grain boundaries and defective regions upon annealing. The kinetics strongly depends on as-received states including concentration of metallic impurities, grain size, dislocations density distribution as the samples from different height positions exhibit different behaviour under the same passivation and thermal treatment (Figure 6.7 and 6.8).

(ii) Defect reconfiguration, whereby defects change state without long range transport. This could include the transformation of one point-like defect to another. In this study, in many cases, interstitial iron concentration decreases substantially upon low-temperature annealing. It is not certain that how interstitial iron transformed into another type defects.

(iii) *External* gettering of impurities, whereby impurities diffuse to a layer at the surface (*e.g.* SiN_x) or the surface itself. The SIMS results show that SiN_x could contain higher iron concentration which could be a driving force for segregation of bulk iron concentration in low-temperature annealing. The source of iron in the SiN_x films needs further experimentation.

(iv) Bulk passivation of defects, whereby a species such as hydrogen could diffuse into the bulk materials and changes the recombination activity of defects. Although silicon nitride is well known for having a large number of hydrogen but in this study, no direct evidence of bulk hydrogenation is presented.

(v) Changes in the surface recombination velocity, whereby the properties of the

interface between silicon and the passivating layer/ substance occur. As presented in Figure 6.2 there is a difference in surface recombination velocity in between I-E and SiN_x passivation schemes. Furthermore, samples with I-E passivation were cleaned prior to every annealing step and re-passivated with a fresh solution in every characterisation step and it is, therefore, surface recombination velocity is assumed to be unchanged. On the other hand, SiN_x passivation was kept on during annealing processes. The surface passivation might degrade in annealing and makes the lifetime analysis further complicated.

(vi) Contamination from outside of the sample, whereby impurities undesirably enter the material in an uncontrolled manner. Although a controlled experiment (discussed in Chapter 5) shows no iron contamination in a Cz single crystal silicon sample in the absence of a dielectric layer. However, the possibility of contamination cannot be ruled out. As the SiN_x passivated samples were annealed with the presence of SiN_x passivation which may act as a barrier for iron diffusion from outside.

Importantly several of the above mechanisms are highly dependent on the specific properties of the mc-Si wafer processed. Lifetime in all as-received mc-Si sample types studied can be improved under the right conditions. However, just as is the case with higher temperature phosphorus diffusion gettering [201] to maximise the benefit the temperature and time should be tailored to the wafer type processed.

6.5. Conclusion

A comprehensive study into the effects of two different passivation types on low-temperature annealing ($\leq$ 500 °C) on minority carrier lifetime and interstitial iron concentration in as-received mc-Si wafers is discussed. Samples are from different height positions are considered, which influences microstructure and initial properties, and have used two different passivation schemes (I-E and SiN_x). Under certain conditions, substantial lifetime improvements have been demonstrated in all sample types studied using either passivation scheme. With the more cell-relevant SiN_x passivation scheme annealing relatively poor bottom samples at 500 °C for 60 h can improve lifetime from 7.2 μs to 27.5 μs. Annealing at 400 °C for 25 h can improve lifetime in middle samples from 113 μs to 171 μs and in top samples from 16.5 μs to 23.3 μs.

The effect of low-temperature annealing on both lifetime and interstitial iron is complex and depends on passivation type. Starting lifetimes and interstitial iron concentrations depend on the choice of passivation scheme, as does the subsequent behaviour with low-temperature annealing. Substantial lifetime reductions observed after short anneal when measured with I-E passivation are not found in the SiN_x case, so it appears that SiN_x offers more lifetime stability. The possibility that this is due to bulk passivation (perhaps by hydrogen) is not excluded in this study. Importantly, this study shows, for the first time, that substantial concentrations of iron exist in the SiN_x film after low-temperature annealing. It is, therefore, can be suggested that gettering of interstitial iron (and probably other impurities) to the SiN_x film is an important consideration which has usually been overlooked in previous studies. The effect of low-temperature annealing on samples already subjected to phosphorus diffusion gettering is discussed in the next Chapter.

Chapter 7 Combining low-temperature gettering with phosphorus diffusion gettering

7.1. Introduction

In this thesis, low-temperature gettering (≤ 500 °C) in as-received multicrystalline silicon samples using iodine-ethanol and silicon nitride passivation is discussed in Chapter 5 and Chapter 6, respectively. In Chapter 5, it has been shown that low-temperature annealing in the absence of a dielectric film on the surfaces can improve lifetime in relatively poor mc-Si wafers by redistribution of impurities [53]. It is also found the lifetime improvement strongly depends on wafer microstructure. The results presented in Chapter 6 show that the passivation method could play a vital role in the change of bulk lifetime and interstitial iron concentration during low-temperature annealing. However, the standard silicon photovoltaic cell fabrication process involves a series of high and low thermal annealing steps [213] which could affect the distribution of impurities. It is therefore important to investigate the effects of low-temperature annealing at different stages in the cell process, particularly after emitter formation.

High temperature *external* gettering technique by phosphorus diffused layers is well established in PV industry and is able to reduce interstitial iron concentration by more than 99 % [39, 40, 45, 46, 129, 131, 214]. It is important to investigate whether low-temperature gettering can improve lifetime in mc-Si after the phosphorus diffusion step used to form the emitter. A very limited amount of research has been performed into low-temperature gettering in combination with *external* gettering [51, 215]. Schön *et al.*

reported that low-temperature annealing at 550 °C after phosphorus diffusion gettetering can reduce interstitial iron concentration by one order of magnitude further [215]. They do not however investigate samples from different parts of ingot, most importantly in bottom 'red zone' material. Furthermore, it is possible their work was influenced by bulk hydrogenation from the silicon nitride films used [137]. Rinio *et al.* studied partially-processed cells and concluded that *external* gettering to the emitter was responsible for most of the improvement observed [51]. As their study also used silicon nitride passivation, the results could have affected by bulk hydrogenation [54, 137, 138]. Most recently, Liu *et al.* have studied *external* gettering of interstitial iron to silicon nitride dielectric films upon thermal annealing of single crystal samples. They report a high and uniformly distributed iron concentration ($> 10^{16}$ cm^{-3}) in the silicon nitride films upon annealing at 700 °C compared to the bulk materials ($10^{12} - 10^{13}$ cm^{-3}) [160]. In summary, whilst low-temperature annealing can improve lifetime after phosphorus diffusion gettering, detailed understanding of its effect without bulk hydrogenation effect in currently lacking. Furthermore, it is not known how different parts of the ingot respond to low-temperature annealing after the standard phosphorus diffusion gettering process.

In this Chapter, a study which aims to investigate the effect of low-temperature *internal* gettering after a standard phosphorus diffusion process for samples from different height positions in the mc-Si ingot. In the first set of experiments, sister samples were subjected to an industrial standard phosphorus diffusion gettering process at 840 °C and annealed later at 300 °C, 400 °C and 500 °C. Temporary iodine-ethanol (I-E) passivation was used for lifetime characterisation. In the second set of experiment, *external* gettering of interstitial iron to the phosphorus diffused emitter layer was investigated upon low-temperature annealing at 400 °C for samples from adjacent locations to samples in the first experiment. In the final set of experiments, the effects of low-temperature annealing at 400 °C prior to and after the PDG process were investigated for the bottom samples with I-E and SiN_x passivation. Bulk and spatial distribution of lifetime and interstitial iron concentration are measured at every annealing step and the results are compared and discussed.

7.2. Experimental methods

In this Chapter, three different set of experiments were performed into the effect of low-temperature annealing in a combination of PDG process. A summary of these experiments is shown in Figure 7.1.

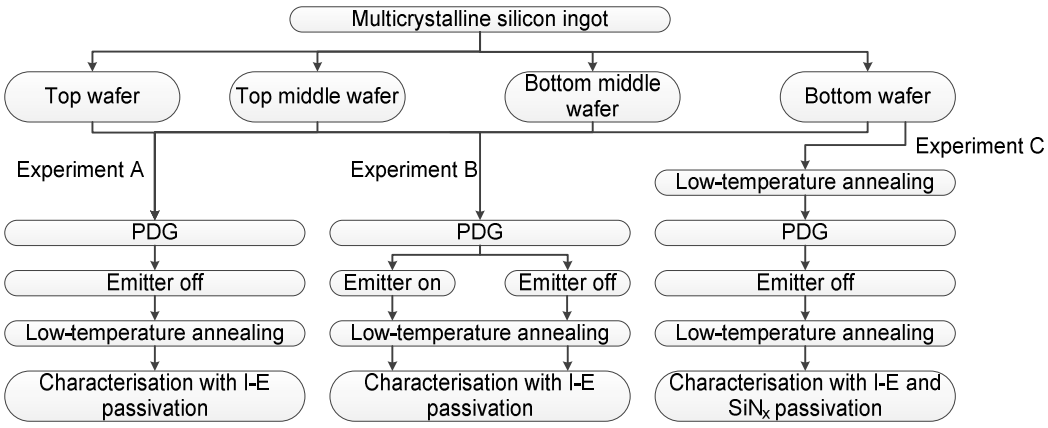

Figure 7.1. Summary of the experiments performed in this Chapter. Details of each individual experiment are presented in Figures 7.2, 7.3 and 7.4.

7.2.1. Experiment A: Low-temperature annealing after PDG

This experiment was performed to investigate whether low-temperature annealing after a standard PDG process can improve bulk lifetime. As-received multicrystalline samples (39 mm × 39 mm) from adjacent locations to the samples in Chapter 5 and Chapter 6. The samples selection process is illustrated in Figure 3.2 in Chapter 3. Resistivities were in the range of 4.7 Ω cm to 7.2 Ω cm.

Sister samples from every height position were first chemically polished with a planar etch solution to remove saw damage, as described in Section 3.5.2 in Chapter 3. Samples were then cleaned using HCl and HF and subjected to the industrial standard phosphorus diffusion process in a tube furnace using $POCl_3$ at 840 °C for 44 min at Universität Konstanz in Germany. The average sheet resistivity is ~ 55 Ω/sq., measured using a four-point-probe resistivity meter at Warwick. A thickness of ~ 5 μm was removed from both sides using a chemical solution at Warwick as described in Section 3.5.2.3 in Chapter 3. This removed the emitter layer from both sides of the samples. Note that samples were carefully agitated to avoid etch pit formation. Samples were then annealed at 300 °C, 400

°C and 500 °C at Warwick under nitrogen ambient. Note that at a particular temperature, samples from all the height positions were subjected to an identical thermal and cooling treatments, as annealing and removal were performed simultaneously.

Samples from every height position were passivated with a liquid iodine-ethanol (I-E) solution using the method described in Section 3.6.1 in Chapter 3. Lifetimes were measured at room temperature using quasi-steady state photoconductance (QSS-PC) with a Sinton WCT-120 lifetime tester at an injection level of 1×10^{15} cm^{-3}. The spatial distribution of lifetime was measured with iron in the FeB and Fe_i state using a BT Imaging LIS-L1 PL imaging tool at every annealing step. The bulk interstitial iron concentration estimated at an injection level of 1×10^{15} cm^{-3} at every annealing step. Detail of characterisation processes is described in Section 3.8 and Section 3.9 in Chapter 3. In the lifetime images, a lower injection was used compared to the injection level (1×10^{15} cm^{-3}) used in the bulk lifetime measurement to avoid unwanted dissociation of FeB pairs during measurement in the PL imaging tool. A summary of the process sequence is presented in Figure 7.2.

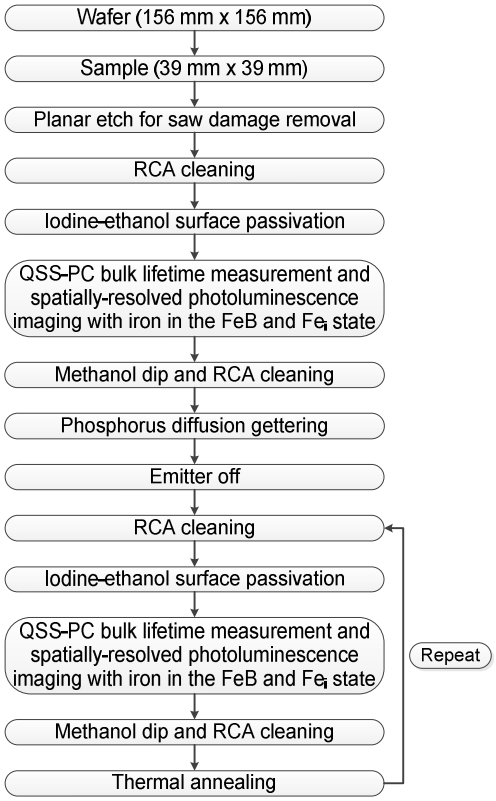

Figure 7.2. Processing and characterisation sequence of low-temperature gettering in multicrystalline silicon material after performing the standard phosphorus diffusion gettering (Experiment A).

7.2.2. Experiment B: Effect of phosphorus diffused emitter in low-temperature gettering

This experiment aims to investigate the role of phosphorus diffused emitter in low-temperature annealing for samples from all the four height positions in the ingot. It is to assess whether any improvements due to low-temperature annealing after emitter formation occur via *external* gettering to the emitter or via *internal* gettering. Two sister samples (from an adjacent location of the samples used in Experiment A) from every height position were subjected to the same industrial standard PDG process. In the first set of samples (one sample from every height position), emitter layers were removed prior to thermal annealing. In the second set of samples (sister sample of the first set), emitter layers were retained during annealing steps. Samples from both sets were subjected to the same thermal treatment at 400 °C for 50 h of cumulative time. After the final annealing step, emitter layers were removed from the second set of samples. Samples were characterised with liquid I-E solution (Section 3.6.1 in Chapter 3). The key processing and characterisation steps used in this study are summarised in Figure 7.3.

7.2.3. Experiment C: Low temperature gettering in bottom wafers after PDG

Experiment C aims to answer following key questions:

1. Can low-temperature annealing improve bulk lifetime in as-received bottom mc-Si sample, as presented in Chapter 5?
2. Is any lifetime improvement (in the first aim) retained after the PDG process?
3. Does PECVD silicon nitride passivation affect bulk lifetime in post-PDG annealing compared to I-E passivation?

Three sister bottom samples (39 mm × 39 mm) were sourced from an adjacent location of the bottom samples used in Experiment A and Experiment B. As-received samples were chemically polished to remove saw damage. The samples were initially characterised using I-E passivation and followed by an RCA cleaning. The first as-received sample was then subjected to an annealing at 400 °C for 25 h of cumulative time.

All the three samples were then subjected to the industrial standard PDG process used in Experiment A. Emitter layers were removed from all the three samples using a chemical solution. The third sample was passivated with silicon nitride (SiN_x) at 375 °C at ISFH, as described in Section 3.6.2. Samples were then annealed at 400 °C for 50 h of cumulative time. Note that silicon nitride passivation was retained on the surfaces of the third sample during thermal annealing steps. QSS-PC bulk lifetime, interstitial iron concentration, lifetime images were achieved at every annealing step with I-E passivation for the first two samples and with silicon nitride passivation for the third sample. A summary of the key process steps is given in Figure 7.4.

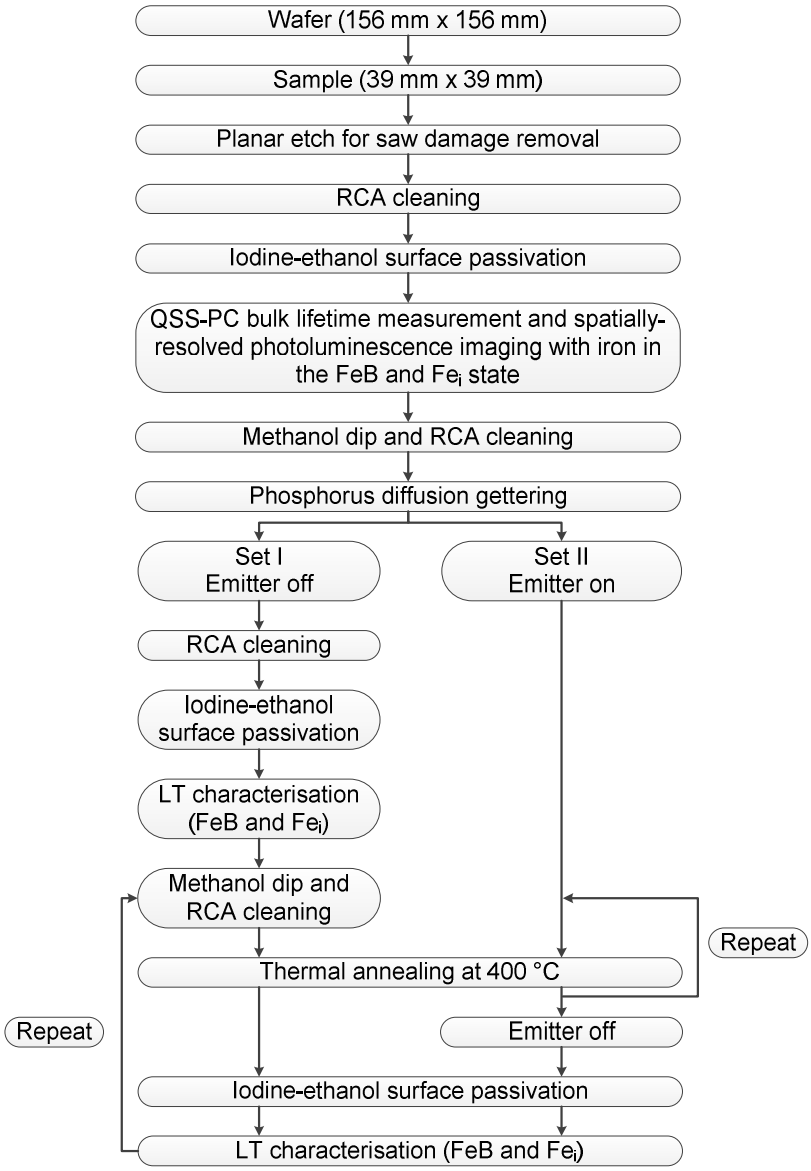

Figure 7.3. The processing and characterisation sequence into the effects of phosphorus diffused emitter layers in low-temperature gettering after the standard PDG process (Experiment B).

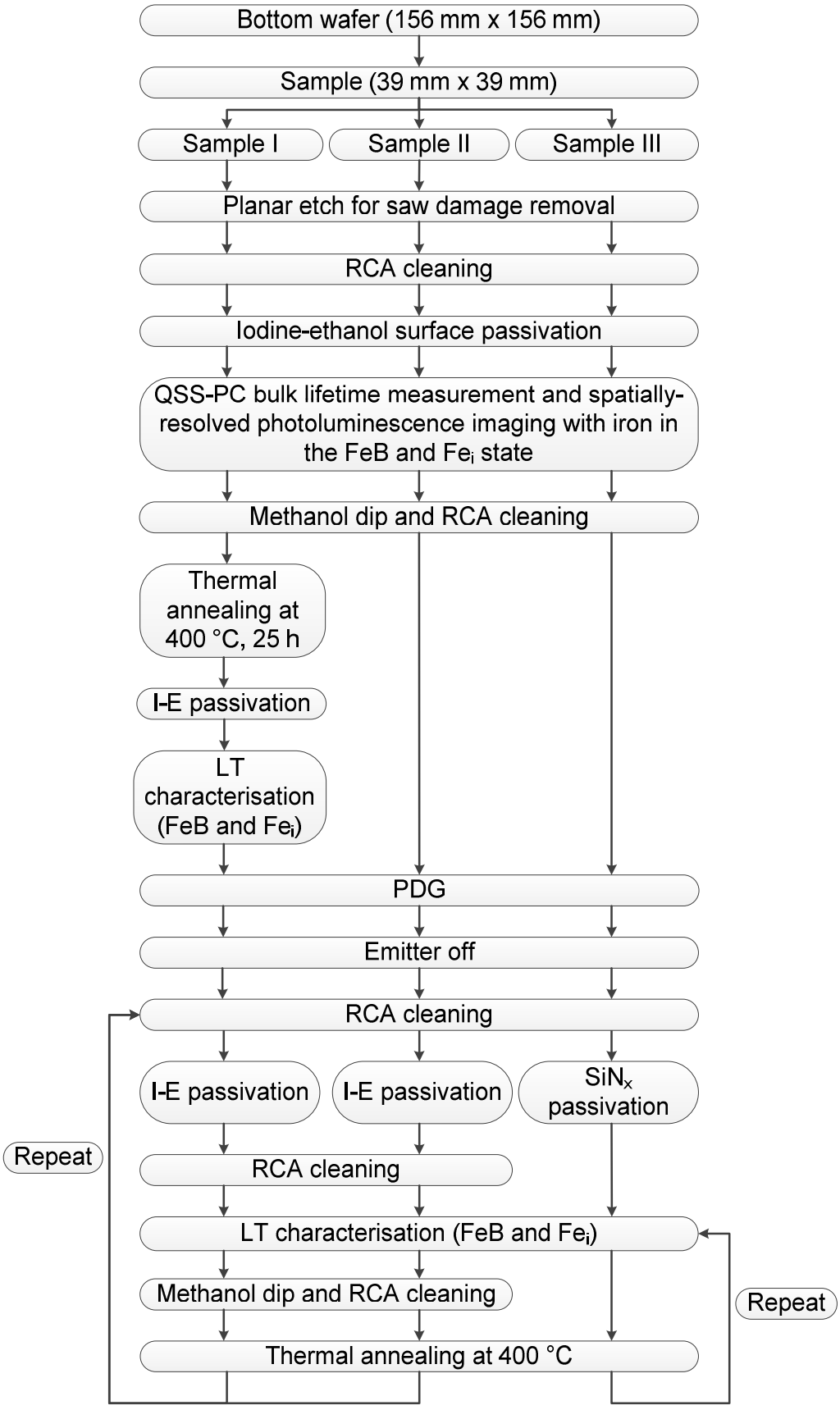

Figure 7.4. Processing and characterisation sequence of low-temperature gettering for the bottom samples after the phosphorus diffusion gettering (PDG) (Experiment C).

7.3. Results

7.3.1. Experiment A: Lifetime changes in post-PDG low-temperature annealing

Figure 7.5 shows the changes in an average bulk lifetime with iron in the FeB state as a function of cumulative time period upon annealing at 300 °C, 400 °C and 500 °C temperatures. Lifetime values are assumed to be accurate to ± 4.3% [177]. Bulk lifetimes in the as-received states vary widely with the ingot height position as expected from Chapter 4. The samples from the bottom part of the ingot show the lowest average lifetime (6 μs). The bottom middle and top middle samples have relatively high average lifetime 68 μs and 36 μs, respectively. The top samples have fairly high average lifetime 11.3 μs compared to the bottom samples. The result shows that the bulk lifetime increases substantially by the PDG process in samples from every height position. The lifetime values after the PDG process are presented by the dashed line plotted on every graph. The most remarkable improvement is observed in the bottom samples where the average lifetime increases to ~60 μs.

After the PDG process lifetime both increases and decreases as a consequence of low-temperature annealing. Lifetime improves in the bottom and top samples upon annealing at 300 °C and 400 °C. The largest improvement is from 54 μs to 78 μs, observed in the bottom sample upon annealing at 300 °C for 50 h of cumulative time. Annealing at 400 °C, lifetime improves by ~ 1.4 times compared to the post-PDG value. In the top samples, lifetime improves by a factor of ~ 1.5 and ~ 1.4 upon annealing at 300 °C and 400 °C, respectively. Annealing at 500 °C, lifetime decreases in both the bottom and top samples. In the samples from the middle part of the ingot, lifetime improves slightly upon annealing at 300 °C. With annealing at 400 °C and 500 °C, both the bottom middle and top middle samples show a lot of scatter in data and do not have an ultimate improvement after 50 h of cumulative time.

The spatial distribution of lifetime with iron in the FeB state at three key stages (as-received, post-PDG and after the final annealing step) for the samples from top, top middle, bottom middle and bottom samples are presented in Figures 7.6(a), 7.6(b), 7.7(a) and 7.7(b), respectively. Different scales are maintained for samples from different height

positions to show the changes in grain features as the lifetime after the PDG process varies widely with ingot height position. In the bottom and top as-received samples, lifetime is very low throughout the samples. Lifetime improves in the bulk grain regions after the PDG process in all the samples. Lifetime improves further in the bulk grain regions in the bottom and top samples upon annealing at 300 °C and 400 °C whereas annealing at 500 °C reduces lifetime compared to the post-PDG values. In the middle samples, lifetime generally falls in the most of the bulk grain regions upon annealing at all three temperatures investigated. These data are discussed in detail in Section 7.4.1 and Section 7.4.2.

7.3.2. Experiment A: Interstitial iron concentration in low-temperature annealing after PDG

The bulk interstitial iron concentration was measured for every sample at every annealing step and presented as a function of cumulative annealing time in Figure 7.8. The as-received bottom samples have the highest average interstitial iron concentration 3×10^{12} cm^{-3}. Samples from the centre parts of the ingot have one order of magnitude low interstitial iron concentration ($\sim 3 \times 10^{11}$ cm^{-3}) compared to the bottom samples. This distribution is similar to those wafers used in Chapter 5 and Chapter 6. After phosphorus diffusion gettering, the interstitial iron concentrations decrease by more than one order of magnitude in most of the samples. The iron concentrations after the PDG are represented by dashed lines in every graph. The largest reduction is observed in the bottom samples which is ~ 5 orders of magnitude compared to the as-received values. Low-temperature annealing after the PDG process does not reduce interstitial iron concentration further in any case. In the top samples, interstitial iron concentrations slightly increase upon annealing at 400 °C and 500 °C. These data are discussed later is Section 7.4.1 and Section 7.4.2.

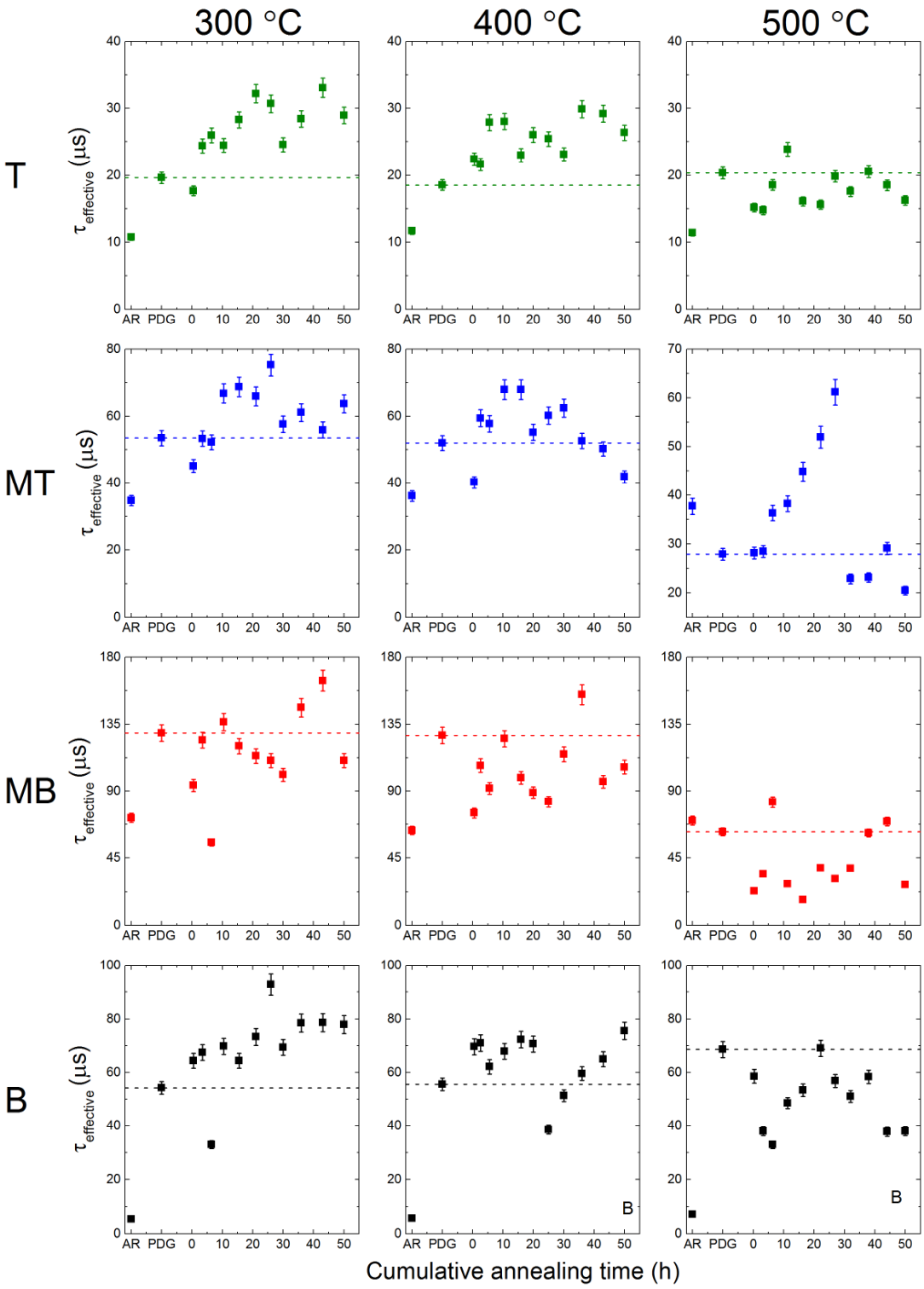

Figure 7.5. Effective minority carrier lifetime with iron in the FeB state measured at an injection level of 1×10^{15} cm^{-3} for samples from the top (T), top middle (MT), bottom middle (MB) and bottom (B) of the mc-Si ingot. As-received (AR) sister samples were processed with standard phosphorus diffusion gettering (PDG) process and emitter layers were removed prior to annealing at 300 °C, 400 °C and 500 °C for the cumulative annealing time shown. The dashed lines represent the lifetime values after PDG.

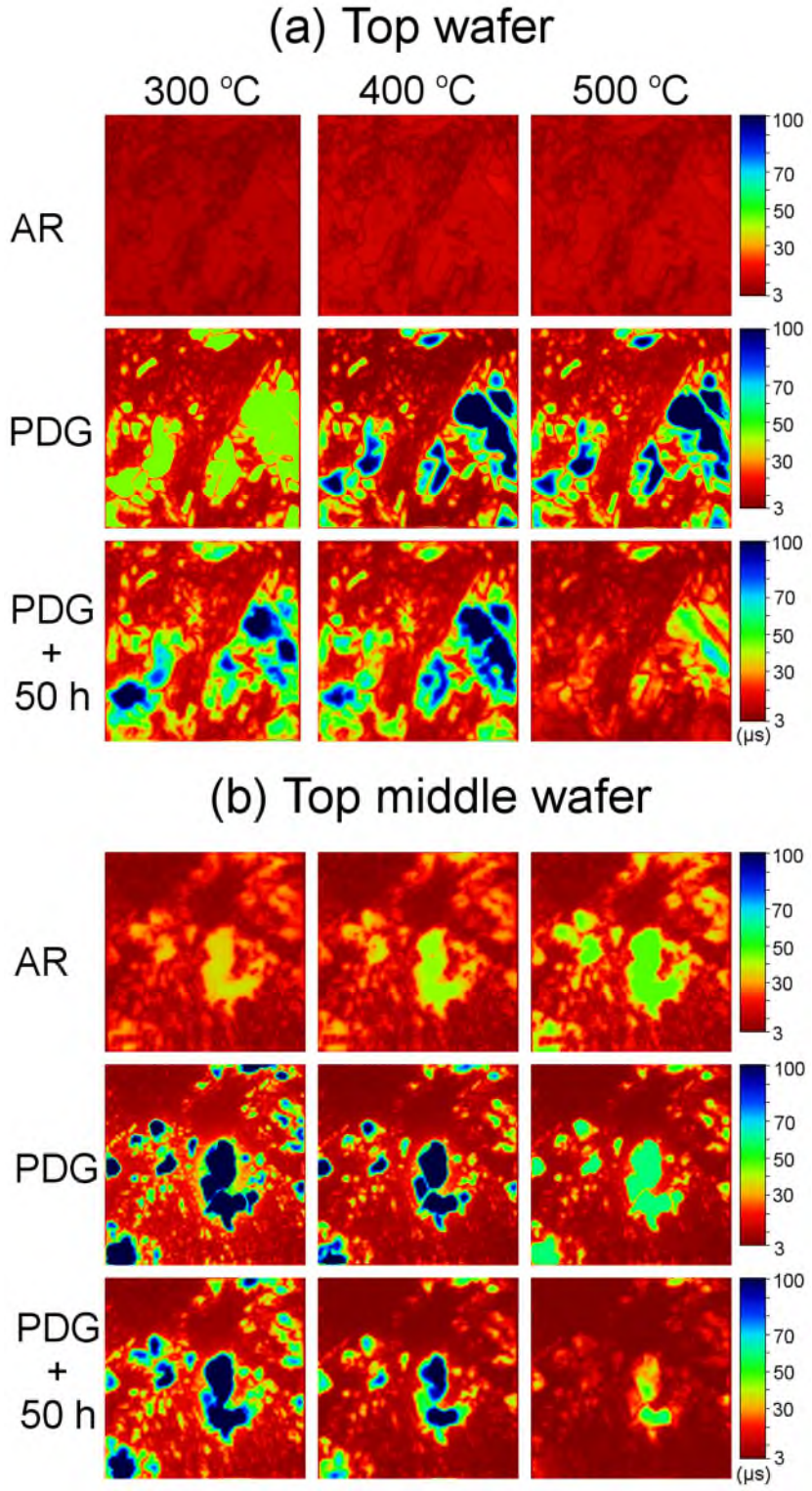

Figure 7.6. Spatial distribution of minority carrier lifetime with iron in the FeB state for sister samples (39 mm × 39 mm) from the (a) top and (b) top middle part of the ingot at as-received (AR), after phosphorus diffusion gettering (PDG) and after subsequent annealing at 300 °C, 400 °C and 500 °C for 50 h of cumulative time. The injection level is lower than the one used in bulk lifetime in Figure 7.5.

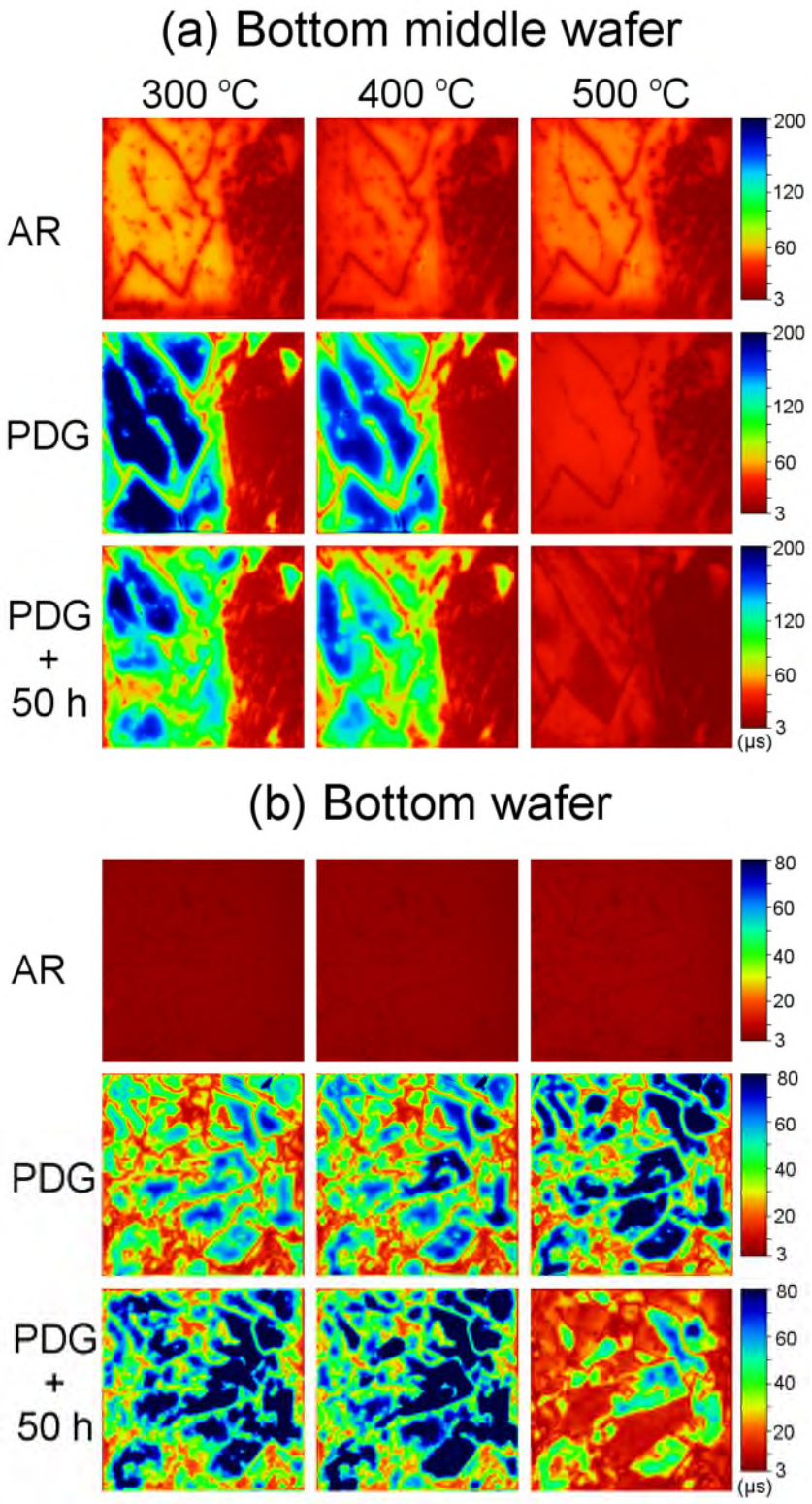

Figure 7.7. Spatial distribution of minority carrier lifetime with iron in the FeB state for sister samples (39 mm × 39 mm) from the (a) bottom middle and (b) bottom part of the ingot at as-received (AR), after phosphorus diffusion gettering (PDG) and after subsequent annealing at 300 °C, 400 °C and 500 °C for 50 h of cumulative time. The injection level is lower than the one used in bulk lifetime in Figure 7.5.

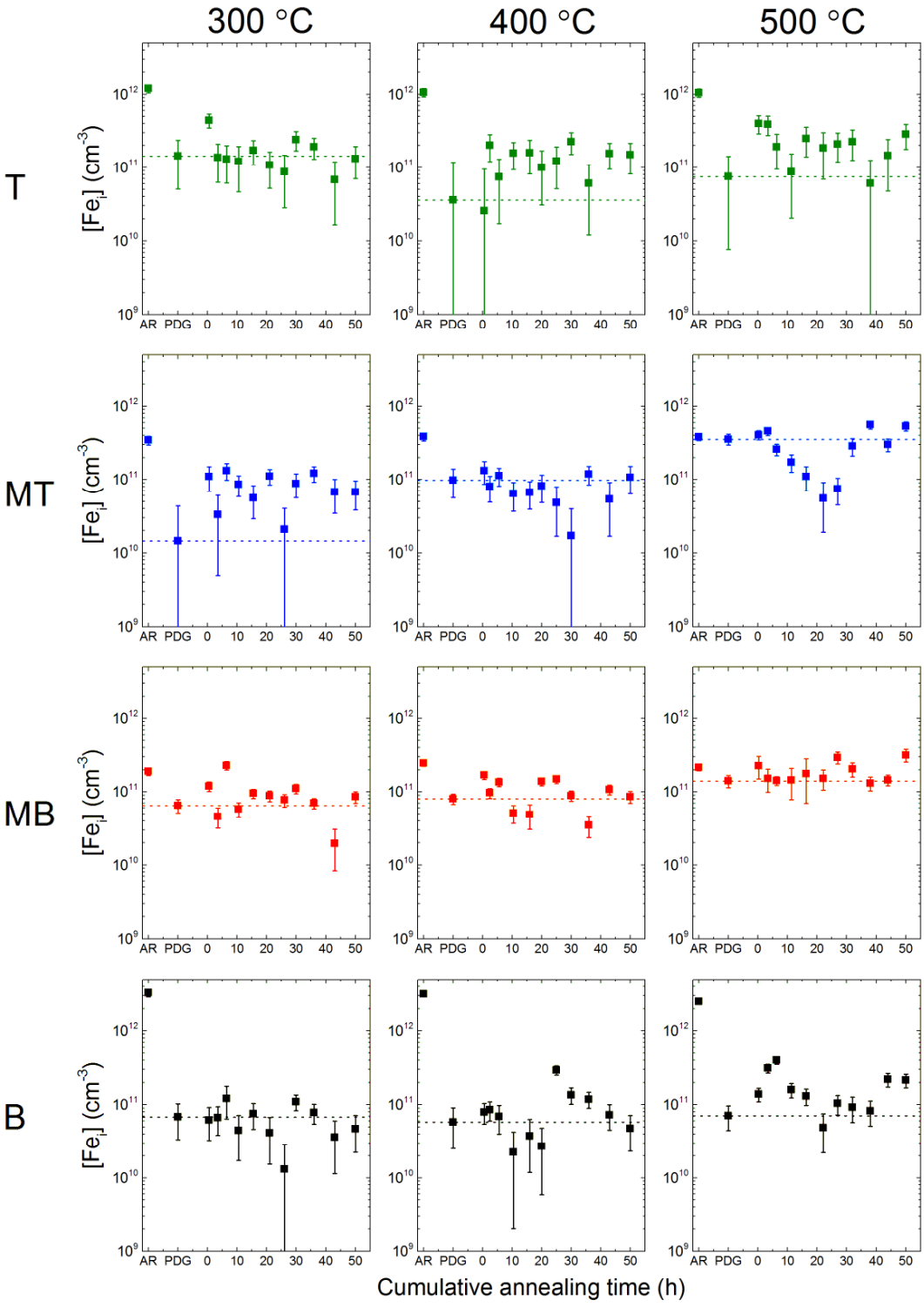

Figure 7.8. Interstitial iron concentration ([Fe$_i$]) from QSS-PC measurement at an injection level of 1×10^{15} cm^{-3} for samples from the top (T), top middle (MT), bottom middle (MB) and bottom (B) of the mc-Si ingot. Sister samples were subjected to phosphorus diffusion gettering and emitter layers were removed before annealing at 300 °C, 400 °C and 500 °C for the cumulative annealing time plotted. The dashed lines represent the values after PDG.

7.3.3. Experiment B: Lifetime and interstitial iron in low-temperature gettering

Figure 7.9 shows the changes in the bulk lifetime and bulk interstitial iron concentration for the samples from four different height positions (T, MT, MB and B) annealed with and without emitter layer at 400 °C. The distribution of as-received lifetime and interstitial iron concentration are similar to those samples used in Experiment A, as shown in Figure 7.5 and Figure 7.8, respectively. The average as-received lifetime is lowest in the bottom samples (~ 5 μs) and the largest in the middle samples. Phosphorus diffusion gettering process improves lifetime substantially, represented by dashed lines in every graph. In the bottom and top samples, PDG process improves lifetime by ~10 times and ~ 2 times, respectively compared to the as-received values. For annealing at 400 °C, there is a lot of scatter in data for the bottom sample (annealed without emitter) but lifetime ultimately improves marginally from 39 μs to 44 μs after 50 h of cumulative time. In the middle sample (annealed without emitter), the result also shows a lot of scatter and it not clear whether substantial stable lifetime improvements are ever realised upon annealing after the PDG process. The samples annealed with emitter layer show both the increase and decrease in lifetime. In the bottom sample, annealing with emitter layers does not show a significant difference compared to the sample annealed without emitter. In the bottom middle and top samples, lifetimes improve marginally upon annealing with emitter layers.

As-received bulk interstitial iron (in Figure 7.9) is the highest (4.7×10^{12} cm^{-3}) in the bottom samples and the lowest (~ 3×10^{11} cm^{-3}) in samples at the centre parts of the ingot. After the PDG process, the interstitial iron concentration decreases substantially in all cases, particularly in the bottom samples where it reduces by ~ 3 order of magnitude compared to the as-received value. Interstitial iron concentration both increases and decreases in samples (without emitter layer) upon annealing at 400 °C for 50 h. There is a lot of scatter in data for sample from every height position. In the bottom sample (annealed without emitter layer), the interstitial iron concentration decreases from 1.6×10^{11} cm^{-3} to 6×10^{10} cm^{-3} after 50 of cumulative time. The interstitial iron concentration remains unchanged in the middle samples whereas it increases slightly in the top samples upon annealing at 400 °C for 50 h. In samples (with emitter layer), interstitial iron

concentration generally decreases marginally upon annealing compared to the PDG values. These data are discussed in detail in Section 7.4.3.

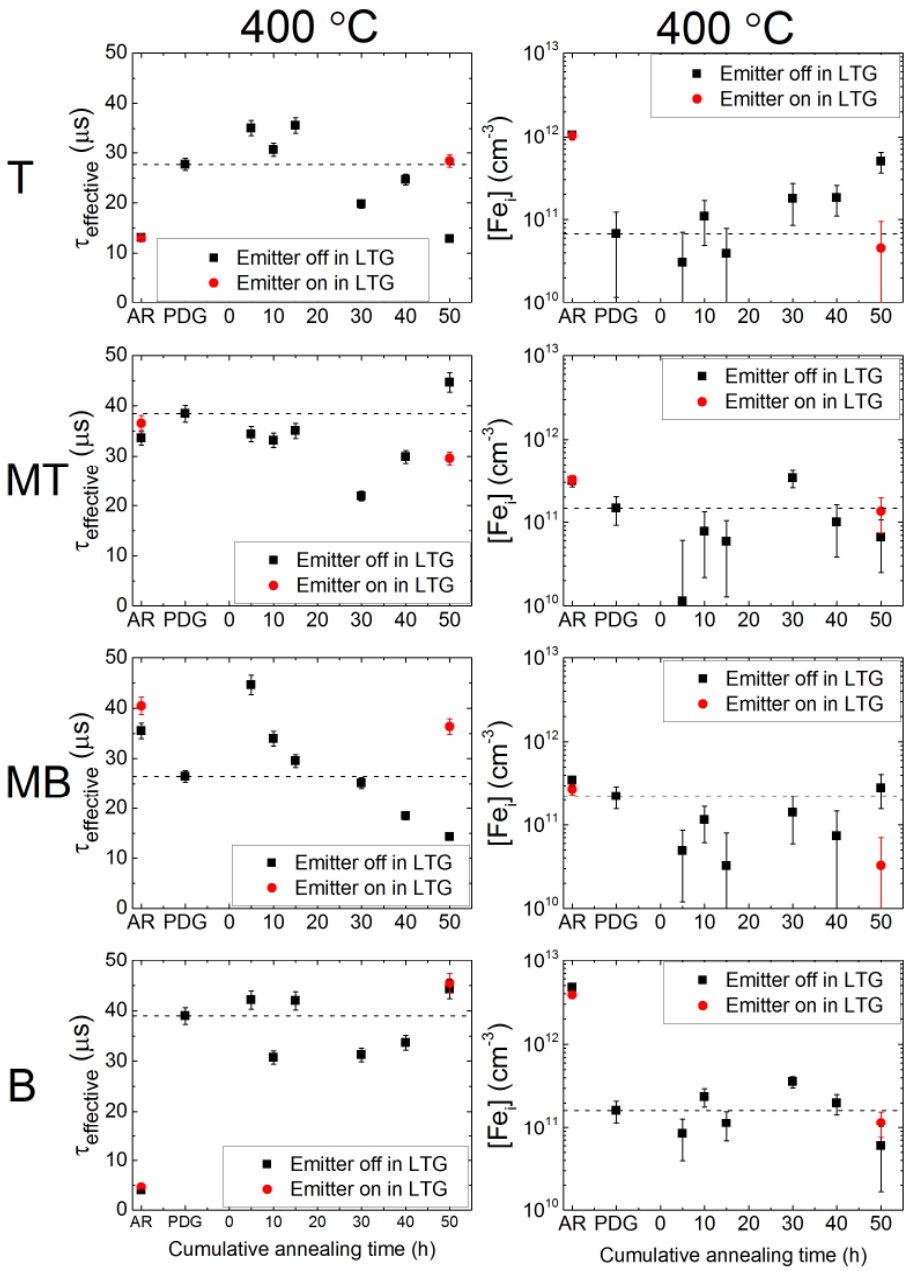

Figure 7.9. Effect of phosphorus diffused emitter on lifetime (with iron in the FeB state) (first column) and interstitial iron concentration (second column) in low-temperature gettering. Two as-received (AR) sister samples from the top (T), top middle (MT), bottom middle (MB) and bottom (B) of the mc-Si ingot were subjected to phosphorus diffusion gettering (PDG) process. Set I and II samples were annealed at 400 °C for the cumulative annealing period shown without and with the emitter, respectively. The dashed lines represent the values after PDG.

7.3.4. Experiment C: Lifetime and interstitial iron changes in prior to and post-PDG annealing

Figure 7.10 shows the changes in the bulk lifetime and interstitial iron concentration in the bottom samples with iodine-ethanol and silicon nitride passivation upon annealing as a function of cumulative annealing time. The average as-received lifetime is 6 ± 2 μs in all three sister samples. In the first sample, as-received lifetime increase from 5.1 μs to 26.1 μs upon annealing at 400 °C for 25 h prior to the PDG process. PDG process improves lifetime substantially in all three samples compared to the as-received values. In the first and second samples, lifetime improves to 82 μs and 68 μs, respectively after the PDG process with I-E passivation. In the third sample, measured lifetime after PDG process is 201 μs with silicon nitride passivation. Note that, the second and third samples were not annealed prior to the PDG process. The lifetime values after PDG are represented by the dashed lines plotted on every graph. The effect of annealing at 400 °C on lifetime is complex. Note that silicon nitride passivation was retained on the third sample during annealing. There is a lot of scatter in the data and do not show an ultimate improvement in lifetime upon annealing in all the three samples.

The average as-received interstitial iron concentration is ~ 3×10^{12} cm^{-3} in all the three bottom samples with I-E passivation. In the first sample, the interstitial iron concentration decreases by ~1 order to magnitude compared to the as-received value upon annealing at 400 °C for 25 h prior to the PDG process. PDG process decreases bulk interstitial iron concentration further to 2.8×10^{10} cm^{-3}, 1.4×10^{11} cm^{-3} and 4.3×10^{9} cm^{-3} in the first, second and third sample, respectively. The bulk interstitial iron concentrations are measured in the first and second samples with iodine-ethanol passivation and in the third sample with silicon nitride passivation. The effect of low-temperature annealing gives a lot of scatter in data points in all the three samples. There is no ultimate reduction in interstitial iron concentration upon annealing in all three cases. These data are discussed in detail in Section 7.4.4.

Figure 7.11 shows the spatial distribution of lifetime images at the key stages for all three samples. The scale is maintained in the first two samples which is different from the scale in the third sample as the lifetime values after the PDG process vary widely. In the as-received states, lifetime is very low throughout the samples. In the first sample,

lifetime increases in most of the bulk grain regions upon annealing at 400 °C for 25 h prior to the PDG process. After PDG process in all three samples, lifetime increases in most the bulk grain regions and becomes worse in the grain boundaries. In the third sample (with silicon nitride passivation), most of the bulk grain regions have lifetime >150 μs where it is ≤ 100 μs for the first and second samples. In post-PDG annealing at 400 °C for 50 h of cumulative time, lifetime appears as increases in some bulk grain regions and decreases or remain unchanged in most the bulk grain regions. These data are discussed in detail later in Section 7.4.4.

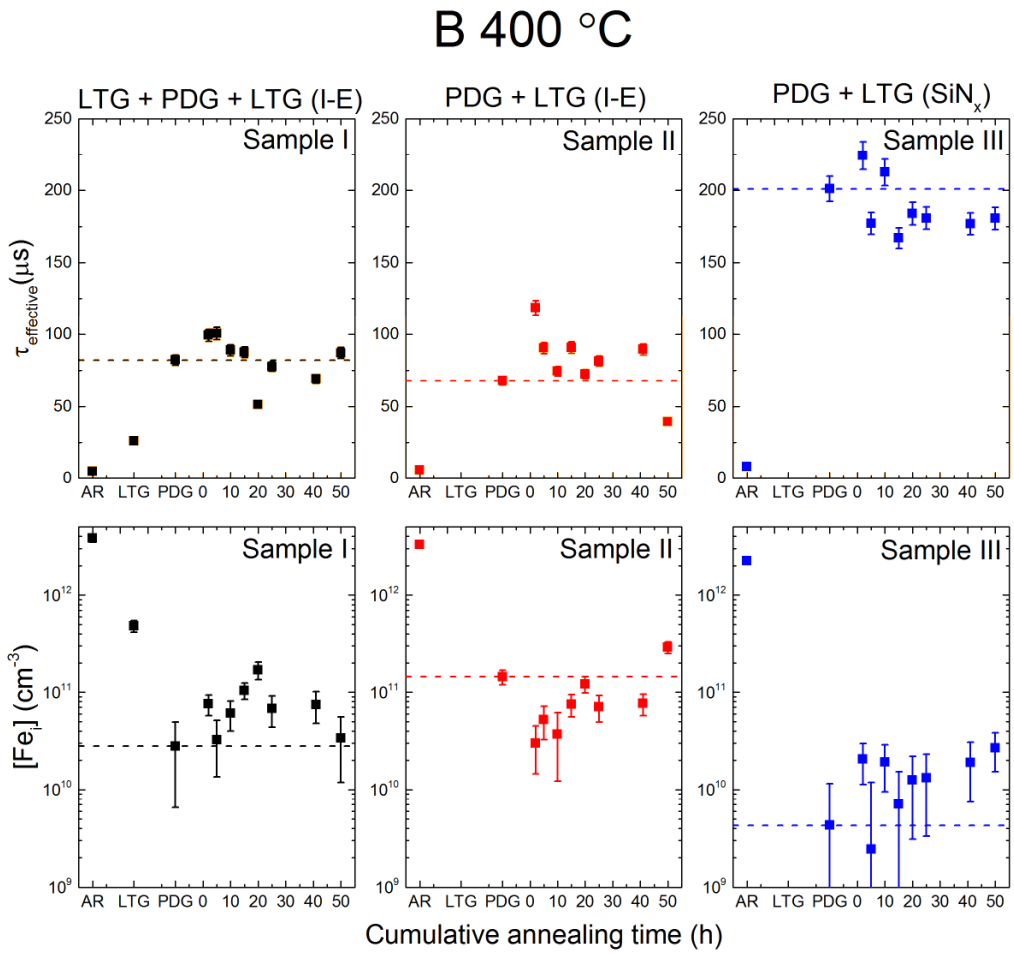

Figure 7.10. A comparison of bulk lifetime and interstitial iron concentration in low-temperature annealing before and after phosphorus diffusion gettering for the bottom samples. The first and second samples were passivated with I-E passivation and the third sample with silicon nitride. The first sample (left column) was annealed at 400 °C for 25 h prior to the PDG. All three samples were annealed at 400 °C for the cumulative annealing time shown. The dashed lines represent the values after PDG process.

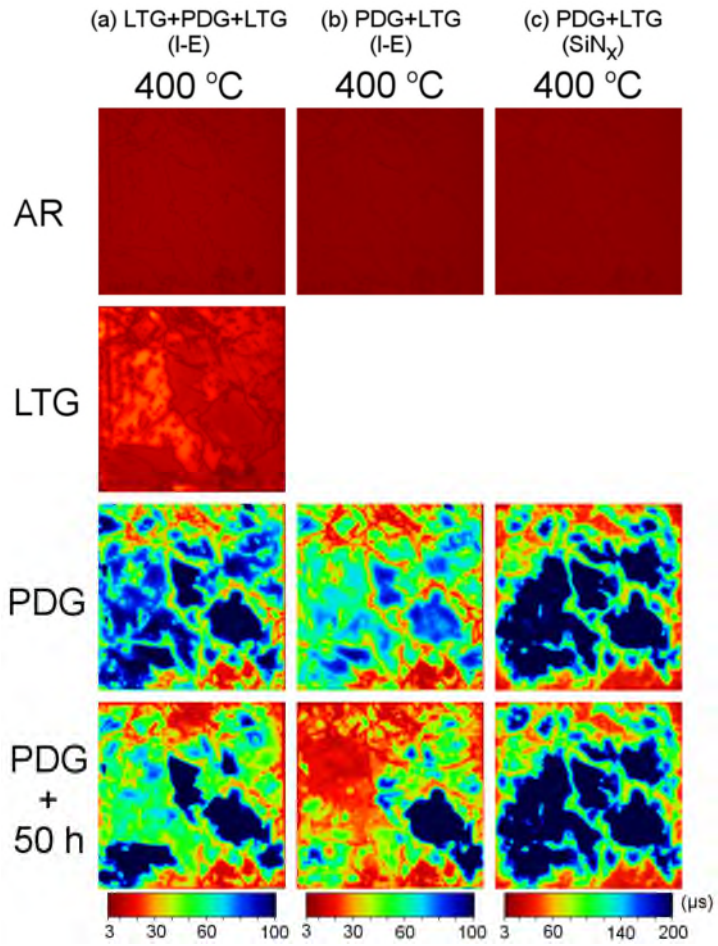

Figure 7.11. Spatial distribution of minority carrier lifetime with iron in the FeB state for three sister bottom samples (39 mm × 39 mm) at different key process stages such as as-received (AR), after low-temperature gettering at 400 °C for 25 h (LTG) prior to phosphorus diffusion gettering (PDG), after PDG and low-temperature annealing at 400 °C for 50 h. The first two samples (a) and (b) are passivated with I-E throughout the process. The third sample (c) is passivated with an I-E solution in the as-received state and with PECVD SiN_x after the PDG process.

7.3.5. Correlation of lifetime and interstitial iron changes in Experiment A

The correlation between lifetime changes and interstitial iron concentration changes is analysed to check whether the interstitial iron concentration is responsible for lifetime changes or not. The change in normalised recombination rate and normalised change in iron concentration with respect to the value after the PDG process was calculated according to:

$$\frac{\frac{1}{\tau_{effective}(t)}-\frac{1}{\tau_{effective}(0_{PDG})}}{\frac{1}{\tau_{effective}(0_{PDG})}}=A\left(\frac{[Fe_i](t)-[Fe_i](0_{PDG})}{[Fe_i](0_{PDG})}\right) \quad (7.1)$$

where *A* is a proportionality function. Figure 7.12 shows plots for the samples (in Figure 7.5 and Figure 7.8) from the different height positions in accordance with Equation 7.1. The diagonal dashed lines represent a 1:1 relationship between normalised recombination rate changes and normalised bulk interstitial iron concentration changes. Annealing at 300 °C, 400 °C, the samples from the centre part of the ingot show some relationship. The relationships are particularly very poor in samples from all four height positions upon annealing at 500 °C.

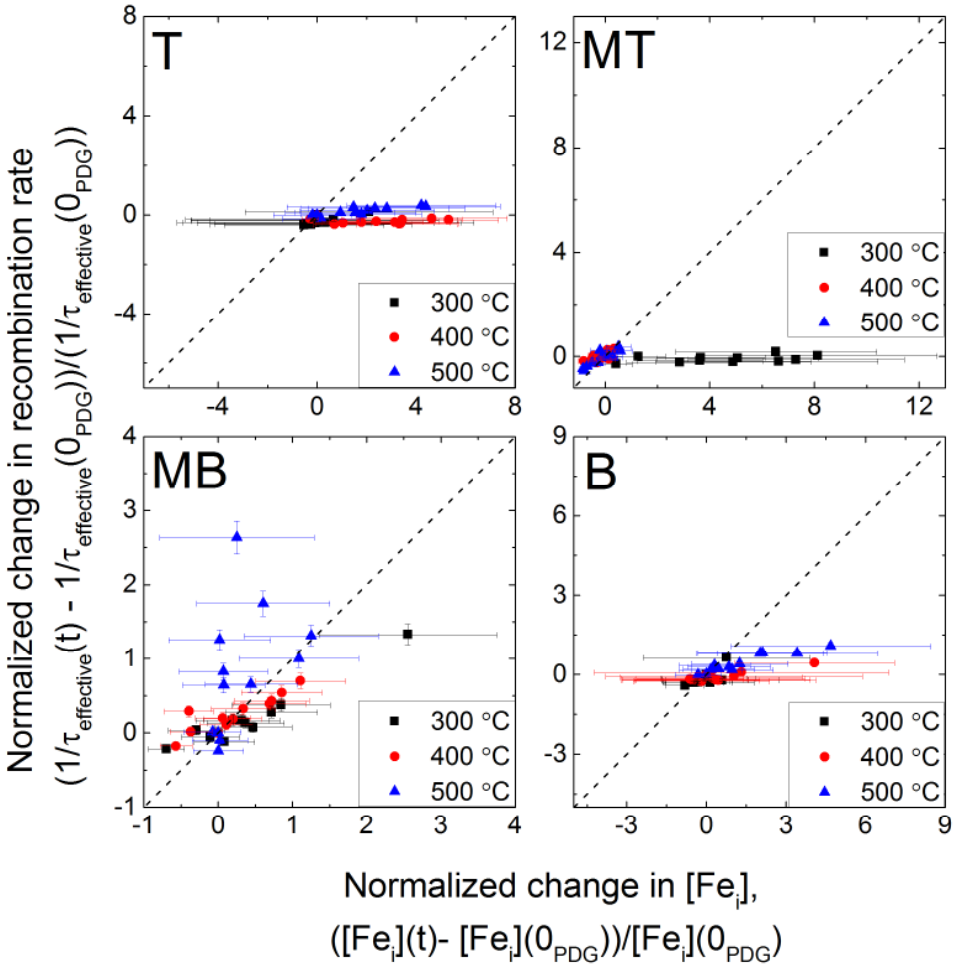

Figure 7.12. Change in recombination rate normalised by recombination rate after PDG versus change in bulk interstitial iron concentration normalised by bulk iron concentration after PDG for samples from the top (T), top middle (MT), bottom middle (MB) and bottom (B) of the mc-Si ingot. The dashed lines represent a 1:1 relationship.

7.4. Discussion

7.4.1. Lifetime and interstitial iron changes in PDG process

In experiment A and B, as-received samples were initially characterised with an I-E passivation then subjected to a standard PDG process. The distribution of bulk lifetime (Figures 7.5 and 7.9) and bulk interstitial iron concentration (Figures 7.8 and 7.9) in the as-received samples are consistent with the distribution found in Section 4.2.1 and Section 4.3.1 in Chapter 4. Lifetime is lowest in the bottom samples and highest in the middle samples. Interstitial iron concentration is highest in the bottom of the ingot, fairly high at the top of the ingot, and relatively low at the middle of the ingot.

Figures 7.5, 7.8 and 7.9 show that the PDG process improves the bulk lifetimes and reduces interstitial iron concentration substantially in samples from all four height positions in the ingot. The most remarkable improvement is observed in the bottom sample which is ~10 times higher compared to the as-received value. In the bottom middle, top middle and top samples, PDG process improves lifetime by ~ 2 times, ~ 1.5 times and ~ 2 times compared the as-received values, respectively. It is important to note that emitter layers were removed from the surfaces to measure bulk lifetime. As I-E passivation was used, these results do not have an additional effect (*e.g.* bulk hydrogenation) from the surface passivation. The bulk iron concentration decreases substantially by the PDG process in all cases, particularly in the samples from the bottom part of the ingot. In the best case, interstitial iron concentration is decreased by ~5 orders of magnitude compared to the as-received value in the bottom sample which is consistent with the findings reported in Phang and Macdonald [131]. The top samples show a relatively low reduction in interstitial iron concentration upon the PDG process compared to the bottom samples. One possible reason is the relatively low dislocation density in the bottom samples compared to the top samples, as discussed in Chapter 4. The spatial distribution of lifetime after the PDG process (presented in Figure 7.6 and 7.7) shows that lifetime improves in most of the bulk grain regions, which is similar to the findings in Bentzen *et al.* [35]. Grain boundaries become more visible after PDG process which indicates gettering of impurities during PDG process and thus increases in detectable recombination contrast. The middle samples (in Figure 7.6(b) and 7.7(a)) used for

annealing at 500 °C show no improvement upon the PDG process compared to their sister samples. This discrepancy could be a result of a deviation in the standard PDG process.

7.4.2. Lifetime and interstitial iron at post-PDG low-temperature annealing (Experiment A)

Figure 7.5 shows the changes in the average lifetime by annealing at all temperatures investigated for samples from all four height positions in absence of emitter layers. Samples are annealed without surface passivation and re-passivated with a freshly made iodine-ethanol solution at every annealing step. Therefore, the changes in the bulk lifetime is a result of thermal effect only and bulk hydrogenation is not involved. Low-temperature annealing on samples after PDG affects lifetime, with both increases and decreases are observed. The bottom and top samples show a similar behaviour where lifetime is improved upon annealing at 300 °C and 400 °C. The largest improvement is in the bottom sample at 300 °C when 50 h of cumulative annealing increases the lifetime from 54 μs to 78 μs. Annealing at 400 °C, the lifetime improves from 56 μs to 76 μs in the bottom sample. In the top samples, lifetime improves by ~ 1.5 and ~ 1.4 times compared to the post-PDG values. The improvement is not consistent with annealing temperature and time. It can, therefore, be concluded that lifetime improvement is not due to temperature dependent diffusion of metallic impurities to the crystallographic defects. Annealing at 500 °C, lifetime decreases in both the top and bottom samples in primary annealing steps and does not show an overall improvement after the final annealing step. The bottom middle and top middle samples show a different behaviour compared to the bottom and top samples. The data points are scattered in both the cases and show a complex relationship. Lifetime decreases abruptly upon the primary annealing steps at all three annealing temperatures. It is interesting to note that the lifetime improves in the top middle samples upon primary annealing at all three temperatures and starts decreasing upon further annealing steps. Annealing in the bottom middle samples does not show an ultimate improvement upon annealing at all temperatures investigated.

Figure 7.8 shows an ultimate change in the average interstitial iron concentration in the samples from all the height positions. Note that there is a small change in lifetime before and after dissociation of FeB pairs and it is almost constant over annealing time period. Although there is some scatter in the data, no decay in interstitial iron

concentration is observed in any case compared to the post-PDG values. Surprisingly, in the top samples, interstitial iron concentration increases slightly upon primary annealing steps at 400 °C and 500 °C and remains unchanged upon further annealing. Whilst low-temperature annealing reduces iron concentration for as-received samples (as discussed in Chapter 5 and Chapter 6), the effect of low-temperature annealing after the PDG process is likely to be less effective in reducing interstitial iron concentration further. Note that the bulk interstitial iron concentrations after the PDG process are generally lower compared to the concentrations found after the final annealing step in Chapter 5 and Chapter 6. Interstitial iron concentration increases in some cases upon annealing after the PDG could be attributed to release of interstitial iron from the grain boundaries. This result is contrary to those found in Schön *et al.* [215] which reported a reduction in interstitial iron by more than one order of magnitude reduction in post-PDG low-temperature annealing with silicon nitride passivation. This discrepancy could be attributed to silicon nitride passivation dielectric layer as it stongly affects interstitial iron concentration, as discussed in Chapter 6 and in Ref. [54]. A comparative study between iodine-ethanol and silicon nitride passivations in low-temperature gettering after PDG process is discussed in Section 7.4.4. The effects of low-temperature annealing in the top middle and bottom middle samples are similar. There is no reduction in interstitial iron concentration in any cases compared to the post-PDG values. Perhaps surprisingly, interstitial iron concentration increases slightly upon annealing at 300 °C in the top middle sample.

Spatially resolved lifetime images were acquired at each processing step for every sample. The changes spatial distribution of lifetime at three key stages (as-received, after phosphorus diffusion gettering and after subsequent annealing for 50 h) in the top and bottom samples upon annealing at all three temperatures are shown in Figure 7.6(a) and Figure 7.7(b), respectively. Lifetime is initially low in the bulk grain regions and very low at certain grain boundaries in samples from both the positions. Lifetime increases in certain bulk grain regions after the PDG process. It is important to note that recombination contrast at most of the grain boundaries apparently become more visible after the PDG process which indicates that a certain level of *internal* gettering also occurs during the PDG process. In post-PDG annealing, the average lifetime is high in most of the bulk grain regions for the bottom samples annealed at 300 °C and 400 °C whereas in the top samples few bulk grain regions show high average lifetime time. This could be attributed

to high dislocation density in samples from the top part of the ingot compared to the bottom part of the ingot, as presented and discussed in Chapter 4. Annealing at 500 °C does not show a substantial reduction in lifetime in most of the bulk grain regions in both sample types. It is likely that annealing at 500 °C has caused an injection of impurities in some bulk grain regions. The spatial distribution of lifetime for the top middle and bottom middle samples are shown in Figure 7.6(b) and Figure 7.7(a), respectively. Lifetime after PDG process is high in most of the bulk grain regions in the bottom middle samples and in some bulk grain regions in the top middle samples. The average lifetime after the last annealing step is decreased marginally in most of the bulk grain regions. The defective regions do not show any improvement in lifetime upon annealing at all three temperatures.

Figure 7.12 shows the correlation between change in recombination rate (reciprocal lifetime) normalised by post-PDG value and change in interstitial iron concentration normalised by post-PDG value. At all temperatures investigated, lifetime improvements do not correlate with changes in interstitial iron in samples from all the height positions. This means lifetime improvement in the bottom and top samples upon annealing at 300 °C and 400 °C cannot be explained by changes in interstitial iron concentration. This indicates that defects other than interstitial iron are gettering at low-temperature annealing. In annealing at 500 °C, lifetime degrades compared to the PDG value whereas interstitial iron concentration remains unchanged in samples from all the height position investigated. This indicates an increase in recombination activity due to other defects than interstitial iron upon annealing at 500 °C.

7.4.3. Effect of emitter in post-PDG low-temperature annealing (Experiment B)

Figure 7.9 shows the effective lifetime and interstitial iron concentration in two sister samples subjected to post-PDG low-temperature gettering at 400 °C. In the first set of samples, the emitters were removed prior to annealing whereas they were retained for annealing in the sister samples. As the samples from every height position have an identical microstructure and were subjected to the same thermal treatment, any difference in lifetime and interstitial iron concentration could be attributed to the presence of emitter layer during thermal annealing. The result shows that effects of emitter layers on the bulk

lifetime and interstitial iron concentration is not straightforward. In the bottom samples, the effect of the emitter on lifetime improvement and interstitial iron concentration reduction is marginal at 400 °C for 50 h of cumulative annealing. The middle samples show both increases and decreases in lifetime in samples annealed with emitter compared to the samples annealed without the emitter. The top samples show different behaviour compared to bottom samples. Lifetime decreases slightly and interstitial iron concentration increases upon annealing in samples without emitter whereas no significant change is observed in sample annealed with the emitter. These findings indicate that the presence of phosphorus diffused emitter during low-temperature annealing has a very poor perhaps no effect in improving lifetime and reducing interstitial iron concentration. This result is contrary to those found by Rinio *et al.* [51] which concluded *external* gettering to the emitter was more likely to be responsible for lifetime improvement than *internal* gettering. This discrepancy could be a result of using different passivation schemes as their work used silicon nitride passivation and having different microstructures.

7.4.4. Effect of pre-PDG annealing and passivation in post-PDG low-temperature gettering (Experiment C)

The effects of low-temperature annealing and effects of two different passivation schemes (I-E and SiN_x) at annealing for as-received samples are discussed in Chapter 5 and Chapter 6. Figure 7.10 shows the changes in lifetime and interstitial iron concentration upon annealing at 400 °C prior to PDG and post-PDG process for the bottom samples using I-E and SiN_x passivations. The result in this study (Figure 7.10 and Figure 7.11) focuses on the following investigations:

(i) Repeatability in lifetime improvement and interstitial iron concentration reduction for the as-received bottom samples upon annealing at the best condition (400 °C) found in Chapter 5.

(ii) Effects of the standard PDG process on the bulk lifetime and interstitial iron concentration and to find whether low-temperature annealing prior to PDG process can improve lifetime further in the PDG process.

(iii) Effects of silicon nitride passivation on the bulk lifetime and interstitial iron concentration after the PDG process and in the subsequent low-temperature annealing at 400 °C compared to the I-E passivation.

The as-received lifetime and interstitial iron concentration with the I-E passivation are 6 μs and 3.12×10^{12} cm^{-3}, respectively. This is consistent with the distribution presented in Chapter 4. The pre-PDG annealing at 400 °C in the first sample improves lifetime by ~ 5.1 times and reduces interstitial iron concentration by ~ 0.8 order of magnitude compared to the as-received values, which is consistent with the findings discussed in Chapter 5. Phosphorus diffusion gettering improves lifetimes and reduces interstitial iron concentration substantially in all three samples. In the first sample, lifetime is found as 1.2 times higher and interstitial iron concentration is lower by ~ 0.5 order of magnitude compared to the second sample after PDG process. As both the samples are passivated with I-E passivation in lifetime measurement, the difference could be attributed to pre-PDG low-temperature annealing applied in the first sample. This means applying low-temperature annealing in as-received samples can improve further in PDG process.

It is discussed in Chapter 4 that silicon nitride passivation in the as-received samples can give higher lifetime compared to I-E passivation. A substantial difference in lifetime and interstitial iron concentration is also observed with I-E and SiN_x passivation schemes after PDG process. The lifetime in the third sample (with silicon nitride passivation) is higher by 3 times and interstitial iron concentration is lower by ~ 3.3 order of magnitude compared to the values in the second sample (with I-E passivation). As both the samples (second and third) have an identical microstructure and are not subjected to any thermal treatment prior to the PDG process, the discrepancy in lifetime after the PDG process is a result of using different passivation schemes. It can, therefore, be suggested that SiN_x deposition process can passivate a high concentration of interstitial iron concentration. This confirms the findings presented in Chapter 6 where possible effects of silicon nitride passivation are discussed.

In post-PDG annealing at 400 °C, all the three samples show no further improvement in lifetime compared to lifetime values after the PDG process. This is likely to be a contrary to the results found in Experiment A. It is interesting to note that the lifetime in the third sample decreases slightly which could partially be attributed to degradation in SiN_x passivation during low-temperature annealing. The result also indicates no

hydrogenation effect occurs in low-temperature annealing after the PDG process. The evolution of interstitial iron concentrations in post-PDG annealing at 400 °C shows a fairly scattered behaviour in all the three samples. However, there is not an overall reduction in interstitial iron concentration after the final annealing step in all the cases. This finding is consistent with the results found in Experiment A (discussed in Section 7.4.2). However, it requires further investigation at what conditions lifetime can be improved by a low-temperature annealing even after PDG process.

Figure 7.11 shows the evolution of the spatially resolved lifetime at four key stages. In the as-grown samples, the lifetime is initially low in the bulks of the grains and very low at certain grain boundaries. With the pre-PDG annealing, lifetime improves, particularly in the bulks of the grains in the first sample. Lifetime improves substantially in most of the bulk grain regions in all cases. In annealing, lifetime decreases in some bulk grain in regions in the first and second samples whereas lifetime remains almost unchanged in the third sample. A similar observation for as-received samples is discussed in Chapter 6 where silicon nitride is likely to prevent the formation of the recombination centres which form with I-E passivation.

7.5. Conclusion

A comprehensive study was performed on the effect of low-temperature annealing on bulk lifetime and interstitial iron concentration in samples after the phosphorus diffusion gettering process. In the first set of experiment, samples sourced from four different positions are annealed at 300 °C to 500 °C using I-E passivation. Relatively poor samples from the bottom and top part of the ingot show a lifetime improvement upon annealing at 300 °C and 400 °C. The largest improvement was achieved from 54 μs to 73 μs in the bottom sample annealed at 300 °C for 50 h cumulative time. The samples from the middle part of the ingot do not show an overall improvement in any case in post-PDG annealing. There is no overall reduction in interstitial iron concentration and do not show a correlation with lifetime improvement in all samples and temperature investigated. The lack of correlation with interstitial iron shows that other defects can also play a role.

In the second set of experiment, *external* gettering of interstitial iron to phosphorus diffused emitter layers for samples four different height positions are investigated upon

annealing at 400 °C. The effect of phosphorus diffused layer is not straightforward as lifetime was both increased and decreased. In relatively poor lifetime samples, particularly in the bottom sample, the presence of emitter layer during annealing process does not play a significant influence on the bulk lifetime improvement.

In the third set of experiments, the effect of low-temperature annealing in pre-PDG and post-PDG was investigated in the bottom samples using both the iodine-ethanol and silicon nitride passivation schemes. Lifetime is improved in the pre-diffusion annealing process by a factor of 5.1 compared the as-received value. Lifetime and interstitial iron concentration after phosphorus diffusion process strongly depend on the passivation scheme used. The post-diffusion annealing process does not show an overall lifetime improvement in both the passivation schemes.

In summary, the results demonstrate that PDG process improves lifetime substantially. Post-diffusion low-temperature gettering has the potential to improve lifetime further particularly in poor lifetime samples. Lifetime improvements do not correlate with changes in interstitial iron, so gettering of another impurity is likely. Passivation scheme might play a vital role in improving lifetime and in reducing interstitial iron concentration even after the PDG process.

Chapter 8 Conclusions

8.1. Introduction

In this thesis, a series of experiments was performed into the effect of low-temperature (≤ 500 °C) annealing on multicrystalline silicon materials with the aim to improve bulk carrier lifetime. As-received samples were sourced from different height positions of a commercially grown ingot. The effect of low-temperature annealing and the effect of surface passivation schemes were investigated for as-received samples in Chapters 5 and 6, respectively. The effect of low-temperature annealing after performing standard phosphorus diffusion gettering process was also investigated in Chapter 7. Samples from every height position were characterised by bulk lifetime, interstitial iron concentration, dislocation density mapping, spatially resolved lifetime imaging, interstitial iron mapping. In the following sections, the key findings and suggestions for potential follow-up work are presented.

8.2. Summary

8.2.1. Distribution of properties in as-received multicrystalline silicon ingot

Results presented in Chapter 4 focus on the distribution of average bulk minority carrier lifetime and bulk interstitial iron concentration for multicrystalline wafers sourced from four different height positions (top (T), top middle (MT), bottom middle (MB) and bottom(B)) of an edge block from a commercially-grown boron doped ingot. It is found that the average as-received lifetime varies widely with ingot height position. The average

lifetime is lowest at the bottom (~ 5 μs) and top wafers (~12 μs) with iodine-ethanol passivation scheme. With the same I-E passivation, in the top middle and bottom middle samples, the average lifetimes are 28 μs and 44 μs, respectively. The lifetime distribution observed in this Chapter is consistent with previous studies [161, 193]. Sister samples at every height position show the same characteristics. The results show that surface passivation schemes affect the starting lifetime measurement substantially. The silicon nitride passivation scheme shows higher average bulk lifetime and lowers iron concentration compared to the I-E passivation scheme in samples from all the height positions, with the difference more pronounced for the middle samples. The biggest difference is observed in the bottom middle samples where the average bulk lifetime is 114.2 μs with silicon nitride passivation compared to 44.3 μs with I-E passivation scheme. The results show that this is not due to a substantial difference in surface recombination velocity. One possibility is that this is due to bulk hydrogenation from silicon nitride films deposition method.

The interstitial iron concentration also varies widely with the ingot height position and passivation scheme used. The highest average concentration found with I-E passivation was in the bottom samples and was 3×10^{12} cm^{-3}. The average concentrations in samples of the centre part of the ingot are substantially lower (2×10^{11} cm^{-3}) and fairly high in top samples (1×10^{12} cm^{-3}). The trend found in this work is consistent with other studies [16, 92, 194]. Silicon nitride passivation affects as-grown interstitial iron concentration in compared to the I-E passivated samples. A substantial difference (more than one order of magnitude) in interstitial iron concentration is found in samples from the centre part of the ingot with silicon nitride passivation. This is possibly due to bulk passivation during the silicon nitride treatment (perhaps by hydrogen). The average iron concentration in the bottom and top samples are similar with both the passivation scheme.

The distribution of crystallographic defects such as grain boundaries and as-grown dislocations are also discussed in Chapter 4. The top and top middle part have high dislocation density compared to the bottom and bottom middle part of the ingot, which is consistent with the findings in Ryningen *et al*. [66]. Although the bottom samples have a relatively low density of dislocations, poor lifetime is found partially due to having a relatively high interstitial iron concentration. Photoluminescence images for samples from different height positions suggested that areas with higher dislocations density show

very low PL signals. Twin boundaries are found in samples at every height position which do not appear as recombination active in PL imaging.

8.2.2. Low-temperature gettering in as-grown samples

Results presented in Chapter 5 discuss the effects of low-temperature annealing (300 °C, 400 °C and 500 °C) in multicrystalline silicon wafers. The results show, for the first time, that low-temperature annealing can dramatically improve the carrier lifetime in mc-Si materials. A temporary iodine-ethanol passivation scheme was used at room temperature prior to lifetime characterisation and removed afterwards to avoid any complexity arising from the passivation scheme. Unlike previous studies [36, 48, 50, 51] the results of this study are a representation of the effects of thermal annealing on lifetime and interstitial iron concentration. Lifetime improves substantially in relatively poor samples in all three annealing temperatures and it shows a correlation with the reduction in interstitial iron concentration. The best result was achieved in the bottom sample upon annealing at 400 °C for 35 h where lifetime improves from 5.5 μs to 38.7 μs. Like the bottom sample, in the top sample, the best result was achieved from 12.1 μs to 23.8 μs upon annealing at 400 °C. The lifetime improvement in the middle samples was found marginal. Upon annealing at 400 °C and 500 °C, lifetime is decreased substantially in primary annealing steps in both the bottom middle and top middle samples and followed by a slow recovery.

The evolution in the bulk interstitial iron concentration is not straightforward and not consistent with those findings in previous work by Krain *et al*. [36]. The decay in interstitial iron concentration is not systematically dependent on annealing time and temperature. The decay rate is not determined only by the diffusion of interstitial iron to crystallographic defects. Bulk interstitial iron concentration is surprisingly increased in primary annealing step in many cases particularly in the high lifetime samples from the centre part of the ingot, despite the interstitial iron concentration being well above the solubility limit. Although a slow recovery is found, no overall improvement is observed compared to the as-received states. The relations between the normalised changes and normalised changes in bulk iron concentration shows a linear relationship in the bottom samples only. Samples from the other part of the ingot show a little perhaps no relationship.

8.2.3. Effect of passivation in low-temperature gettering

Results presented in Chapter 5 show a stark contrast to a similar study by Krain *et al*. [36] who used silicon nitride passivation. It is therefore concluded that the surface passivation layer might play a vital role in improving lifetime and reducing interstitial iron concentration in low-temperature annealing. Results presented in Chapter 6 demonstrate a quantitative analysis on the effects of with silicon nitride and iodine-ethanol passivation on bulk lifetime and interstitial iron concentration upon annealing at low-temperature (300 °C, 400 °C or 500 °C). The results suggest that passivation scheme can make a substantial difference in as-grown lifetime values (discussed in Chapter 4) and in low-temperature annealing. Lifetime improves with silicon nitride passivation scheme for samples from all the height positions compared to the iodine-ethanol passivation scheme. In poor samples from the bottom part of the ingot, the largest lifetime improvement is from 7.2 μs to 27.5 μs upon annealing at 500 °C for 60 h of cumulative time. A substantial difference is observed in the bottom middle samples where lifetime improves from 113 μs to 171 μs upon annealing at 400 °C.

The results show that silicon nitride passivation strongly affects the bulk interstitial iron concentration in low-temperature annealing compared to the I-E passivation scheme. This finding is consistent with the study of Karzel *et al*. [137], who used quinhydrone-methanol passivation at room temperature (similar to I-E passivation in this study). A different response is observed for samples from different height positions in the ingot. In the bottom and top samples, the decay rate in interstitial iron concentration is similar in both the I-E and SiN_x passivation schemes. In the middle samples, the effect of passivation is clearly visible where interstitial iron concentration reduces substantially upon annealing at 400 °C. The secondary ion mass spectrometry (SIMS) result shows, for the first time, that high iron concentrations ($> 1\times10^{16}$ cm^{-3}) exist in the SiN_x film after low-temperature annealing. The results suggest that lifetime improvement in low-temperature annealing with silicon nitride passivation scheme is complicated and multiple mechanisms including bulk hydrogenation, diffusion of metallic impurities to crystallographic defects, *external* gettering to the passivation layer are involved. It is, therefore, concluded that lifetime and interstitial iron concentration in low-temperature annealing depend upon passivation scheme but to understand exact mechanisms further experiments need to be performed.

8.2.4. Improving lifetime by low-temperature gettering after phosphorus diffusion gettering

The results presented in Chapter 7 show effects of low-temperature gettering after performing a standard phosphorus diffusion gettering process. The PDG process improves lifetime and reduces interstitial iron concentration remarkably. The largest lifetime improvement was found by a factor of ~10 compared to the as-received values in the bottom sample. Interstitial iron concentration reduces by more than one order of magnitude by PDG process in most cases. The post-diffusion low-temperature gettering suggested that lifetime can be improved further particularly in relatively poor samples from the bottom and top part of the ingot at 300 °C and 400 °C. The results show that lifetime improvement is not due to a reduction in interstitial iron concentration. It is concluded that low-temperature annealing has a potential to improve lifetime even after phosphorus diffusion gettering where gettering of other impurities is likely.

The results presented in Chapter 7 are also suggested that effect of phosphorus diffused layer in low-temperature annealing has a minimal effect on reducing interstitial iron concentration. Although samples from different height positions show different behaviours, phosphorus diffused layer has minimal effect in relatively poor lifetime samples from the bottom part of the ingot. It is, therefore, concluded that phosphorus diffused layer does not act as an effective *external* gettering site for interstitial iron concentration upon low-temperature annealing at 400 °C. This finding is not consistent with the study by Rinio *et al*. [51] who concluded *external* gettering to the emitter was more likely to be responsible for lifetime improvement than *internal* gettering.

The final set of results presented in Chapter 7 shows changes in the lifetime and interstitial iron concentration in pre-PDG and post-PDG annealing at 400 °C for the bottom samples. Lifetime improves by a factor of ~ 5 and interstitial iron concentration reduces by ~ 1 order of magnitude upon pre-PDG annealing at 400 °C for 25 h of cumulative time. PDG process improves lifetime in all the samples substantially. The sample with pre-PDG annealing exhibits higher lifetime after the PDG process compared to the sample without a pre-PDG annealing. Lifetime and interstitial iron concentration after the PDG process strongly depend upon passivation type.

8.3. Further work

8.3.1. Iodine-ethanol passivation study

In this thesis, a temporary liquid iodine-ethanol passivation scheme was used at room temperature before every lifetime characterisation process. It is necessary to investigate the mechanism of the I-E passivation scheme. The primary experiment shows that the stability of passivation quality suffers after first few minutes of passivation. Sopori *et al.* [152] reported that iodine-ethanol passivation improves lifetime further under illumination. As the interstitial iron concentration measurement technique involves more than 50 number of intense flashing to dissociate iron-boron pairs, an extensive study needs to be performed on iodine-ethanol passivation under illumination. Single crystal silicon wafers can be used to avoid any complexity arise from the bulk material. Furthermore, it is also important to investigate at what conditions stability of I-E passivation can be improved. Sopori *et al*. [151] suggested that iodine-ethanol passivation leaves some iodine residue on the surface which strongly depends on surface preparation. In this thesis, an investigation was made under an optical microscope whether iodine-ethanol passivation leaves any residue or not. The preliminary results indicate that surface cleanliness after performing I-E passivation depends on chemical polishing of the samples. However, it is necessary to perform a detail experiments into the effect of surface preparation and cleaning process prior to the passivation work. Furthermore, an injection-dependent parameterisation needs to be performed [115].

8.3.2. Defect interactions in low-temperature gettering

A distribution of as-grown dislocation density was performed in samples from different height positions in the ingot (Chapter 4). The spatially resolved interstitial iron maps (Chapter 5) suggested that lifetime improvement is substantially low in grains with higher dislocation density. Furthermore, a primary analysis into the correlation of dislocation density and change in interstitial iron concentration upon low-temperature annealing (discussed in Chapter 5) suggest that dislocation densities affect the gettering of interstitial iron. It is necessary to perform an extensive research how crystallographic defects such as as-grown dislocations density interact with interstitial iron upon low-

temperature annealing and under what conditions interstitial iron likely to be gettered at defects. This experiment could be performed with a set of mc-Si sample with different density of crystallographic defects (*e.g*. dislocation density) and the same level of metallic contamination. The kinetics can be determined upon annealing at different temperatures and a binding energy between metallic impurities and defects can be estimated. The microscopic techniques such as transmission electron microscopy (TEM) and atom probe tomography (APT) can be used to determine metal compositions at the defects [216].

8.3.3. Non-iron metallic impurities in multicrystalline silicon

This thesis focuses mainly on the kinetics of interstitial iron concentration as it has relatively high concentration and the most detrimental effect on lifetime. Furthermore, it can be determined using a non-destructive method. In many cases, lifetime improvement shows a very poor perhaps no relationship with the reduction in interstitial iron concentrations. As multicrystalline silicon materials also contain transition metals other than interstitial iron [9, 92], it is necessary to investigate whether low-temperature gettering can affect their concentrations. The sister multicrystalline silicon samples can be used in low-temperature annealing and changes in other metallic impurities can be determined prior and post-annealing step. X-ray fluorescence microscopy (μ-XRF) can be used to determine spatial distribution, elemental composition and dimensions of metallic impurities [9].

8.3.4. Effect of grain orientation in low-temperature gettering

In this thesis, photoluminescence imaging and interstitial iron concentration mapping were performed at every annealing step. In most cases, it was found that lifetime improvement varies at different bulk grain regions. Some grain shows relatively high lifetime improvement compared to others. One possibility is that crystallographic orientation could affect lifetime improvement and reduction in interstitial iron concentration [59]. Additional possibility is that the spatial distribution of dislocations in the bulk grain regions and their interaction with impurities upon thermal annealing. An extensive experiment needs to be performed to investigate whether crystallographic orientations affect lifetime improvement or not. An electron backscatter diffraction (EBSD) analysis could be performed on the existing sister samples in which low-

temperature gettering was already performed and lifetime improvement was found different in different bulk grain regions. Additionally, dislocation density distributions also need to be determined to distinguish the effect crystallographic orientation.

8.3.5. Hydrogenation in low-temperature gettering

The quantitative comparison results between silicon nitride and iodine-ethanol (in Chapter 4 and Chapter 6) show that lifetime improvement in as-grown state and low-temperature annealing is large in relatively high lifetime samples with silicon nitride passivation compared to I-E passivation scheme. One possibility is that hydrogenation might passivate interstitial iron and improves lifetime [137, 138, 207]. However, it is important to investigate the influence of hydrogen present in silicon nitride layer in improving lifetime. A set of controlled single crystal silicon samples needs to be used to keep minimal effect arise from the bulk material.

Due to a lack in silicon nitride passivation facility in Warwick, samples were passivated prior to annealing step and were not re-passivated after every annealing step. It is desirable to perform an experiment how the passivation quality degrades over low-temperature annealing period. Recent studies [205] reported that illumination in low-temperature annealing affects lifetime substantially for silicon nitride passivated samples. A study can also be performed into the effect low-temperature gettering with silicon nitride passivation under illumination for mc-Si samples from different height positions in the ingot.

8.3.6. Saw damage gettering at low temperatures

Multicrystalline silicon wafers usually contain damages on the surfaces after wire sawn (as shown in Figure 3.7) and they can introduce sinks for diffusing impurities upon thermal annealing. The gettering of impurities at these surface defects induced by the sawing process is commonly known as saw damage gettering (SDG). Martins *et al.* studied SDG using high-temperature process ($\geq$ 850 °C) and reported a substantial improvement in the bulk lifetime [200]. As a high-temperature process is more likely to be contaminated and may not be cost-effective, it is necessary to investigate whether SDG using a low-temperature annealing can improve lifetime or not. A preliminary experiment

was performed in an annealing at 400 °C for 25 h for relatively poor lifetime multicrystalline silicon samples from the bottom part of the ingot, as shown in Figure 8.1 and Figure 8.2. A temporary liquid iodine-ethanol passivation was used to avoid additional effect from the dielectric layers. A substantial lifetime improvement (a factor of ~2) is observed in the sample annealed with saw damages on the surfaces compared to the sample polished prior to thermal annealing. The sample annealed with saw damages shows 2.9 order of magnitude low interstitial iron concentration compared to the as-received value whereas it is 0.7 in the polished sample. However, more experiments need to be performed on sister mc-Si samples to investigate the annealing temperature and annealing time where lifetime improvement and iron reduction are maximised. A comprehensive study also needs to be performed to investigate whether saw damage gettering has a potential to improve lifetime in samples from different height positions in an ingot. A set of sister mc-Si samples from the adjacent location of the samples used in this thesis can be used.

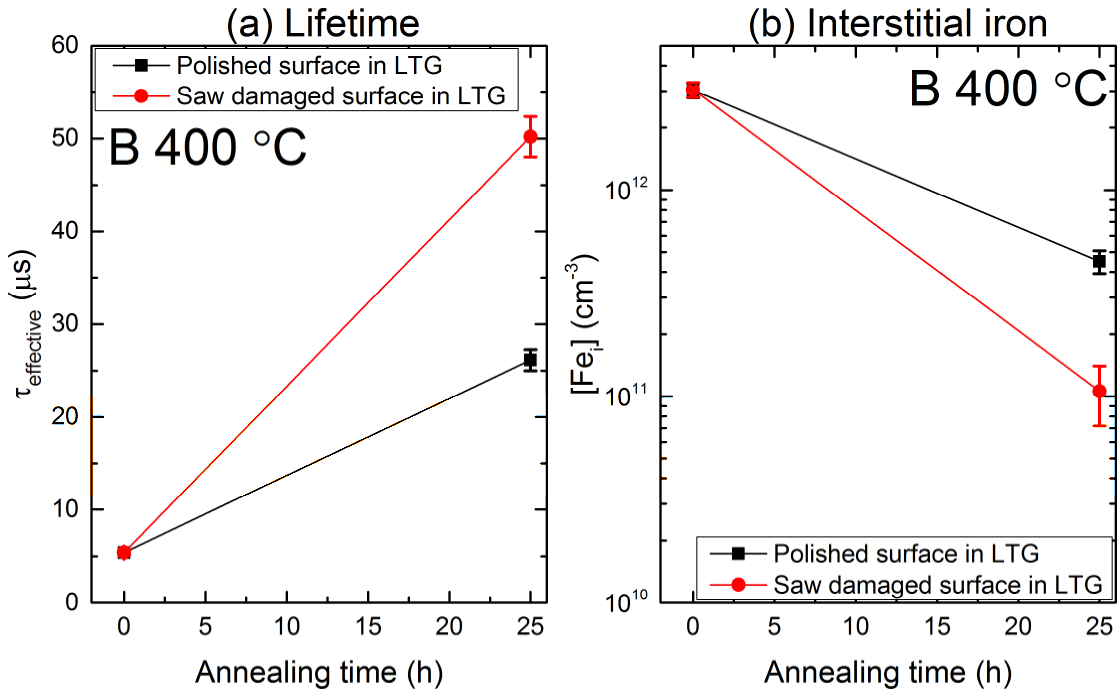

Figure 8.1. Comparison in QSS-PC lifetime (a) and interstitial iron concentration (b) at an injection level of 1×10^{15} cm^{-3} for samples from the bottom part of the ingot. Two sister samples were annealed at 400 °C for 25 h of cumulative time. The first sample was polished prior to annealing and the second sample was annealed with saw damages.

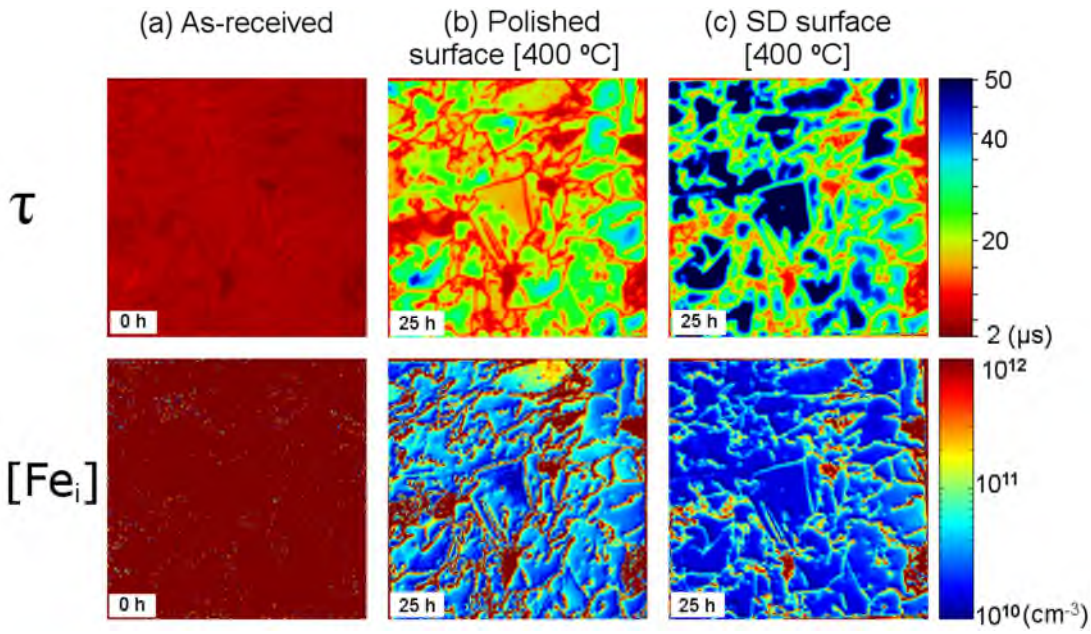

Figure 8.2. Spatial distribution of lifetime with iron in the FeB state (top row) and corresponding interstitial iron concentration maps (bottom row) for two sister bottom samples (39 mm × 39 mm). Samples were annealed at 400 °C for 25 h of cumulative time. Column (a) represents the as-received state, column (b) represents the sample annealed with polished surface and column (c) represents the sample annealed with saw-damage.

Further experiments on low-temperature saw damage geterring were carried out as a continuation of preliminary study as presented in the above section. In this study, sister wafers with near-identical microstructures were sourced from the top of a *p*-type conventionally-grown (*i.e.* not high performance) mc-Si ingot. The manufacturer had used a diamond saw to cut the ingot into ~200 μm thick wafers. Samples measuring 3.9 cm × 3.9cm with a ~0.7 Ω cm resistivity were studied.

A planar chemical etch comprising HF (50%), HNO_3 (69%) and CH_3COOH (100%) in the ratio of 24:58:18 was used to remove saw damage from half of the as-sawn samples. At least ~30 μm of material was removed from each side, with the final thickness estimated from weighing the sample. Annealing of pairs of identically RCA cleaned sister samples (one with saw damage; one without) was performed at temperatures from 300 to 700 °C. This annealing is referred to as saw damage gettering (SDG) where saw damage was present or a control anneal (CA) where saw damage had been removed. Annealing times were increased with decreasing temperature guided by the simulation of interstitial iron to both surfaces from Ref. for which the results are shown in Figure 8.3(a). Experimental annealing times were 80 h at 300 °C, 12 h at 400 °C, 3 h at 500 °C, 1 h at

600 °C and 0.5 h at 700 °C, and these times are sufficient for interstitial iron to reach the solubility for pre-annealed samples from Ref. [128] or to be well below our detection limit. After annealing, the saw damage was removed from the other half of the sample set using the same method as above.

Samples were characterised by quasi-steady-state photoconductance (QSS-PC) lifetime measurement using a Sinton WCT-120 lifetime tester and photoluminescence imaging with a BT Imaging LIS-L1 PL system. Prior to each lifetime measurement step samples were passivated with subjected to RCA cleaning and iodine-ethanol surface passivation. This surface passivation scheme was chosen as it avoids potential hydrogenation and external gettering associated with dielectric films. QSS-PC lifetimes are reported at 1×10^{15} cm^{-3} injection, and all reported lifetimes are with iron in the FeB state.

The Figure 8.3(b) shows that an effect of SDG on interstitial iron concentration upon annealing at 300 °C to 700 °C. The average interstitial iron concentration in the as-received state is $\sim 1 \times 10^{12}$ cm^{-3} which is consistent with the samples used in Chapters 5, 6 and 7. The averaged interstitial iron concentration decreases by 1 order of magnitude compared to the as-received state for samples annealed with saw damage present in the temperatures investigated. In CA samples (polished before thermal annealing), the interstitial iron concentration decreases upon annealing at 300 °C and 400 °C, remains same at 500 °C and increases at 600 °C and 700 °C. This is consistent with the findings with results presented in Chapter 5.

Figure 8.4 shows the evolution of bulk minority carrier lifetime as a function of cumulative annealing time at 300 °C for both the SDG and CA samples. A clear difference is found between samples annealed with and without saw damage at the surface. When saw damage is present at the surface the lifetime is improved at all temperatures. The largest lifetime improvement is a factor of 4 after 100 h of annealing at 300 °C compared to as-received values for SDG samples (Figure 8.4(a)). In CA samples, lifetime degrades substantially after primary annealing step at temperatures from 500 °C to 700 °C (Figure 8.4(b)). Lifetime improves upon further annealing at 300 °C in most of the cases.The overall effect of SDG is substantial when samples are annealed at high temperatues (≥ 500 °C) whereas it appears to be less effective at 300 °C and 400 °C in a combination of a secondary annealing at 300 °C for 100 h.

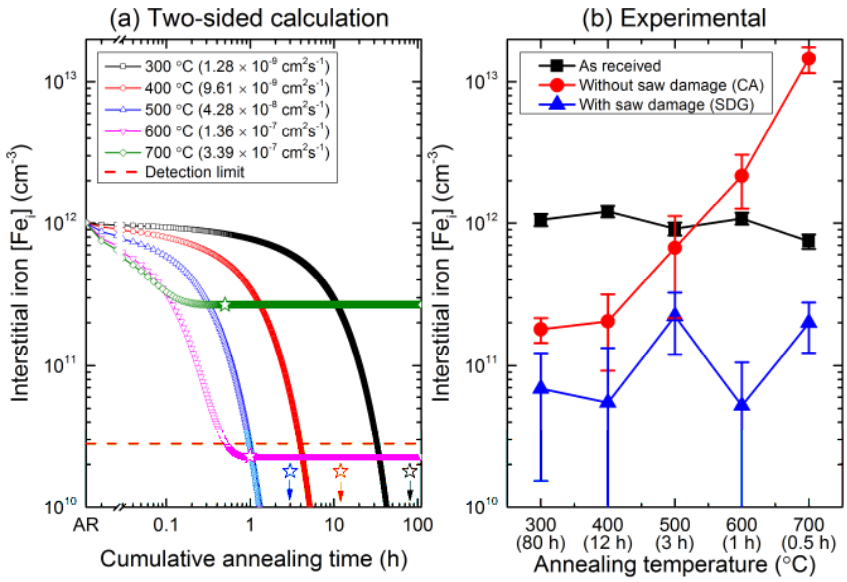

Figure 8.3. (a) Simulation of interstitial iron concentration as supersaturated interstitial iron diffuses to saw damage at both surfaces. The legend shows diffusion coefficients and the starting concentration is the mean from etched samples. Starred symbols indicate the annealing times used (well below the scale for ≤ 500 °C). (b) Experimental interstitial iron values in the as-received (AR) state, after saw damage gettering (SDG) and after a control anneal (CA).

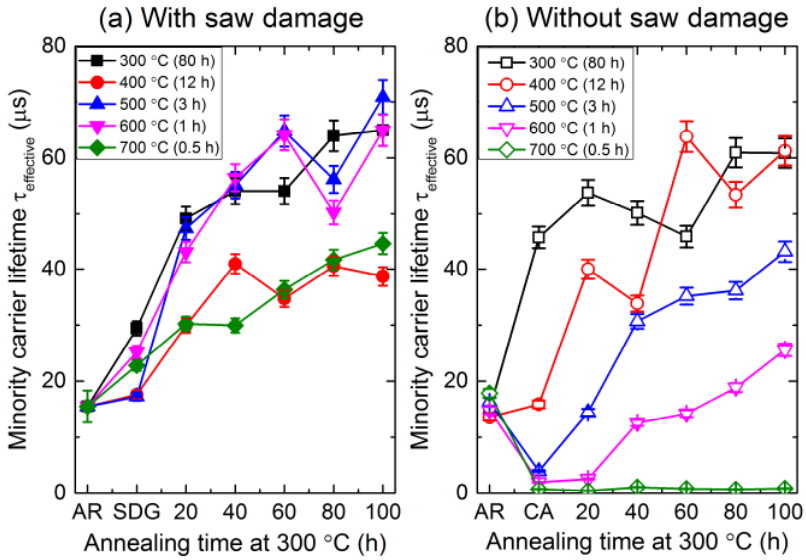

Figure 8.4. QSS-PC lifetime for mc-Si sister samples subjected to (a) saw damage gettering (SDG) and (b) a control anneal (CA) at the same time but with the saw damage removed. After SDG or the CA samples were subjected to annealing at 300 °C. It is not possible to measure lifetime with saw damage present, so the as-received (AR) lifetimes in (a) is the mean of those in (b).

8.3.7. Low-temperature gettering in mc-Si solar cells

The results presented in Chapter 5 and Chapter 6 suggest that low-temperature annealing can improve bulk lifetime for as-received mc-Si samples. The results presented in Chapter 7 suggest that lifetime can be improved even after a standard phosphorus diffusion gettering (PDG) process by low-temperature annealing for relatively poor lifetime samples from the bottom and top parts of the ingot. It is necessary to investigate how these low-temperature annealing processes (in the as-received state and after PDG process) do affect solar cell efficiency. Technology computer-aided design (TCAD) computer-based modelling can be used to predict cell performance [134, 217, 218]. Solar cells can also be processed using the existing samples in this study where lifetime improvements were observed. Low-temperature gettering can also be performed after completion of the solar cell process. Pickett and Buonassisi [50] and Rinio *et al*. [51] studied low-temperature annealing for mc-Si solar cells and reported an improvement in cell efficiency. The mechanism of improvement is not well established as their work likely to be a combined effect of *external* gettering, *internal* gettering and bulk passivation. It is also not known how solar cells made from different parts of the ingot respond to low-temperature annealing. An extensive experiment needs to be performed into the effect of low-temperature annealing on mc-Si solar cells with different defect distributions. Mc-Si samples available from different ingot height positions can be used for this study.

8.4. Conclusion

A series of experiments was performed into the effects of low-temperature annealing for as-received samples and after a phosphorus diffusion gettering process. In as-grown wafers, the thermal effects of annealing have been separated from any bulk passivation which may occur during surface passivation in lifetime measurement. The key findings are summarized as follows:

- Low-temperature annealing in absence of any dielectric layer has the potential to improve lifetime compared to the as-received states in relatively poor samples (‘red zone’ wafers) from the bottom and top parts of the ingot. A substantial

improvement in lifetime by a factor of 7 was realised by annealing bottom samples at 400 °C for 35 h.

- The effect of low-temperature annealing depends upon passivation type. The results demonstrated that annealing as-grown wafers with SiN_x surface passivation also results in substantial lifetime increases, but differences occur due to *external* gettering to the SiN_x film and bulk passivation (possibly by hydrogen).

- Low-temperature annealing even after a standard PDG process improves lifetime in the bottom and top samples. Lifetime improvements do not correlate with changes in interstitial iron, so gettering of another impurity is likely.

To understand the effects of low-temperature gettering at different stages in the cell production process and after the cell process in improving cell efficiency, further research needs to be performed.

References

[1] Key world energy statistics, *International Energy Agency*, 2016.

[2] M. Schmela, G. Masson, and N. N. T. Mai, "Global Market Outlook For Solar Power / 2016 - 2020," ed: European photovoltaic industry association, 2016.

[3] A. Goodrich, P. Hacke, Q. Wang, B. Sopori, R. Margolis, T. L. James, and M. Woodhouse, "A wafer-based monocrystalline silicon photovoltaics road map: Utilizing known technology improvement opportunities for further reductions in manufacturing costs," *Solar Energy Materials and Solar Cells*, vol. 114, 110-135, 2013, doi:10.1016/j.solmat.2013.01.030.

[4] M. A. Green, "Silicon photovoltaic modules: a brief history of the first 50 years," *Progress in Photovoltaics: Research and Applications*, vol. 13, 447-455, 2005, doi:10.1002/pip.612.

[5] M. Taguchi, A. Yano, S. Tohoda, K. Matsuyama, Y. Nakamura, T. Nishiwaki, K. Fujita, and E. Maruyama, "24.7% Record Efficiency HIT Solar Cell on Thin Silicon Wafer," *IEEE Journal of Photovoltaics*, vol. 4, 96-99, 2014, doi:10.1109/JPHOTOV.2013.2282737.

[6] Pvinsight. (2016, 11 Nov). *PV poly silicon weekly spot price*. Available: http://pvinsights.com.

[7] B. Bruno, K. Kiefer, C. Kost, S. Nold, S. Philipps, R. Preu, J. Rentsch, T. Schlegl, G. Stryi-Hipp, G. Willeke, H. Wirth, I. Brucker, A. Häberle, and W. Warmuth, Photovoltaics Report, *Fraunhofer Institute for Solar Energy Systems*, 20 October, 2016.

[8] J. Bultman, I. Cesar, B. Geerligs, Y. Komatsu, and W. Sinke, "Methods of emitter formation for crystalline silicon solar cells," *Photovoltaics International*, vol. 8, 69-80, 2010.

[9] T. Buonassisi, A. A. Istratov, M. D. Pickett, M. Heuer, J. P. Kalejs, G. Hahn, M. A. Marcus, B. Lai, Z. Cai, S. M. Heald, T. F. Ciszek, R. F. Clark, D. W. Cunningham, A. M. Gabor, R. Jonczyk, S. Narayanan, E. Sauar, and E. R. Weber, "Chemical natures and distributions of metal impurities in multicrystalline silicon materials," *Progress in Photovoltaics: Research and Applications*, vol. 14, 513-531, 2006, doi:10.1002/pip.690.

[10] M. A. Green, K. Emery, Y. Hishikawa, W. Warta, and E. D. Dunlop, "Solar cell efficiency tables (version 46)," *Progress in Photovoltaics: Research and Applications*, vol. 23, 805-812, 2015, doi:10.1002/pip.2637.

[11] H. J. Möller, C. Funke, M. Rinio, and S. Scholz, "Multicrystalline silicon for solar cells," *Thin Solid Films,* vol. 487, 179-187, 2005, doi:10.1016/j.tsf.2005.01.061.

[12] D. Kohler, A. Zuschlag, and G. Hahn, "On the origin and formation of large defect clusters in multicrystalline silicon solar cells," *Solar Energy Materials and Solar Cells,* vol. 120, 275-281, 2014, doi:10.1016/j.solmat.2013.09.018.

[13] I. Takahashi, N. Usami, H. Mizuseki, Y. Kawazoe, G. Stokkan, and K. Nakajima, "Impact of type of crystal defects in multicrystalline Si on electrical properties and interaction with impurities," *Journal of Applied Physics,* vol. 109, 033504, 2011, doi:10.1063/1.3544208.

[14] A. R. Peaker, V. P. Markevich, B. Hamilton, G. Parada, A. Dudas, A. Pap, E. Don, B. Lim, J. Schmidt, L. Yu, Y. Yoon, and G. Rozgonyi, "Recombination via point defects and their complexes in solar silicon," *Physica Status Solidi A,* vol. 209, 1884, 2013, doi:10.1002/pssa.201200216.

[15] S. Rein and S. W. Glunz, "Electronic properties of interstitial iron and iron-boron pairs determined by means of advanced lifetime spectroscopy," *Journal of Applied Physics,* vol. 98, 113711, 2005, doi:10.1063/1.2106017.

[16] G. Coletti, R. Kvande, V. D. Mihailetchi, L. J. Geerligs, L. Arnberg, and E. J. Ovrelid, "Effect of iron in silicon feedstock on *p*- and *n*-type multicrystalline silicon solar cells," *Journal of Applied Physics,* vol. 104, 104913, 2008, doi:10.1063/1.3021355.

[17] A. A. Istratov , H. Hieslmair, and E. R. Weber, "Iron contamination in silicon technology," *Applied Physics A,* vol. 70, 46, 2000, doi:10.1007/s003390000458.

[18] A. A. Istratov , H. Hieslmair, and E. R. Weber, "Iron and its complexes in silicon," *Applied Physics A,* vol. 69, 13-44, 1999, doi:10.1007/s003399900059.

[19] M. Seibt, A. Sattler, C. Rudolf, O. Voß, V. Kveder, and W. Schröter, "Gettering in silicon photovoltaics: current state and future perspectives," *Physica Status Solidi (a),* vol. 203, 696-713, 2006, doi:10.1002/pssa.200664516.

[20] I. Périchaud, "Gettering of impurities in solar silicon," *Solar Energy Materials and Solar Cells,* vol. 72, 315-326, 2002, doi:10.1016/S0927-0248(01)00179-9.

[21] J. S. Kang and D. K. Schroder, "Gettering in silicon," *Journal of Applied Physics,* vol. 65, 2974, 1989, doi:10.1063/1.342714.

[22] C. S. Chen and D. K. Schroder, "Kinetics of gettering in silicon," *Journal of Applied Physics,* vol. 71, 5858, 1992, doi:10.1063/1.350482.

[23] M. Aoki, A. Hara, and A. Ohsawa, "Fundamental properties of intrinsic gettering of iron in a silicon wafer," *Journal of Applied Physics,* vol. 72, 895, 1992, doi:10.1063/1.351764.

[24] M. Apel, I. Hanke, R. Schindler, and W. Schröter, "Aluminum gettering of cobalt in silicon," *Journal of Applied Physics,* vol. 76, 4432, 1994, doi:10.1063/1.357339.

[25] J. L. Benton, P. A. Stolk, D. J. Eaglesham, D. C. Jacobson, J. Y. Cheng, J. M. Poate, N. T. Ha, T. E. Haynes, and S. M. Myers, "Iron gettering mechanisms in silicon," *Journal of Applied Physics,* vol. 80, 3275, 1996, doi:10.1063/1.363236.

[26] P. A. Stolk, J. L. Benton, D. J. Eaglesham, D. C. Jacobson, J. Y. Cheng, J. M. Poate, S. M. Myers, and T. E. Haynes, "The mechanism of iron gettering in boron-doped silicon," *Applied Physics Letters,* vol. 68, 51, 1996, doi:10.1063/1.116754.

[27] O. Porre, S. Martinuzzi, M. Pasquinelli, I. Perichaud, and N. Gay, "Gettering effect of aluminum in mc-Si and c-Si wafers and in solar cells,"*25th IEEE Photovoltaic Specialists Conference*, Washington D.C, 629-632, 1996, doi:10.1109/PVSC.1996.564207.

[28] H. Hieslmair, S. McHugo, and E. R. Weber, "Aluminium backside segregation gettering,"*25th IEEE Photovoltaic Specialists Conference*, Washington D.C, 441-444, 1996, doi:10.1109/PVSC.1996.564038.

[29] S. A. McHugo, H. Hieslmair, and E. R. Weber, "Gettering of metallic impurities in photovoltaic silicon," *Journal of Applied Physics A,* vol. 64, 127-137, 1997, doi:10.1007/s003390050453.

[30] D. Macdonald, A. Cuevas, and F. Ferrazza, "Response to phosphorus gettering of different regions of cast multicrystalline silicon ingots," *Solid-State Electronics,* vol. 43, 575-581, 1999, doi:10.1016/S0038-1101(98)00283-4.

[31] S. M. Myers, M. Seibt, and W. Schröter, "Mechanisms of transition-metal gettering in silicon," *Journal of Applied Physics,* vol. 88, 3795, 2000, doi:10.1063/1.1289273.

[32] Y. Kim, K. Lee, H. Chung, D. Hwang, H. Kim, H. Cho, and B. Lee, "Internal gettering of Fe, Ni and Cu in silicon wafers," *Journal of the Korean Physical Society,* vol. 39, 348-351, 2001, doi:10.3938/jkps.39.348.

[33] J. Boudadena, R. Monnac, M. Loghmartib, and J. C. Muller, "Comparison of phosphorus gettering for different multicrystalline silicon," *Solar Energy Materials and Solar Cells,* vol. 72, 381-387, 2002, doi:10.1016/S0927-0248(01)00186-6.

[34] P. Manshanden and L. J. Geerligs, "Improved phosphorous gettering of multicrystalline silicon," *Solar Energy Materials and Solar Cells,* vol. 90, 998-1012, 2006, doi:10.1016/j.solmat.2005.05.015.

[35] A. Bentzen, A. Holt, R. Kopecek, G. Stokkan, J. S. Christensen, and B. G. Svensson, "Gettering of transition metal impurities during phosphorus emitter diffusion in multicrystalline silicon solar cell processing," *Journal of Applied Physics,* vol. 99, 093509, 2006, doi:10.1063/1.2194387.

[36] R. Krain, S. Herlufsen, and J. Schmidt, "Internal gettering of iron in multicrystalline silicon at low temperature," *Applied Physics Letters,* vol. 93, 152108, 2008, doi:10.1063/1.2987521.

[37] J. Hofstetter, J. F. Lelièvre, C. del Cañizo, and A. Luque, "Study of internal vs external gettering of iron during slow cooling process for silicon solar cell fabrication," *Solid State Phenomena,* vol. 156-158, 387-393, 2009, doi:10.4028/www.scientific.net/SSP.156-158.387.

[38] A. Haarahiltunen, H. Savin, M. Yli-Koski, H. Talvitie, M. I. Asghar, and J. Sinkkonen, "As-grown iron precipitates and gettering in multicrystalline silicon," *Materials Science and Engineering: B,* vol. 159-160, 248-252, 2009, doi:10.1016/j.mseb.2008.10.053.

[39] A. Bentzen and A. Holt, "Overview of phosphorus diffusion and gettering in multicrystalline silicon," *Materials Science and Engineering: B,* vol. 159-160, 228-234, 2009, doi:10.1016/j.mseb.2008.10.060.

[40] H. Talvitie, V. Vähänissi, A. Haarahiltunen, M. Yli-Koski, and H. Savin, "Phosphorus and boron diffusion gettering of iron in monocrystalline silicon," *Journal of Applied Physics,* vol. 109, 093505, 2011, doi:10.1063/1.3582086.

[41] A. Liu, D. Walter, S. P. Phang, and D. Macdonald, "Investigating internal gettering of iron at grain boundaries in multicrystalline silicon via photoluminescence imaging," *IEEE Journal of Photovoltaics,* vol. 2, 479-484, 2012, doi:10.1109/JPHOTOV.2012.2195550.

[42] V. Osinniy, A. Nylandsted Larsen, E. Hvidsten Dahl, E. Enebakk, A. K. Søiland, R. Tronstad, and Y. Safir, "Gettering improvements of minority-carrier lifetimes in solar grade silicon," *Solar Energy Materials and Solar Cells,* vol. 101, 123-130, 2012, doi:10.1016/j.solmat.2012.02.027.

[43] D. P. Fenning, J. Hofstetter, M. I. Bertoni, G. Coletti, B. Lai, C. del Cañizo, and T. Buonassisi, "Precipitated iron: a limit on gettering efficacy in multicrystalline silicon," *Journal of Applied Physics,* vol. 113, 044521, 2013, doi:10.1063/1.4788800.

[44] D. Macdonald, A. Y. Liu, and S. P. Phang, "External and internal gettering of interstitial iron in silicon for solar cells," *Solid State Phenomena,* vol. 205-206, 26-33, 2013, doi:10.4028/www.scientific.net/SSP.205-206.26.

[45] D. P. Fenning, A. S. Zuschlag, M. I. Bertoni, B. Lai, G. Hahn, and T. Buonassisi, "Improved iron gettering of contaminated multicrystalline silicon by high-temperature phosphorus diffusion," *Journal of Applied Physics,* vol. 113, 214504, 2013, doi:10.1063/1.4808310.

[46] P. Karzel, M. Ackermann, L. Gröner, C. Reimann, M. Zschorsch, S. Meyer, F. Kiessling, S. Riepe, and G. Hahn, "Dependence of phosphorus gettering and hydrogen passivation efficacy on grain boundary type in multicrystalline silicon," *Journal of Applied Physics,* vol. 114, 244902, 2013, doi:10.1063/1.4856215.

[47] J. D. Murphy, R. E. McGuire, K. Bothe, V. V. Voronkov, and R. J. Falster, "Competitive gettering of iron in silicon photovoltaics: Oxide precipitates versus phosphorus diffusion," *Journal of Applied Physics,* vol. 116, 053514, 2014, doi:10.1063/1.4892015.

[48] Y. Boulfrad, A. Haarahiltunen, H. Savin, E. J. Øvrelid, and L. Arnberg, "Enhanced performance in the deteriorated area of multicrystalline silicon wafers by internal gettering," *Progress in Photovoltaics: Research and Applications,* vol. 23, 30-36, 2015, doi:10.1002/pip.2391.

[49] A. Y. Liu and D. Macdonald, "Precipitation of iron in multicrystalline silicon during annealing," *Journal of Applied Physics,* vol. 115, 114901, 2014, doi:10.1063/1.4868587.

[50] M. D. Pickett and T. Buonassisi, "Iron point defect reduction in multicrystalline silicon solar cells," *Applied Physics Letters,* vol. 92, 122103, 2008, doi:10.1063/1.2898204.

[51] M. Rinio, A. Yodyunyong, S. Keipert-Colberg, Y. P. B. Mouafi, D. Borchert, and A. Montesdeoca-Santana, "Improvement of multicrystalline silicon solar cells by a low temperature anneal after emitter diffusion," *Progress in Photovoltaics: Research and Applications,* vol. 19, 165-169, 2011, doi:10.1002/pip.1002.

[52] P. Krenckel, P. Saring, M. A. Falkenberg, V. Kveder, and M. Seibt, "Interaction of Iron with Extended Defects in Multicrystalline Silicon Studied by Local Gettering," *Energy Procedia,* vol. 38, 582-588, 2013, doi:10.1016/j.egypro.2013.07.320.

[53] M. Al-Amin and J. D. Murphy, "Increasing minority carrier lifetime in as-grown multicrystalline silicon by low temperature internal gettering," *Journal of Applied Physics,* vol. 119, 235704, 2016, doi:10.1063/1.4954010.

[54] M. Al-Amin and J. D. Murphy, "Passivation effects on low temperature gettering in multicrystalline silicon," *IEEE Journal of Photovoltaics,* vol. 7, 68-77, 2016, doi:10.1109/JPHOTOV.2016.2618608.

[55] F. Ferrazza, "Large size of multicrystalline silicon ingots," *Solar Energy Materials and Solar Cells,* vol. 72, 77-81, 2002, doi:10.1016/S0927-0248(01)00152-0.

[56] S. Pizzini, *Advanced silicon materials for photovoltaic applications,* 1st ed., Chichester: John Wiley & Sons, Ltd, 2012.

[57] F. Cleri, P. Keblinski, L. Colombo, S. R. Phillpot, and D. Wolf, "Correlation between atomic structure and localized gap states in silicon grain boundaries," *Physical Review B,* vol. 57, 6247-6250, 1998, doi:10.1103/PhysRevB.57.6247.

[58] Z. Wang, S. Tsurekawa, K. Ikeda, T. Sekiguchi, and T. Watanabe, "Relationship between electrical activity and grain boundary structure configuration in polycrystalline silicon," *Interface Science,* vol. 7, 197-205, 1999, doi:10.1023/A:1008796005240.

[59] B. Ziebarth, M. Mrovec, C. Elsässer, and P. Gumbsch, "Interstitial iron impurities at grain boundaries in silicon: A first-principles study," *Physical Review B,* vol. 91, 035309, 2015, doi:10.1103/PhysRevB.91.035309.

[60] K. Kutsukake, T. Abe, N. Usami, K. Fujiwara, K. Morishita, and K. Nakajima, "Formation mechanism of twin boundaries during crystal growth of silicon," *Scripta Materialia,* vol. 65, 556-559, 2011, doi:10.1016/j.scriptamat.2011.06.028.

[61] A. A. S. Al-Omar and M. Y. Ghannam, "Direct calculation of two-dimensional collection probability in pn junction solar cells, and study of grain-boundary recombination in polycrystalline silicon cells," *Journal of Applied Physics,* vol. 79, 2103, 1996, doi:10.1063/1.361078.

[62] J. Chen, T. Sekiguchi, D. Yang, F. Yin, K. Kido, and S. Tsurekawa, "Electron-beam-induced current study of grain boundaries in multicrystalline silicon," *Journal of Applied Physics,* vol. 96, 5490, 2004, doi:10.1063/1.1797548.

[63] K. Fujiwara, M. Ishii, K. Maeda, H. Koizumi, J. Nozawa, and S. Uda, "The effect of grain boundary characteristics on the morphology of the crystal/melt interface of multicrystalline silicon," *Scripta Materialia,* vol. 69, 266-269, 2013, doi:10.1016/j.scriptamat.2013.04.015.

[64] T. Buonassisi, A. A. Istratov, M. D. Pickett, M. A. Marcus, T. F. Ciszek, and E. R. Weber, "Metal precipitation at grain boundaries in silicon: Dependence on grain boundary character and dislocation decoration," *Applied Physics Letters,* vol. 89, 042102, 2006, doi:10.1063/1.2234570.

[65] J. Chen, D. Yang, Z. Xi, and T. Sekiguchi, "Recombination activity of Σ3 boundaries in boron-doped multicrystalline silicon: Influence of iron contamination," *Journal of Applied Physics,* vol. 97, 033701, 2005, doi:10.1063/1.1836009.

[66] B. Ryningen, G. Stokkan, M. Kivambe, T. Ervik, and O. Lohne, "Growth of dislocation clusters during directional solidification of multicrystalline silicon ingots," *Acta Materialia,* vol. 59, 7703-7710, 2011, doi:10.1016/j.actamat.2011.09.002.

[67] D. Hull and D. J. Bacon, *Introduction to dislocations,* 4th ed., Oxford: Butterworth-Heinemann, 2001.

[68] J. P. Hirth and J. Lothe, *Theory of dislocations*, 2nd ed., New York: John Wiley and Sons, 1982.

[69] K. Kutsukake, T. Abe, N. Usami, K. Fujiwara, I. Yonenaga, K. Morishita, and K. Nakajima, "Generation mechanism of dislocations and their clusters in multicrystalline silicon during two-dimensional growth," *Journal of Applied Physics,* vol. 110, 083530, 2011, doi:10.1063/1.3652891.

[70] I. Takahashi, N. Usami, K. Kutsukake, G. Stokkan, K. Morishita, and K. Nakajima, "Generation mechanism of dislocations during directional solidification of multicrystalline silicon using artificially designed seed," *Journal of Crystal Growth,* vol. 312, 897-901, 2010, doi:10.1016/j.jcrysgro.2010.01.011.

[71] A. Autruffe, R. Søndenå, L. Vines, L. Arnberg, and M. Di Sabatino, "Influence of pulling rate on multicrystalline silicon ingots' properties," *Journal of Crystal Growth,* vol. 386, 199-203, 2014, doi:10.1016/j.jcrysgro.2013.09.037.

[72] G. Stokkan, "Relationship between dislocation density and nucleation of multicrystalline silicon," *Acta Materialia,* vol. 58, 3223-3229, 2010, doi:10.1016/j.actamat.2010.01.042.

[73] M. Seibt, R. Khalil, V. Kveder, and W. Schröter, "Electronic states at dislocations and metal silicide precipitates in crystalline silicon and their role in solar cell materials," *Applied Physics A,* vol. 96, 235-253, 2008, doi:10.1007/s00339-008-5027-8.

[74] M. Seibt, V. Kveder, W. Schröter, and O. Voß, "Structural and electrical properties of metal impurities at dislocations in silicon," *Physica Status Solidi (a),* vol. 202, 911-920, 2005, doi:10.1002/pssa.200460515.

[75] M. Seibt, D. Abdelbarey, V. Kveder, C. Rudolf, P. Saring, L. Stolze, and O. Voß, "Interaction of metal impurities with extended defects in crystalline silicon and its implications for gettering techniques used in photovoltaics," *Materials Science and Engineering: B,* vol. 159-160, 264-268, 2009, doi:10.1016/j.mseb.2008.12.044.

[76] M. Kivambe, G. Stokkan, T. Ervik, S. Castellanos, J. Hofstetter, and T. Buonassisi, "The impact of dislocation structure on impurity decoration of dislocation clusters in multicrystalline silicon," *Solid State Phenomena,* vol. 205-206, 71-76, 2013, doi:10.4028/www.scientific.net/SSP.205-206.71.

[77] P. R. Wilshaw, A. Ourmazd, and G. R. Booker, "Some aspects of the measurements of electrical effects of dislocations in silicon using a computerised EBIC system," *Le Journal de Physique Colloques,* vol. 44, 445-450, 1983, doi:10.1051/jphyscol:1983452.

[78] A. Ourmazd, P. R. Wilshaw, and G. R. Booker, "The temperature dependence of EBIC contrast from individual dislocations in silicon," *Le Journal de Physique Colloques,* vol. 44, 289-295, 1983, doi:10.1051/jphyscol:1983434.

[79] P. R. Wilshaw and T. S. Fell, "The electronic properties of dislocations in silicon," *Proceedings of the 6th International Symposium on the Structure and Properties of Dislocations in Semiconductors,* 85-96, 1989,

[80] T. S. Fell and P. R. Wilshaw, "The effect of different transition metals on the recombination efficiency of dislocations," *Le Journal de Physique IV,* vol. 01, C6-211-C6-216, 1991, doi:10.1051/jp4:1991632.

[81] T. S. Fell, P. R. Wilshaw, and M. D. D. Coteau, "EBIC investigations of dislocations and their interactions with impurities in silicon," *Physica Status Solidi A,* vol. 138, 695–704, 1993, doi:10.1002/pssa.2211380241.

[82] P. R. Wilshaw and T. S. Fell, "Electron beam induced current investigations of transition metal impurities at extended defects in silicon," *Journal of Electrochemical Society,* vol. 142, 4298-4304, 1995, doi:10.1149/1.2048501.

[83] S. Senkader, K. Jurkschat, P. R. Wilshaw, and R. J. Falster, "A study of oxygen dislocation interactions in Cz-Si," *Materials Science and Engineering: B,* vol. 73, 111-115, 2000, doi:10.1016/S0921-5107(99)00445-6.

[84] M. I. Bertoni, D. P. Fenning, M. Rinio, V. Rose, M. Holt, J. Maser, and T. Buonassisi, "Nanoprobe X-ray fluorescence characterization of defects in large-area solar cells," *Energy and Environmental Science,* vol. 4, 4252, 2011, doi:10.1039/c1ee02083h.

[85] V. Kveder, M. Kittler, and W. Schröter, "Recombination activity of contaminated dislocations in silicon: A model describing electron-beam-induced current contrast behavior," *Physical Review B,* vol. 63, 2001, doi:10.1103/PhysRevB.63.115208.

[86] C. Donolato, "Modeling the effect of dislocations on the minority carrier diffusion length of a semiconductor," *Journal of Applied Physics,* vol. 84, 2656, 1998, doi:10.1063/1.368378.

[87] E. Schmid, S. Würzner, C. Funke, V. Galindo, O. Pätzold, and M. Stelter, "The effect of the growth rate on the microstructure of multi-crystalline silicon," *Journal of Crystal Growth,* vol. 359, 77-82, 2012, doi:10.1016/j.jcrysgro.2012.08.028.

[88] N. J. Gregori, J. D. Murphy, J. M. Sykes, and P. R. Wilshaw, "Chemical etching to dissolve dislocation cores in multicrystalline silicon," *Physica B: Condensed Matter,* vol. 407, 2970-2973, 2012, doi:10.1016/j.physb.2011.07.049.

[89] K. Hartman, M. Bertoni, J. Serdy, and T. Buonassisi, "Dislocation density reduction in multicrystalline silicon solar cell material by high temperature annealing," *Applied Physics Letters,* vol. 93, 122108, 2008, doi:10.1063/1.2990644.

[90] K. Arafune, T. Sasaki, F. Wakabayashi, Y. Terada, Y. Ohshita, and M. Yamaguchi, "Study on defects and impurities in cast-grown polycrystalline silicon substrates for solar cells," *Physica B: Condensed Matter,* vol. 376-377, 236-239, 2006, doi:10.1016/j.physb.2005.12.062.

[91] A. A. Istratov, T. Buonassisi, R. J. McDonald, A. R. Smith, R. Schindler, J. A. Rand, J. P. Kalejs, and E. R. Weber, "Metal content of multicrystalline silicon for solar cells and its impact on minority carrier diffusion length," *Journal of Applied Physics,* vol. 94, 6552, 2003, doi:10.1063/1.1618912.

[92] D. Macdonald, A. Cuevas, A. Kinomura, Y. Nakano, and L. J. Geerligs, "Transition-metal profiles in a multicrystalline silicon ingot," *Journal of Applied Physics,* vol. 97, 033523, 2005, doi:10.1063/1.1845584.

[93] G. Coletti, P. C. P. Bronsveld, G. Hahn, W. Warta, D. Macdonald, B. Ceccaroli, K. Wambach, N. Le Quang, and J. M. Fernandez, "Impact of metal contamination in silicon solar cells," *Advanced Functional Materials,* vol. 21, 879-890, 2011, doi:10.1002/adfm.201000849.

[94] K. Graff, *Metal impurities in silicon-device fabrication,* 2nd ed., New York: Springer Science & Business Media, 2013.

[95] H. Nakashima, T. Sadoh, and T. Tsurushima, "Electrical and thermal properties of structurally metastable iron-boron pairs in silicon," *Physical Review B,* vol. 49, 16983-16993, 1994, doi:10.1103/PhysRevB.49.16983.

[96] D. Macdonald, L. G. Geerligs, and A. Azzizi, "Iron detection in crystalline silicon by carrier lifetime measurements for arbitrary injection and doping," *Journal of Applied Physics,* vol. 95, 1021, 2004, doi:10.1063/1.1637136.

[97] W. Wijaranakula, "The reaction kinetics of iron-boron pair formation and dissociation in *p*-type silicon," *Journal of The Electrochemical Society,* vol. 140, 275-281, 1993, doi:10.1149/1.2056102.

[98] L. J. Geerligs and D. Macdonald, "Dynamics of light-induced FeB pair dissociation in crystalline silicon," *Applied Physics Letters,* vol. 85, 5227, 2004, doi:10.1063/1.1823587.

[99] D. Macdonald, T. Roth, P. N. K. Deenapanray, K. Bothe, P. Pohl, and J. Schmidt, "Formation rates of iron-acceptor pairs in crystalline silicon," *Journal of Applied Physics,* vol. 98, 083509, 2005, doi:10.1063/1.2102071.

[100] X. Zhu, X. Yu, X. Li, P. Wang, and D. Yang, "Quantification of characteristic parameters for the dissociation kinetics of iron–boron pairs in Czochralski silicon," *Scripta Materialia,* vol. 64, 217-220, 2011, doi:10.1016/j.scriptamat.2010.10.021.

[101] D. K. Schroder, *Semiconductor material and device characterization*, 3rd ed., New Jersey: John Wiley and Sons, 2006.

[102] H. Schlangenotto, H. Maeder, and W. Gerlach, "Temperature dependence of the radiative recombination coefficient in silicon," *Physica Status Solidi (a),* vol. 21, 357-367, 1974, doi:10.1002/pssa.2210210140.

[103] T. Trupke, M. A. Green, P. Würfel, P. P. Altermatt, A. Wang, J. Zhao, and R. Corkish, "Temperature dependence of the radiative recombination coefficient of intrinsic crystalline silicon," *Journal of Applied Physics,* vol. 94, 4930, 2003, doi:10.1063/1.1610231.

[104] H. T. Nguyen, S. C. Baker-Finch, and D. Macdonald, "Temperature dependence of the radiative recombination coefficient in crystalline silicon from spectral photoluminescence," *Applied Physics Letters,* vol. 104, 112105, 2014, doi:10.1063/1.4869295.

[105] A. Luque and S. Hegedus, *Handbook of photovoltaic science and engineering*, 2nd ed., West Sussex: John Wiley and Sons, 2003.

[106] M. J. Kerr and A. Cuevas, "General parameterization of Auger recombination in crystalline silicon," *Journal of Applied Physics,* vol. 91, 2473, 2002, doi:10.1063/1.1432476.

[107] J. Dziewior and W. Schmid, "Auger coefficients for highly doped and highly excited silicon," *Applied Physics Letters,* vol. 31, 346, 1977, doi:10.1063/1.89694.

[108] A. Hangleiter and R. Hacker, "Enhancement of band-to-band Auger recombination by electron-hole correlations," *Physical Review Letters,* vol. 65, 215-218, 1990, doi:10.1103/PhysRevLett.65.215.

[109] J. Schmidt, M. Kerr, and P. P. Altermatt, "Coulomb-enhanced Auger recombination in crystalline silicon at intermediate and high injection densities," *Journal of Applied Physics,* vol. 88, 1494, 2000, doi:10.1063/1.373878.

[110] A. Richter, S. W. Glunz, F. Werner, J. Schmidt, and A. Cuevas, "Improved quantitative description of Auger recombination in crystalline silicon," *Physical Review B,* vol. 86, 165202, 2012, doi:10.1103/PhysRevB.86.165202.

[111] M. A. Green, "Intrinsic concentration, effective densities of states, and effective mass in silicon," *Journal of Applied Physics,* vol. 67, 2944, 1990, doi:10.1063/1.345414.

[112] W. Shockley and W. Read, "Statistics of the recombinations of holes and electrons," *Physical Review,* vol. 87, 835-842, 1952, doi:10.1103/PhysRev.87.835.

[113] R. Hall, "Electron-hole recombination in germanium," *Physical Review,* vol. 87, 387-387, 1952, doi:10.1103/PhysRev.87.387.

[114] S. Rein, *Lifetime spectroscopy: a method of defect characterization in silicon for photovoltaic applications,* Berlin: Springer Science & Business Media, 2006.

[115] J. D. Murphy, K. Bothe, R. Krain, V. V. Voronkov, and R. J. Falster, "Parameterisation of injection-dependent lifetime measurements in semiconductors in terms of Shockley-Read-Hall statistics: An application to oxide precipitates in silicon," *Journal of Applied Physics,* vol. 111, 113709, 2012, doi:10.1063/1.4725475.

[116] J. D. Murphy, K. Bothe, V. V. Voronkov, and R. J. Falster, "On the mechanism of recombination at oxide precipitates in silicon," *Applied Physics Letters,* vol. 102, 042105, 2013, doi:10.1063/1.4789858.

[117] J. D. Murphy, R. E. McGuire, K. Bothe, V. V. Voronkov, and R. J. Falster, "Minority carrier lifetime in silicon photovoltaics: The effect of oxygen precipitation," *Solar Energy Materials and Solar Cells,* vol. 120, 402-411, 2014, doi:10.1016/j.solmat.2013.06.018.

[118] J. Schmidt and K. Bothe, "Structure and transformation of the metastable boron- and oxygen-related defect center in crystalline silicon," *Physical Review B,* vol. 69, 024107, 2004, doi:10.1103/PhysRevB.69.024107.

[119] K. Bothe and J. Schmidt, "Electronically activated boron-oxygen-related recombination centers in crystalline silicon," *Journal of Applied Physics,* vol. 99, 013701, 2006, doi:10.1063/1.2140584.

[120] R. S. Bonilla and P. R. Wilshaw, "A technique for field effect surface passivation for silicon solar cells," *Applied Physics Letters,* vol. 104, 232903, 2014, doi:10.1063/1.4882161.

[121] R. S. Bonilla, F. Woodcock, and P. R. Wilshaw, "Very low surface recombination velocity in n-type c-Si using extrinsic field effect passivation," *Journal of Applied Physics,* vol. 116, 054102, 2014, doi:10.1063/1.4892099.

[122] A. G. Aberle and R. Hezel, "Progress in low-temperature surface passivation of silicon solar cells using remote-plasma silicon nitride," *Progress in Photovoltaics: Research and Applications,* vol. 5, 29-50, 1997, doi:10.1002/(SICI)1099-159X(199701/02)5:1<29::AID-PIP149>3.0.CO;2-M.

[123] M. J. Kerr, "Surface, emitter and bulk recombination in silicon and development of silicon nitride passivated solar cells," *PhD Thesis,* The Australian National University, 2002.

[124] R. S. Bonilla, C. Reichel, M. Hermle, and P. R. Wilshaw, "Extremely low surface recombination in 1 Ω cm n-type monocrystalline silicon," *Physica Status Solidi (RRL) - Rapid Research Letters,* vol. 11, 1600307, 2017, doi:10.1002/pssr.201600307.

[125] A. Cuevas and D. Macdonald, "Measuring and interpreting the lifetime of silicon wafers," *Solar Energy,* vol. 76, 255-262, 2004, doi:10.1016/j.solener.2003.07.033.

[126] A. A. Istratov, W. Huber, and E. R. Weber, "Experimental evidence for the presence of segregation and relaxation gettering of iron in polycrystalline silicon layers on silicon," *Applied Physics Letters,* vol. 85, 4472, 2004, doi:10.1063/1.1819512.

[127] J. D. Murphy and R. J. Falster, "Contamination of silicon by iron at temperatures below 800 °C," *Physica Status Solidi (RRL) - Rapid Research Letters,* vol. 5, 370-372, 2011, doi:10.1002/pssr.201105388.

[128] J. D. Murphy and R. J. Falster, "The relaxation behaviour of supersaturated iron in single-crystal silicon at 500 to 750 °C," *Journal of Applied Physics,* vol. 112, 113506, 2012, doi:10.1063/1.4767378.

[129] J. Tan, D. Macdonald, N. Bennett, D. Kong, A. Cuevas, and I. Romijn, "Dissolution of metal precipitates in multicrystalline silicon during annealing and the protective effect of phosphorus emitters," *Applied Physics Letters,* vol. 91, 043505, 2007, doi:10.1063/1.2766664.

[130] T. Buonassisi, A. A. Istratov, S. Peters, C. Ballif, J. Isenberg, S. Riepe, W. Warta, R. Schindler, G. Willeke, Z. Cai, B. Lai, and E. R. Weber, "Impact of metal silicide precipitate dissolution during rapid thermal processing of multicrystalline silicon solar cells," *Applied Physics Letters,* vol. 87, 121918, 2005, doi:10.1063/1.2048819.

[131] S. P. Phang and D. Macdonald, "Direct comparison of boron, phosphorus, and aluminum gettering of iron in crystalline silicon," *Journal of Applied Physics,* vol. 109, 073521, 2011, doi:10.1063/1.3569890.

[132] D. Abdelbarey, V. Kveder, W. Schröter, and M. Seibt, "Aluminum gettering of iron in silicon as a problem of the ternary phase diagram," *Applied Physics Letters,* vol. 94, 061912, 2009, doi:10.1063/1.3080666.

[133] K. Kurobe, M. Miura, K. Hirano, and H. Matsunami, "Spatial distribution of minority-carrier lifetime and local concentration of impurities in multicrystalline silicon solar cells," *Solar Energy Materials and Solar Cells,* vol. 74, 183-193, 2002, doi:10.1016/S0927-0248(02)00063-6.

[134] D. M. Powell, D. P. Fenning, J. Hofstetter, J.-F. Lelièvre, C. d. Cañizo, and T. Buonassisi, "TCAD for PV- A fast method for accurately modelling metal impurity evolution during solar cell processing," *Photovoltaics International,* vol. 15, 91-100, 2012,

[135] J. Hofstetter, D. P. Fenning, M. I. Bertoni, J. F. Lelièvre, C. d. Cañizo, and T. Buonassisi, "Impurity-to-efficiency simulator: predictive simulation of silicon solar cell performance based on iron content and distribution," *Progress in Photovoltaics: Research and Applications,* vol. 19, 487-497, 2011, doi:10.1002/pip.1062.

[136] P. S. Plekhanov, R. Gafiteanu, U. M. Gösele, and T. Y. Tan, "Modeling of gettering of precipitated impurities from Si for carrier lifetime improvement in solar cell applications," *Journal of Applied Physics,* vol. 86, 2453, 1999, doi:10.1063/1.371075.

[137] P. Karzel, A. Frey, S. Fritz, and G. Hahn, "Influence of hydrogen on interstitial iron concentration in multicrystalline silicon during annealing steps," *Journal of Applied Physics,* vol. 113, 114903, 2013, doi:10.1063/1.4794852.

[138] A. Liu, C. Sun, and D. Macdonald, "Hydrogen passivation of interstitial iron in boron-doped multicrystalline silicon during annealing," *Journal of Applied Physics,* vol. 116, 194902, 2014, doi:10.1063/1.4901831.

[139] W. Soppe, H. Rieffe, and A. Weeber, "Bulk and surface passivation of silicon solar cells accomplished by silicon nitride deposited on industrial scale by microwave PECVD," *Progress in Photovoltaics: Research and Applications,* vol. 13, 551-569, 2005, doi:10.1002/pip.611.

[140] A. G. Aberle, "Surface passivation of crystalline silicion solar cells: a review," *Progress in Photovoltaics: Research and Applications,* vol. 8, 362-376, 2000, doi:10.1002/1099-159X(200009/10)8:5<473::AID-PIP337>3.0.CO;2-D.

[141] M. J. Kerr, J. Schmidt, A. Cuevas, and J. H. Bultman, "Surface recombination velocity of phosphorus-diffused silicon solar cell emitters passivated with plasma enhanced chemical vapor deposited silicon nitride and thermal silicon oxide," *Journal of Applied Physics,* vol. 89, 3821-3826, 2001, doi:10.1063/1.1350633.

[142] J. Schmidt, A. Merkle, R. Brendel, B. Hoex, M. C. M. v. de Sanden, and W. M. M. Kessels, "Surface passivation of high-efficiency silicon solar cells by atomic-layer-deposited Al_2O_3," *Progress in Photovoltaics: Research and Applications,* vol. 16, 461-466, 2008, doi:10.1002/pip.823.

[143] S. Dauwe, J. Schmidt, and R. Hezel, "Very low surface recombination velocities on p-and n-type silicon wafers passivated with hydrogenated amorphous silicon films," *29th IEEE Photovoltaic Specialists Conference*, 1246-1249, 2002, doi:10.1109/PVSC.2002.1190834.

[144] M. Schaper, J. Schmidt, H. Plagwitz, and R. Brendel, "20.1%-efficient crystalline silicon solar cell with amorphous silicon rear-surface passivation," *Progress in Photovoltaics: Research and Applications*, vol. 13, 381-386, 2005, doi:10.1002/pip.641.

[145] F. Duerinckx and J. Szlufcik, "Defect passivation of industrial multicrystalline solar cells based on PECVD silicon nitride," *Solar Energy Materials and Solar Cells*, vol. 72, 231-246, 2002, doi:10.1016/s0927-0248(01)00170-2.

[146] A. W. Stephens and M. A. Green, "Effectiveness of 0.08 molar iodine in ethanol solution as a means of chemical surface passivation for photoconductance decay measurements," *Solar Energy Materials and Solar Cells*, vol. 45, 255-265, 1997, doi:10.1016/S0927-0248(96)00061-X.

[147] N. Batra, Vandana, S. Kumar, M. Sharma, S. K. Srivastava, P. Sharma, and P. K. Singh, "A comparative study of silicon surface passivation using ethanolic iodine and bromine solutions," *Solar Energy Materials and Solar Cells*, vol. 100, 43-47, 2012, doi:10.1016/j.solmat.2011.04.028.

[148] B. Chhabra, S. Bowden, R. L. Opila, and C. B. Honsberg, "High effective minority carrier lifetime on silicon substrates using quinhydrone-methanol passivation," *Applied Physics Letters*, vol. 96, 063502, 2010, doi:10.1063/1.3309595.

[149] K. L. Pollock, J. Junge, and G. Hahn, "Detailed investigation of surface passivation methods for lifetime measurements on p-type silicon wafers," *IEEE Journal of Photovolotaics*, vol. 2, 1-6, 2012, doi:10.1109/JPHOTOV.2011.2174337.

[150] B. Sopori, P. Rupnowski, J. Appel, V. Mehta, C. Li, and S. Johnston, "Wafer preparation and iodine-ethanol passivation procedure for reproducible minority-carrier lifetime measurement,"*33rd IEEE Photovoltaic Specialists Conference*, San Diego, California, 1-4, 2008, doi:10.1109/PVSC.2008.4922688.

[151] B. Sopori, S. Devayajanam, P. Basnyat, H. Moutinho, B. Nemeth, V. LaSalvia, S. Johnston, J. Binns, and J. Appel, "Some challenges in making accurate and reproducible measurements of minority carrier lifetime in high-quality Si wafers," *IEEE 40th Photovoltaic Specialists Conference*, Denver, Colorado, 0649-0654, 2014, doi:10.1109/PVSC.2014.6925006.

[152] B. Sopori, P. Rupnowski, J. Appel, D. Guhabiswas, and L. Anderson-Jackson, "Light-induced passivation of Si by iodine ethanol solution," *MRS Proceedings*, 07-10, 2008, doi:10.1557/PROC-1123-1123-P07-10.

[153] J. Schmidt and M. Kerr, "Highest-quality surface passivation of low-resistivity p-type silicon using stoichiometric PECVD silicon nitride," *Solar Energy Materials and Solar Cells*, vol. 65, 585-591, 2001, doi:10.1016/S0927-0248(00)00145-8.

[154] N. M. Johnson, D. K. Biegelsen, and M. D. Moyer, "Deuterium passivation of grain-boundary dangling bonds in silicon thin films," *Applied Physics Letters,* vol. 40, 882-884, 1982, doi:10.1063/1.92934.

[155] J. I. Hanoka, C. H. Seager, D. J. Sharp, and J. K. G. Panitz, "Hydrogen passivation of defects in silicon ribbon grown by the edge-defined film-fed growth process," *Applied Physics Letters,* vol. 42, 618-620, 1983, doi:10.1063/1.94022.

[156] C. Dubé, J. I. Hanoka, and D. B. Sandstrom, "Hydrogen diffusion along passivated grain boundaries in silicon ribbon," *Applied Physics Letters,* vol. 44, 425-427, 1984, doi:10.1063/1.94797.

[157] S. N. Rashkeev, M. Di Ventra, and S. T. Pantelides, "Hydrogen passivation and activation of oxygen complexes in silicon," *Applied Physics Letters,* vol. 78, 1571-1573, 2001, doi:10.1063/1.1355297.

[158] B. J. Hallam, P. G. Hamer, S. Wang, L. Song, N. Nampalli, M. D. Abbott, C. E. Chan, D. Lu, A. M. Wenham, L. Mai, N. Borojevic, A. Li, D. Chen, M. Y. Kim, A. Azmi, and S. Wenham, "Advanced hydrogenation of dislocation clusters and boron-oxygen defects in silicon solar cells," *Energy Procedia,* vol. 77, 799-809, 2015, doi:10.1016/j.egypro.2015.07.113.

[159] M. Sanati, N. Gonzalez Szwacki, and S. K. Estreicher, "Interstitial Fe in Si and its interactions with hydrogen and shallow dopants," *Physical Review B,* vol. 76, 125204, 2007, doi:10.1103/PhysRevB.76.125204.

[160] A. Y. Liu, C. Sun, V. P. Markevich, A. R. Peaker, J. D. Murphy, and D. Macdonald, "Gettering of interstitial iron in silicon by plasma-enhanced chemical vapour deposited silicon nitride films," *Journal of Applied Physics,* vol. 120, 193103, 2016, doi:10.1063/1.4967914.

[161] K. Bothe, R. Krain, R. Falster, and R. Sinton, "Determination of the bulk lifetime of bare multicrystalline silicon wafers," *Progress in Photovoltaics: Research and Applications,* vol. 18, 204-208, 2010, doi:10.1002/pip.975.

[162] J. Clark, "Multiheight microposition probe: instruction manual," J. E. Limited, 1st ed., 2013.

[163] E. Vazsonyi, K. D. Clercq, R. Einhaus, E. V. Kerschaver, K. Said, J. Poortmans, J. Szlufcik, and J. Nijs, "Improved anisotropic etching process for industrial texturing of silicon solar cells," *Solar Energy Materials and Solar Cells,* vol. 57, 179-188, 1999, doi:10.1016/S0927-0248(98)00180-9.

[164] P. K. Singh, R. Kumar, M. Lal, S. N. Singh, and B. K. Das, "Effectiveness of anisotropic etching of silicon in aqueous alkaline solutions," *Solar Energy Materials and Solar Cells,* vol. 70, 103-113, 2001, doi:10.1016/S0927-0248(00)00414-1.

[165] M. Shikida, K. Sato, K. Tokoro, and D. Uchikawa, "Differences in anisotropic etching properties of KOH and TMAH solutions," *Journal of Sensors and Actuators,* vol. 80, 179–188, 2000, doi:10.1016/S0924-4247(99)00264-2.

[166] P. Papet, O. Nichiporuk, A. Kaminski, Y. Rozier, J. Kraiem, J. F. Lelievre, A. Chaumartin, A. Fave, and M. Lemiti, "Pyramidal texturing of silicon solar cell with TMAH chemical anisotropic etching," *Solar Energy Materials and Solar Cells,* vol. 90, 2319-2328, 2006, doi:10.1016/j.solmat.2006.03.005.

[167] R. Hull, *Properties of crystalline silicon*, 1st ed., London: The Institution of Electrical Engineers, 1999.

[168] E. S. Kooij, K. Butter, and J. J. Kelly, "Silicon etching in HNO_3-HF solution charge balance for te oxidation reaction," *Electrochemical and Solid-State Letters,* vol. 2, 178-180, 1999, doi:10.1149/1.1390775.

[169] Y. Nishimoto, T. Ishihara, and K. Namba, "Investigation of Acidic Texturization for Multicrystalline Silicon Solar Cells," *Journal of The Electrochemical Society,* vol. 146, 457-461, 1999, doi:S0013-4651(98)04-009-9.

[170] B. Schwartz and H. Robbins, "Chemical etching of silicon," *Journal of The Electrochemical Society,* vol. 123, 1903, 1976, doi:10.1149/1.2132721.

[171] F. S. d. Aragona, "Dislocation etch for (100) Planes in Silicon," *Journal of The Electrochemical Society,* vol. 119, 948-951, 1972, doi:doi: 10.1149/1.2404374.

[172] B. L. Sopori, "A new defect etch for polycrystalline silicon," *Journal of The Electrochemical Society,* vol. 131, 1984, doi:10.1149/1.2115670.

[173] Y. Kashiwagi, R. Shimokawa, and M. Yamanaka, "Highly sensitive etchant for delineation of defects in single-and polycrystalline silicon materials," *Journal of The Electrochemical Society,* vol. 143, 4079-4087, 1996, doi:10.1149/1.1837339.

[174] D. B. Needleman, H. Choi, D. M. Powell, and T. Buonassisi, "Rapid dislocation-density mapping of as-cut crystalline silicon wafers," *Physica Status Solidi (RRL) - Rapid Research Letters,* vol. 7, 1041-1044, 2013, doi:10.1002/pssr.201308150.

[175] M. M. Kivambe, G. Stokkan, T. Ervik, B. Ryningen, and O. Lohne, "The microstructure of dislocation clusters in industrial directionally solidified multicrystalline silicon," *Journal of Applied Physics,* vol. 110, 063524, 2011, doi:10.1063/1.3641978.

[176] B. Sopori, S. Devayajanam, P. Basnyat, V. Mehta, H. Moutinho, B. Nemeth, V. LaSalvia, S. Johnston, N. M. Ravindra, J. Binns, and J. Appel, "A comparison of surface passivation techniques for measurement of minority carrier lifetime in thin Si wafers: toward a stable and uniform passivation," *Material Research Society Proceeding,* vol. 1670, mrss14-1670-h05-02, 2014, doi:10.1557/opl.2014.591.

[177] A. L. Blum, J. S. Swirhun, R. A. Sinton, F. Yan, S. Herasimenka, T. Roth, K. Lauer, J. Haunschild, B. Lim, K. Bothe, Z. Hameiri, B. Seipel, R. Xiong, M. Dhamrin, and J. D. Murphy, "Interlaboratory study of eddy-current measurement of excess carrier recombination lifetime," *IEEE Journal of Photovoltaics,* vol. 4, 525-531, 2014, doi:10.1109/JPHOTOV.2013.2284375.

[178] T. Lauinger, J. Moschner, A. G. Aberle, and R. Hezel, "Optimization and characterization of remote plasma-enhanced chemical vapor deposition silicon

nitride for the passivation of *p*-type crystalline silicon surfaces," *Journal of Vacuum Science & Technology A: Vacuum, Surfaces, and Films,* vol. 16, 530, 1998, doi:10.1116/1.581095.

[179] R. A. Sinton and A. Cuevas, "Contactless determination of current–voltage characteristics and minority-carrier lifetimes in semiconductors from quasi-steady-state photoconductance data," *Applied Physics Letters,* vol. 69, 2510, 1996, doi:10.1063/1.117723.

[180] J. Hornbeck and J. Haynes, "Trapping of Minority Carriers in Silicon. I. P-Type Silicon," *Physical Review,* vol. 97, 311-321, 1955, doi:10.1103/PhysRev.97.311.

[181] D. Macdonald and A. Cuevas, "Trapping of minority carriers in multicrystalline silicon," *Applied Physics Letters,* vol. 74, 1710, 1999, doi:10.1063/1.123663.

[182] R. A. Sinton, "WCT-120 photoconductance lifetime tester: user manual," S. Instruments, V3.0 ed., 2013.

[183] D. Macdonald, R. A. Sinton, and A. s. Cuevas, "On the use of a bias-light correction for trapping effects in photoconductance-based lifetime measurements of silicon," *Journal of Applied Physics,* vol. 89, 2772, 2001, doi:10.1063/1.1346652.

[184] T. Trupke, R. A. Bardos, M. C. Schubert, and W. Warta, "Photoluminescence imaging of silicon wafers," *Applied Physics Letters,* vol. 89, 044107, 2006, doi:10.1063/1.2234747.

[185] T. Trupke, R. A. Bardos, M. D. Abbott, P. Würfel, E. Pink1, Y. Augarten, F. W. Chen, K. Fisher, J. E. Cotter, M. Kasemann, M. Rüdiger, S. Kontermann, M. C. Schubert, M. The, S. W. Glunz, W. Warta, D. Macdonald, J. Tan, A.Cuevas, J. Bauer, R. Gupta, O. Breitenstein, T. Buonassisi, G. Tarnowski, A. Lorenz, H. P. Hartmann, D. H. Neuhaus, and J. M. Fernandez, "Progress with luminescence imaging for the characterisation of silicon wafers and solar cells," *22nd European Photovoltaic Solar Energy Conference,* Milan, Italy, 22-31, 2007,

[186] T. McHedlidze, W. Seifert, M. Kittler, A. T. Blumenau, B. Birkmann, T. Mono, and M. Müller, "Capability of photoluminescence for characterization of multi-crystalline silicon," *Journal of Applied Physics,* vol. 111, 073504, 2012, doi:10.1063/1.3699275.

[187] G. Zoth and W. Bergholz, "A fast, preparation-free method to detect iron in silicon," *Journal of Applied Physics,* vol. 67, 6764, 1990, doi:10.1063/1.345063.

[188] J. D. Murphy, K. Bothe, M. Olmo, V. V. Voronkov, and R. J. Falster, "The effect of oxide precipitates on minority carrier lifetime in p-type silicon," *Journal of Applied Physics,* vol. 110, 053713, 2011, doi:10.1063/1.3632067.

[189] D. Macdonald, J. Tan, and T. Trupke, "Imaging interstitial iron concentrations in boron-doped crystalline silicon using photoluminescence," *Journal of Applied Physics,* vol. 103, 073710, 2008, doi:10.1063/1.2903895.

[190] B. Mitchell, J. Greulich, and T. Trupke, "Quantifying the effect of minority carrier diffusion and free carrier absorption on photoluminescence bulk lifetime imaging of silicon bricks," *Solar Energy Materials and Solar Cells,* vol. 107, 75-80, 2012, doi:10.1016/j.solmat.2012.07.022.

[191] S. P. Phang, H. C. Sio, and D. Macdonald, "Carrier de-smearing of photoluminescence images on silicon wafers using the continuity equation," *Applied Physics Letters,* vol. 103, 192112, 2013, doi:10.1063/1.4829658.

[192] B. Ziebarth, M. Mrovec, C. Elsässer, and P. Gumbsch, "Interstitial iron impurities at cores of dissociated dislocations in silicon," *Physical Review B,* vol. 92, 195308, 2015, doi:10.1103/PhysRevB.92.195308.

[193] E. Olsen and E. J. Øvrelid, "Silicon nitride coating and crucible—effects of using upgraded materials in the casting of multicrystalline silicon ingots," *Progress in Photovoltaics: Research and Applications,* vol. 16, 93-100, 2008, doi:10.1002/pip.777.

[194] R. Kvande, L. J. Geerligs, G. Coletti, L. Arnberg, M. Di Sabatino, E. J. Øvrelid, and C. C. Swanson, "Distribution of iron in multicrystalline silicon ingots," *Journal of Applied Physics,* vol. 104, 064905, 2008, doi:10.1063/1.2956697.

[195] D. Macdonald, A. Cuevas, A. Kinomura, Y. Nakano, and L. J. Geerligs, "Transition-metal profiles in a multicrystalline silicon ingot," *Journal of Applied Physics,* vol. 97, 033523, 2005, doi:10.1063/1.1845584.

[196] T. U. Nærland, L. Arnberg, and A. Holt, "Origin of the low carrier lifetime edge zone in multicrystalline PV silicon," *Progress in Photovoltaics: Research and Applications,* vol. 17, 289, 2009, doi:10.1002/pip.876.

[197] S. Kleekajai, L. Wen, C. Peng, M. Stavola, V. Yelundur, K. Nakayashiki, A. Rohatgi, and J. Kalejs, "Infrared study of the concentration of H introduced into Si by the postdeposition annealing of a SiN x coating," *Journal of Applied Physics,* vol. 106, 123510, 2009, doi:10.1063/1.3267317.

[198] A. A. Istratov, T. Buonassisi, R. J. McDonald, A. R. Smith, R. Schindler, J. A. Rand, J. P. Kalejs, and E. R. Weber, "Metal content of multicrystalline silicon for solar cells and its impact on minority carrier diffusion length," *Journal of Applied Physics,* vol. 94, 6552, 2003, doi:10.1063/1.1618912.

[199] A. E. Morishige, H. S. Laine, J. Schön, A. Haarahiltunen, J. Hofstetter, C. del Cañizo, M. C. Schubert, H. Savin, and T. Buonassisi, "Building intuition of iron evolution during solar cell processing through analysis of different process models," *Applied Physics A,* vol. 120, 1357, 2015, doi:10.1007/s00339-015-9317-7.

[200] G. Martins, R. S. Bonilla, T. Burton, P. MacDonald, and P. R. Wilshaw, "Minority carrier lifetime improvement of multicrystalline silicon using combined saw damage gettering and emitter formation," *Solid State Phenomena,* vol. 242, 126-132, 2015, doi:10.4028/www.scientific.net/SSP.242.126.

[201] J. Hofstetter, D. P. Fenning, D. M. Powell, A. E. Morishige, H. Wagner, and T. Buonassisi, "Sorting metrics for customized phosphorus diffusion gettering," *IEEE Journal of Photovoltaics,* vol. 4, 1421-1428, 2014, doi:10.1109/JPHOTOV.2014.2349736.

[202] R. Falster, "Process for contamination removal and minority carrier lifetime improvement in silicon," US Patent 5,272,119, 1993.

[203] K. J. Fraser, R. J. Falster, and P. R. Wilshaw, "Cathodoluminescence assessment of annealed silicon and a novel technique for estimating minority carrier lifetime in silicon," *Material Science and Engineering B,* vol. 159–160, 194, 2009, doi:10.1016/j.mseb.2008.05.006.

[204] G. Hahn, M. Käs, and B. Herzog, "Hydrogenation in crystalline silicon materials for photovoltaic application," *Solid State Phenomena,* vol. 156-158, 343-349, 2009, doi:10.4028/www.scientific.net/SSP.156-158.343.

[205] P. Hamer, B. Hallam, S. Wenham, and M. Abbott, "Manipulation of hydrogen charge states for passivation of *p*-type wafers in photovoltaics," *IEEE Journal of Photovoltaics,* vol. 4, 1252-1260, 2014, doi:10.1109/JPHOTOV.2014.2339494.

[206] S. Leonard, V. P. Markevich, A. R. Peaker, B. Hamilton, and J. D. Murphy, "Evidence for an iron-hydrogen complex in *p*-type silicon," *Applied Physics Letters,* vol. 107, 032103, 2015, doi:10.1063/1.4927323.

[207] C. Sun, A. Liu, S. P. Phang, F. E. Rougieux, and D. Macdonald, "Charge states of the reactants in the hydrogen passivation of interstitial iron in *p*-type crystalline silicon," *Journal of Applied Physics,* vol. 118, 085709, 2015, doi:10.1063/1.4929757.

[208] H. M'saad, J. Michel, J. J. Lappe, and L. C. Kimerling, "Electronic passivation of silicon surfaces by halogens," *Journal of Electronic Materials,* vol. 23, 487, 1994, doi:10.1007/BF02671234.

[209] M. Kouketsu and S. Isomae, "Hydrogen passivation of iron-related hole traps in silicon," *Journal of Applied Physics,* vol. 80, 1485, 1996, doi:10.1063/1.363018.

[210] T. Sadoh, K. Tsukamoto, A. Baba, D. Bai, A. Kenjo, T. Tsurushima, H. Mori, and H. Nakashima, "Deep level of iron-hydrogen complex in silicon," *Journal of Applied Physics,* vol. 82, 3828, 1997, doi:10.1063/1.365746.

[211] X. Gao, H. Mollenkopf, and S. Yee, "Annealing and profile of interstitial iron in boron-doped silicon," *Applied Physics Letters,* vol. 59, 2133, 1991, doi:10.1063/1.106103.

[212] T. Heiser and A. Mesli, "How far does the charge state affect the iron behavior in silicon?," *Applied Physics Letters,* vol. 58, 2240, 1991, doi:10.1063/1.104938.

[213] A. J. McEvoy, L. Castaner, and T. Markvart, *Solar cells: materials, manufacture and operation*, 2nd ed., Oxford: Elsevier, 2012.

[214] N. Khedher, M. Hajji, M. Hassen, A. Ben Jaballah, B. Ouertani, H. Ezzaouia, B. Bessais, A. Selmi, and R. Bennaceur, "Gettering impurities from crystalline silicon by phosphorus diffusion using a porous silicon layer," *Solar Energy Materials and Solar Cells,* vol. 87, 605-611, 2005, doi:10.1016/j.solmat.2004.09.017.

[215] J. Schön, H. Habenicht, M. C. Schubert, and W. Warta, "Understanding the distribution of iron in multicrystalline silicon after emitter formation: Theoretical model and experiments," *Journal of Applied Physics,* vol. 109, 063717, 2011, doi:10.1063/1.3553858.

[216] Y. Ohno, K. Kutsukake, M. Deura, I. Yonenaga, Y. Shimizu, N. Ebisawa, K. Inoue, Y. Nagai, H. Yoshida, and S. Takeda, "Recombination activity of nickel, copper, and oxygen atoms segregating at grain boundaries in mono-like silicon crystals," *Applied Physics Letters,* vol. 109, 142105, 2016, doi:10.1063/1.4964440.

[217] N. E. B. Cowern and C. Ahn, "TCAD in the semiconductor industry and its advantages for solar cell manufacturing," *Photovoltaics International,* vol. 12, 72-80, 2011,

[218] D. Berney Needleman, H. Wagner, P. P. Altermatt, Z. Xiong, P. J. Verlinden, and T. Buonassisi, "Dislocation-limited performance of advanced solar cells determined by TCAD modeling," *Solar Energy Materials and Solar Cells,* vol. 158, 29–36, 2016, doi:10.1016/j.solmat.2016.06.031.